Factors affecting toxicant sensitivity of LUHMES-derived human neurons

Dissertation zur Erlangung des

akademischen Grades eines

Doktors der Naturwissenschaften (Dr. rer. Nat.)

vorgelegt von

Gutbier, Simon

an der

Universität Konstanz

Mathematisch-Naturwissenschaftliche Sektion

Fachbereich Biologie

Konstanz, 2018

Tag der mündlichen Prüfung: 06.07.2018

1. Referent/Referentin: Prof. Dr. Marcel Leist

2. Referent/Referentin: Prof. Dr. Thomas Brunner

3. Referent/Referentin: Prof. Dr. Marcus Groettrup

Summary

The use of cell-based models in neurotoxicology and for neurodegenerative diseases is driven by limitations of animal data predictivity, legislative pressure and the increased availability of relevant cells. As all model systems cell-based *in vitro* models have their restrictions and limitations. For instance, the toxicological sensitivity of neuronal cells might be affected by genetic variability, differences in the metabolic state and the presence or absence of secondary cell types (e.g. astrocytes).

The aim of this thesis was to characterize different factors affecting toxicity outcomes in neurons derived from a dopaminergic neuronal cell line (LUHMES: Lund human mesencephalic cells).

In a first project, the conditionally immortalized cell line LUHMES was characterized with respect to changes in cellular metabolism occurring while differentiating from neuronal precursor cells to mature dopaminergic neurons. It was observed that changes in metabolic utilization and demands, i.e. the developmental state of the cells, correlate with an increase or decrease in toxicant sensitivity. The direction of the sensitivity change was defined for toxicants of different mode of action.

In the second project, genomic stability and reproducibility within different subpopulations of this cell line were investigated. Notably, even though LUHMES have an intact set of chromosomes, a few passages in different environments (i.e. transfer to a different lab and deposition at a cell bank) were sufficient to introduce differences between subpopulations, as revealed by whole genome sequencing. These differences did not manifest as obvious genetic alterations, (i.e. larger chromosomal aberrations or mutations directly changing amino acids), but were rather founded in SNPs in non-coding regions or pleiotropic effects, which strongly influenced the toxicant sensitivity of the subpopulations.

In the third project, the LUHMES cell line was used to discover stress pathways which increase cellular resilience against disturbance of the ubiquitin-proteasome system, one major hallmark of Parkinson's disease (PD). NRF-1 was identified as a major transcription factor coordinating proteasomal recovery. Increased external glutathione (GSH) supply was found to increase NRF-1 expression and to allow cellular survival. By co-culturing LUHMES cells with astrocytes, it was observed that astro-

cytes are of great importance for neuronal thiol-supply and increase neuronal GSH, thereby reducing neuronal sensitivity for proteasomal inhibitors.

In summary, these findings suggest that most model systems, used as basis for animal free methods, require more scientific characterization of robustness and resilience factors. By the characterization of these factors further insight into underlying mechanisms of physiological cell-cell-interactions, cellular resilience pathways as well as modes of toxicity can be discovered, and interpretation of toxicological data can be facilitated.

Zusammenfassung

Forschung an zellbasierten *in vitro* Modellen für Neurotoxizitätsstudien und zur Modellierung von neurodegenerativen Erkrangungen gewinnt immer mehr an Bedeutung. Die Gründe hierfür liegen zum einen in einer eingeschränkten Anwendbarkeit und Vorhersagekraft von Tiermodellen für den Menschen und zum anderen in einem erhöhten Druck durch neue Gesetze und Regularien. Wie alle Modelle unterliegen auch zellbasierte *in vitro* Modelle Einschränkungen, was ihre Vorhersagekraft und Gültigkeit betrifft. Zum Beispiel kann die Sensitivität von Neuronen gegenüber Neurotoxikantien durch verschiedene Faktoren beeinflusst werden. Hierzu zählen unter anderem der metabolische Status der Zellen, genetische Veränderungen in den Zellen und die Anwesenheit weiterer Zelltypen in der Kultur.

Ziel dieser Arbeit war es zu untersuchen wie diese Faktoren die Sensitivität von dopaminergen Neuronen, die von der LUHMES (LUHMES: Lund human mesencephalic cells) Zelllinie generiert wurden, beeinflussen.

Im ersten Projektteil wurden die metabolischen Veränderungen während der Zell-Differenzierung verfolgt. Es konnte beobachtet werden, dass sich die Substratabhängigkeit und die Verwendung von metabolischen Reaktionswegen über den Verlauf der Differenzierung verändern. Diese Veränderungen konnten mit unterschiedlichen Sensitivitäten gegenüber verschiedener Toxikantien in Verbindung gebracht werden und waren abhängig vom Wirkmechanismus dieser Toxikantien.

Im zweiten Teilprojekt dieser Arbeit, wurden zwei Subklone der LUHMES Zellen auf phänotypische und genetische Unterschiede untersucht. Trotz eines intakten Sets an Chromosomen und nur geringen genetischen Abweichungen waren wenige Passagen in unterschiedlicher Umgebung (Zellbank und ursprüngliches Labor) genug um deutliche Unterschiede in ihrem Differenzierungsverhalten zu dopaminergen Neuronen hervorzurufen. Diese Unterschiede führten zu eine veränderten Sensitivität gegenüber einem Toxikant, der häufig zur Modellierung der parkinsonschen Krankheit verwendet wird.

Außerdem wurden die LUHMES Zellen verwendet um neue Signalwege und Mechanismen zu identifizieren, die eine erhöte Wiederstandskraft der Zellen

gegenüber Störungen im Ubiquitin-Proteasom System ermöglichen. Ein gestörter Proteinabbau, der durch Defekte in diesem System hervorgerufen werden kann, ist ein Hauptcharakteristikum der parkinsonschen Krankheit und dadurch von großem Interesse. Es konnte gezeigt werden, dass NRF-1 eine entscheidende Rolle in dieser Stressantwort spielt und für das Überleben der Zellen von großer Bedeutung ist. Durch das Hinzufügen von Astrocyten zu den Neuronen konnte Glutathione (GSH) aus Astrocyten als wichtiger Modulator der Stressantwort auf Proteasominhibition ermittelt werden. Das GSH verstärkte die NRF-1 Antwort und ermöglichte das Überleben der Neuronen in Anwesenheit von Proteasominhibitoren.

Zusammenfassend benötigen die meisten zellulären Modellsysteme eine eingehende Charakterisierung von potentiellen Faktoren, die die Robustheit und Ausfallsicherheit beeinflussen. Durch eine solche Charakterisierung können neue Einsichten in zu Grunde liegende Mechanismen gewonnen und die Interpretation von toxikologischen Daten erleichtert werden.

Table of content

1. Introduction[1]:

1.1 Challenges in Neurotoxicology and neurodegeneration

Regulatory toxicology is undergoing a major transition from an animal-experiment driven discipline to a mechanism-based science, promoting also *in vitro* experimentation (1, 2). This change extends in related fields as well, such as neuro degeneration, where cellular models are the first choice to study underlying mechanisms. The transition from the current 'black box' approach of animal experiments towards a new approach using mainly *in vitro* testing to identify the mechanism is driven by many practical considerations (3-6). This includes, but is not limited to: (i) the concordance and transferability between animal and human toxicity is in a lot of cases low. For example rodents have been described to be predictive of human toxicity in less than 50 % of the studies (7); (ii) *in vitro* safety testing and mechanistic characterization can minimize the number of animals needed; (iii) reduction of animal use and transition to high-throughput methods should decrease the cost and time, and increase the reliability of experimental results.

If we consider neurotoxicology and neurodegeneration, the scientific reasons supporting the complementation or substitution of the current methods utilizing animals by *in vitro* testing using human cells are multifaceted. Even though the basic composition of the human brain is not as different from a rodent one as once thought (8), there are still significant and important differences (9). For example, there are species-specific differences in: (i) the constitution and architecture of the neocortex (10); (ii) the timing of neurogenesis (11); (iii) the spatial and temporal expression patterns of developmental genes (12);(iiii) the occurrence of cell types (i.e. Von Economo neurons) (13, 14).

[1]: parts of this introduction are taken and modified from the Review:
In vitro acute and developmental neurotoxicity screening: an overview of cellular platforms and high-throughput technical possibilities.
Gutbier S[*], Schmidt BZ*, Lehmann M*, Nembo E, Noel S, Smirnova L, Forsby A, Hescheler J, Avci HX, Hartung T, **Leist** M, Kobolák J, Dinnyés A.
Arch Toxicol. 2017 Jan;91(1):1-33. doi: 10.1007/s00204-016-1805-9. Epub 2016 Aug 4. Review
[*]shared first authors

The species differences also extend to astrocytes, which are more abundant (15, 16), larger, have 10 times more processes and exhibit different signaling processes (17) in humans than in rodents. However, the most important difference in brains of diverse species lies in the sequence of human proteins and their rodent counterparts. This differences result in altered receptor affinities and enzyme recognition and can have effects on the inflammatory response (18).

In regard to neurodegeneration one should also consider that significant variation between rodent and human disease biology has been suggested (19) and that this discrepancy in disease models might account for the vast clinical failure of drugs that work in animal models (18).

1.2 The brain: a special environment

The brain's extraordinary structure and function lead to a special sensitivity to toxicity and degeneration: in comparison to other organs, "neurotoxicity" normally does not affect the entire nervous system, like for example hepatotoxicity the entire liver, but only very specific and small areas. However, this can still lead to a dramatic loss of function. A prominent example here is the selective loss of dopamine neurons in the *substantia nigra pars compacta*, which only accounts for 3% of the human central nervous system (CNS). The death of this neurons leads to Parkinson's disease (20, 21). There are six specific properties, which make the brain a special environment and contribute to this selective toxicity affecting subpopulations. These should be definitely considered in the choice of models of neurotoxicology and neuro degeneration: (i) the blood brain barrier (BBB), (ii) increased lipid content, (iii) the high energy demand of the CNS, (iv) signal transmission, (v) morphology of neural cells, and (vi) the specific biochemistry of neurons (22).

(i) The blood brain barrier protects the brain against several neurotoxicants (23, 24) and shields the cells of the brain from the immune system of the body (24). However, there are several ways how substances can cross the BBB, namely directed transport, diffusion over cell membranes (lipophilic substances) and pericellular passage of water soluble substances across tight junctions (25-27). Another way of a toxicant or a drug to cross the BBB are precursor substances (such as 1-methyl-4-phenyl-1,2,3,6-tetrahydropyridine or L-Dopa) that cross the BBB and are then meta-

bolically activated within the CNS, for example by astrocytes (28). Therefore, in the course of neurotoxicity studies or developing new pharmacological entities, the capability of a substance to come across the BBB should always be assessed (23). However, the protection of the BBB does not include all neurons in the body (29), due to the lack of a BBB in the peripheral nervous system and the circumventricular organs (29).

(ii) The high ratio of membrane to cytoplasm of neurons, and the additional amount of lipids in the membranes from the myelin sheaths forming Schwann cells or oligodendrocytes leads to a high lipid content in the brain. This increased lipid content might affect the vulnerability as it favours the accumulation of lipophilic substances, e.g. methylmercury(30).

(iii) The maintenance and generation of membrane potential are the main reasons for the high ATP demand of neurons. In addition, directed transport and long transport-distances increase the demand of energy compared to other cell types. This includes mainly transport of organelles, such as mitochondria (31, 32) and of components of the translational machinery (33).

(iv) Signal transmission between neurons is the major function of the nervous system. For a successful transmission of signals, neurotransmitters have to be released into the synaptic cleft and bind to their target receptors on the postsynaptic neuron. Essential for the correct signal transmission are the packaging of neurotransmitters into vesicles, and the removal of released neurotransmitters from the synaptic cleft. These delicate processes are susceptible to disturbances by neurotoxicants and once malfunctioning may cause neurodegeneration (22).

(v) Compared to other cell types, neurons have a specific morphology, as they possess long projections called axons. These projections can reach a length that is >100,000 fold the length of the cell body and therefore create special requirements on intracellular transport and represent a special site of loss susceptibility (31).

(vi) Subgroups of neurons display specific biochemical properties**,** which are associated with specific vulnerability of these neurons compared to their neighboring cells. One example are dopaminergic neurons that produce and release the neurotransmitter dopamine, which autoxidizes quickly. Disturbances in the release of dopamine (by toxicants such as methamphetamine) or inhibition of dopamine re-uptake (e.g. by

cocaine), can result in increased autoxidation of dopamine causing oxidative stress for these neurons (34, 35).

Another point, also addressed in this thesis is cell maturity, which can have also substantial influence on the susceptibility to neurotoxicants (23, 36). On one hand, the development of the nervous system requires strict control of several processes (e.g. neural tube formation and closure). This control is mediated by sensitive signalling pathways, which are susceptible to very small perturbations (37-41). On the other hand, with progressing differentiation the metabolic demands might change resulting in an altered toxicant sensitivity (42).

These aspects should be taken into account when selecting and establishing cellular platforms and methods to test for neurotoxicity or to model neurodegeneration.

1.3 Endpoints and analytical methods in *in vitro* models of neurotoxicity and neurodegeneration

Hundreds of targets may be affected by neurotoxicants or altered after the neurodegenerative stressor is applied. One principle that facilitates neurotoxicity testing *in vitro*, is the concept of adverse outcome pathways (AOP). It summarizes and connects a sequence of molecular initiating events (MIE) and downstream key events (KE). Even though all of this MIE and KE might be assessed on their own, the more practical and rational approach is to develop an assay for downstream key events (KE), which correspond to essential neuronal functions and are affected by more than one MIEs. Thus, the approach of AOP might therefore provide a basis for *in vitro* neurotoxicity testing and may also be applicable for the choice of neurodegenerative models (43-46).

Even though there are many endpoints and methods that might be applicable to neurodegeneration or neurotoxicology, the focus in the following is on “high-throughput” methods, such as cell viability, neurite outgrowth and integrity, monitoring spontaneous electrical activity of neuronal networks, and on analytical methods, such as transcriptomics and metabolomics. An overview about the different experimental approaches to define neurotoxicity and neurodegeneration is given in scheme 1.

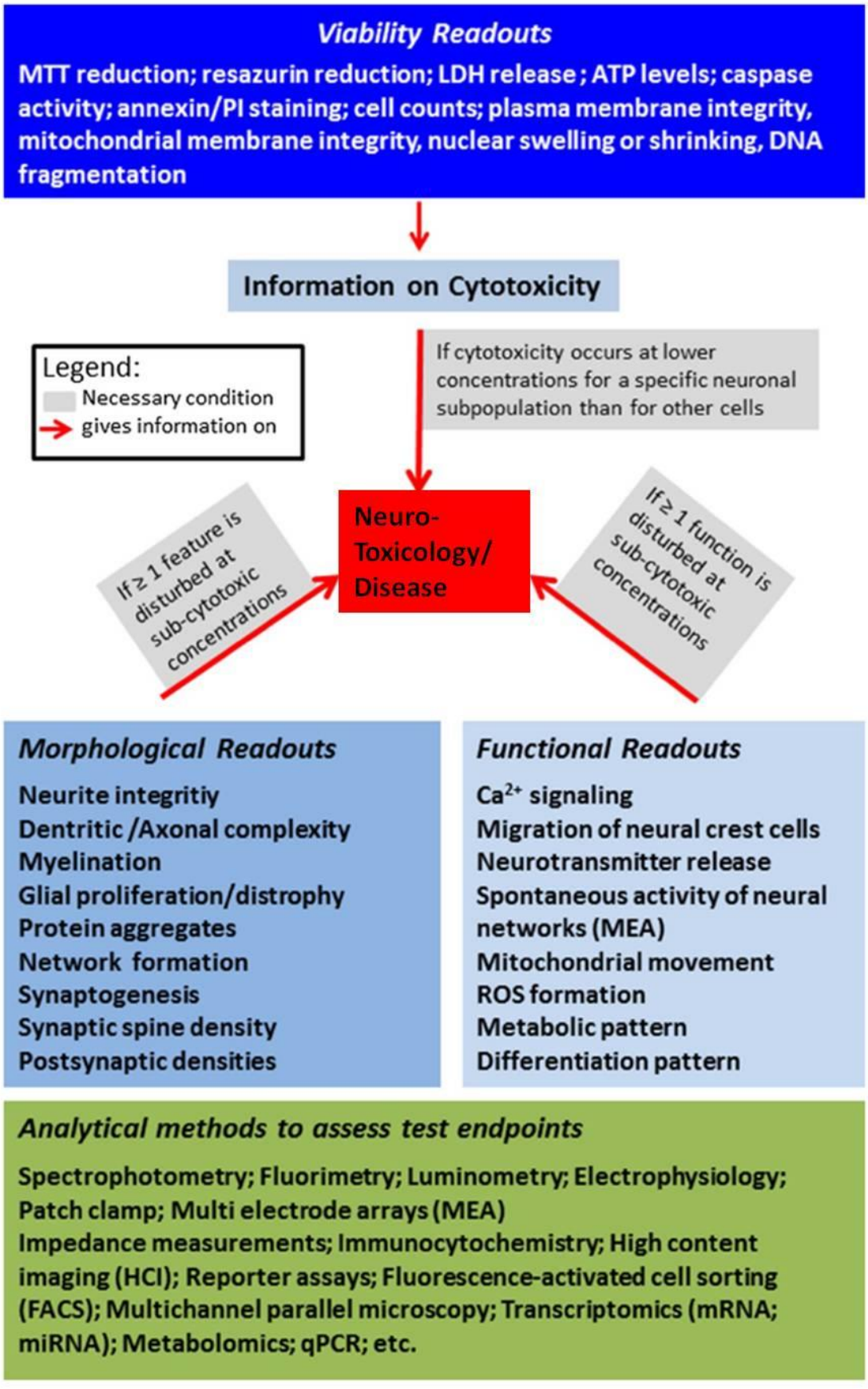

Scheme 1: modified from Schmidt, et al. (22). Summary of readouts and analytical methods for defining neurotoxicology and to assess neurodegenerative processes.

1.3.1 Cell viability assessment

Measurement of ATP as readout for functional metabolism (47, 48) or quantifying the reduction of resazurin or tetrazolium salts (e.g. MTT) by viable cells (28, 49, 50) are widely used endpoints addressing cell viability. Another high-throughput endpoint is the assessment of lactate dehydrogenase (LDH) release from cells (51, 52), which is an indicator of irreversible cell damage. Like every assay, these methods also have limitations. For example, in cultures consisting of more than one cell type, cell death of one type of cells can be masked by proliferation of another type of cells (53). To circumvent this, methods that involve counting of viable cells are often chosen, which can be combined with further image based methods.

1.3.2 Neurite outgrowth and stability

Exposure of developing neurons to developmental neurotoxicants may inhibit the growth of axons and/or dendrites (54). One of the first high throughput assays measuring the effect of substances on neurite growth (55) used Neuroscreen-1 cells, which is a subline of the PC-12 rat neuronal cell line. For visualization of the neurites immunostaining for β-III-tubulin was used and a scoring algorithm, which distinguished viable from dead cells and neurites from somata was developed. In a similar approach, human mesencephalon derived LUHMES cells were used. This conditionally immortalized cell line grows an intricate neurite network, upon cessation of proliferation. Using this cells in the phase of rapid neurite growth and measuring neurite growth and cell viability, allowed the identification of specific neurotoxicants by comparison of the EC50 values for viability and neurite growth (56, 57). This assay was already applied to screen larger compound libraries. Furthermore, the results were compared to the effect on the neurite outgrowth of stem cell derived peripheral neurons. Thereby selective differences have been observed (58).

A further readout, more relevant to neurodegenerative models can be to monitor degeneration of already formed neurites (56). The human neuroblastoma SH-SY5Y cell line can be used for both neurite outgrowth studies (59, 60), and neurite degeneration assays (49), simply by quantifying the number of neurites per cell. These assays have also been improved for high-throughput, since they use calcein staining of live

cell structures instead of time-consuming and cost intensive tubulin staining as end-point (56).

1.3.3 Detection of reactive oxygen species

Oxidative stress within cells has been reported as a secondary effect for many neurotoxicants targeting the mitochondrial electron transport and is one major hallmark of the cellular stress in many neurodegenerative diseases, such as PD. Since the mitochondrial pathway is the major energy source of neurons, they have a particularly high intrinsic ROS formation, which has to be controlled. Methods to detect and quantify oxidative stress within cells, encompass quantification of oxygen radicals with colorimetric or fluorescence-based probes (49, 61), determination of glutathione (35, 61-64), or monitoring of the regulation of oxidative stress-responsive transcription factors (e.g. Nrf-2)(65).

1.3.4 Detection of spontaneous neuronal activity

The key function of the nervous system is the transmission and storage of information within the neuronal network. This is achieved by electrical communication between neurons. One approach to measure this uses multielectrode arrays (MEA) that measure non-invasively changes in the extracellular electrical fields of neurons. With MEA one can detect spontaneous or induced electrical activity of neuronal networks *in vitro*. One big advantage regarding the throughput is that MEA instruments are available in multiwell format (22).

In order to address mechanistic questions, it is of high interest to combine the MEA endpoints with other technologies. For example, by addition of metabolomics one can correlate changes in cellular physiology with changes in the metabolism of neuronal cells or neurotransmitters and vice versa (66).

1.3.5 Mitochondrial trafficking

Neurons are particularly vulnerable to toxicants affecting mitochondrial function, as they depend on the oxidative phosphorylation for energy (ATP) production (67). Mitochondrial transport, and fission and fusion of mitochondria are essential for the functionality of mitochondria and for the correct energy supply of the cell. The requirements on transport of mitochondria are different in neurons compared to other cell types due to their long processes. Regarding neurodegeneration, alterations in mitochondrial fission and fusion, increase of mitophagy and decrease of motility have been observed. These endpoints might also be sensitive markers for neurotoxicity (68, 69). For instance, dopaminergic neurons were found to change their mitochondrial motility already 6 h after MPP^+ exposure, which is very early before cell death occurs (after 60-72 h) (70). Interestingly, several studies have used high content imaging (HCI) approaches to monitor mitochondrial dynamics in various cell types and these protocols might be applicable to neurons as well (71-73).

1.3.6 High content imaging

One widely used analytical method to measure several of the beforehand mentioned endpoints is high content imaging (HCI), which refers to automated high-throughput multicolour fluorescence microscopy (74). For this analytical method, cells are either stained with cell permeable dyes, or fixed and immunocytochemically stainined. Alternatively, cells, which express fluorescent proteins, can be employed and changes in fluorescence intensity and distribution, cell morphology and cell movement can be monitored. The major challenge of HCI is data analysis. Therefore, automated analysis tools such as “NeurphologyJ” (an ImageJ plugin) and “HCS-Neurons” are of big interest (75, 76). Other software tools provide automated neuronal feature extraction algorithms (77) or focus on the high throughput application by allowing scripts that can be applied for unlimited number of pictures (i.e. Cellprofiler or KNIME)(78, 79). However, issues such as acquired data, manual correction of analysis, assay development and the speed of data acquisition still limit the throughput of this method and therefore needs improvement.

1.3.7 Transcriptomics

Another analytical method to address toxicant induced changes or cellular changes prior to neurodegeneration, caused by non-toxic concentrations, is transcriptomics (40, 80-82). For example, in a report from the pan-European ESNATS research project (Embryonic Stem Cell-based Novel Alternative Testing Strategies) the feasibility of this method for developmental neurotoxicity testing was investigated (83). Enrichment of transcription factor binding sites (TFBS) in response toxicant exposure across several cellular systems was observed. This points to the possibility to identify a set of “common cytotoxicity TFBS” or specific patterns for toxicant groups. Several studies also demonstrated that transcriptome changes correlate with toxicant concentrations (84, 85), which can be employed to identify biomarkers, and to classify compounds in an unbiased way (80, 86).

1.3.8 Metabolomics

Metabolomics includes measurement of metabolites inside and outside of cells. This technology can be used for identification of potential biomarkers, which indicate cellular stress adaptions following neurotoxicant exposure or changes leading to neurodegeneration (87). Metabolomics can either be untargeted or targeted. In targeted metabolomics, known and predefined metabolites are measured. This approach can be further extended by feeding 13C-labeled glucose or glutamine to the cells, which allows time resolved metabolic activity monitoring (88). Meanwhile, untargeted metabolomics is naïve of prior knowledge and thus may help to elucidate unknown metabolic features triggered by toxicants, such as upregulation of compensatory pathways or activation of secondary metabolism.

Given the possible applications and information gain by the use of metabolomics, one should be careful with this relatively new and promising technique. Awareness of the pitfalls, especially of untargeted metabolomics (e.g. identification of the metabolites measured, and appropriate quality assurance and reproducibility) is mandatory for meaningful data interpretation (89). Another relevant issue that should be considered is that both, the extraction and analytical methods applied, influence and limit the set of metabolites that can be assessed.

1.4 Cellular platforms

Cellular platforms, established for neurotoxicity testing and modeling of neurodegenerative diseases, are diverse. They comprise the complete range from non-human primary cells to human induced pluripotent stem cell (hiPSC)-derived neurons. The current development trends to more elaborate cellular systems, including cell types, and even cell combinations, in which all organ specific cell types and functions are combined to a human on a chip system (23). A short summary of the described cell sources and their advantages and shortcomings is depicted in scheme 2.

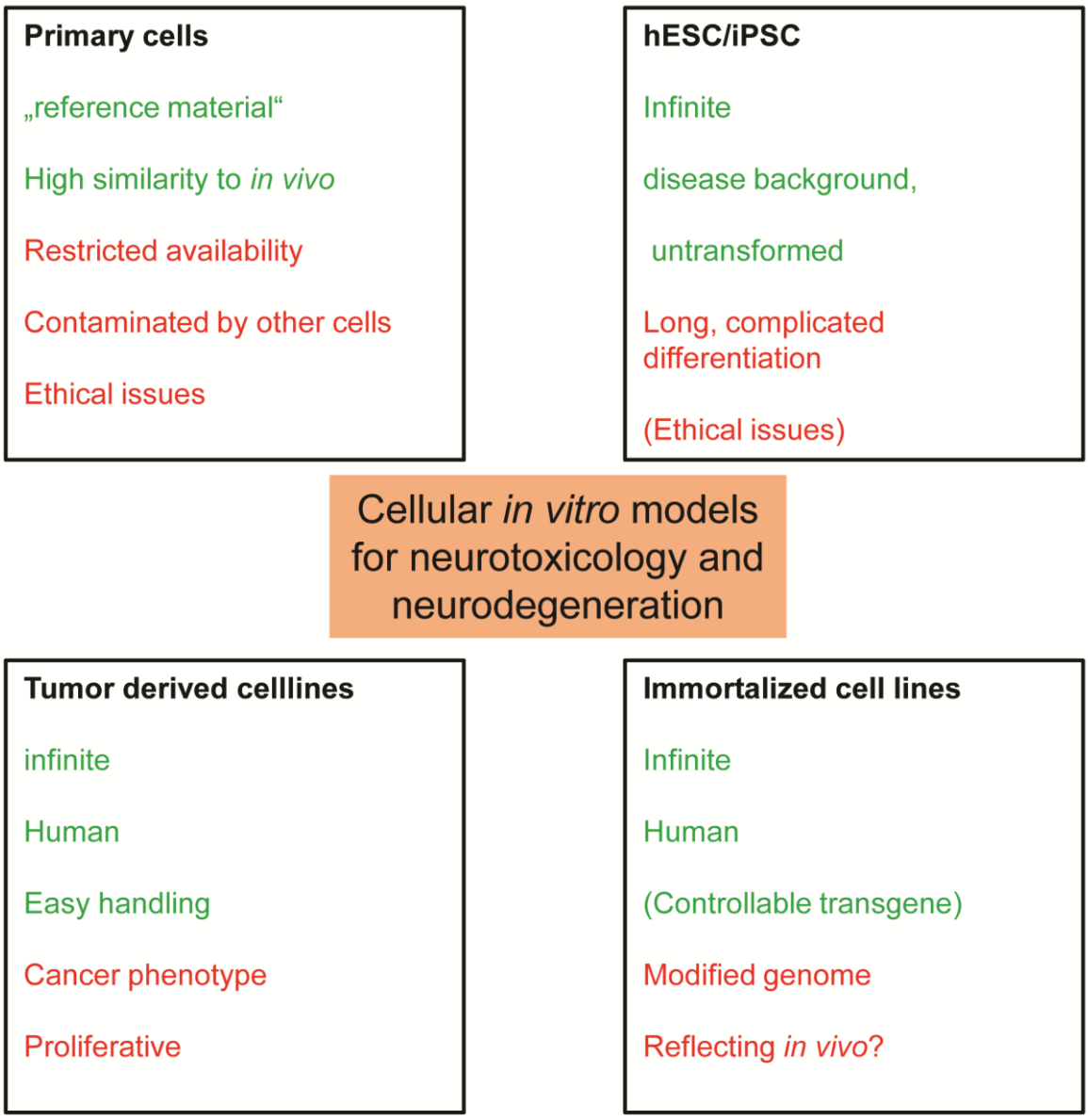

Scheme 2: Overview of main sources of cells used in cellular *in vitro* models for neurotoxicity testing and modelling of neurodegenerative diseases. Main advantages of each origin are listed in green and disadvantages in red.

1.4.1 Non-human primary neural cells and neural cell lines

In the field of non primary cells, re-aggregated spheroids (90, 91) or enriched cultures of neurons (48, 90, 92, 93), or astrocytes (94) are still frequently used. However, primary cells always require fresh preparation from animals. Therefore, immortalized cell lines, which reflect a neuronal phenotype derived from murine or rat, have been established (95-97). They were generated either from neoplasms (neuroblastomas, phaeochromocytomas) (e.g. the Neuro-2a; PC-12, HT22(98)) or cells were immortalized by oncogenes (e.g. IMA(15, 99)).

1.4.2 Human primary cells and immortalized human neural progenitor cell lines

Availability of human primary cells is very limited and often there are ethical issues limiting the use even further. Most of this human cell material is derived from abortions or brain surgery resections. Some, more relevant for neurodegenerative studies, might also come from brain donations. This diverse background has strong effects on batch differences and therefore affects reproducibility to a far extent. However, there are protocols existing that describe how to obtain pure populations of neurons, microglia, oligodendrocytes, and astrocytes from fetal human brains (100). Moreover, primary cells have been used in neurotoxicological studies as well (101).

The generation of immortalized cell lines from neurons obtained from the mesencephalon (102-106) the cortex (107), the subventricular zone (108) or from the spinal cord (109) is a second strategy to circumvent the beforehand mentioned limitations. These cells were generated either by over-expression of an oncogene, or, to avoid the use of oncogenes, over-expression of human telomerase. The neuronal progenitor cell lines obtained by these means provide a proliferative cell population which can be used to generate large numbers of cells. Further alternatives for neurotoxicological modelling arise from advancing in 3D cultures and employing these cells as cell source (110).

A second strategy for the generation of human cell lines is the isolation from tumor tissue. The most widely used example for such a cell line is the SH-SY5Y human

neuroblastoma cell line, which might be used in their standard phenotype, or be differentiated to cells displaying more neuronal properties (111).

A third source are human neural stem cells, which can be expanded *in vitro* and differentiated to various cell types (22, 112, 113).

1.4.3 Human embryonic stem cells (hESCs)

Embryonic stem cells (ESCs), firstly isolated from the inner cell mass of murine blastocysts, are pluripotent cells, which have the potential of continuous self-renewal and the capacity to differentiate into any cell type of the body (114, 115). After the generation of murine ESCs, protocols for the isolation of cells of human origin have been developed (116, 117).

Murine ESC have been in use already a long time for *in vitro* developmental toxicity testing (118) and the murine ESC-based Embryonic Stem Cell Test (EST) became an OECD and ECVAM validated platform for embryotoxicology testing (119). The protocols developed for neuronal differentiation from mESC are robust and still in use for DNT testing (37, 40, 120).

Nevertheless, concerns about species differences were the main drivers for the development of *in vitro* toxicology screens based on hESCs (121). Therefore, in order to establish new model systems of neurotoxicology and neurodegeneration differentiation protocols for hESCs have been developed. These protocols allow the differentiation into various neuronal subpopulations (e.g. dopaminergic, glutamatergic), astrocytes, microglia and oligodentrocytes (122, 123). Recently, a neurite outgrowth assay, based on hESC derived neurons and using automated high-content screening, proved the validity and importance of hESC derived cells as *in vitro* toxicological model (124, 125).

1.4.4 Human Induced Pluripotent Stem Cells (hiPSC) and induced neurons (iNeurons)

In 2006 the successful reprogramming of murine somatic cells into stem cells was achieved (126), and one year later the generation of human induced pluripotent stem cells (hiPSCs) was also accomplished (126, 127). Nowadays, the generation of hiPSCs, using defined factors and diverse methodologies are well established and frequently used (128, 129). A large body of research is showing that hiPSCs share most characteristics of hESCs (130, 131) and the self-renewal ability makes hiPSCs an unlimited source of practically all cell types of the body. The visions for potential uses range from cell replacement therapy through drug-screening and disease modelling to toxicity testing (132-134).

The most important point, when applying hiPSC derived cells for toxicity models, is to differentiate cells that model closely the desired celltype found *in vivo*. Although, there are many protocols for the generation of different neuronal cell types from hESC exisiting, most have to be adopted for the use with hiPSC(130, 135-137). Nevertheless, within the last 10 years, several protocols have been published which generate neuronal cells from hiPSC, e.g. dopaminergic -, spinal motor -, cholinergic – and glutamatergic neurons as well as astrocytes and oligodendrocytes (122, 123, 131, 138-142).

An alternative way to full differentiation of certain cell types from hiPSC is the generation of the self-renewing progenitor cells of the distinct organ (e.g. neuronal stem cells). Different attempts aimed to directly convert somatic cells into neurons (iNeurons) without prior reprogramming to hiPSC (143-145). This technique might allow faster, simpler and cost effective generation of neurons. Nevertheless, the resulting neuronal populations need to be properly characterized and validated prior to potential practical applications.

1.5 Advantages of LUHMES

MESC 2.10, the cells from which the LUHMES (Lund Human Mesencephalic) subclone was generated, were created from the mesencephalic tissue of an aborted eight week old embryo by conditional immortalization. For the immortalization, a retroviral LINX v-myc vector enabling a tetracycline-controlled v-myc expression, was introduced (102). Cells that are transfected by this vector express v-myc (in the ab-

sence of tetracycline), which enables them to stay in a proliferating state. The addition of tetracycline stops the v-myc expression and initiates the differentiation. The LUHMES subclone was selected for a robust dopaminergic phenotype by Lotharius et al. in 2005 (34).Once differentiated this subclone forms an intricate network of neurites and displays biochemical and morphological properties of mature dopaminerigic neurons. Differentiated LUHMES expressthe characteristic markers of DA neurons and are sensitive towards MPP^+ (35, 63, 104). These characteristics make this cell line an ideal candidate for manifold PD *in vitro* studies. The fast proliferation in the proliferative state and the highly synchronized and fast differentiation allow the large scale generation of neurons with highly robust and reproducible properties. The nearly unlimited availability and fast generation of a defined cell population makes this cell line ideal for the use in biochemical and multi-omics studies where the required cell number or homogeneity are often the limiting factors in other cellular systems. In contrast to neuroblastoma cell lines, e.g. SH-SY5Y, LUHMES have an intact set of female chromosomes (103) and might therefore have a more relevant phenotype for disease and neurotoxicity modeling. Since its creation, the LUHMES cell line has been used in several studies about neurodegeneration and neurotoxicity (35, 49, 63) and has been deposited in 2006 at the American Type Culture Collection (ATCC).

According to our knowledge about LUHMES cells, they represent a suitable and promising model for both, neurodegeneration and neurotoxicity studies. Further characterization of their properties and awareness about potential pitfalls (e.g myc artifacts) render them as a state of the art model system, worth to be understood and explored further.

1.6 Requirement of cell authentication and characterization

Reproducibility in preclinical research is estimated to be lower than 50% and irreproducible clinical research is assumed to cost 28 billion dollar per year only in the US (146). Primary causes for reproducibility problems, besides study design, laboratory protocols, reporting, data analysis and biological reagents, are reference materials, such as cell lines (146). Despite their importance to biological and biomedical research, a lot of cell lines are misidentified or contaminated by other cells. For exam-

ple over 400 cell lines thought to be derived from one tissue have been shown to originate from a different tissue (147). Moreover, a lot of cell lines thought to be tissue specific have been shown to be HeLa, but are still used as tissue specific models in a lot of publications (148).Therefore, cell line authentication and characterization is a topic concerning all scientist (147).

It has been shown that over-subculturing with too many passages may affect as well cell line characteristics and reproducibility. Genetic heterogeneity of the parental line and sub-selection during culturing is suspected to be the underlying mechanism leading to genetic drift that might result in genetic distinct subclones (149). To increase reproducibility, accurate documentation of species, sex and tissue as well as the monitoring of genotypic and phenotypic changes over time is thought to be essential. Furthermore, cellular maintenance should move into focus as potential driver of genetic drift (149).

Chromosome painting and short tandem repeat (STR) profiling cannot fulfill quality assurance requirements, therefore single nucleotide polymorphism (SNP) profiling should be conducted additionally. Furthermore, the sharing of cell lines has been suggested to be discouraged or actively banned (150). Since changes in phenotype might also be caused by small mutations in promoter regions or alterations in the epigenetic landscape, quality controls such as marker expression and functional tests for toxicant sensitivity might be necessary when using and qualifying a cell model for toxicant testing.

1.7 Stability and drift in cell culture

As mentioned in chapter 1.6 genetic stability and drift might have strong influence on experimental outcome and reproducibility. The genetic stability might vary between cell lines. Nevertheless, it is an issue affecting every cell type, from tumor origin to stem cells. For example, sequencing of the genome of HeLa cells and comparison of copy numbers displayed a high level of aneuploidy and large structural variants. Gene expression analysis identified alterations in cell cycle and DNA repair pathways compared to normal human tissue (151). Another cell type often used in models of neurotoxicity and neurodegeneration are the neuroblastoma cells SH-SY5Y. For this

cell line mycn amplification, gain of 17q and deletion of 1p36 (152, 153), as well as overall strong alterations in the integrity of the genome, have been reported. This genetic alterations might affect the suitability of this cell lines as disease model as well as the outcomes of neurotoxicity studies conducted with them.

In contrast to cancer cells, one would expect euploidy and a stable genome in hESC and iPS cells. However, there is evidence that stem cells start accumulating SNPs in coding regions in later passages due to subclonal growth. Suggesting a mosaic genome structure and a subclonal selection due to cell culture conditions (154). Moreover, some hESC and iPS cell lines tend to manifest aneuploidy (i.e. trisomy 12 or X and amplification 17q) which provide a selection advantage by multiplication of stemness or anti apoptotic genes (149).

Therefore, detailed characterization and quality controlling over time of the cell lines used for disease modeling or neurotoxicity studies should always be an integral part of the model setup in order to increase reproducibility and validity of the system.

1.8 Influence of differentiation status on toxicity

An important aspect, when using complex cellular models including differentiation of cells to another cell type, is that differentiation can lead to differences in the susceptibility to neurotoxicants. Differentiation of neurons is characterized by the arrest of the cell cycle, resulting in a stop of cellular division. This process is accompanied by obvious morphological changes (e.g. neuritogenesis), and a strong alteration in the metabolic phenotype (67, 155). The latter is mainly due to changes in the demand of glucose and glutamine, which contribute to the generation of ATP (156, 157) and are essential metabolites for growth (158, 159). Glucose and glutamine sustain oxidative phosphorylation for ATP production (157). The different metabolic demands can be the underlying cause of observed differences in the response to neurotoxicants. Metabolic characterization of the different cellular differentiation states, can therefore substantially increase the understanding of the cellular model.

1.9 Neurotoxicology and neurodegenerative diseases

Since several epidemiologic studies correlated the exposure to neurotoxicants (e.g. paraquat, rotenone, 1-methyl-4-phenyl-1,2,3,6- tetrahydropyridine (MPTP) and meth-amphetamine) with PD symptoms, these neurotoxicants are nowadays in use as experimental models for neurodegenerative diseases such as PD (21, 160).

For example, rotenone, which is a herbicide, pesticide and fish poison has been found to cross the blood brain barrier (BBB) easily, due to its lipophilic properties. Within the cells it inhibits complex I of the mitochondrial respiratory chain and triggers selectively the loss of DA neurons (20). A second widely used neurotoxicant in animal and cellular models of the neurodegenerative disease Parkinson's is MPTP and its active metabolite MPP^+ (161-163). The discovery of its toxicity in 1983 was triggered by the observation that drug addicts, who injected meperidine-analogs intravenously, developed rapidly severe PD like symptoms. It was reported that the actual drug 1-methyl-4-phenyl-4-propionoxy-peridine (MPPP) was contaminated with MPTP(164). Further studies identified the actual toxic compound as a metabolite of MPTP, MPP^+ (165). The uncharged contaminant MPTP easily enters the brain where it is mainly converted by the monoamine oxygenase B of astrocytes to the unstable intermediate $MPDP^+$. $MPDP^+$ autoxidizes to MPP^+, which is accumulated in dopaminergic neurons via the dopamine transporter (DAT) (28, 161, 165-169). Within the neurons it leads to block of complex I of the respiratory chain and therefore to neurodegeneration.

Neurotoxicant based cellular models for neurodegeneration are often used for mechanistic studies and drug screening approaches, since they are fast and highly reproducible. By targeting complex I, causing oxidative stress and disturbances in the ubiquitin-proteasome system (UPS), they reflect key hallmarks underlying the neurodegenerative process in this diseases. However, they do not completely resemble all processes of age related neurodegeneration as the toxicity in this models occurs within hours to several days and a lot of neurodegenerative diseases are characterized by the continuous slow demise of neurons over several decades (170).

1.10 Influence of astrocytes on neuronal stress response - The advantage of co-cultures

Astrocytes are one of the four major cell types in the brain, with various supportive functions (i.e. nutrient supply of neurons, influence on neuronal growth and differentiation, trophic support, and maintenance of homeostasis) and direct contribution to signal transduction (i.e. release and removal of neurotransmitters) (171). For a long time, astrocytes were described to be the structural framework of the brain, but recently, the discovery of the various other functions changed the perception of astrocytes and increased the interest in this cell type. One aspect contributing to this change is the role of astrocytes in the immune response in acute conditions and neurodegenerative processes, such as AD and PD (172). Another aspect is the observation that the presence of astrocytes also alters toxicological responses and might also affect the outcome of pharmacological interventions (15, 173). Therefore, advancing from a single cell type model to a co-culture model, composed of differentiated dopaminergic neurons and astrocytes, for mechanistic studies might increase the insight in cellular interactions and alterations of stress pathways (99). Identification of endogenous resilience pathways with the involvement of multiple cell types might open new perspectives on possible drug targets.

2. Aim of the thesis:

The aim of this thesis was to characterize different factors affecting toxicity in neurons derived from the dopaminergic cell line LUHMES (Lund human mesencephalic cells). Three particular objectives of the thesis were:

1. The impact of metabolic changes in the course of differentiation on neuronal toxicant sensitivity
2. Characterization of the genetic and phenotypic stability of the LUHMES cell line and the impact on toxicant sensitivity
3. Investigation of the influence of a second cell type on neuronal toxicant sensitivity and trans-cellular resilience pathways

3. Results

3.1 Manuscript #1:

This manuscript has already been accepted for publication in Toxicology and applied pharmacology:

Stage-specific metabolic features of differentiating neurons: Implications for toxicant sensitivity.

Gutbier S*, Delp J*, Cerff M*, Zasada C*, Niedenführ S, Zhao L, Smirnova L, Hartung T, Borlinghaus H, Schreiber F, Bergemann J, Gätgens J, Beyss M, Azzouzi S, Waldmann T, Kempa S, Nöh K, **Leist** M.

Toxicol Appl Pharmacol. 2017 Dec 24. pii: S0041-008X(17)30494-5. doi: 10.1016/j.taap.2017.12.013. [Epub ahead of print]

***shared first authorship**

Stage-specific metabolic features of differentiating neurons: implications for toxicant sensitivity

Simon Gutbier*[1*]*, *Johannes Delp*[1*]*, Martin Cerff*[2*]*, Christin Zasada*[3*]*, Sebastian Niedenführ*[2]*, Liang Zhao*[4]*, Lena Smirnova*[4]*, Thomas Hartung*[4]*, Hanna Borlinghaus*[7]*, Falk Schreiber*[6]*, Jörg Bergemann*[8]*, Jochem Gätgens*[2]*, Martin Beyss*[2]*, Salah Azzouzi*[2]*, Tanja Waldmann*[1]*, Stefan Kempa*[3#]*, Katharina Nöh*[2#]*, Marcel Leist*[1,5#]

1: In vitro Toxicology and Biomedicine, Dept inaugurated by the Doerenkamp-Zbinden foundation, University of Konstanz, 78457 Konstanz, Germany
2: Institute of Bio- and Geosciences, IBG-1: Biotechnology, Forschungszentrum Jülich GmbH, 52425 Jülich, Germany
3: Max-Delbrück-Center of Molecular Medicine in the Helmholtz Association, 13125 Berlin, Germany.
4: Johns Hopkins University, Bloomberg School of Public Health, Center for Alternatives to Animal Testing (CAAT), Baltimore, MD, USA.
5: CAAT-Europe, University of Konstanz, 78457 Konstanz, Germany.
6: Department of Computer and Information Science, University of Konstanz, Konstanz, Germany and Faculty of Information Technology, Monash University, Melbourne, Australia
7: Department of Computer and Information Science, University of Konstanz, Konstanz, Germany
8: Department of Life Sciences, Albstadt-Sigmaringen University of Applied Sciences, Sigmaringen, Germany.

****: shared first author***
#: shared last author

Running title: Neuronal metabolic switch

Correspondence to be sent to:
Marcel Leist, PhD
In vitro Toxicology and Biomedicine, Dept inaugurated by the Doerenkamp-Zbinden foundation at the University of Konstanz, Konstanz, Germany

3.1.1 Abstract

Developmental neurotoxicity (DNT) may be induced when chemicals disturb a key neurodevelopmental process, and many tests focus on this type of toxicity. Alternatively, DNT may occur when chemicals are cytotoxic only during a specific neurodevelopmental stage. The toxicant sensitivity is affected by the expression of toxicant targets and by resilience factors. Although cellular metabolism plays an important role, little is known how it changes during human neurogenesis, and how potential alterations affect toxicant sensitivity of mature vs. immature neurons. We used immature (d0) and mature (d6) LUHMES cells (dopaminergic human neurons) to provide initial answers to these questions. Transcriptome profiling and characterization of energy metabolism suggested a switch from predominantly glycolytic energy generation to a more pronounced contribution of the tricarboxylic acid cycle (TCA) during neuronal maturation. Therefore, we used pulsed stable isotope-resolved metabolomics (pSIRM) to determine intracellular metabolite pool sizes (concentrations), and isotopically non-stationary ^{13}C-metabolic flux analysis (INST ^{13}C-MFA) to calculate metabolic fluxes. We found that d0 cells mainly use glutamine to fuel the TCA. Furthermore, they rely on extracellular pyruvate to allow continuous growth. This metabolic situation does not allow for mitochondrial or glycolytic spare capacity, i.e. the ability to adapt energy generation to altered needs. Accordingly, neuronal precursor cells displayed a higher sensitivity to several mitochondrial toxicants than mature neurons differentiated from them. In summary, this study shows that precursor cells lose their glutamine dependency during differentiation while they gain flexibility of energy generation and thereby increase their resistance to low concentrations of mitochondrial toxicants.

3.1.2 Keywords

Developmental neurotoxicity, metabolomics, energy metabolism, metabolic flux, ^{13}C labeling experiment, oxygen consumption

3.1.3 Highlights

- Precursor cells have less energetic buffer than mature neurons
- The resilience towards mitochondrial toxicants is reduced in neural precursor cells
- A map of the central carbon metabolism of precursor cells has been established
- Metabolism studies suggest dependence of neural precursor on pyruvate and glutamine

3.1.4 Abbreviations

aKG- α-ketoglutarate
AA- amino acid
BM- biomass
CCM- central carbon metabolism
CDW- cell dry weight
DNT- Developmental neurotoxicity
ECAR- extracellular acidification rate
ESI- Electrospray ionization
FCCP- Carbonyl cyanide-4-(trifluoromethoxy)phenylhydrazone
GC-MS- gas chromatography-mass spectrometry
GO- gene ontology
INST ^{13}C-MFA - isotopically non-stationary ^{13}C metabolic flux analysis
IVT- *in vitro* transcription
LUHMES- Lund human mesencephalic cells
ME- malic enzyme
MID- mass isotopomer distribution
OCR- oxygen consumption rate

PC- pyruvate carboxylase

PCA- principal component analysis

PDH- pyruvate dehydrogenase

pSIRM- pulsed stable isotope-resolved metabolomics

RQI- RNA quality indicator

SD- standard deviation

SEM- standard error of the mean

TCA- tricarboxylic acid cycle

3.1.5 Introduction

Developmental neurotoxicity (DNT) testing is currently undergoing a major transition from expensive, time consuming animal based studies to cell-based assays (22). Most *in vitro* tests model a narrow window of development, and they reflect only one or few neurodevelopmental processes. Therefore, in order to obtain toxicity predictions with a high confidence level, several assays will have to be combined to a test battery (174, 175). To cover all actions of DNT toxicants, it is important to focus not only on specific disturbances of key developmental processes. Also blunt cytotoxicity can play a role, if it is specific for a subpopulation of cells that is only present during a particular phase of organ development. For instance exposure to the general cytotoxicant 5-flurouracil can affect facial and hindlimb development in specific ways (176) and exposure to the cell cycle toxicant methylazoxymethylacetat (MAM) is a standard tool to trigger structural and functional DNT (38, 39, 41). The understanding of specific sensitivities to cytotoxicants (82) and of the underlying biological and metabolic basis will be important for mechanistic validation of test systems and for the assessment of their biological relevance (5, 116, 177, 178).

In the early fetus, most cells are highly proliferative in order to generate body growth. For instance, neural precursor cells (NPC) generate abundant progeny to create the nervous system. Some DNT test methods are based on the differentiation of pluripotent cells to NPCs (179, 180). Others use specific precursors of the peripheral nervous system to study their function (79, 181), or such cells are being used to examine for instance astrocytogenesis (182, 183). Monitoring of many of the diverse proliferation and differentiation steps in the nervous system is a pivotal aspect of DNT testing (38, 184). Until now, such monitoring is mainly descriptive, based on the quantification of markers for various cell populations. A step towards a more mechanistic understanding of transitions between cells are time-resolved studies of transcriptional markers (185-188). A further important step requires detailed studies on metabolic changes (189-193) .

Differentiation of neurons implies cell cycle arrest and cessation of proliferation. Besides the obvious morphological changes (e.g. neuritogenesis), this process is accompanied by a strong alteration in the metabolic phenotype (67, 155). Proliferating cells have a higher demand of glucose and an increased glycolytic rate, which contributes to the generation of ATP (156, 157). In addition, glutamine is taken up to

generate essential metabolites for growth (158, 159) and to sustain oxidative phosphorylation for ATP production (157). Post-mitotic neurons in brain tissue cope with a different metabolic situation: they have a higher basal energy demand, but they don't have to generate new cells. Under these conditions, adult neurons metabolize glucose to CO_2 through oxidative phosphorylation via the tricarboxylic acid cycle (TCA) (194). The use of glutamate and glutamine as alternative carbon source is limited to few special situations (195).

Most available data on the central carbon metabolism (CCM) of cells are derived either from cancer cells or from tissue measurements, and there are only few studies comparing different stages of the same cell line. Some data on changes of the metabolic phenotype during cellular differentiation and de-differentiation have been reported for induced pluripotent stem cells and for neural progenitor lines (189, 196-198).

Several other studies characterized metabolic changes when cells switched from exponential growth to growth arrest. For example, two studies reported differences between CHO cells in either growth or stationary phases. Changes occurring during the transition from proliferation to a stationary state were mainly observed in the pentose phosphate pathway, glycolysis and the carbon supply to the TCA (anaplerosis) (199, 200). A further study compared the metabolic differences upon differentiation of neuronal precursor cells to astrocytes (189). All these data sets suggest distinct metabolic differences between proliferating and differentiated cells. The metabolism of cancer cells and of other proliferating cells shows many similarities, presumably due to their shared need to generate new biomass during proliferation (198, 201, 202). Recent data from cultured murine cortical neurons suggest that changes in glycolysis and in the glutamine-glutamate pathway also may play a key role in the process of neuronal differentiation (67). However, there is still a need for detailed information about metabolic alterations during human neuronal differentiation, not at least because this feature might affect the toxicant sensitivity of these cells in different stages of neuronal maturation.

There are multiple examples for cell-type specific toxicity. For a variety of toxicants it has been observed that proliferating progenitor cells are more susceptible to undergo cell death following toxicant exposure than their differentiated progeny (203-206). It has been discussed intensively, whether this might be due to their different levels of

anti-apoptotic proteins, their differences in drug transporter expression, or the replication machinery. However, there are also many situations, when differentiated cells are more toxicant-sensitive than their precursors. Examples are the paracetamol toxicity to primary hepatocytes *vs.* immature hepatic precursors (207) or the neurotoxicity of the parkinsonian toxicant MPP^+ (28, 35, 110). Further examples are astrocyte-specific toxicants such as fluoroacetate, fluorocitrate or 6-aminonicotinamide that selectively affect the energy metabolism of astrocytes (208, 209).

In summary, such altered susceptibilities may depend on a differential expression of targets, receptors, transporters or metabolizing enzymes. Alternatively, altered metabolic states may be responsible for cell stage specific toxicity. To obtain more information on this issue, the present study sets out to characterize metabolic changes upon neuronal differentiation. We used conditionally immortalized dopaminergic neuronal precursor cells (LUHMES cells), which proliferate in their basal condition (d0), and which can be differentiated to post-mitotic dopaminergic cells within 6 days (d6). Proliferating cells express the neuronal precursor markers SOX2, PAX3, BRN3A, ASCL1 and nestin. Upon differentiation, gene expression changes and genes coding for synaptic proteins (e.g. GRIN1, DLG4) and dopaminergic markers like tyrosine hydroxylase (TH), dopamine D2-receptor (DRD2) and the dopamine transporter (DAT) are upregulated. The differentiation process is characterized by its uniformity and synchronization (34, 49, 56, 104). This model system is therefore suitable for biochemical studies that require large numbers of cells at the same differentiation stage. We made use of this model to measure the role of media constituents and the susceptibility to few selected toxicants. To obtain a better understanding of the metabolic states of LUHMES cells, we profiled extracellular key nutrients/products by their rates of consumption/production. Furthermore, we combined the use of stable isotope tracers with state-of-the-art metabolomics and fluxomics approaches. Especially, we applied mass spectrometry based pulsed stable isotope-resolved metabolomics (pSIRM) and isotopically non-stationary ^{13}C metabolic flux analysis (INST ^{13}C-MFA) for the measurement of intracellular metabolite pool sizes and dynamic labeling incorporation profiles as well as the calculation of intracellular metabolic fluxes.

3.1.6 Material and Methods

3.1.6.1 Cell culture

Handling of LUHMES human neuronal precursor cells was performed as previously described in detail (34, 49, 104). Briefly, the conditionally-immortalized cells (expressing a v-myc transgene under the control of a tet-off system maintained in proliferation medium (PM: advanced DMEM/F12, 2 mM L-glutamine, 1 x N2 supplement (Invitrogen), and 40 ng/ml FGF-2) in a 5% CO_2/95% air atmosphere at 37° C. Passaging was three times a week. For differentiation, 8 million cells were seeded in a Nunclon T175 tissue culture flask in PM. After 24 h, medium was changed to differentiation medium (DM: advanced DMEM/F12, 2 mM L-glutamine, 1 x N2, 2.25 µM tetracycline, 1 mM dibutyryl 3',5'-cyclic adenosine monophosphate (cAMP) and 2 ng/ml recombinant human glial cell derived neurotrophic factor (GDNF)). At 48 h later, cells were trypsinised, and seeded in a density of $1.8*10^5$ cells/cm² on dishes precoated with 50 µg/ml poly-L-ornithine (PLO) and 1 µg/ml fibronectin in DM. On day 4 of differentiation, medium was replaced.

3.1.6.2 Standard experimental setup

To generate d6 cells, LUHMES differentiated for 2 days were replated at a density of $1.5*10^5$ cells per cm^2 in DM and left to differentiate for additional 4 days. To obtain d0 cells, proliferating cells were seeded at a density of $6.5*10^4$ cells per cm^2 in PM on PLO/fibronectin coated dishes. At 24 hours after seeding they were used for experiments.

3.1.6.3 Determination of cell numbers and cellular growth

Cells were seeded at standard density into 96 well plates in the respective medium, containing the indicated supplements. The cell number was assessed several times after seeding by live cells imaging, using Hoechst-33342 and calcein-AM dyes, which were applied 30 min prior to imaging. Automated microscopy was used to image, and subsequent algorithmic analysis was used to determine viability: double positive cells were counted as live cells whereas cells only positive for H-33342 were counted as dead. The number of live cells was expressed relatively to the amount of seeded cells.

3.1.6.4 Determination of glucose, lactate and pyruvate in cell culture medium

Glucose and lactate were determined by a commercially available colorimetric cuvette assay (GLU-142 and LAC-142, respectively. Diaglobal, Berlin, Germany). In brief, glucose or lactate was converted by enzymes into colorimetric products which were quantified by spectrophotometric measurements and comparison to calibration standards. Pyruvate was quantified through enzymatic conversion to lactate for which NADH was used up. The decrease in NADH was quantified spectrophotometrically (λ = 340 nm) and compared to calibration standards.

3.1.6.5 Determination of total cellular protein

Total protein content and weight of d0 and d6 cells was measured in cell populations (about 5 x 10^7 cells) detached by trypsinization. The cells were washed, counted and weighed (wet weight). After that, cells were lysed in 1 M NaOH for 24 h, then protein was quantified (BCA assay kit, according to the manufacturer's instructions (Pierce/Thermo Fisher Scientific, Rockford, IL, USA)).

3.1.6.6 Cell viability measurement

Resazurin measurement: Metabolic activity was detected by a resazurin assay. Briefly, resazurin solution was added to the cell culture medium to obtain a final concentration of 2 µg/ml. After incubation for 60 min at 37° C, the fluorescence signal was measured at an excitation wavelength of 530 nm, using a 590 nm long-pass filter to record the emission. After background subtraction, fluorescence values were normalized by setting fluorescence values of untreated control wells to 100%.

LDH release: LDH activity was detected separately in the supernatant and cell homogenate. Cells were lysed in PBS / 0.1% Triton X-100 (V/V) for 1 hour. Ten µl of sample was added to 100 µl of reaction buffer containing NADH (100 µM) and sodium pyruvate (600 µM) in KPP-buffer. Absorption at 340 nm was measured at 37°C in 1 min intervals over a period of 15 min. The slope of the absorption intensity was calculated. The ratio of $LDH_{supernatant}/LDH_{total}$ was calculated using the slopes of supernatant and homogenate. LDH release was expressed in percent (49).

ATP determination: To determine intracellular ATP, cells grown in 24-well plates were scratched and sonicated in PBS-buffer and boiled at 95 °C for 10 min followed by

centrifugation at 10,000 g for 5 min for the removal of cell debris. For the detection of ATP levels, a commercially available ATP assay reaction mixture (Sigma, Steinheim, Germany), containing luciferin and luciferase, was used. Fifty microliters sample and 100 µl of assay-mix were added to a black 96-well plate. Standards were prepared by serial dilutions of ATP disodium salt hydrate (Sigma, Steinheim, Germany) to obtain final concentrations ranging from 1000 nM to 7.8 nM. Determination of protein concentration was performed by using a BCA protein assay kit (Pierce/Thermo Fisher Scientific, Rockford, IL, USA) (35, 47, 210).

3.1.6.7 Extracellular amino acid and ammonia determination

Medium was collected after the indicated time and mixed with 10% (W/V) 5-sulfosalicylic acid (SSA) in a volume ratio of 4 to 1 to obtain a final SSA concentration of 2% in biological triplicates. After shaking for 15 min at 1400 rpm at 4 °C in an Eppendorf Thermomix (Hamburg, Germany), the solution was centrifuged for 15 min at 16,000 x g at 4 °C to separate the supernatant from the protein precipitations. For amino acid analysis, a 1 to 1 mixture of supernatant and sample dilution buffer (pH 2.2, 0.12 M) (Sykam, Fürstenfeldbruck, Germany) was prepared. The amino acids were then quantified using a Sykam S433 Amino acid analyzer (Sykam, Fürstenfeldbruck, Germany). Shortly, amino acids and ammonia were separated by HPLC and subsequent post-column derivatization with ninhydrin. Samples were directly injected in a volume of 100 µl. Chromatography was performed using a lithium based anion exchange column loaded with spherical polystyrene resin (7 µm diameter, 10% crosslinks, cat# 5125022). Elution was performed using buffers with increasing pH and ion strength (pH 2.9 --> pH 12; buffer concentration 0.12 M to 0.45 M), supported by a temperature gradient. Absorbance of the reaction products was quantified at 440 nm (intermediate product; quantifies cysteine and proline) or 570 nm (quantifies all other amino acids). Amino acid concentrations were determined relative to a reference standard using the area under the peak method in the ChromStar 7 software (SCPA, Weyhe-Leehste, Germany) (173). Ammonia was quantified following the same protocol.

3.1.6.8 Determination of cell-specific extracellular metabolic rates

Cell stage-specific extracellular (net) metabolic rates for proliferating d0 cells, i.e., growth rate [h^{-1}], uptake and secretion rates [nmol x 10^6 $cells^{-1}$ x h^{-1}], were jointly es-

timated from extracellular concentration time courses of detectable carbon sources present in the medium and viable cell numbers (0-12 h), using first order ordinary differential equations while accounting for degradation of glutamine (Gln) with a degradation rate $k_{Gln}=2.0\cdot10^{-3}$ [h^{-1}] (199). Confidence intervals of the rate estimates were derived by parametric bootstrapping with 5,000 samples. For post-mitotic (non-growing) d6 cells, cell stage-specific extracellular rates were determined by linear regression of the extracellular concentration time courses (0-24 h) and normalization with the average cell concentration. Cell concentrations were calculated from cell numbers based on a volume of the liquid phase of 2 ml per well and accounting for volume losses of 1.5-4.5% due to evaporation. Standard deviations were obtained using Gaussian error propagation. Calculations were performed with Matlab (The MathWorks Inc., Natwick, USA).

3.1.6.9 Seahorse measurements

Cells were plated 24 h prior to the experiment in PLO/fibronectin-coated “Seahorse 24 well plates” at a density of 100,000 cells (d6 cells) per well or 60,000 cells per wells (d0 cells) in their normal media.

Mitostress test: One hour prior to analysis, medium was changed to Seahorse XF base medium, supplemented with 18 mM glucose, 2 mM glutamine and 1 mM pyruvate. Mitochondrial oxygen consumption was assessed (i) basally and after addition of (ii) 1 µM oligomycin, (iii) 1.5 µM carbonyl cyanide-4-(trifluoromethoxy)phenylhydrazone (FCCP) and (iv) 0.5 µM rotenone with 0.5 µM antimycin A. Mitochondrial parameters were calculated as described in results. After assaying mitochondrial function, cells were counted to normalize oxygen consumption relative to total cell number.

Glycostress test: One hour prior to analysis, medium was changed to Seahorse XF base medium, supplemented with no glucose, 2 mM glutamine and 1 mM pyruvate. Extracellular acidification rate was assessed (i) basally and after addition of (ii) 10 mM glucose, (iii) 1 µM oligomycin and (iv) 50 mM 2-deoxyglucose. Glycolytic parameters were calculated as described in results. After assaying glycolytic function, cells were counted as described above to normalize extracellular acidification relative to total cell number.

3.1.6.10 Non-targeted metabolomics analysis

D0 and d6 cells were cultured according to standardized culture conditions. Metabolite extraction and measurement was performed as described earlier (49). In brief, cells were washed with ice cold PBS and extracted with 80%/20% MeOH/water solution. Supernatants were evaporated to dryness at room temperature in a Speedvac concentrator (Savant, Thermo Fisher Scientific, Waltham, MA, USA). The dried samples were reconstituted and measured by liquid chromatography using Agilent 1260 high performance liquid chromatography system with a Cogent Diamond Hydride column (MicroSol, Eatontown, NJ, USA), followed by a 6520 accurate-mass Q-TOF LC-MS system (Agilent) equipped with a dual electrospray (ESI) ion source operated in negative-ion mode for metabolic profiling. Raw data were processed with Mass Hunter Qualitative Analysissoftware (Agilent, version 5.0) (49).

3.1.6.11 Pulsed stable isotope-resolved metabolomics (pSIRM):

LUHMES cells were cultured as described above. To assure standardized conditions, fresh PM or DM (containing 5.5 mM glucose) was added 4 h prior to start of the labeling (t= -4 h). At t= 0 h, medium was changed again to glucose-free and glutamine-free AdvDMEM/F12 medium (either supplemented with 5.5 mM [U-^{13}C] glucose plus 2 mM [U-^{12}C] glutamine or 5.5 mM [U-^{12}C] glucose plus 2 mM [U-^{13}C] glutamine). Both tracers were purchased from Campro Scientific (Berlin, Germany, cat. numbers CS01-183_417 (glc) and CS01-183_434 (gln), both 99% atom-%). After 0, 2, 8, 16, 30, 60, 180, 360, 480, 1440 and 2880 min, samples were harvested according to the pSIRM protocol for adherent cells in 6-well plates (88). Every biological replicate consisted of two pooled wells of independent differentiations. Cell extracts were stored in 50%-Methanol (Sigma) until further sample processing. The extraction solvent methanol had been supplemented with cinnamic acid (Sigma, 2 µg/ul) as an internal extraction standard control.

Extracts were supplemented with chloroform (Sigma) for methanol:chlorofom:water extraction (5:2:1 v/v/v) and incubated for 30 min at 4°C on a rotary wheel, and subsequently centrifuged for phase separation (15min, maximum speed). Equal volumes of polar phase were collected from each sample separately and dried under vacuum. Extracts were stored at -25°C until continuing with the preparation for GC-MS measurement.

3.1.6.12 GC-MS pSIRM sample preparation

Derivatization was carried out as described with modifications (211). First, dried extracts were dissolved in 20 µl of methoxyamine hydrochloride solution (Sigma, 40 mg/ml in pyridine (Roth)) and incubated for 90 min at 30°C under constant shaking. In a second phase samples were incubated with 80 µl of N-methyl-N-[trimethylsilyl]trifluoroacetamide (MSTFA; Machery-Nagel, Dueren, Germany) at 37°C for 45 min. The in-house alkane standards were added prior to the MSTFA for retention time analysis (10 µl/ 1 ml MSTFA). The extracts were centrifuged for 10 min at 10,000 × g, aliquoted and transferred in 30 µl into glass vials (Th. Geyer, Berlin, Germany) for GC-MS measurement.

Formulation of GC-MS standards for retention index determination, as well as for identification and quantification of metabolites are described in (88). Identification and quantification of standards was performed parallel with the samples. The quantification-standard is an in-lab developed mixture, composed of 65 compounds with known quantities (88). The primary stock is prepared in eight concentrations from 1:1 to 1:200. All eight standards were extracted, derivatized and measured in parallel to the samples. For each batch of measurements a fresh aliquot of quantification standards has been prepared.

3.1.6.13 GC-MS measurements of pSIRM experiments

Metabolite analysis was performed on a gas chromatography coupled to time of flight mass spectrometer (Pegasus III- TOF-MS-System, LECO Corp., St. Joseph, MI, USA), complemented with an auto-sampler (MultiPurpose Sampler 2 XL, Gerstel, Mülheim an der Ruhr, Germany). The samples and quantification standards were injected in split (split 1:5, injection volume 1 µl) and splitless mode (injection volume 1 µl) in a temperature-controlled injector (CAS4, Gerstel) with a baffled glass liner (Gerstel). The following temperature program was applied during sample injection: initial temperature of 80°C for 30 s followed by a ramp with 12 °C/min to 120°C and a second ramp with 7 °C/min to 300°C and final hold for 2 min. Gas chromatographic separation was performed on an Agilent 6890 N (Agilent, Santa Clara, CA, USA), equipped with a VF-5 ms column of 30-m length, 250-µm inner diameter, and 0.25-µm film thickness (Varian, Palo Alto, CA, USA). Helium was applied as carrier gas with a flow rate of 1.2 ml/min. Gas chromatography was performed with the tempera-

ture gradient: 2-min heating at 70 °C, first temperature gradient with 5 °C/min up to 120 °C and hold for 30 s; subsequently, a second temperature step of 7 °C/min up to 200 °C and a final ramp of 12 °C/min up to 320 °C with a hold time of 2 min. The spectra were recorded in a mass range of 60 to 600 U with 20 spectra/s at a detector voltage of 1750 V.

3.1.6.14 Data analysis of pSIRM experiments

File processing and analysis was performed with the vendor software ChromaTOF Version 4.42 (LECO). Processing parameters: baseline offset of 1, peak width of 4 s, signal/ noise of 20, and peak smoothing of 11 data points. Retention index determination and metabolite annotation was performed with the in-house developed software MAUI-VIA (212). Quantification of metabolites was performed by external calibration as described in (211). Absolute quantities were normalized to internal extraction standard controls and further quality parameters. Mass isotopomer distributions (MID) for each metabolite and measurement were exported by an extended module of MAUI-VIA and manually validated prior the implementation for metabolic flux analysis. Selected mass ranges for MIDs have been described in (88).

3.1.6.15 Metabolic flux analysis (MFA): modeling and computational procedures

A metabolic network model was constructed for LUHMES d0 cells using metabolic reaction databases (www.genome.jp/kegg) and literature knowledge (199, 213-215). The model includes all major metabolic pathways of central carbon metabolism (glycolysis, pentose phosphate pathway, TCA, anaplerosis), and condensed versions of amino acid biosynthesis, lactate- and fatty acid metabolism pathways (acetyl-CoA as precursor). Cellular growth is modelled by a lumped biomass equation. The biomass equation accounts for synthesis of proteins, lipids, DNA, RNA and carbohydrates. Biomass coefficients from (216) [mmol/g_{CDW}] were converted to [nmol/10^6 cells] with the conversion factor 0.14 $mg_{cdw}/10^6$ cells estimated from total protein content of LUHMES cells (0.07 $mg_{Protein}/10^6$ cells), and the assumption that the total cell mass consists of ~50% proteins (217). Although LUHMES cells undergo morphological changes during differentiation, both stages were comparable in weight/cell and protein/cell, hence comparable total cell sizes can be assumed (data not shown). Metabolic reactions were allocated to one of three compartments (cytosol, mitochondria

and extracellular space). Transport reactions of intra- and extracellular amino acids were specified according to the medium specification and extracellular rate measurements. Catabolic reactions of amino acids were modelled as lumped reactions fueling succinate, glutamate and acetyl-CoA pools. Carbon atom transitions were formulated for all metabolic reactions. In case of C-symmetric reactants, scrambling reactions were specified assuming equal fluxes for each variant. In total, the model consists of 72 reactions (51 unidirectional, 21 reversible), as well as 32 balanced intracellular, and 11 unbalanced extracellular metabolite pools. The metabolic network model used for ^{13}C-MFA along with the carbon atom transitions is given in Suppl. Tab. 3.

With this model, isotopically non-stationary (INST) ^{13}C-MFA was performed. To this end, the high-performance simulation suite 13CFLUX2 (218) with extension for INST ^{13}C-MFA was used according to the workflow described in (219) and Suppl. Fig. S2. In brief, cell stage-specific extracellular rates of d0 cells were calculated as described. Mass isotopomer distributions (MIDs) were obtained from two carbon labeling experiments with d0 cells: 1) [U-^{13}C] glucose + [^{12}C] glutamine and 2) [^{12}C] glucose + [U-^{13}C] glutamine. Both data sets were corrected for natural isotope abundance (220). Data sets were simultaneously inferred with the INST ^{13}C-MFA model, justified by the finding that the cell-specific extracellular rates were found very comparable across the three independent biological replicates. In total, 89 unknown parameters (15 net fluxes, 19 exchange fluxes, 31 metabolite pool sizes, 24 group-scale factors) were estimated from 13 cell stage-specific extracellular rate, 15 metabolite pool sizes (averaged over 1) and 2)) and 1,002 single time-resolved MID (4-10 time points, 24 metabolites) measurements. Fitting of the unknown model parameters was done by minimizing the variance-weighted least squares function quantifying the difference between the measured and model-predicted measurements. The fitting procedure was repeated 1,000 times from random starting points to minimize the risk of getting trapped in local minima. Lastly, for visualization of the best fits the Omix® software was used (Omix Visualization GmbH, Lennestadt, Germany, (221).

3.1.6.16 Proteomics analysis

Cells were grown under normal culture conditions until the desired stage of differentiation. For harvesting, cells were washed with 100 mM Tris-HCl-buffer and harvested

by applying urea harvesting solution (8 M urea in 100 mM Tris-HCl, pH 8.5). Subsequently, tandem LC/MS 'shot gun' proteomics was performed.

3.1.6.17 Affymetrix gene chip analysis

Analysis was performed as described earlier (49, 83). Briefly, samples from approximately 5 x10^6 cells were collected using RNA protect reagent from Qiagen. The RNA was quantified using a NanoDrop N-1000 spectrophotometer (NanoDrop, Wilmington, DE, USA), and the integrity of RNA was confirmed with an automated gel electrophoresis system (Experion, Bio-Rad, Hercules, CA, USA). The samples were used for transcriptional profiling when the RNA quality indicator (RQI) number was >8. First-strand cDNA was synthesized from 100 ng total RNA using an oligo-dT primer with an attached T7 promoter sequence, followed by the complementary second strand. The double-stranded cDNA molecule was used for *in vitro* transcription (IVT, standard Affymetrix procedure) using Genechip 30 IVT Express Kit. During synthesis of the aRNA (amplified RNA, also commonly referred to as cRNA), a biotinylated nucleotide analogue was incorporated, which serves as a label for the message. After amplification, aRNA was purified with magnetic beads and 15 µg of aRNA was fragmented with fragmentation buffer as per the manufacturer's instructions. Then, 12.5 µg fragmented aRNA were hybridized with Affymetrix Human Genome U133 plus 2.0 arrays as per the manufacturer's instructions. The chips were placed in a GeneChip Hybridization Oven-645 for 16 h at 60 rpm and 45 °C. For staining and washing, Affymetrix HWS kits were used on a Genechip Fluidics Station-450. For scanning, the Affymetrix Gene-Chip Scanner-3000-7G was used, and the image and quality control assessments were performed with Affymetrix GCOS software. All reagents and instruments were acquired from Affymetrix (Affymetrix, Santa Clara, CA, USA). The generated CEL files were used for further statistical analyses. The authors declare that microarray data were produced according to MIAME guidelines.

3.1.6.18 Transcriptomics data processing and analysis

The microarray data analysis workflow was assembled using the Konstanz Information Miner (KNIME) open source software (http://www.knime.com). The raw data was preprocessed using Robust Multiarray Analysis (RMA). Background correction, quantile normalization, and summarization were applied to all expression data samples, using the RMA function from the affy package of Bioconduct (179, 186, 222).

Low-expression genes with a signal below an intensity of 64 in any one of the conditions were filtered out. The limma package (R & Bioconductor) was used to identify differentially expressed genes, with untreated cells set as control group. The moderated t-statistics was applied and was used for assessing the raw significance of differentially expressed genes. Then, final p-values were derived by using the Benjamini-Hochberg method to control the false discovery rate (FDR) due to multiple hypothesis testing. Transcripts with FDR adjusted p-value of ≤ 0.05 and fold change values ≥ |4| were considered significantly regulated. Gene Ontology (GO) analysis for regulated genes were performed using DAVID platform (223, 224). Transcriptomics data were deposited at GEO database and can be accessed under the number GSE107999.

3.1.6.19 Statistics and data display

If not otherwise specified, the data shown are the means +/- SD of three independent experiments (each with several technical replicates). Independent experiments were performed with different cell batches and they are here termed biological replicates (22) to distinguish them from technical replicates. Significance calculations are based on ANOVA followed by a suitable post-hoc test (unless otherwise indicated). For data display, the program GraphPad Prism 5 (La Jolla, CA, USA) was used.

3.1.7 Results

3.1.7.1 Basic Omics data for test system characterization

LUHMES cells have been characterized in their proliferating state (d0) and as differentiated neurons (d6) for expression of characteristic markers (34, 35), for the sensitivity to the neurotoxicant MPP^+ (63) and for electrophysiological properties (104). To get systems-wide information on the cells and the main features that distinguish d0 and d6 cells, we measured gene expression on the whole genome level. Using Affymetrix microarray analysis, we identified about 1400 genes that were ≥ 4 times higher expressed in one stage compared to the other (Fig. 1A_1). Overrepresented GO terms were determined separately for genes specific for d0 and for genes expressed higher on d6. As expected, GO terms related to cell cycle and proliferation were found for the d0 LUHMES. The GO characteristic for d6 LUHMES were mainly related to the neuronal phenotype (Fig. 1A_1). Additionally, overrepresented pathways were identified using the Panther and Reactome databases (225-228). The pathway enrichment corroborated the findings from the GO term analysis (e.g. downregulation of cell cycle pathways and DNA building-block synthesis) and confirmed neuronal differentiation as well as out previous observation that the pathway of amyloid beta production is upregulated in mature LUHMES cells (d6) (229). Amongst the DEG upregulated on d6, no single pathway linked to cellular metabolism was enriched. Thus, the differential gene expression indicates clear differences between the two stages of the cell line on the transcriptome level, but metabolic differences could not be identified from this type of data (Suppl. Fig. S3_1).

The transcriptomics observations were supported by proteome analysis, which showed a clear difference in the proteome of the two cell differentiation stages with large groups of differentially-abundant proteins in either d0 or d6 cells (Fig. 1B_1). A substantial fraction of proteins related to oxidative phosphorylation, the TCA and fatty acid metabolism were found to be more abundant in d6 LUHMES. For instance, the proteomics data showed upregulation of the TCA-associated proteins isocitrate dehydrogenase-1 and 2 (IDH1, IDH2) and of the respiratory chain complex II protein SDHAF2 upon differentiation. Proteins typically more abundant in d0 cells related to the cell cycle and to synthesis of nucleotides (required for DNA synthesis in proliferating cells). Of the pivotal central carbon metabolism (CCM) proteins, malic enzyme 1 (ME-1) was stronger expressed in undifferentiated neurons compared to differentiat-

ed ones (data not shown). Malic enzyme (ME) facilitates the channeling of carbon from TCA intermediates into glycolysis to generate pyruvate (gluconeogenesis). Besides added carbon supply of pyruvate, the reaction through ME allows synthesizing NADPH. Within the group of transporters, the strongest upregulations observed upon differentiation were found for the mitochondrial citrate and ATP transporters (SLC25A1/A24).

A typical cellular strategy of metabolic switching involves isoenzyme changes. Examples were observed here for hexokinase (HK) and phosphofructokinase (PFK). The isoenzymes HK2 and PFKP were strongly downregulated in d6 LUHMES, which was compensated by stronger expression of HK1 and PFKM (Fig. 1C_1). This is consistent with general biochemical knowledge associating HK2 with muscle, adipose tissue, cancer, neural progenitor cells and anabolic metabolism, and HK1 with expression in the brain (230-232). Concordantly, PFKM is known to be predominantly expressed in muscle and brain (233). These findings corroborate on the proteomics level that LUHMES cell differentiate from precursor cells to typical brain tissue parenchymal cells.

The strong alterations in gene transcription and protein expression suggested clear differences in the metabolome of the cells. This was confirmed by metabolomics measurements. The data allowed the clear distinction between different stages of cell differentiation according to their metabolome (Fig. 1D_1). By a non-targeted metabolomics approach, 38 metabolites were identified and 3 representative metabolites that were downregulated and 6 representatively upregulated metabolites were quantified on the basis of standards. The lower abundance of AMP in differentiated cells is in concordance with the downregulation of purine synthesis genes (Fig. 1B_1). The higher abundance of glutamine and creatine indicates changes in the CCM and substrate usage while the higher abundancy of D-erythrose may indicate changes in the pentose phosphate pathway.

In summary, this basic characterization of d0 and d6 neuronal cell differentiation stages suggests metabolic switches that could affect resilience or susceptibility to toxicants. The suggested metabolic shift, which was not predictable on transcriptome level, but indicated on proteome level, was therefore further investigated.

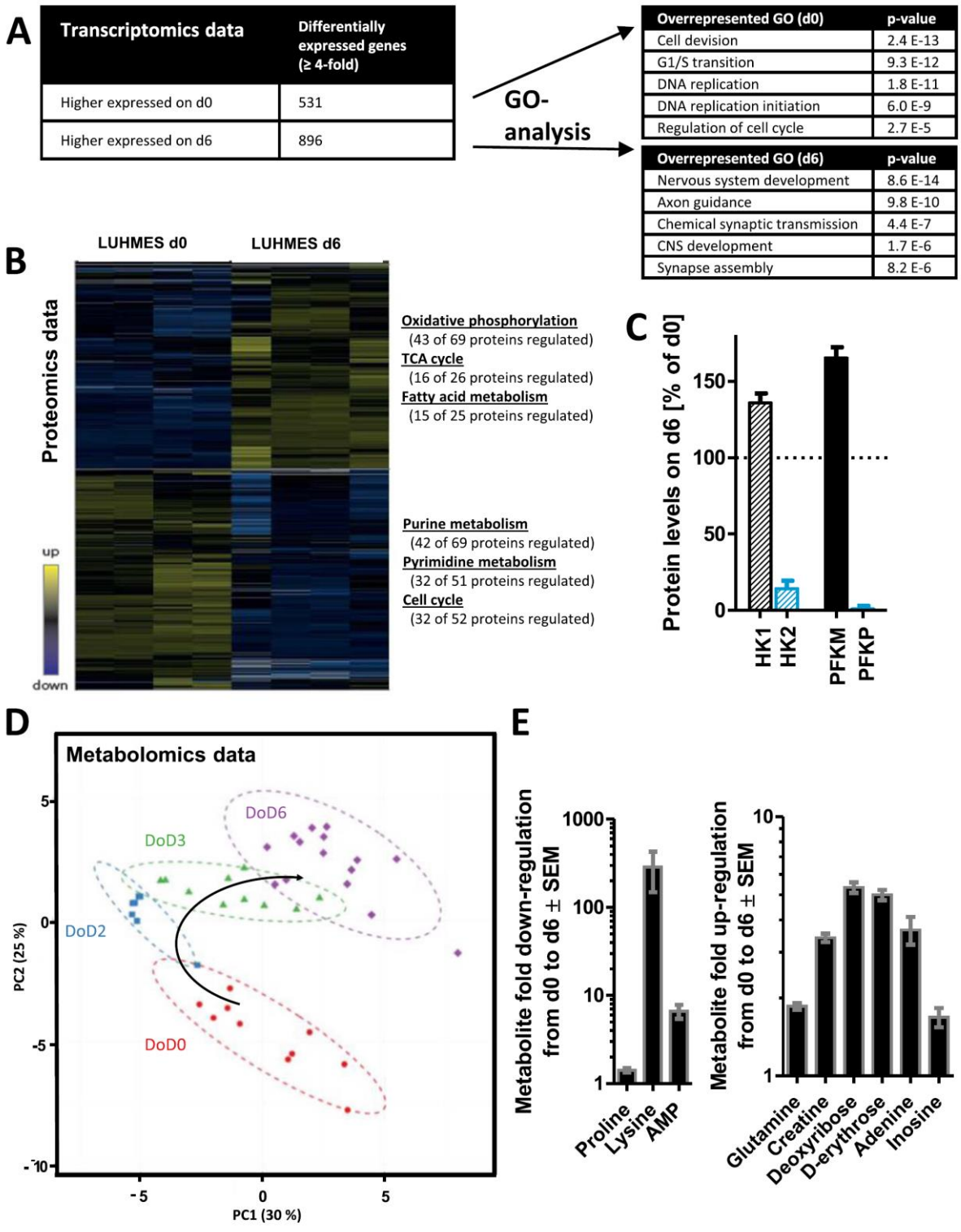

Fig. 1_1: Changes on transcriptional, proteomic and metabolic level during neuronal differentiation

For characterization of the proliferating (d0) and differentiated (d6) LUHMES cells, standardized cell culture conditions were used to generate samples from the two types of untreated control cells for further analysis. **A**: The mRNA expression of four independent cultures of proliferating (d0) and differentiated LUHMES (d6) cells was measured using Affymetrix microarray analysis. Expression levels were determined genome-wide. From these data, differentially expressed genes (DEG) were identified by sorting for probe sets (=Affymetrix gene probes) that were expressed in d6 cells ≥ 4 times higher or lower than in d0 cells. Then, a modulated Limma test was applied to further select those genes for which the differential expression was significant at the 5% level, after the correction for multiple testing. The number of these genes was then displayed. The DEG were analyzed for statistical overrepresentation of gene ontology (GO) groups using DAVID software. The p-values indicate

the likelihood of a random overrepresentation of the respective GO. The five most-highly overrepresented GO are indicated for the group of genes specific for d0 or d6. **B**: Four independent cultures of proliferating (d0) and differentiated (d6) LUHMES cells were used for proteome analysis. Differential abundance of proteins is depicted in a heatmap displaying row-wise z-factors of expression levels (blue= lower expression, black= no change, yellow= higher expression). Rows and columns are sorted by similarity after non-supervised clustering. For each major cluster (=proteins dominating in d0 (bottom) or d6 (top)), three typical overrepresented metabolic pathways were selected. The numbers indicate how many different proteins of the total pathway are differentially abundant. **C**: Two enzymes (each with two isoforms) important for switching metabolic regulation were selected to display the type of changes occurring during LUHMES differentiation. Protein levels were quantified by a shotgun proteomics approach. The protein ratio of d6/d0 is displayed for hexokinase 1 and 2 (HK1, HK2) and for phosphofructokinase M and P (PFKM, PFKP). **D**: Proliferating (d0) LUHMES cells were differentiated for 6 days. On day of differentiation zero (DoD0, red), two (DoD2, blue), three (DoD3, green) and six (differentiated, DoD6, purple; = d6) the cells were lysed to prepare samples for metabolome analysis. The samples were analyzed by LC-MS, and metabolite peaks with differential abundance were detected. For 38 compounds, unambiguous identification was possible and their changes are displayed as a principal component analysis (PCA). Each point displayed in the PCA map represents one sample analyzed for the respective day of differentiation. The dashed lines indicate the PCA space occupied by samples from each differentiation stage (n=6-15). The black arrow suggests how differentiating cells move through the 2D PCA space during differentiation. **E**: Three metabolites, which were specifically downregulated and six that were specifically upregulated from d0 to d6 of LUHMES differentiation were selected to display the changes occurring during differentiation. Data are means ± SEM from 6-15 samples.

3.1.7.2 Change of mitochondrial function during differentiation

To characterize the potential metabolic changes identified by omics approaches in greater detail, mitochondrial physiology was assessed by measurements of the oxygen consumption rate (OCR) using Seahorse technology. A strategy of sequential injection of tool compounds interfering with the mitochondrial respiration was chosen (Fig. 2A_1). This allowed the calculation of various functional parameters for mitochondria (Fig. 2B_1). D6 neurons had a slightly higher basal respiration compared to d0 precursor cells, and massive differences became evident, when mitochondria were uncoupled (Fig. 2C_1). The OCR data showed that the maximal mitochondrial respiration, the spare mitochondrial capacity and the amount of oxygen consumption used for ATP production was significantly increased in d6 cells compared to their d0 precursors (Fig 2D_1). Overall, the data suggest that mitochondria run at their maximum in d0 cells, while d6 cells have a large spare capacity to increase mitochondrial function according to demand.

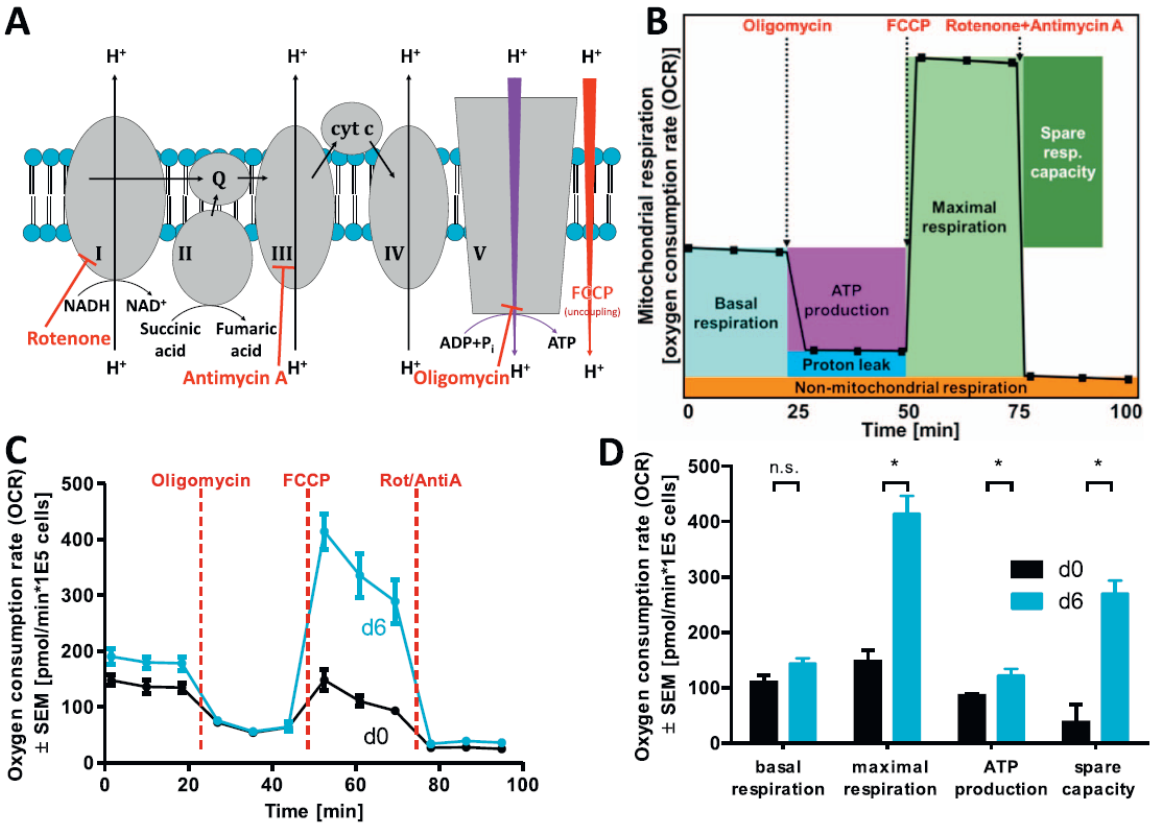

Fig. 2_1: Differences in mitochondrial function between d0 and d6 LUHMES cells

A: Scheme of the mitochondrial electron transport chain, with a display of complexes I-V on the inner mitochondrial membrane. Sites of electron and proton transport and their flow are displayed in black, ATP generation driven by the proton-motive force is shown in purple. Targets of inhibitors used for functional analysis are indicated in red. The uncoupling agent FCCP was used to disrupt the proton gradient across the inner mitochondrial membrane. **B**: Exemplary time course (black curve) of mitochondrial oxygen consumption rate (OCR) under the influence of added inhibitors used by the mitostress test. The scheme displays the standardized schedule of inhibitor injection (time axis). Moreover it indicates how various parameters of mitochondrial physiology are calculated from the OCR of the four experimental phases. **C**: Proliferating (d0, black) and differentiated (d6, blue) LUHMES cells were analyzed for their mitochondrial functionality using the Seahorse mitostress test. OCR was normalized to the cell number, and the injection of the mitochondrial inhibitors/uncoupler is indicated in red. D: The data from C were used to calculate mitochondrial physiology parameters as indicated in B. All data are means ± SEM from two-three biological replicates. *: $p < 0.05$, by one-way ANOVA followed by Dunnett's post-hoc test.

3.1.7.3 Change of glycolytic parameters during differentiation of neurons

To further characterize the central carbon metabolism, glycolysis was investigated for both differentiation stages by measuring extracellular acidification (ECAR; mainly caused by glycolytic lactate secretion). To obtain a broad set of data, ECAR was assessed for different metabolic situations that were provoked by a scheduled injection of tool compounds into cell culture medium (Fig. 3A_1). D0 and d6 cells differed in their glycolytic capacity (Fig. 3B_1): proliferative d0 LUHMES cells have a much higher glycolytic rate and capacity in comparison to differentiated d6 neurons. However, d0 cells had no glycolytic reserve to adapt to a higher demand, while d6 cells

showed a significant capacity to upregulate glycolysis, when challenged by a mitochondrial inhibitor (Fig. 3B+C_1).

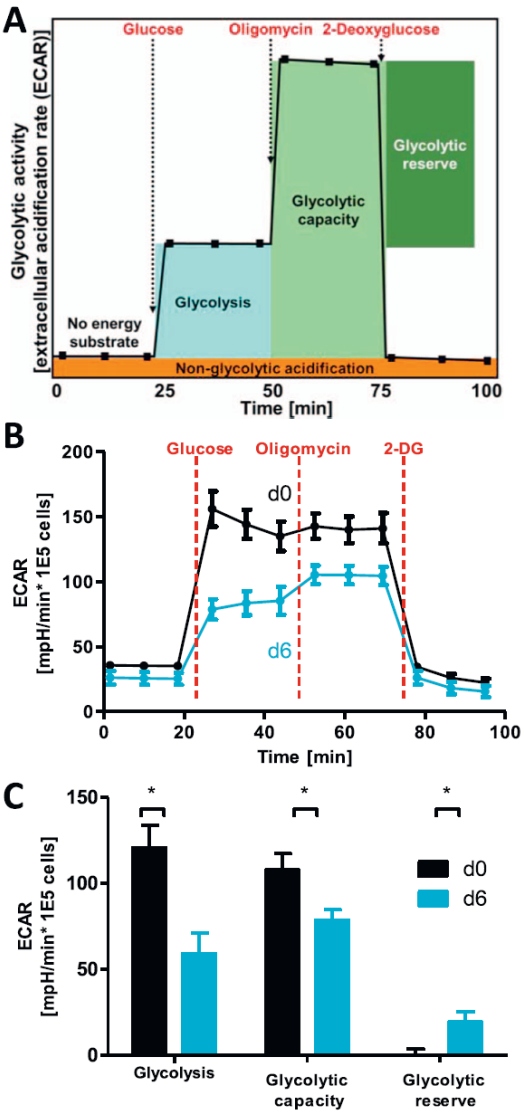

Fig. 3_1: Differences in glycolytic activity during neuronal differentiation

A: Exemplary time course (black curve) of extracellular acidification rate (ECAR) under the influence of added glucose and of inhibitors used by the glycostress test. The scheme displays the standardized schedule of inhibitor injection (time axis). Moreover, it indicates how various parameters of glycolytic physiology are calculated from the ECAR of the four experimental phases. **B**: Proliferating (d0, black) and differentiated (d6, blue) LUHMES cells were analyzed for their glycolytic functionality using the Seahorse glycostress test. ECAR was normalized to the cell number, and the injection of glucose and inhibitors is indicated in red. **C**: The data from B were used to calculate glycolytic parameters as indicated in A. All data are means ± SEM from two-three biological replicates. *: $p < 0.05$, by one-way ANOVA followed by Dunnett's post-hoc test.

3.1.7.4 Macroscopic view on the overall metabolic activity

For further evaluation of the metabolism, the cell numbers of the two cultures were determined. D6 cells were confirmed to be post-mitotic, i.e. their cell number remained constant over 72 h (Fig. 4A_1), implying zero growth. In stark contrast, d0 cells proliferated (doubling time about 10-16 h) with a specific growth rate of $\mu = 0.074 \pm 0.013\ h^{-1}$ within the first 12 h of cultivation (SD from at least three biological replicates) (Fig. 4A_1). After 12-18 h, the 5.5 mM glucose of the labelling medium were exhausted (Fig. 4C_1). The subsequent metabolic shift resulted in a significant drop of the growth rate (Fig. 4A) and decreased lactate production (Fig. 4D). Thus, the time regime for INST ^{13}C-MFA was limited to 0-12 h, to make sure that cells were still in non-limiting culture conditons. Normalized to their protein content, both cell differentiation stages, d0 and d6, were found to contain the same amount of ATP (Fig. 4B_1). Absolute cell-specific extracellular rates for both cell differentiation stages are summarized in Suppl. Tab. 2_1. These rates provide a means to compare the associated metabolic phenotypes. In concordance with the mitochondrial and glycolytic physiology parameters determined above (Fig. 2+3_1), d0 cells took up glucose much faster from the medium than d6 cells: glucose uptake rates were 220 ± 44 and 109 ± 13 nmol/10^6 cells/h for d0 and d6, respectively. In case of d0, the increased glycolytic turnover was paralleled with high uptake and secretion of certain amino acids into the medium. In particular, serine and isoleucine were consumed much faster by d0 than by d6 cells. Moreover, proline and alanine were secreted at 3.6-4.9 fold higher rates by proliferative cells (8 ± 4 vs. 2 ± 1 nmol/10^6 cells/h and 68 ± 8 vs. 19 ± 1 nmol/10^6 cells/h for proline and alanine in d0 and d6, respectively) (Fig. 4E-H, Suppl. Tab. 2_1). Both, d0 and d6 cells experienced high relative lactate secretion rates (232mol-% vs. 282mol-% related to glucose uptake rates, respectively) which again underlines high glycolytic activity in both cell stages. Expectedly, on an absolute level d0 cells released more lactate into the medium compared to d6 cells (509 ± 56 vs. 307 ± 24 nmol/10^6 cells/h, respectively) (Fig. 4C+D_1).

These findings are well in line with the different metabolic situations of proliferative and adult neuronal cells (Fig 4I_1). In post-mitotic d6 neurons, metabolism mainly serves for energy (ATP) production to maintain the functionality of the cell. For this purpose, glucose is metabolized to the level of pyruvate through glycolysis, and likely to CO_2 (experimentally not accessible) in subsequent steps in the TCA. The prolifer-

ating d0 cells can also use this pathway, but their major objective is production of biomass. To use their full metabolic capacity, they also take up amino acids (Fig. 4E+F_1), in particular glutamine, at much higher rates than d6 cells (78 ± 10 vs. 6 ± 3 nmol/10^6 cells/h, respectively) (Suppl. Tab. 2_1) (158, 159, 234, 235). In addition, glycolysis is used in d0 cells in part to provide building blocks like serine or glycine, which are essential for both protein and nucleic acid (purine and pyrimidine) synthesis. If glutamine, serine and isoleucine are used by cells to generate energy or to build up biomass (including lipids), then cells have to get rid of the excess nitrogen. The need to dispose nitrogen equivalents thus may explain the secretion of alanine (Fig. 4H_1), ornithine (data not shown) and ammonia (Suppl. Tab. 2_1) by d0 cells. If glycolysis accounts for a large portion of cellular ATP production, as in d0 cells, then large amounts of reduction equivalents (NADH) are generated besides pyruvate. Conversion of pyruvate to lactate and subsequent secretion of lactate is one way to maintain this type of metabolism. Similarly, proline can be generated from glutamine/glutamate (Fig. 4G_1) as a way for cells to get rid of reduction equivalents, when glutamine is used as energy source (Fig. 4I_1) (234).

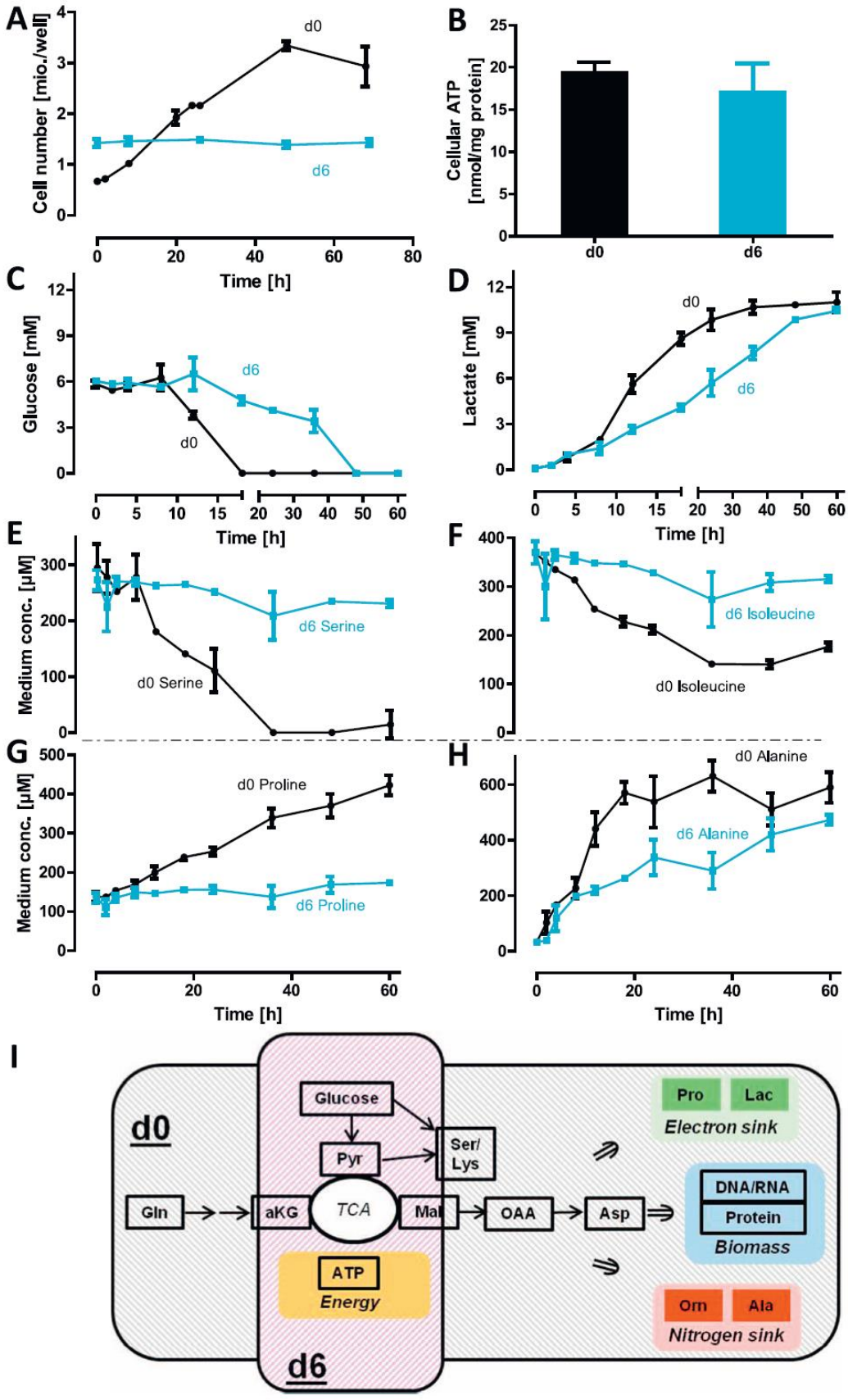

Fig. 4_1: Change of substrate utilization during neuronal differentiation

LUHMES cells (d0 or d6) were cultured under standardized conditions. Various culture parameters were analyzed for up to 72 h, i.e. d0 cells (black) were allowed to continue proliferation for up to three days, and d6 cells (blue) remained in the state of differentiated neurons for up to 72 h. Data are means ± SD from three independent experiments. **A**: Change in cell number (depicted in million cells per well) for d0 and d6 LUHMES over 72 h. B: ATP levels of d0 and d6 LUHMES. Data are normalized to cellular protein content, which was determined in parallel. **C+D**: Pool sizes (concentrations) of glucose (C) and lactate (D) in the cell culture medium. Measurements were performed for up to 60 h in cultures of d0 and d6 cells. **E-H**: Pool sizes (concentrations) of serine (E), isoleucine (F), proline (G) and alanine (H) in the cell culture medium. Measurements were performed for up to 60 h in cultures of d0 and d6 cells. **I:** Schematic illustration of differences in metabolism between d0/d6 cells. The metabolism of post-mitotic d6 neurons mainly serves the energy production (ATP) to maintain the cells functional. For this purpose, glucose is metabolized to the level of CO_2 through glycolysis and subsequent steps in the tricarboxylic acid cycle (TCA) and respiratory chain. The proliferating d0 cells can use similar pathways, but their major objective is production of biomass (proliferation). Therefore, they take up amino acids, in particular glutamine being a building block for proteins and a nitrogen carrier for nucleotide synthesis. Also glycolysis is used in part to provide building blocks like serine or lysine. Aspartate is exemplified as key building block that can be imported and/or assembled from multiple sources, and that is essential for both protein and nucleic acid (purine and pyrimidine) synthesis. Secretion of ornithine, alanine or urea/ammonia serves as nitrogen sink. If glycolysis is used for energy production, as in d0 cells, then excess reducing equivalents need to be disposed of in mitochondria (electron sink). Alternatively, this can be achieved by disposal of lactate, or by generation of proline from glutamate (when glutamine is used as energy source).

3.1.7.5 Direct insights from metabolic pool sizes and isotopic labeling incorporation profiles

To unravel the intracellular metabolic situation, we used the pulsed stable isotope-resolved metabolomics (pSIRM) approach. For this purpose, parallel cultures of cells were exposed to either [U-^{13}C] glucose or [U-^{13}C] glutamine label (all carbon atoms ^{13}C labeled). At defined times, cellular metabolites were extracted and measured by GC-MS. The resulting data delivered twofold information: first, the overall pool sizes (metabolite amount per cell) of CCM metabolites; second, the label incorporation dynamics into CCM metabolites. Both were used for direct interpretation as well as later on for INST ^{13}C-MFA. The pool sizes were used for metabolic flux determination by INST ^{13}C-MFA.

For most intracellular metabolites measured, we found that their pool sizes (concentrations) were within the same order of magnitude in d0 and d6 cells; for some glycolysis intermediates and amino acids, d6 cells had higher pool sizes, but the difference was not statistically significant (Fig. 5A_1). Overall, pool sizes spanned several orders of magnitude with glutamate being the largest pool amounting to 45.3 and 82.4 nmol/10^6 cells in d0 and d6 cells, respectively. Aspartate was below the detection limit in d6 cells, while sizable amounts were measured in d0 precursors. The reverse situation was observed for glutamine. This may be explained by the fact that d0 cells need to maintain a sizable pool size of aspartate for biomass generation which they derive from cellular metabolism. Furthermore, it could be expected that d0 cells rapidly convert all glutamine to glutamate which is, in turn, in rapid equilibrium with α-ketoglutarate (aKG) feeding into the TCA.

Following the path of glycolytic carbon revealed that incorporation of labeled carbon from [U-^{13}C] glucose into the cellular metabolite pools followed the expected order (Fig. 5B_1): the 3-phosphoglycerate (3-PG) pool was >80% labeled after 1 h (as determined by the [1,2]-fragment as proxy). This means that most 3-PG present in all cells at that time point was derived from freshly added (labeled) glucose. For lactate and alanine it already took 6 h to reach 60% label incorporation, and labeling dynamics of citrate was found to be even slower.

Assuming clockwise (oxidative) operation of the TCA, labeled citrate may be formed from the reaction of non-labeled oxaloacetate (derived from unlabeled glutamate channeled into the TCA via aKG) and m+3 labeled oxaloacetate (derived from [U-^{13}C] glucose via pyruvate carboxylase) with m+2 labeled (mitochondrial) acetyl-CoA (derived from fully-labeled pyruvate). This theoretically yields m+2, and m+5 labeled citrate while m+0 citrate is also the result of the continuous inflow of unlabeled glutamate into the TCA, thereby limiting the labeling fraction of the higher mass traces of citrate. In contrast to these theoretical considerations, only a fragment of citrate could be observed within our analytical setup, i.e., the internal carboxylic acid group is lost during analytical analysis (Suppl. Fig. S1F_1). This shifts the theoretical considerations above towards the in reality observed m+0, m+2 and m+4 traces as shown in Fig. 5B_1. Although this qualitatively exemplifies the flow of labeled carbons through the metabolic pathways (Fig. 5B_1), the considerations neglect important aspects of the metabolic network such as malic enzyme, the potential influx of lipids via AcCoA or the label exchange from and to amino acids, e.g. between oxaloacetate and aspartate. To resolve these fluxes, a computational approach is needed (see next section).

The comparison of ^{13}C label incorporation profiles in d0 and d6 cells revealed differences in label incorporation speed depending on whether [U-^{13}C] glucose or [U-^{13}C] glutamine tracers were administered (Fig. 5C_1, Suppl. Fig. 1_1). For [U-^{13}C] glucose we found that d0 cells produced lactate faster compared to d6 cells (Fig. 5C_1 and Suppl. Fig. S1A,C_1), which is in line with the data generated by the Seahorse measurements indicating a higher lactate efflux in d0 cells (Fig. 3C_1). Furthermore, label incorporation dynamics in the malate pool suggests that malate was turned over faster in d6 cells while the turnover of citrate was slightly slower in d6 (Fig. S1,C_1). This might point towards pronounced channeling of carbon, derived from glucose, or

further species, such as extracellular pyruvate, into mitochondria of mature cells via TCA and/or anaplerotic reactions compared to d0 cells (Fig. 5C_1). However, labeling data of citrate was only obtained for a short labeling time (6 h), and the situation would need to be clarified for longer labeling periods (24 h).

Feeding [U-^{13}C] glutamine to both cell stages and following the incorporation of labeled ^{13}C into metabolites of the TCA gave additional information: for both citrate and malate the fraction of labeled metabolite increased much faster in d0 than in d6 cells (Fig. 5C_1, Fig. S1B,D_1). Thus, glutaminolysis is significantly enhanced in d0 compared to d6 cells which is in line with extracellular rate measurements. Since the central carbon metabolism can also potentially operate in glyconeogenetic direction (215), we also studied whether glutamine was converted to lactate. The labeling fraction of intracellular lactate in cells exposed to [U-^{13}C] glutamine informed about a potential channeling of TCA metabolites back into glycolysis (Fig. S1E_1). Here, only a minor degree of label incorporation was observed in lactate compared to TCA metabolites (Fig. S1D_1). There was also no difference between d0 and d6 cells, although ME was expressed stronger in d0 cells (Fig.1_1). This data provides evidence that LUHMES cells do not use glutamine to generate glycolysis metabolites (Suppl. Fig. S1_1). To approach the metabolic activities in LUHMES cells, knowledge of the actual intracellular metabolic carbon fluxes is required.

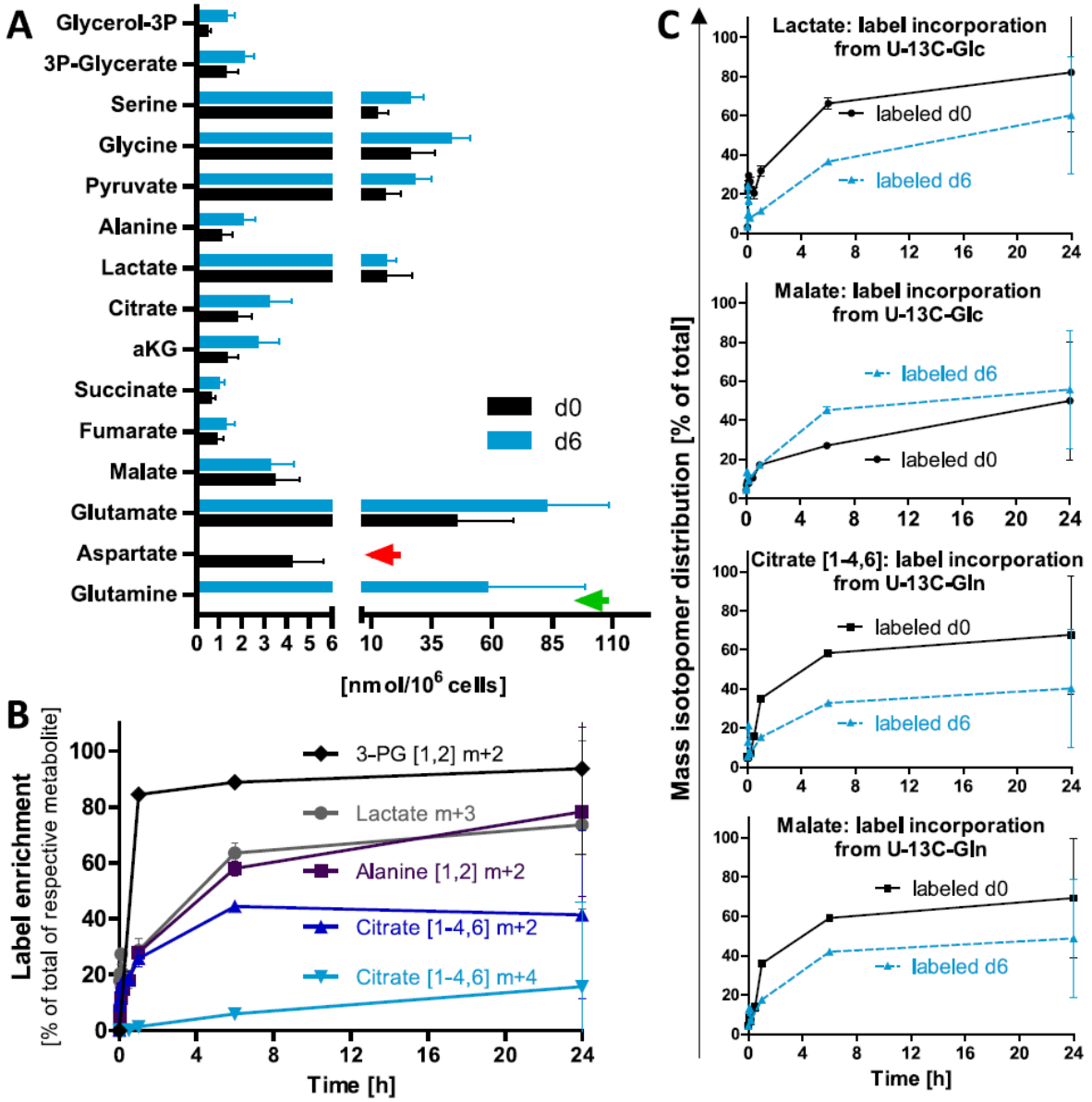

Fig. 5_1: Intracellular metabolite pool sizes and label incorporation

LUHMES cells (d0 or d6) were cultured under standardized conditions, until medium was replaced with fresh media 4 h prior to label experiments. At 0 h, medium was replaced again with culture medium either supplemented with [U-^{13}C] glucose + [U-^{12}C] glutamine or [U-^{12}C] glucose + [U-^{13}C] glutamine. Various culture parameters, such as intracellular metabolite pool sizes and label incorporation into metabolites were analyzed for up to 24 h. For 3-PG, alanine and citrate only the [1,2], [1,2] and [1-4,6] fragments, respectively, were observed (InChI enumeration). **A**: Comparison of intracellular central carbon metabolism (CCM) metabolites of d0 and d6 LUHMES. The red arrow highlights the aspartate pool, only identified in d0 cells; the green arrow indicates the glutamine pool, only identified in d6 neurons. **B**: Label incorporation into CCM metabolites in d0 LUHMES after the exposure to [U-^{13}C] glucose. The number of incorporated heavy atoms is indicated (e.g. m+2 means two ^{13}C atoms instead of ^{12}C atoms). **C**: Time-resolved label incorporation over 24 h into CCM metabolites from [U-^{13}C] glucose or [U-^{13}C] glutamine, as indicated. For better visualization, the summarized percentage of all label containing fragments is displayed (y-axis). All data are means ± SD from three independent experiments.

3.1.7.6 Metabolic flux analysis of d0 neuronal precursors

While time-resolved label incorporation dynamics gives qualitative insights into the metabolic operation modes of LUHMES cells, the quantification of intracellular fluxes requires a model-based approach. INST ^{13}C-MFA integrates measurements of extracellular rates, metabolite pool sizes and CCM labeling incorporation measurements into a metabolic network model to jointly infer metabolic fluxes and pool sizes on the basis of mass balances. The final result of this analysis is a flux and pool size distribution giving absolute numbers for all parameters of the ^{13}C flux model. From this distribution, a so called flux map is generated that shows the calculated fluxes and pool size distributions in the context of the metabolic network. In this study, we applied INST ^{13}C-MFA to derive the flux map of d0 cells. The computational process is overviewed in Suppl. Fig. S2_1. Best solutions for all reaction parameters of the metabolic model were determined in an iterative parameter fitting procedure by minimization of the deviation between the model-predicted values and real measurements. Good fits are obtained for all but one extracellular rate (i.e. influx into mitochondrial acetyl-CoA), all MIDs and pool sizes. The flux map of the best fit is shown in Fig. 6_1 with fluxes expressed in absolute numbers ([nmol/h/106 cells]). Flux values in absolute numbers as well as in % of the glucose uptake rate are found in Suppl. Tab. 3_1.

A major metabolic feature immediately evident from the d0 flux map is the predominant glucose to lactate metabolism (Fig. 6A_1). Experimentally determined cell-number specific extracellular fluxes, particularly glucose uptake, and the dominant lactate efflux, are well reproduced by the model (Fig. 6B,E_1). Also extracellular uptake and secretion rates of amino acids coincide well, such as aspartate and glutamine uptake rates (Fig. 6C_1), as well as alanine and proline secretion rates (Fig. 6E_1). Additional carbon influx into the CCM occurred through mitochondrial acetyl-CoA and succinate as well as the glutamate pool due to catabolism of extracellular amino acids (Fig. 6C_1) and metabolic requirements for biomass synthesis. It should be noted that in the model threonine, leucine, isoleucine, phenylalanine, tyrosine, tryptophan and lysine entered the CCM via mitochondrial acetyl-CoA, valine, methionine, isoleucine, phenylalanine and tyrosine via succinate as well as histidine and arginine via glutamate.

INST ^{13}C-MFA provides detailed insight into glycolytic as well as glutaminolytic intracellular fluxes into the TCA. Fluxes (in % of glucose uptake) (Fig. 6D_1) suggest that

the TCA is approximately equally fueled through glycolysis and glutaminolysis. While the net flux through citrate synthase is 25%, the net flux from glutamate to aKG (involving glutamate dehydrogenase) is 18%. As a consequence, the succinate dehydrogenase flux from succinate towards fumarate within the TCA is 42%. The results stress the important role of glutaminolysis, on the one hand, to fuel the TCA and, on the other hand, to accomplish the required demand for biomass synthesis, e.g. for fatty acid synthesis via acetyl-CoA. The flux from the cytosolic acetyl-CoA pool into the biomass was 10% of the glucose uptake, while the flux from mitochondrial acetyl-CoA pool into biomass was approximately found to be twice as high (19%) (Fig. 6A_1, Suppl. Tab. 2_1). The overall flux into the biomass was determined to be 139.7 nmol/10^6 cells/h (or 405 C-nmol/10^6 cells/h, i.e. number of carbon atoms), representing 53% of the glucose uptake. Thus, the high flux into the biomass in d0 underlines the need of biomass precursors to accomplish cellular proliferation expressed by the high specific growth rate compared to zero growth in d6 (μ = 0.074 h^{-1} vs. 0.0 h^{-1}).

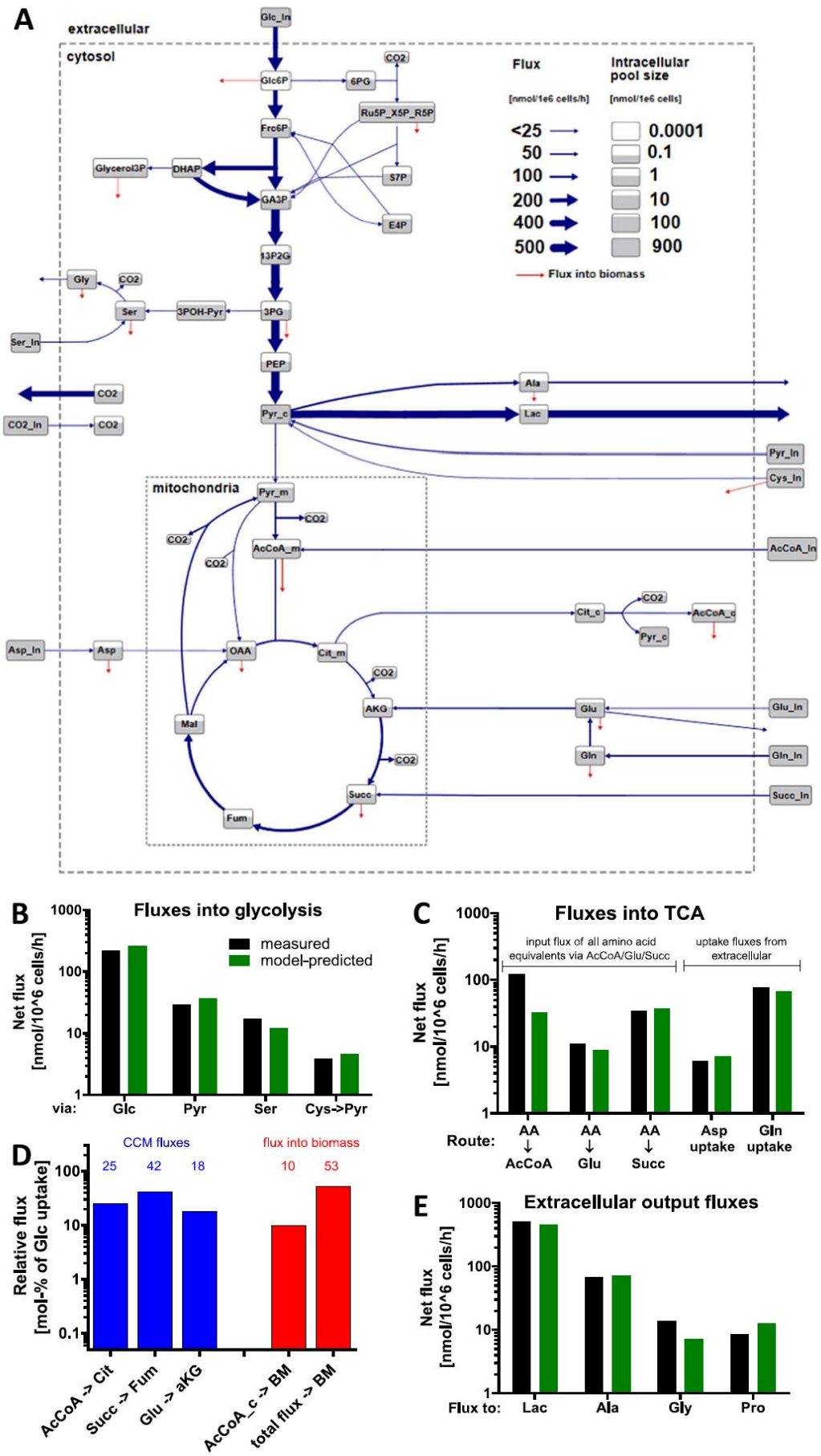
A
extracellular
cytosol
Glc_In
Glc6P
6PG
CO2
Ru5P_X5P_R5P
Frc6P
Glycerol3P
DHAP
S7P
GA3P
E4P
13P2G
Gly
CO2
Ser
3POH-Pyr
3PG
Ser_In
PEP
CO2
CO2_In
CO2
Ala
Pyr_c
Lac
Pyr_In
Cys_In
mitochondria
Pyr_m
CO2
CO2
AcCoA_m
AcCoA_In
Cit_c
CO2
AcCoA_c
Pyr_c
Asp_In
Asp
OAA
Cit_m
CO2
AKG
Glu
Glu_In
Mal
Gln
Gln_In
CO2
Succ
Succ_In
Fum
Flux
[nmol/1e6 cells/h]
Intracellular pool size
[nmol/1e6 cells]
<25
50
100
200
400
500
0.0001
0.1
1
10
100
900
Flux into biomass
B
Fluxes into glycolysis
measured
model-predicted
Net flux [nmol/10^6 cells/h]
1000
100
10
1
via:
Glc
Pyr
Ser
Cys->Pyr
C
Fluxes into TCA
input flux of all amino acid equivalents via AcCoA/Glu/Succ
uptake fluxes from extracellular
Net flux [nmol/10^6 cells/h]
Route:
AA ↓ AcCoA
AA ↓ Glu
AA ↓ Succ
Asp uptake
Gln uptake
D
CCM fluxes
flux into biomass
25
42
18
10
53
Relative flux [mol-% of Glc uptake]
AcCoA -> Cit
Succ -> Fum
Glu -> aKG
AcCoA_c -> BM
total flux -> BM
E
Extracellular output fluxes
Net flux [nmol/10^6 cells/h]
Flux to:
Lac
Ala
Gly
Pro

Fig. 6_1: Flux map of proliferating LUHMES cells

For proliferating LUHMES cells, metabolic flux analysis (MFA) was performed according to Suppl. Fig. S2_1, and the data are summarized in a metabolic flux map. **A**: The CCM-fluxmap features glycolysis, the TCA, as well as input and output fluxes of metabolites. Flux velocity was encoded by the arrow size, the metabolite pool size (=concentration) was encoded by the amount of background coloring in the text boxes. Fluxes into biomass are depicted as red arrows pointing to no specific target. The model assumes three compartments (extracellular space, cytosol and mitochondria). A list of abbreviations regarding metabolic pools used for the flux map can be found in Suppl. Tab. 1_1. **B,C**: Measured fluxes were compared to simulated fluxes derived from the MFA flux model. The net input fluxes into glycolysis (B), and into the TCA (C) are displayed. Additional relative information on the metabolic routes considered is added to the data displays. **D**: Selected intracellular fluxes, relative to glucose uptake (AcCoA_c = cytosolic acetyl-CoA, BM = biomass). **E**: Measured secretion rates (e.g. lactate secretion) are displayed together with data derived on the same fluxes from MFA modeling as shown in A.

In d0 cells we observed strict clockwise (oxidative) operation of the TCA, potentially to enable the cells to meet their NADH and ATP requirements. In particular, no reversible carboxylation of aKG to citrate occurs (<10e-6 nmol/10^6 cells/h). Interestingly, this is in contrast to the findings reported by Sá et al. (189) for murine neural stem cells. Notably, by integrating all available measurements in the network model, fluxes entering the TCA via pyruvate dehydrogenase (PDH, lower glycolysis) and pyruvate carboxylase (PC, anaplerosis) can be destinguished by ^{13}C-MFA. A high PDH-flux of 32% was estimated by ^{13}C-MFA. This would satisfy the demands for acetyl-CoA precursors for biomass generation and fuel the TCA. The PC-flux contributed only to a minor extent (ca. 5%). From these flux estimates, a PDH/PC ratio of ca. 0.15 is derived for d0 cells, which is only slightly lower than the ratio of 0.18 determined for neural stem cells by Sá et al. (189).

Assuming that intracellular serine is exclusively used for purine synthesis, an upper bound for the purine synthesis flux can be derived from the total flux into the serine pool. This gives a maximal purine synthesis flux of ca. 7% of the glucose uptake (2.5% and 4.5% derived from the uptake of glucose and serine, respectively), which is in-line with the low carbon fluxes through the pentose phosphate pathway (Suppl. Tab. 3_1).

Summarizing, a model-based representation of the CCM network of d0 LUHMES cells was has been established explaining specific extracellular rates, metabolic pool sizes and labeling incorporation dynamics in a consistent manner. The ensuing flux map showed a metabolism that is focused on aerobic glycolysis, but also involved the TCA and amino acid metabolism to a substantial extent. The same MFA approach, as applied for d0 cells was attempted for d6 cells. In this case we found that the

quality standards for quantitative flux modeling could not be met (Suppl. Fig. S2_1). Here, future research work is required to collect data in the quality needed by mathematical modeling to allow the assembly of highly resolved flux maps for complex mammalian cells and in particular to answer the question whether the altered mitochondrial physiology parameters in d6 cells are reflected by respective changes in metabolic fluxes.

3.1.7.7 Loss of glutamine dependency upon differentiation

Further experiments were conducted to investigate the impact of media components such as pyruvate and glutamine on cell growth. The data showed that not only glutamine, but also glutamate and aspartate were rapidly taken up by d0 cells from the medium, while d6 cells reduced the medium composition of these amino acids only marginally (Fig. 7A_1). To follow up on this, we examined to which extend the cells required glutamine supplementation. The d6 cells survived for 24 h in medium devoid of glutamine and pyruvate, while d0 cells all died. Glutamine was able to keep cells surviving, but it did not allow proliferation, while combination of glutamine and pyruvate allowed a doubling of the cell number (Fig. 7B_1). These results point to a crucial importance of pyruvate for proliferation in d0 cells although the pyruvate uptake rate was only about 10% of the glucose uptake rate (29 ± 8 nmol/10^6 cells/h, Suppl. Tab. 2_1).

In the following, the differential effects of medium supplements were studied for d0 LUHMES cells over a period of 60 h. This series of experiments confirmed that LUHMES cells could not be maintained alive in medium lacking glutamine. Moreover, it was confirmed that the presence of pyruvate enhanced the effect of glutamine (a significant further increase in proliferation), while pyruvate alone had no effect (Fig. 7C_1).

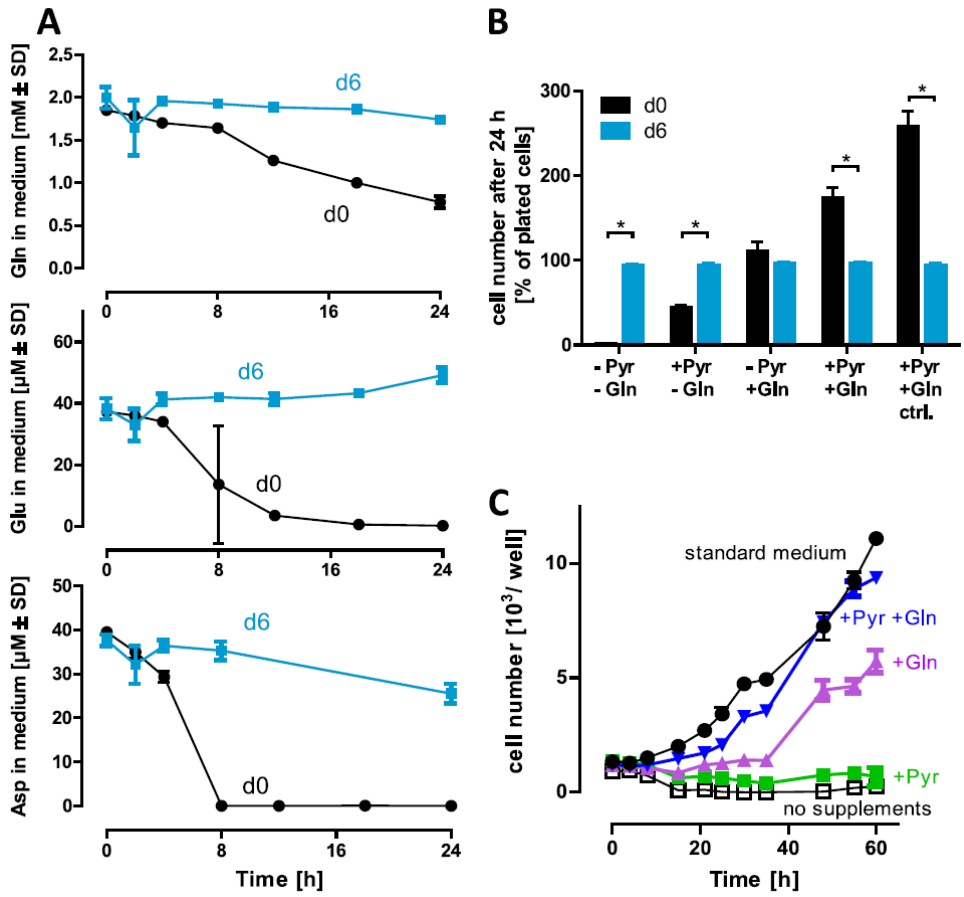

Fig.7_1: Loss of glutamine dependency of LUHMES upon differentiation

LUHMES cells (d0 or d6) were cultured under standardized conditions. Various culture parameters were analyzed for up to 60 h, i.e. d0 cells (black) continuing proliferation for up to three days, and for d6 cells (blue) remaining in the state of differentiated neurons for up to 60 h. **A:** Concentrations of glutamine (Gln), glutamate (Glu) and aspartate (Asp) in the cell culture medium. Measurements were performed for 0 h to 24 h in cultures of d0 and d6 cells. **B+C:** Cultures of d0 and d6 were prepared so that they contained similar and standardized numbers of cells at the time point when the experiment was initiated. Then, the medium was changed and cell numbers were recorded for the following 60 h. The medium contained either no supplements or combinations of pyruvate [1 mM] and l-glutamine [2 mM]. As control, the standard Adv. DMEM/F12 medium (ctrl.) with all supplements added by the commercial supplier was used. The cell number was assessed 24 h after medium change and expressed as percent of the amount of seeded cells at t=0. Alternatively, the absolute cell count was quantified by automated live cell microscopy over a 60 h time period. The number of cells per well is indicated. All data are means ± SD from three biological replicates. *: $p < 0.05$, by one-way ANOVA followed by Dunnett's post-hoc test.

These data suggested that glutaminolysis (i.e. uptake of glutamine and feeding into the TCA via glutamate to aKG) is a pivotal cellular metabolic process that is necessary for the proliferation of neural precursor cells by supplying carbon backbones for anaplerotic processes, such as building block synthesis, while pyruvate may support this process by acting as electron-sink (Fig. 4I_1) (158, 159).

3.1.7.8 Differential sensitivity of d0 vs d6 cells for metabolic toxicants

This study found by several approaches that d0 cells differ particularly from d6 cells in their limited capacity to upregulate mitochondrial metabolism and in their dependency on glutamine. The latter requires the mitochondrial TCA to be channeled into various metabolic pathways. Therefore, the question raised, whether this metabolic situation might sensitize d0 cells to mitochondrial toxicants. To obtain experimental data, the toxicity of antimycin A (ETC complex III inhibitor), rotenone (ETC complex I inhibitor) and UK-5099 (inhibitor of mitochondrial pyruvate transporter) was assessed by measuring resazurin reduction (viability assay) and lactate dehydrogenase (LDH) release (cell death assay). Generally, both assays give similar data on toxicant potency. The comparison of the EC50 values for d0 and d6 cells showed that proliferating cells were more sensitive to toxicants inhibiting mitochondrial metabolism. To get an indication on whether the cell-stage dependent toxicity was related to the energetic flexibility of the cells, we measured lactate release in the presence of rotenone. As expected, the d6 cells increased this parameter (a measure of glycolytic activity) by 100% in the presence of the toxicant, while d0 cells showed little adaptation (data not shown).

In a next step, it was tested whether d0 cells were generally more vulnerable. Thus, both cell stages were exposed to 3-bromopyruvate, a toxicant that affects energy metabolism not on the stage of mitochondria, but at glycolysis. In this experiment, d6 cells proved to be more sensitive than d0 cells (Fig. 8_1). For two non-specific toxicants, the proteasome inhibitor MG-132 and thiol-reactive reagent thiomersal, both cell stages showed similar sensitivities (data not shown).

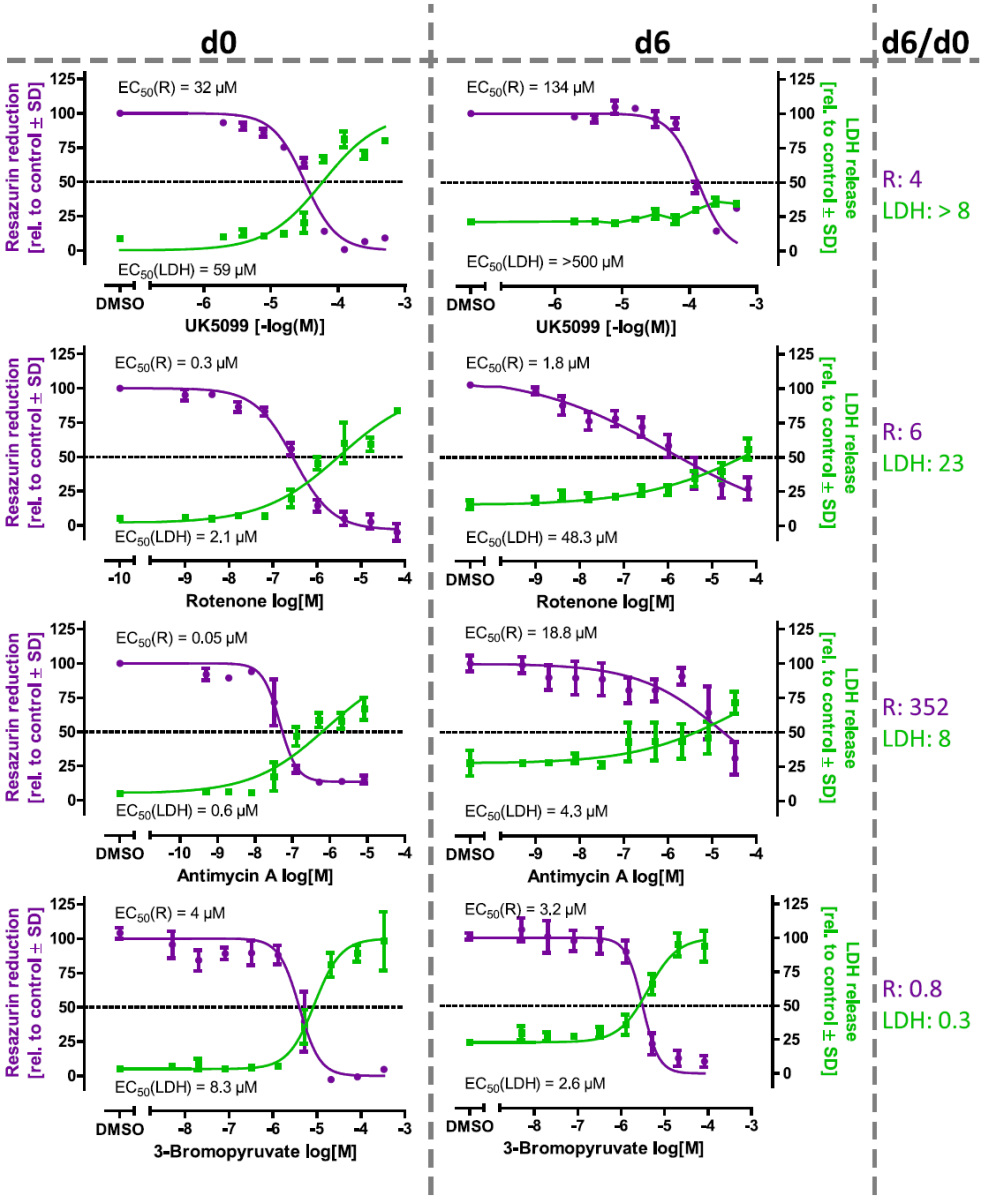

Fig.8_1: Differential sensitivity to toxicants of differentiated neurons versus immature precursors

Proliferating (d0) or differentiated (d6) LUHMES neurons were used in 96-well plates to determine the cytotoxicity of mitochondrial inhibitors and of toxicants not inhibiting mitochondrial complexes. After 24 h exposure to serial dilutions of toxicants, resazurin reduction (R, purple) and lactate dehydrogenase release (LDH, green) were determined. Log-logistic curves were fit to the data, and these were used to determine EC_{50} values. The right hand column (d6/d0) indicates ratios for either R or LDH. They were derived by dividing the EC_{50} value of differentiated cells (d6) by the EC_{50} value of the progenitor cells (d0), respectively. All data are means ± SD from three independent experiments.

3.1.8 Discussion

In this study, we linked key observations on metabolic changes occurring during neuronal differentiation to different stage specific toxicological sensitivities. Using multiple analytical approaches, including p-SRIM followed by metabolic flux modeling (INST ^{13}C-MFA), we found that the strong metabolic changes upon differentiation are mainly due to the changing metabolic needs of the cells undergoing differentiation from

proliferating precursors to mature neurons. Proliferative cells were found to be particularly sensitive to toxicants that challenge the cellular metabolic buffering capacity. Since their metabolic spare capacities were minor, metabolic insults could not be compensated, e.g. by increased glycolysis. Previous approaches in toxicology have already used the combination of two or three omics techniques to attempt a system-wide characterization of cells and of a specific stress response after toxicant exposure (49, 236-238). This study contributed a comprehensive multi-omics approach comprising transcriptomics, proteomics, metabolomics, and fluxomics technologies. Two major insights were: (1) an extreme glutamine dependence of neural stem cells (d0) and (2) cell stage-specific neurotoxicity.

Metabolic states in LUHMES cells were inaccessible for traditional ^{13}C-MFA relying on steady-state labeling enrichment due to long label incorporation times. Therefore, INST ^{13}C-MFA with shortened labeling periods and time-resolved observations was implemented (219, 239). This approach made use of the metabolomics data and allowed resolving the contribution of key metabolic pathways by joint inference of metabolite pool sizes, cell-specific extracellular rates and labeling incorporation profiles.

The first major observation of our study was the high dependency of neuronal precursor cells on extracellular glutamine. It is used for anaplerotic reactions of the citric acid cycle, when products of the cycle are used as cellular building blocks. In addition, glutamine is known to be a donor of amino-groups for non-essential amino acids as serine and glycine, which are also needed for building block and protein synthesis (240). Furthermore, glutamine is a precursor of glutathione (via prior conversion to glutamate) and might thereby aid the maintenance of the cells' antioxidative potential and redox homeostasis (240, 241). A recent publication found that proliferating cells, especially during S-phase, rely on glutamine anaplerosis of the TCA (242), which is in line with d0 LUHMES showing a high dependence on glutamine.

D0 LUHMES may fuel their TCA from glutamine, also in order to produce aspartate, as it has been described for cancer cells (156). Such aspartate production has been shown for tumor cell lines to be limiting for purine and pyrimidine synthesis (158, 243), as well as for NADPH production and maintenance of mitochondrial membrane potential and integrity (244). Additionally, glutamine can be metabolized to AcCoA without generation of NADH and thereby not further burdening cells' mitochondria (234, 235). Differentiated d6 cells have much less need for nucleotide synthesis and,

therefore, require less glutamine and aspartate. Still these cells maintain a high non-growth related metabolic activity. Label incorporation profiles indicate that mitochondrial metabolism might be enhanced in d6 compared to d0 cells, but further comparative ^{13}C-MFA studies are required to finally answer this question. Being successfully applied to a test system, this study provides an important basis for probing specific metabolic states for future studies on the mode of action of toxicants. Ultimately, mechanistic models of CCM will be needed to study these modes of action (245) and to predict toxicological properties of unknown compounds (87, 243, 246, 247).

A potential flaw of the model we use is the expression of the myc transgene to maintain neural precursor state. We cannot exclude that myc also affects the metabolism, but there are several lines of evidence that suggest that this is a rather minor effect: (i) while we performed our study, a similar study was published on the basis iPSC-derived neurons (without myc transgene). The findings of this study (although related more to proteome changes) are quite similar to ours (232); (ii) the expression levels of v-myc in LUHMES are quite moderate compared to endogenous c-myc and we found that the protein amounts were about similar; (iii) neural stem cells/neural crest cells do naturally express myc, and it plays an important role at this stage (248-251); (iv) it is known for some other cells that overexpression of myc (cancer environment) caused minimal changes in glutamine and glucose consumption, although spare respiratory capacity was increased (252).

Second, in the field of DNT, there has been a strong focus on fundamental neurodevelopmental processes as basis for test systems and assays (43, 175). Here, we show that also different susceptibilities of a given cell differentiation stage can be important as target of developmental neurotoxicants. Our data suggest a link between the metabolic switch during differentiation and alterations in the sensitivity to toxicants. The lack of energetic buffering capacity, both mitochondrial and glycolytic, of proliferating d0 cells accounts for their higher sensitivity to UK5099, rotenone and antimycin. Instead, the d6 neurons were able to increase the glycolytic activity to counteract the mitochondrial inhibition, and therefore they showed higher tolerance to those toxicants. There are several other cases known, in which stage-specific toxicity occurs, e.g. exposure to the cell cycle toxicant methylazoxymethylacetat (MAM) (39). However, it should not be concluded from this example that proliferating cells are generally more sensitive to toxicants. Other literature data show that differentiated

LUHMES cells are more susceptible to the toxicants colchicine, vincristine and methylmercury (206). A differential toxicity is not only observed for specific neurotoxicants, but it was also found for the glycolytic inhibitor 3-bromopyruvate, for which d6 cells were twice as sensitive as their proliferating counterparts. These data suggest that mature neurons may on the one hand compensate certain metabolic stresses (e.g. partial mitochondrial inhibition), but they succumb more readily to the complete shut-down of energy production by a glycolytic inhibitor. The data from LUHMES cells on glycolytic compensation for mitochondrial inhibition are well in agreement with data from primary neurons (48) and e.g. lymphocytes (253, 254). It also needs to be noted that our study did not address activity-dependent energy consumption of cells. For instance some adult neuronal populations, like nigrostriatal dopaminergic neurons, are particularly sensitive to mitochondrial inhibitors. The reason for this is the extremely high energy demand of these cells, when they are synaptically integrated (170). This example shows, that metabolic balance may depend not only on basic biochemical features of cells (as studied here), but also on their cellular context. Ways to mimic this would be co-cultures (15, 173) or 3D-cultures (110), and applying metabolomics to such advance models is an additional future challenge.

In summary, our study shows that a thorough characterization of the test system can be helpful, or sometimes is even pivotal for the understanding of toxicological observations and for the interpretation of their relevance. By using an approach combining classical omics techniques with ^{13}C-MFA and cellular respiration measurements, we identified metabolic differences that accounted for changes in toxicant sensitivity. In the future this approach will be refined and expanded towards the description of toxicant effects in the nervous system. Key metabolic pathways have to be identified and mapped for various standard toxicants. This knowledge could allow for more targeted measurements at lower cost. By focusing on few pathways, metabolites and time points, the procedure could reach a throughput allowing broader screening (255). As a hit-follow-up of the screening, a full mechanistic characterization may be added. This approach may identify cell stage-specific toxicants not easily detected by assays focusing on developmental processes. Since the loss of a highly proliferative subpopulation during neuro-development might result in a pronounced effect in later life, cell death of the proliferative precursors can be as fatal as impairment of migration (256), neurite outgrowth (56) or neuronal network formation (257, 258).

3.1.9 Acknowledgements

This work was supported by the DFG (RTG1331), the Land-BW (INVITE), the BMBF (e:ToP program) and the EC project EU-ToxRisk.

3.1.10 Conflict of interest

The authors declare no conflict of interest.

3.1.11 Supplementary information

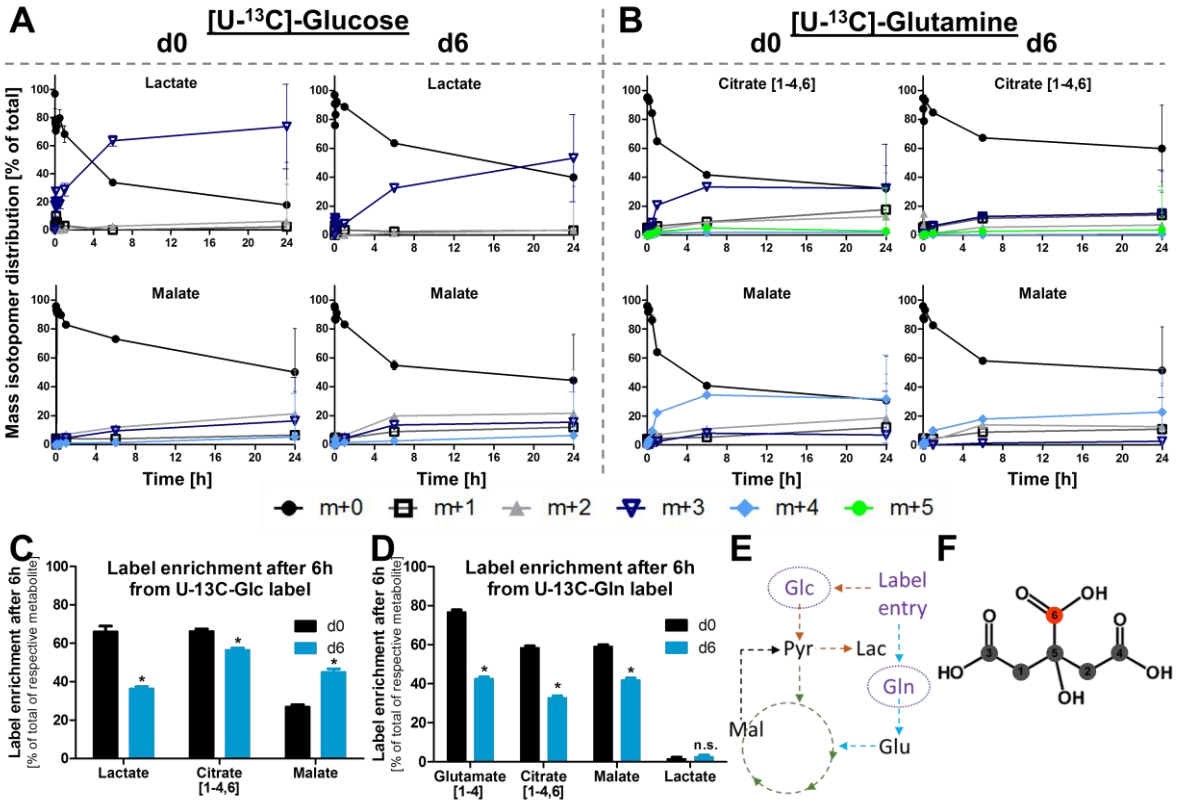

Supplementary Fig. S1_1:

LUHMES cells (d0 or d6) were cultured under standardized conditions, until medium was replaced with fresh media 4 h prior to label experiments. At 0 h, medium was replaced again with culture medium either supplemented with [U 13C]-glucose + [U 12C]-glutamine or [U 12C]-glucose + [U 13C]-glutamine. Label incorporations into various metabolites were analyzed for up to 24 h. For citrate only the [1-4,6] fragment and for glutamate only the [1-4] fragment, was observed (InChI enumeration). **A**: Label influx in lactate and malate of d0 (left) and d6 (right) LUHMES originating from labeled glucose. **B**: Label influx in citrate and malate of d0 (left) and d6 (right) LUHMES originating from labeled glutamine. **C+D**: Label enrichment (100%-unlabeled) after 6 h of label exposure into metabolites from 13C-Glc or 13C-Gln, as indicated data are means ± SD from three independent experiments. **E**: Graphical depiction of label entry routes into CCM from glucose or glutamine (purple: label entry; blue: TCA anaplerosis by Gln; green: TCA; orange: glycolysis; black: malic enzyme). **F**: depiction of the citrate molecule with InChI enumeration of the carbon atoms (numbered circles). The green carbons were identified by the MS measurement. All data are means ± SD from three independent experiments, *: $p < 0.05$, by one-way ANOVA followed by Dunnett's post-hoc test.

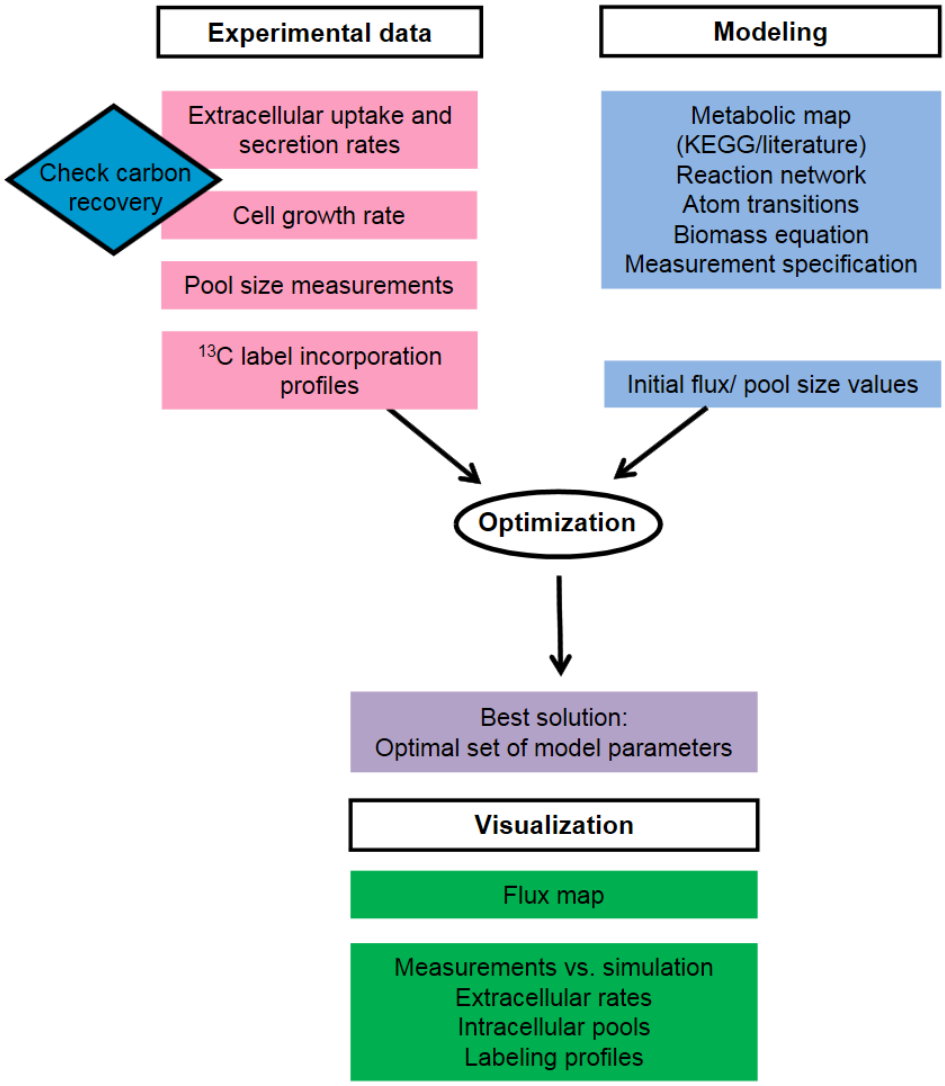

Supplementary Fig. S2_1:

Experimental data are incorporated in a metabolic network model to obtain a flux map, showing the reaction rates (fluxes) of cellular metabolism *in vivo*. Unknown model parameters are fitted to the experimental data ("optimization") and the result (the flux map) is visualized in the context of the metabolic network representation. The main steps are briefly summarized. For further information about the general procedure of ^{13}C MFA, the reader is referred to the literature (below).

Experimental data generation step (see also "Extracellular rate determination" in the main text):

Extracellular uptake and secretion (net) rates quantify how fast substrates are taken up by the cells, or are secreted as products, respectively. Extracellular rates are estimated from experimentally determined extracellular concentration courses over time of the respective chemical compound.

Equipped with the rates, the carbon balance is checked to be closed in order to account for all important carbon fluxes into and out of the cells. Likewise, the specific growth rate of the cells is estimated, e.g. from numbers of viable cells over time. The period in which the cell culture is in a metabolic (pseudo)steady state, dictates the time window for the INST ^{13}C MFA experiments. Sampling times are chosen in such a way that the dynamic labeling enrichment in the different intracellular metabolites can be followed. During the INST ^{13}C MFA experiment, cell culture samples were taken (3 biological replicates) quenched, and subjected to chemical analysis. Mass spectrometry was used to obtain i) ^{13}C label incorporation profiles of the intracellular metabolites and ii) absolute intracellular pool sizes (using external standards). Additionally, ^{13}C label incorporation profiles were corrected for natural abundance.

Modeling step: A metabolic network is usually constructed from data bases and literature sources. Reaction directions are assigned in consistency with thermodynamic knowledge. During the model building and testing process, constraints for fluxes and metabolite pool sizes are added, if required. To model proliferation, a biomass equation is added to account for the cellular investments of growth which are related to the precursor metabolites. Metabolite pools and transport reactions across the cell wall/membrane are added in line with the experimental data. An important part of the process is that carbon atom transitions are specified to describe the fate of each individual carbon atom (e.g. C_2 within lactate) within the network. Another parameter input is the input substrate mixture of the INST 13C MFA experiment. In this context, the analytical measurement configuration is added to the model. To start modeling, feasible initial values for fluxes and metabolite pool sizes are chosen.

Optimization phase: Because intracellular fluxes cannot be directly measured, they are estimated by iteratively fitting the model parameters to the experimentally determined data. Through the optimization process an optimal set of pool sizes and fluxes is calculated by comparing experimental and model-predicted data and minimizing the variance-weighted differences. Because minimization is likely to be trapped in solutions that are not globally optimal, the process of parameter estimation is started repeatedly with randomly sampled initial parameter configurations.
In the end, the best solution of pools and fluxes is visualized in a flux map. Sometimes, it is not possible to suggest a fluxmap that fulfills all conditions. For instance the requirement of a closed carbon balance may not be adoptable to the measured extracellular rates and known atom transitions, without postulates on fluxes that are physiologically highly unlikely.

A

Transcriptomics data	Differentially expressed genes (≥ 4 fold)
Higher expressed on d6	896
Higher expressed on d0	531

pathway enrichment analysis

Number of regulated PWs in database	
Panther	Reactome
27	25
5	196

B

Example up:

Axon guidance mediated by semaphorins (EF 4.6)
Dihydropyrimidinase-related protein 1
Serine/threonine-protein kinase PAK 1
Dihydropyrimidinase-related protein 3
Tyrosine-protein kinase Fyn
Dihydropyrimidinase-related protein 4
Cyclin-dependent-like kinase 5
Rho-related GTP-binding protein RhoC
Ras-related C3 botulinum toxin substrate 2
Tyrosine-protein kinase FRK;FRK
Dihydropyrimidinase-related protein 2
Ras-related C3 botulinum toxin substrate 1
Dihydropyrimidinase-related protein 5
Tyrosine-protein kinase Fes/Fps
Transforming protein RhoA
Plexin-A1
Semaphorin-3A
Semaphorin-4D
Rho guanine nucleotide exchange factor 1
Plexin-B1
Dihydropyrimidinase

Alzheimer disease-amyloid secretase pathway (EF 2.8)
Amyloid beta A4 precursor protein-binding family A member 2
Beta-secretase 1
Gamma-secretase subunit APH-1B
Kinesin light chain 1
Mitogen-activated protein kinase 10
Mitogen-activated protein kinase 11
Mitogen-activated protein kinase 8
Presenilin-1
Protein kinase Cβ/δ/ζtype
Serine/threonine-protein kinase N1
Voltage-dependent L-type calcium channel subunit beta-2
APP-binding family A member 1/3
APP-binding family B member 1
Amyloid beta A4 protein (APP)
Beta-secretase 2
CHRNA7-FAM7A fusion protein
Disintegrin and metalloproteinase domain-containing protein 9/10/17
Furin
Gamma-secretase subunit APH-1A/PEN-2
Histone acetyltransferase KAT5
Kinesin light chain 2/3/4
Mitogen-activated protein kinase 1/3/4/6/7/9/12/13/14/15
Neuroendocrine convertase ½
Neuronal acetylcholine receptor subunit alpha-7
Nicastrin
Presenilin-2
Proprotein convertase subtilisin/kexin type 4/5/6/7
Protein kinase Cα/ε/γ/η/ι/θ/ type
Serine/threonine-protein kinase N2/N3/NLK
Voltage-dep. L-type Ca2+ channel subunit alpha-1C/D/F/S
Voltage-dependent L-type calcium channel subunit beta-1

Example down:

Purine ribonucleoside monophosphate biosynthesis (EF 8.65)
Adenylosuccinate lyase
Amidophosphoribosyltransferase
Bifunctional purine biosynthesis protein PURH
GMP synthase [glutamine-hydrolyzing]
Inosine-5'-monophosphate dehydrogenase 2
Multifunctional protein ADE2
Phosphoribosylformylglycinamidine synthase
Trifunctional purine biosynthetic protein adenosine-3
Adenylosuccinate synthetase isozyme 1
Adenylosuccinate synthetase isozyme 2
Inosine-5'-monophosphate dehydrogenase 1
Phosphoribosylformylglycinamidine synthase

Methionine salvage pathway (EF 8.65)
Methylthioribose-1-phosphate isomerase
Enolase-phosphatase E1
Methylthioribulose-1-phosphate dehydratase
S-methyl-5'-thioadenosine phosphorylase
1,2-dihydroxy-3-keto-5-methylthiopentene dioxygenase
Aspartate aminotransferase, cytoplasmic

C

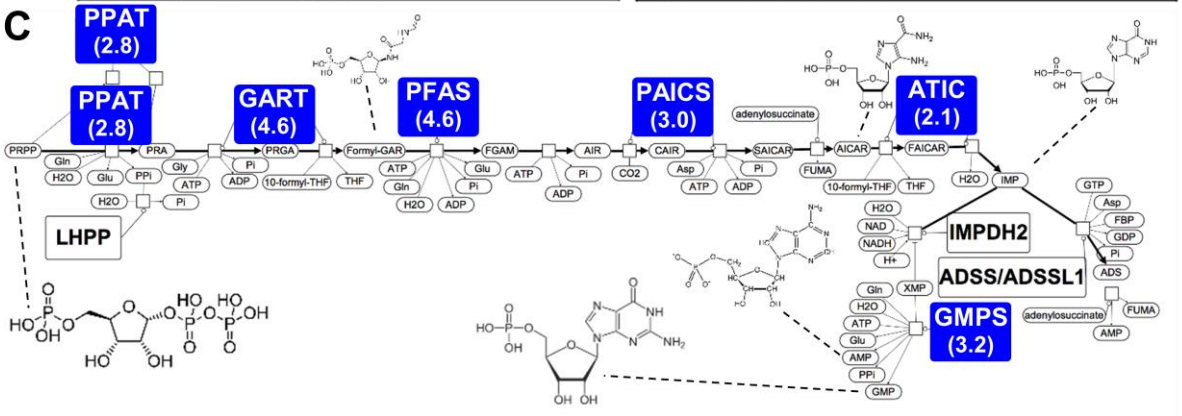

Supplementary Fig. S3_1

Examples of pathways regulated during LUHMES differentiation

For characterization of the proliferating (d0) and differentiated (d6) LUHMES cells, standardized cell culture conditions were used to generate samples from the two types of untreated control cells for further analysis. A: The mRNA expression of four independent cultures of proliferating (d0) and differentiated LUHMES (d6) cells was measured using Affymetrix microarray analysis. Expression levels were determined genome-wide. From these data, differentially expressed genes (DEG) were identified by sorting for probe sets (=Affymetrix gene probes) that were expressed in d6 cells ≥ 4 times higher or lower than in d0 cells. Then, a modulated Limma test was applied to further select those genes for which the differential expression was significant at the 5% level, after the correction for multiple testing. These genes were analyzed for statistical overrepresentation (enrichment) of pathways (PWs) annotated in the Reactome and Panther databases (225-228). The number of PWs found is shown (upregulated: red, downregulated: blue). B: For four regulated PWs, the enrichment factor (EF) and the respective genes are displayed (white: genes of the PW, green: genes of the PW regulated in LUHMES differentiation). C: Visualization of the purine ribonucleoside monophosphate biosynthesis pathway using the Vanted V2 tool (259). Downregulated genes are shown in blue, and numbers indicate the fold change down-regulation (d0 vs d6). Substrates and products are enclosed by boxes with round edges and connected by arrows. Enzymes/genes are enclosed by rectangles.

Abbreviations: PPAT, Amidophosphoribosyltransferase; GART, Trifunctional purine biosynthetic protein adenosine-3; PFAS, Phosphoribosylformylglycinamidine synthase; PAICS, Multifunctional protein ADE2; ATIC, Bifunctional purine biosynthesis protein PURH; IMPDH2, Inosine-5'-monophosphate dehydrogenase; ADSS, Adenylosuccinate synthetase isozyme 2; ADSSL1, Adenylosuccinate synthetase isozyme 1;GMPS, GMP synthase; LHPP, Phospholysine phosphohistidine inorganic pyrophosphate phosphatase.

3.1.12 Supplementary tables

Short name	Full name of chemical compound
AKG	α-ketoglutarate
AcCoA	Acetyl-CoA
Ala	Alanine
Asp	Aspartate
Cit	Citrate
CO_2	Carbon dioxide
DHAP	Dihydroxyacetone phosphate
E4P	Erythrose-4-phosphate
Frc6P	Fructose-6-phosphate
Fum	Fumarate
GA3P	Glyceraldehyde-3-phosphate
Glc6P	Glucose-6-phosphate
Gln	Glutamine
Glu	Glutamate
Gly	Glycine
Glycerol3P	Glycerol-3-phosphate
Lac	Lactate
Mal	Malate
OAA	Oxaloacetate
PEP	Phosphoenolpyruvate
Pyr	Pyruvate
Ru5P_X5P_R5P	Lumped pool (Ribulose-, Xylose- and Ribose-5-phosphate)
S7P	Sedoheptulose
Ser	Serine
Succ	Succinate
13P2G	1,3-Bisphosphoglycerate
3PG	3-Phosphoglycerate
3POH_Pyr	3-Phophohydroxypyruvate
6PG	6-Phosphogluconate

Supplementary table 1_1

Abbreviations used in Fig. 6_1 translate as described above.

	D0	D6
	nmol/10^6 cells/h	
Glucose	-220.2 ± 44	-109.4 ± 12.5
Lactate	509.4 ± 55.5	306.7 ± 23.8
Pyruvate	-29.1 ± 7.8	-14.9 ± 8.1
Ammonium	50.0 ± 5.8	12.9 ± 1.3
Alanine	68.0 ± 7.8	18.5 ± 1.3
Glycine	13.6 ± 11.4	4.8 ± 0.6
Serine	-16.9 ± 7.9	-1.0 ± 0.4
Glutamic Acid	-3.8 ± 0.4	0.3 ± 0.1
Glutamine	-77.7 ± 10.2	-6.0 ± 2.8
Cysteine	- 3.9 ± 0.7	-1.1 ± 0.7
Aspartic Acid	-6.2 ± 3.7	-0.4 ± 0.4
Threonine	-6.9 ± 2.9	-0.4 ± 0.6
Asparagine	-0.4 ± 0.1	0.03 ± 0.04
Valine	-11.2 ± 1.4	-0.8 ± 0.6
Methionine	-2.0 ± 0.3	-0.01 ± 0.1
Leucine	-19.5 ± 2.1	-3.4 ± 0.7
Isoleucine	-15.9 ± 1.7	-2.1 ± 0.6
Phenylalanine	-2.6 ± 4.4	-0.02 ± 0.4
Tyrosine	-2.6 ± 1.7	0.03 ± 0.3
Histidine	-2.5 ± 0.4	-0.1 ± 0.2
Tryptophane	-2.5 ± 1.7	0.03 ± 0.3
Lysine	-7.2 ± 2.5	-1.6 ± 1.0
Proline	8.4 ± 4.2	1.7 ± 0.7
Arginine	-4.8 ± 2.1	-1.2 ± 1.3
	1/h	
μ	0.0742 ± 0.0129	0.0

Supplementary Table 2_1

Cell-specific extracellular rates for d0 and d6 cell lines. Negative values refer to uptake rates from the extracellular medium into the cells while positive values give secretion rates. For calculation procedures see Material and Methods section in the main text.

Short name	Reaction	Fluxes		
		absolute [nmol/10^6 cells/h]		**relative** [% of Glc_IN]
Glycolysis		net	xch	net
emp1	Glc6P(abcdef) ↔ Frc6P(afbcde)	250.45	1074.84	95.52
emp2	Frc6P(abcdef) ↔ DHAP(ebf) + GA3P(dac)	254.66	2400.11	97.13
emp3	DHAP(abc) ↔ GA3P(abc)	253.42	866.03	96.66
emp4	GA3P(abc) ↔ 13P2G(bca)	510.19	886.83	194.59
emp5	13P2G(abc) ↔ 3PG(abc)	510.19	6118.52	194.59
emp6	3PG(abc) ↔ PEP(abc)	502.50	0.08	191.66
emp7	PEP(abc) → Pyr_c(abc)	502.50		191.66
Pentose phosphate pathway (PPP)				
ppp1	Glc6P(abcdef) → 6PG(abcdef)	8.73		3.33
ppp2	6PG(abcdef) → CO2(f) + Ru5P_X5P_R5P(eadbc)	8.73		3.33
ppp3	Ru5P_X5P_R5P(abcde) + Ru5P_X5P_R5P(fghij) ↔ GA3P(ebd) + S7P(agcifjh)	2.10	20.27	0.80
ppp4	S7P(abcdefg) + GA3P(hij) ↔ E4P(gbfd) + Frc6P(iajhec)	2.10	353.83	0.80
ppp5	E4P(abcd) + Ru5P_X5P_R5P(efghi) ↔ GA3P(ifh) + Frc6P(bedcag)	2.10	78.74	0.80
Glycerol-3 phosphate metabolism				
gly1	DHAP(abc) → Glycerol3P(abc)	1.24		0.47
Pyruvate and Lactate metabolism				
pyr1	Pyr_c(abc) → Lac(abc)	453.90		173.12
pyr2	Pyr_c(abc) ↔ Pyr_m(abc)	37.61	5419.79	14.34

Short name	Reaction	Fluxes		
		absolute [nmol/10^6 cells/h]		**relative** [% of Glc_IN]
Tricarboxylic acid cycle (TCA)				
tca1	Pyr_m(abc) → AcCoA_m(ab) + CO2(c)	82.96		31.64
tca2	AcCoA_m(ab) + OAA(cdef) → Cit_m(acbefd)	64.97		24.78
tca3	Cit_m(abcdef) ↔ AKG(fabcd) + CO2(e)	39.69	5.08e-7	15.14
tca4	AKG(abcde) → Succ (½ abcd + ½ badc) + CO2(e)	87.51		33.38
tca5	Succ(½ abcd + ½ badc) ↔ Fum(½ abcd + ½ badc)	111.15	7593.82	42.39
tca6	Fum(½ abcd + ½ badc) ↔ Mal(abcd)	111.15	5131.15	42.39
tca7	Mal(abcd) ↔ OAA(abcd)	51.51	3439.59	19.64

Anaplerosis				
ana1	Pyr_m(abc) + CO2(d) → OAA(abdc)	14.29		5.45
ana2	Mal(abcd) → Pyr_m(abd) + CO2(c)	59.65		22.75
Fatty acid synthesis				
fa1	Cit_m(abcdef) ↔ Cit_c(abcdef)	25.29	4893.22	9.64
fa2	Cit_c(abcdef) → AcCoA_c(ac) + Pyr_c(bfe) + CO2(d)	25.29		9.64
Amino acid metabolism				
aa1	Glu(abcde) ↔ AKG(abcde)	47.82	3688.40	18.24
aa2	Gln(abcde) ↔ Glu(abcde)	64.16	3453.31	24.47
aa3	3PG(abc) → 3POH-Pyr(abc)	6.44		2.46
aa4	3POH-Pyr(abc) → Ser(abc)	6.44		2.46
aa5	Ser(abc) → CO2(a) + Gly(bc)	12.86		4.90
aa6	OAA(abcd) ↔ Asp(abcd)	-0.35	3701.39	-0.13
aa7	Pyr_c(abc) ↔ Ala(abc)	77.78	1612.42	29.67

Short name	**Reaction**	**Fluxes**	
		absolute [nmol/10^6 cells/h]	**relative** [% of Glc_IN]
Extracellular fluxes			
AcCoA_IN	AcCoA_In(ab) → AcCoA_m(ab)	32.52	12.40
Asp_IN	Asp_In(abcd) → Asp(abcd)	7.07	2.70
CO2_IN	CO2_In(a) → CO2(a)	14.29	5.45
Cys_IN	Cys_In(abc) → Pyr_c(abc)	4.60	1.75
Glc_IN	Glc_In(abcdef) → Glc6P(abcdef)	262.19	100.00
Gln_IN	Gln_In(abcde) → Gln(abcde)	67.50	25.74
Glu_IN	Glu_In(abcde) → Glu(cdbea)	8.93	3.41
Pyr_IN	Pyr_In(abc) → Pyr_c(abc)	36.90	14.07
Ser_IN	Ser_In(abc) → Ser(abc)	11.90	4.54
Succ_IN	Succ_In(abcd) → Succ(badc)	36.93	14.09
Ala_ex	Ala(abc) →	71.55	27.29
CO2_ex	CO2(a) →	316.69	120.79
Glu_ex	Glu(abcde) →	12.60	4.81
Gly_ex	Gly(ab) →	7.27	2.77
Lac_ex	Lac(abc) →	453.90	173.12

Short name	Reaction	Fluxes	
		absolute [nmol/10^6 cells/h]	**relative** [% of Glc_IN]
Biomass reactions			
3pg_bm	3PG(abc) →	1.25	0.48
AcCoA_c_bm	AcCoA_c(ab) →	25.29	9.64
AcCoA_m_bm	AcCoA_m(ab) →	50.51	19.26
Ala_bm	Ala(abc) →	6.23	2.38
AspAsn_bm	Asp(abcd) →	6.72	2.56
Cys_bm	Cys_In(abc) →	1.51	0.57
G6P_bm	Glc6P(abcdef) →	3.00	1.15
Gln_bm	Gln(abcde) →	3.34	1.28
Glu_bm	Glu(abcde) →	12.66	4.83
Gly_bm	Gly(ab) →	5.59	2.13
Glyc3P_bm	Glycerol3P(abc) →	1.24	0.47
Oaa_bm	OAA(abcd) →	1.17	0.45
P5P_bm	Ru5P_X5P_R5P(abcde) →	2.42	0.92
Ser_bm	Ser(abc) →	5.48	2.09
Succ_bm	Succ(abcd) →	13.29	5.07

Supplementary table 3_1

Bidirectional and unidirectional reactions are indicated by "↔" and "→", respectively. Net and exchange fluxes are calculated as follows: $v^{net} = v^{\rightarrow} - v^{\leftarrow}$, $v^{xch} = \min(v^{\rightarrow}, v^{\leftarrow})$. Absolute fluxes in [nmol/10^6 cells/h], relative fluxes in [%, related to glucose uptake flux]. Total biomass flux was calculated as: ∑biomass coefficients x growth rate. Biomass coefficients in [nmol/10^6 cells]: AcCoA_c=340.803, AcCoA_m=680.68, Ala=84, Asp=90.58, Cys_In=20.3, Glc6P=40.46, Gln=45.08, Glu=170.66, Gly=75.32, Glycerol3P=16.66, OAA=15.82, Ru5P_X5P_R5P =32.62, Ser=73.92, Succ=179.049, 3PG=16.8. Growth rate in [1/h]: 0.074
Small letters in brackets code for carbon numbers according to InChI enumeration

3.2 Manuscript #2:

Major changes of cell function and toxicant sensitivity by mild, culture-dependent genetic drift

Simon Gutbier[1], Patrick May[2], Sylvie Berthelot[1], Abhimanyu Krishna[2], Timo Trefzer[1], Mehri Behbehani[1], Liudmila Efremova[1], Johannes Delp[1], Gerhard Gstraunthaler[3], Tanja Waldmann[1], and Marcel Leist[1].

[1]:Doerenkamp-Zbinden Chair for alternative *in vitro* methods to replace animal experiments, University of Konstanz, Konstanz, Germany,
[2]: Luxembourg Center for Systems Biomedicine, University of Luxembourg, avenue du swing, L-4367 Belvaux
[3]:Division of Physiology, Innsbruck Medical University, Schöpfstraße 41/1, A-6020 Innsbruck, Austria
Running title: Genetic drift of cultured cells

Send correspondence to:
Marcel Leist
University of Konstanz
PO Box M657
D-78457 Konstanz
Germany
Marcel.Leist@uni-konstanz.de
Tel.: +49-7531-885037
Fax: +49-7531-885039

Figures; X, supplementary tables; 0, tables; 0, pages; 26.

Keywords: human genome; cell stability; dopamine transporter, genome comparison, genotype-phenotype correlation

Acknowledgements:

We are indebted to many colleagues for valuable contributions and insightful discussions during the course of this work. The work was facilitated by grants from the Land Baden Württemberg, EU-ToxRisk and the German Federal Ministry of Education and Research (BMBF)

3.2.1 Abstract

Genomic drift affects the functional properties of cell lines, and the reproducibility of data from *in vitro* studies. While chromosomal aberrations and mutations in single pivotal genes are well explored, little is known about effects of minor, possibly pleiotropic, genome changes. We addressed this question for the human dopaminergic neuronal precursor cell line LUHMES by comparing two subpopulations (SP) maintained either at the American Type Culture Collection ("ATCC") or in the laboratory of the original provider ("UKN"). Both SP showed similar molecular markers, and they differentiated well to intricate neuronal networks. However, drastic differences in susceptibility towards the specific dopaminergic toxicant 1-methyl-4-phenylpyridinium (MPP^+) were observed. Whole genome sequencing was performed to identify underlying genetic differences. While both SP had normal chromosome structures, they displayed about 70 differences on the level of amino acid changing "structural variants", "copy number variations", and "small protein mutations". Some of these differences (e.g. mutation in HSF1) were confirmed biochemically, but none of them offered a direct explanation for the altered toxicant sensitivity pattern. As second approach, markers known to be relevant for the intended use of the cells were specifically tested. The "ATCC" cells rapidly down-regulated the dopamine transporter and tyrosine hydroxylase after neuronal differentiation, while "UKN" cells maintained high functional levels. As the respective genes were not altered themselves, we conclude that polygenic complex upstream changes can have drastic effects on biochemical features and toxicological responses of relatively similar SP of cells.

3.2.2 Introduction

Cell lines, as biological material essential for many research fields, are difficult to define and standardize (260). Methods like short tandem repeat quantification (STR) can show whether two cells are derived from the same donor (261), and classic cytogenetic approaches can provide data on genome integrity at the level of chromosomes or large fragments thereof. Sequencing methods that map individual base pairs (bp) additionally identify small copy number variations (CNVs; 1 kbp - 3 Mbp), larger structural variants (SV; > 3 Mbp) and mutations or single nucleotide variants (SNV) in genes. Such genome alterations continuously occur in dividing cell lines (262-264) and may often be without functional consequences. This background “genetic noise” makes it difficult to identify changes that affect biological features of interest. Distinguishing relevant changes from ongoing background drift is important to the question of whether two subpopulations (SP) of cells are functionally identical. Many fields in fundamental and applied sciences, where cells are the essential material to derive information or to generate bio-products, strongly rely on defining methods for temporal stability of the used cells.

Even with correct cell identity established (e.g. by STR profiling), large genetic variations, such as amplification or loss of chromosomal parts, may go undetected, and apparently identical cells may be genetically diverse (265). For instance, some pluripotent stem cell lines tend to develop aneuploidy or translocations during prolonged culture: trisomy 12 or X, and amplification of 17q provide selection advantages by multiplication of stemness or anti-apoptotic genes (149, 266). Also, it is well established that for cell lines like HeLa, many genetically different SP exist (267). On an even more subtle level, cell identity may be affected by small mutations, and SNP profiling is one of the approaches to document such changes (268). Faster sequencing methods opened the possibility for a closer genetic characterization (by whole genome sequencing (WGS)) at the bp level (149). By comparing differences in the sequence of a cellular genome to the reference genome, single nucleotide variants (SNV; small deletions, insertions or base exchanges in the range of few nucleotides), CNV (sequence parts larger than 1000 bps that show an average ploidy of >2 or <2) and other changes can be detected. Typically, around 4 million SNVs may be detected for iPSC cell lines compared to the reference genome. After removal of already known SNVs, 1000-2000 SNVs are typically identified between cell lines. These are

predominantly heterozygous, and only 5-12 are then expected in coding regions of genes (264, 269). Notably, also genome changes that do not alter the protein structures may have drastic functional consequences. For instance, CNV have been associated with neurological and psychiatric disorders (270-272) .

Studies using WGS point out two factors that favor generation of genetically distinct subpopulations (SP) upon prolonged culture. The first relates to genetic heterogeneity of starting cultures, containing genetically-distinct subpopulations (154). Secondly, genetic variants might arise de-novo during sub-culturing and be selected by further propagation of the cell line. In neuronal precursor cells, a potential additional mechanism responsible for the genome dynamics are L1 retrotransposons, which are highly active during neurodevelopment (273), and may cause insertional mutagenesis.

LUHMES cells, examined in this study, are neural precursor cells of the mesencephalon, obtained from an 8 week old fetus. They were conditionally immortalized with a tetracycline-controlled v-myc transgene (34, 102). Its down-regulation triggers differentiation to electrically active dopaminergic, fully post-mitotic neurons (104). LUHMES have been deposited in 2006 at the American Type Culture Collection (ATCC)(274), and a recent report using the banked cells (275) found that they tolerate up to 60 µM of the neurotoxicant 1-methyl-4-phenylpyridinium (MPP^+), while cells from the original provider laboratory (“UKN”) died at 3-5 µM (35, 49, 63). This large shift in toxicological properties called for a comparative investigation of the cells. As strategies to define functional cell identity are of vast general importance, we explored WGS as a novel approach. Previous studies addressing genetic drift focused mainly on the genome changes arising during prolonged culture. Only little quantitative information is available on how such genetic drift effects cell function. We addressed here the question on whether genome analysis can be comprehensively and unambiguously define cell identity relative to some defined functions. Our results suggest that a prediction of functionality requires more than the genome data, and that cell identity definition needs to follow a fit-for-purpose definition, which mostly requires specifically adopted analytical endpoints.

3.2.3 Materials and Methods

3.2.3.1 Chemicals

Dibutyryl-cAMP (cAMP), fibronectin, Hoechst dye H-33342, resazurin sodium salt, tetracycline, tetramethylrhodamine ethyl ester (TMRE) and MPP^+ were from Sigma (Steinheim, Germany). Recombinant human FGF-2 and recombinant human glial cell derived neurotrophic factor (GDNF) were from R&D Systems (Minneapolis). Tween-20 and sodium dodecyl sulfate (SDS) were from Roth (Karlsruhe, Germany). All culture reagents were from Gibco/Fisher scientific (Hampton, New Hampshire,USA) unless otherwise specified.

3.2.3.2 Cell culture

Handling of LUHMES human neuronal precursor cells was performed exactly as previously described in detail (70, 104). Briefly, maintained in a 5% CO_2/95% air atmosphere at 37° C in proliferation medium (PM), consisting of advanced DMEM/F12 with 2 mM L-glutamine, 1 x N2 supplement (Invitrogen), and 40 ng/ml FGF-2, cells were passaged three times a week. For differentiation, 8 million cells were seeded in a Nunclon T175 tissue culture flask in PM. After 24 h, medium was changed to differentiation medium (DM), consisting of advanced DMEM/F12 supplemented with 2 mM L-glutamine, 1 x N2, 2.25 µM tetracycline (to switch off the transgene), 1 mM dibutyryl 3',5'-cyclic adenosine monophosphate (cAMP) and 2 ng/ml GDNF. At 48 h later, cells were trypsinised, and seeded in a density of $1.5x10^5$ cells/cm² on dishes precoated with 50 µg/ml poly-L-ornithine (PLO) and 1 µg/ml fibronectin in DM. On day 4 of differentiation (d4), medium was exchanged for fresh DM.

3.2.3.3 Cell viability measurement

Resazurin: Metabolic activity was detected by a resazurin assay (35). Briefly, resazurin solution were added to the cell culture medium to obtain a final concentration of 10 µg/ml. After incubation for 30 min at 37° C, the fluorescence signal was measured at an excitation wavelength of 530 nm, using a 590 nm long-pass filter to record the emission. Fluorescence values were normalized by setting fluorescence values of untreated wells as 100%.

LDH release: LDH activity was detected separately in the supernatant and cell homogenate as described earlier (47). The ratio of $LDH_{supernatant}/LDH_{supernatant+\ cell\ lysate}$ was calculated and expressed in percent.

3.2.3.4 Neurite area detection:

Labeling live cells was performed with 1 µM calcein-AM / 1 µg/ml H-33342 for 30 min at 37°C. Images were collected in two different fluorescent channels using an automated microscope (Array-Scan VTI HCS Reader (Thermo Fisher, PA) with high content imaging software (vHCS SCAN, Thermo Fisher, PA). Nuclei were automatically identified in channel 1 (365±50/461±15 nm) as objects according to their size, area, shape, and intensity. The calcein signal was detected in channel 2 (475±40/525±15 nm). An algorithm quantified all calcein positive cells as viable and nuclei stained by H-33342 only as “non viable” cells.

For quantification of the neurite area of d3 cells a well established algorithm was applied (57). For d6 LUHMES, cells were fixed and stained for β-III-tubulin and H-33342, and then the same algorithm was applied.

3.2.3.5 ATP determination:

To determine intracellular ATP, cells grown in 24-well plates were scratched and sonicated in PBS-buffer and boiled at 95 °C for 10 min followed by centrifugation at 10,000 g for 5 min for the removal of cell debris. For the detection of ATP levels, a commercially available ATP assay reaction mixture (Sigma, Steinheim, Germany), containing luciferin and luciferase, was used. 50 µl sample and 100 µl of assay-mix were added to a black 96-well plate. Standards were prepared by serial dilutions of ATP disodium salt hydrate (Sigma, Steinheim, Germany) to obtain final concentrations ranging from 1000 nM to 7.8 nM.

3.2.3.6 GSH determination:

For glutathione determination cells were washed with PBS and lysed in 400 µl of 1% sulfosalicylic acid (w/v). The lysates were collected, sonicated 5 times and centrifuged at 12,000 ×g for 5 min at 4 °C to remove cell debris. Total glutathione content was determined by a DTNB (5,5‘-dithiobis(2-nitrobenzoic acid)) reduction assay. 20 µl sample was mixed with 180 µl assay mixture containing 300 µM DTNB, 1 U/ml glu-

tathione-reductase, 400 µM NADPH, 1 mM EDTA in 100 mM sodium phosphate buffer, pH 7.5 (all Sigma, Steinheim, Germany). DTNB reduction was measured photometrically at 405 nm in 5 min intervals over 30 min. GSH standard curves were performed by serial dilutions ranging from 1000 nM to 7.8 nM, respectively.

3.2.3.7 Western blot analysis

Cells were lysed in RIPA-buffer (50 mM Tris-base, 150 mM NaCl, 1 mM EDTA, 0.25% sodium deoxycholate, 1% NP40, 1 mM Na3VO4, 50 mM NaF, pH 7.5) containing 1x protease inhibitor (Roche) and 0.5 % phosphatase inhibitor cocktail 2 (Sigma, Steinheim, Germany). Determination of protein concentration was performed by using a BCA protein assay kit (Pierce/Thermo Fisher Scientific, Rockford, IL, USA). Thirty-five µg of total protein were loaded onto 12% SDS gels. Proteins were transferred onto nitrocellulose membranes (Amersham, Buckinghamshire, UK). Loading and transfer were checked by brief Ponceau staining. Washed membranes were blocked with or 5% BSA in TBS–Tween (0.1%) for 1 h. Primary antibodies were incubated at 4° C over night. Following washing steps with TBS–Tween (0.1%), horseradish peroxidase-conjugated secondary antibodies were incubated for 1 h at RT. For visualization, ECL Western blotting substrate (Pierce/Thermo Fisher Scientific, Rockford, IL, USA) was used.

3.2.3.8 Immunocytochemistry

Cells were grown on 13 mm glass cover slips (Menzel, Braunschweig, Germany) in 24-well plastic cell culture plates (NunclonTM) and fixed with 4% paraformaldehyde. After incubation with the primary antibody overnight (see Table. S1_2) and with the appropriate secondary antibody for 1 h, Hoechst-33342 (1 µg/ml) was added for 10 min prior to the final washing step. Cover slips were mounted on glass slides with Fluorsave reagent (Calbiochem/Merck/Darmstadt, Germany).

3.2.3.9 EdU incooperation

Cells were grown and differentiated on coated glass cover slips and fixed with PBS, 4% paraformaldehyde, 2% sucrose for 15 minutes. For EdU-staining cells were incubated with 10 µM EdU 30 minutes previous to fixation. To detect EdU incorporation the Click-iT®EdU Alexa Fluor®555 Imaging Kit from Life Technologies (Carlsbad, CA, USA) was used as described by the provider. For the quantitative image analysis

we used KNIME Image Processing Extension (Version 1.1.2). KNIME (Konstanz Information Miner) (https://www.knime.com/) is a user-friendly and comprehensive open-source data integration, processing, analysis, and exploration platform designed to handle large amounts of heterogeneous data. The Image Processing Extension (http://tech.knime.org/community/image-processing) of KNIME allows the documentation of the Image Analysis steps in a so-called workflow. Total nuclei and EdU positive nuclei were counted automatically.

3.2.3.10 Quantitative real time PCR (qPCR)

For reverse transcription quantitative PCR analysis, RNA was extracted with the PureLink RNA mini Kit (invitrogen, Darmstadt, Germany) according to the manufacturer's instructions. For transcript analyses of LUHMES, primers (Eurofins MWG Operon, Ebersberg, Germany) were designed using AiO (All in One) bioinformatics software (276) and can be found in Table S2_2. All RT-qPCRs were based on the SsoFast EvaGreen detection system and were run in a CFX96 Cycler (Biorad, München, Germany) and analyzed with Biorad iCycler software. The threshold cycles (Ct) were determined for each gene and gene expression levels were calculated as relative expression compared to GAPDH ($2^{-(\Delta Ct)}$) or as fold change relative to control ($2^{-(\Delta\Delta Ct)}$). ΔCt and ΔΔCt were calculated using following formulas:

ΔCt = Ct(conditionX/gene Y) – Ct(conditionX/GAPDH).

ΔΔCt = ΔCt(conditionX/gene Y) – ΔCt(untreated control/gene Y).

3.2.3.11 Dopamine measurement

Predifferentiated LUHMES cells (d2) were seeded in T75 Nuclon Flask and differentiated according to the protocol. On day 6, cells were lysed in 0.2% Trition X-100, 0.01 M HCl, 1 mM EDTA, 4 mM sodium metabisulfite and 1 mM Ascorbate. Cells were scraped with cell scraper, sonicated, centrifuged at 3000 g for 5 minutes and supernatants were frozen at -20°C. The dopamine content in cell lysates was analyzed by using Dopamine ELISA Kit (Abnova) according to the manufacturer's protocol.

3.2.3.12 ^{3}H-MPP+ Uptake

Cells were incubated with 5 µM ^{1}H-MPP^{+} and 0.125 µCi per 200 µl (15 nM) volume radioactively labeled ^{3}H-MPP^{+} at 37 °C for different incubation times. The supernatant and the cells were separated. Cells were washed 3 times in PBS and then mechanically removed from the multiwell plate in an equal volume PBS. 2 ml Ultima Gold AB solution was added to supernatant and lysed cells. Light emission was measured by Beckman LS 6500 scintillation counter(28).

3.2.3.13 Sequencing and genome comparison

DNA was prepared from the “UKN” and “ATCC” LUHMES SP by using the Gentra Purgene Cell kit (Qiagen; Venly, Netherlands) s. After sequencing, the reads were mapped against the NCBI Build 37.2 reference genome. The “UKN” SP was paired-end sequenced with Complete Genomics (CG), Inc (Mountain View, CA), using their proprietary sequencing-by-ligation technology (277) at a read-depth of 30x full genome coverage. CG performed primary data analysis as part of their Standard Sequencing Service pipeline (v 2.4.0.43) including image analysis, base calling, quality control, mapping, and variant calling. The “ATCC” SP was paired-end sequenced with the Illumina FastTrack Service (average 30 x full genome coverage), pipeline version v4.0.2 using the Isaac Aligner (6.15.01) for mapping, Isaac Variant Caller (2.1.4) for calling germline SNVs and small insertions and deletions (indels, max size ~50 bp), the Isaac Copy Number Variant Caller (1.1.0) for germline copy number variant (CNV) calls (278), and Isaac Structural Variant (SV) caller (0.23.1)

3.2.3.14 Definitions of calls

The significant differences from the reference genome (=calls) were categorized as follows: CNV were defined as parts of the genome larger than 1000 bp and with an average ploidy of >2 or <2. SV were defined as rearrangements in the genome structure that affect a sequence length > 3Mb, such as large deletions, duplications and inversions. SNV were defined as single nucleotide exchanges. While small insertions and deletions are subsequently called indels (max size ~50 bp).

For CG, SNVs and indels were derived from the “var file”. CNV calls were taken from cnvSegmentsNondiploidBeta-* file and high-confidence structural variation, SV

events were taken from /highConfidenceSvEventsBeta-* file. For Illumina, SNVand indels, CNV and SV were extracted from the different VCF files.

SNV from both platforms were combined into CG testvariant format and compared using custom perl/python scripts. For CG data, coverage statistics were derived from coverage and coverageRefScore files for each chromosome. Coverage at every base was assessed directly from these files. For Illumina, coverage information was extracted directly from BAM (Binary Sequence Alignment format) files. ANNOVAR (Wang et al. 2010) (v20150322) was used to annotate the SNV, SV and CNV with RefSeq and Ensembl gene annotations and additional annotation data like allele frequencies, regulatory elements, known variants that are downloadable from the ANNOVAR web page. The genome data will be made publicly accessible after the acceptance of the manuscript.

3.2.3.15 Genetic identity analysis of ATCC and UKN LUHMES genomes

To compare the genetic identity of both LUHMES SP, the PLINK software (279) was used. PLINK is designed to identify kinship levels in genomes based on the comparison of chromosome stretches that show identity-by-descent (IBD). IBD DNA segments share a common ancestor, i.e. they are identical-by-state (IBS) and lack recombination events in the corresponding sequence. Two individuals can share 0,1, or 2 alleles referring then to IBD=0, IBD=1 and IBD=2, respectively. IBD was determined on the basis of common SNVs and small indels from the HapMap project (downloaded from the Broad resource bundle as part of the GATK toolkit: https://www.broadinstitute.org/gatk/guide/article.php?id=1213). The SNVs and indels called in both genomes were used for IBD analysis. As measure of similarity, we used the so called PI_HAT score, that ranges from 0 (no relationship) to 1 (identity across the genome), and which is calculated from a weighted sum of probabilities for a large number of genome segments to be IBD(PI_HAT= p(IBD=2)+0.5* p(IBD=1)).

3.2.3.16 Comparison of CNV and visualization on chromosomal level

For CNV detection the Illumina BAM files and complete genomics REF coverage files were screened by the RCP pipeline (280), which compares a given BAM file or coverage profile against Reference Coverage Profiles (RCPs) taken from a large set of whole genome sequences. RCP performs coverage binning with a bin size of 1000

bp, GC correction, normalization using reference coverage profiles and merging into larger segments. Thereby it detects and reports changes in ploidy of the classified fragments. Resulting CNVs were visualized on the chromosomal level using the open source visualization tool (http://db.systemsbiology.net/cgi-pub/genomeMapBlocks.pl)

3.2.3.17 CNV in protein coding regions

To identify candidate genes in protein coding regions that differ in copy number between the two SP. DGV was used to filter out CNVs (≥50% overlap) that are common in the general population (Database of genomic variants, (281)). The CNVs not annotated in DGV (Database of Genomic Variants), but occuring in the ATCC or UKN genome are listed in Figure S3_2.

3.2.3.18 Comparison of SNVs, small indels and block substitutions across genomes

To exclude variants arising from technological differences, the data was re-analyzed using a already published filtering strategy (282) allowing better comparison between the two platforms. This reduced the number of SNV and increased the overall concordance between the two platforms. Post filtering, we substracted variants present in either one of the above mentioned platforms and obtained rare events. We filtered this reduced number of variants detected against variants found in one of the following databases: dbSNP 138, 1000 Genome Project, Exome Sequencing Project 6500, ExAC (Exome Aggregation Consortium) and avSNP 138 (by ANNOVAR). Variants found in one of those databases were considered common or known variants and only the variants, which were not present in any database (called “somatic”) were considered further. In order to detect differences of potential phenotypic impact, the somatic events were screened for variants potentially affecting splicing and amino acid sequence using the ANNOVAR annotations from RefSeq and Ensembl. The genes annotated to this amino acid changing mutations were sorted for specific occurrence in the “ATCC” or “UKN” genome.

3.2.3.19 Ingenuity pathway analysis

For Ingenuity pathway analysis all CNV, SV and SNV specific for each SP were used to test for pathway overrepresentation.

3.2.3.20 STR phenotyping

Identity of the used SP was confirmed by STR (Short Tandem Repeat) analysis as described previously (283). Briefly, DNA samples from the SPs were prepared using a commercial kit (Puregene Cell Kit, Qiagen). The kit GlobalFiler® PCR Amplification Kit (Thermofisher) was then used to determine the cell-specific profile for 16 different genomic loci using an Applied Biosystems GeneMapper Device. STR results showed 100% identity of the profiles of both SP.

3.2.3.21 Statistics and data mining

Cytotoxicity data (ATP, GSH, LDH, resazurin) and qPCR are presented as means of at least three independent experiments, and statistical differences were tested by ANOVA or students t-test with post-hoc tests as appropriate, using GraphPad Prism 5.0 (Graphpad Software, La Jolla, USA).

3.2.4 Results

Similarities and differences in the response to toxicants:

The two subpopulations (SP) of LUHMES cells, “UKN” and “ATCC” were used for comparative neurotoxicity experiments. As reported earlier, the established parkinsonian model toxicant MPP^+ (170), at a concentration of 5 µM, triggered cell death in “UKN” but no sign of degeneration in “ATCC” for up to 72 h (Fig 1_2A). This was confirmed in an alternative setup, in which “UKN” LUHMES died after 48 h, when exposed to ≥5 µM MPP^+ while the “ATCC” SP tolerated up to 100 µM (Fig. 1_2B). In line with the observed difference in cell death, “ATCC” LUHMES maintained their pool of the intracellular redox-buffer glutathione for 72 h, when exposed to MPP^+, while this was severely depleted in “UKN” (Fig. 1_2C). Essentially similar observations were made for ATP (Fig. 1_2D), an energy metabolite particularly sensitive to MPP^+ toxicity.

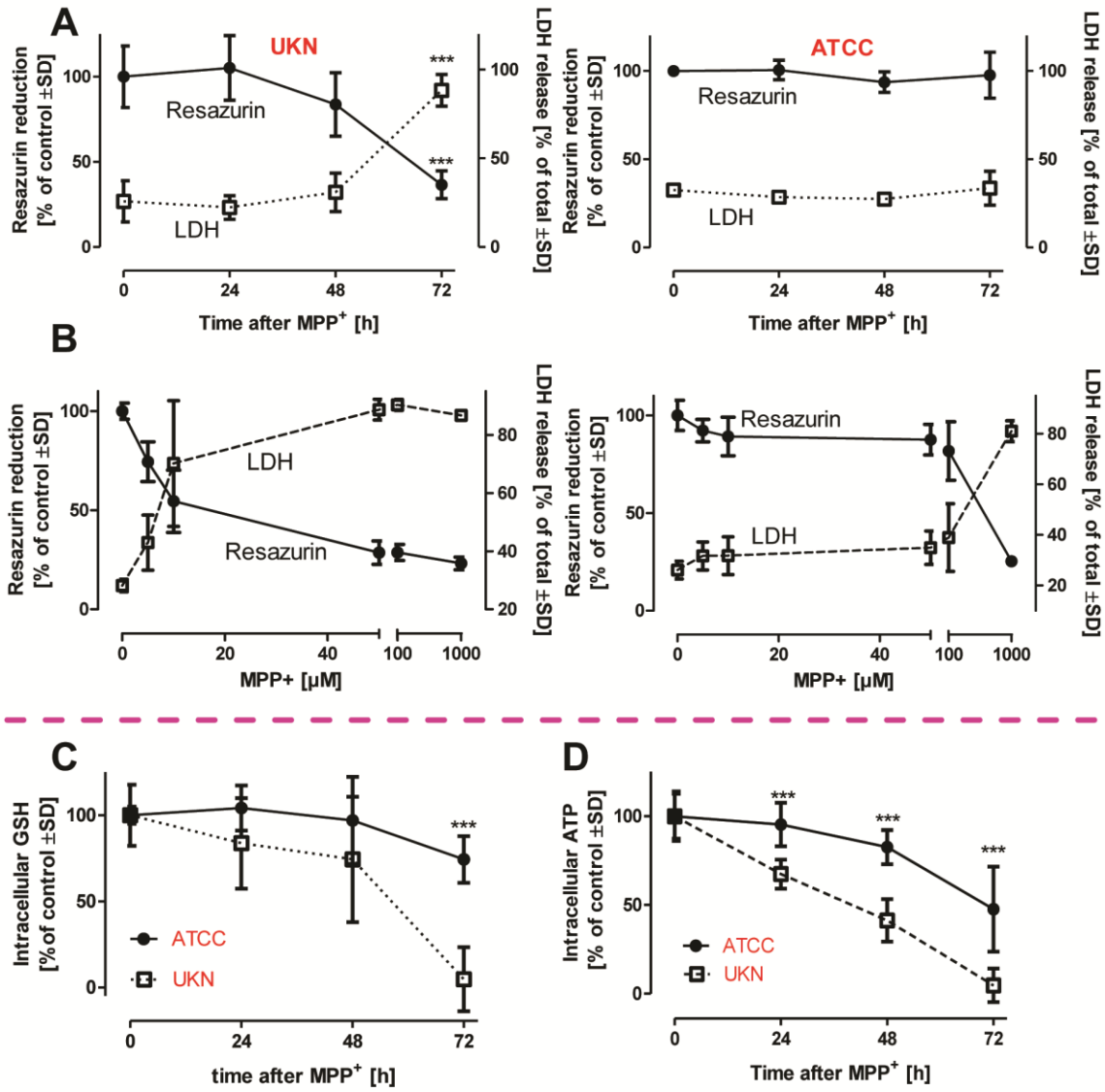

Figure 1_2: Similarities and differences in the reaction to different toxicants

LUHMES cells from two different sources (University of Konstanz (UKN); American Type Culture Collection (ATCC)) were cultured according to a standard protocol.
LUHMES cells were seeded at a density of $1.5*10^5$ cells/cm^2 at d2. Medium was exchanged at d4 and exposed to MPP^+ starting at d6. **A:** Viability was assessed at d9 by measuring resazurin reduction and LDH release after cells have been exposed to MPP^+ [5 µM] for times as indicated. Data are means ±SD of three independent experiments.***:$p \leq 0.001$ **B: "**UKN" and "ATCC" LUHMES were incubated with indicated concentrations of MPP^+. After 48 h viability was assessed measuring resazurin reduction and LDH release, Data are means ±SD of three independent experiments. **C:** Intracellular levels of total glutathione (GSH+GSSG) were measured in cells treated with MPP^+ [5 µM] for indicated time periods and represent means ±SD of three independent experiments. **D:** Intracellular levels of total ATP were measured in cells treated with MPP^+ [5 µM] for indicated time periods. Data are means ±SD of three independent experiments.***:$p \leq 0.001$

Comparison of the genome structures of the two LUHMES SP:

Having observed this differences, we tested whether the "UKN" and "ATCC" SP were really the same cell line. To exclude cross contamination, and to verify the same origin of the SP we compared their STR-profiles. We found 100% conformity of

“UKN” and “ATCC”(Fig. S1_2). Moreover, this profile agreed with the one provided by ATCC (Fig. S1_2).

To obtain broader information on the genome status of the cells, whole genome sequencing was performed. The first use we made of WGS data was to establish the kinship-level of the two SP. Using software originally developed for paternity testing (PLINK, (279)) or profiling of tumor heterogeneity, the two genomes were mapped for their “identity by descent” (IBD) and the corresponding PI_HAT score was calculated. The result of 0.9959 is in the range usually found for monozygotic twins or for duplicate tissue samples (284). This solidly confirmed the common ancestry of the two SP, and indicated that there was no contamination.

In a next step, the genome data were compared to the human reference genome at a ≈1 kbp resolution. Overall chromosomal structure and ploidy were normal for both SP (Fig. 2_2A). Overall 221 structural variants (SV; typically between 1 kbp and 3 Mbp) not reported in the common genome databases were identified (Fig S2_2A). Out of these 15 SV were present in both SP, 3 were identified only for the “UKN” SP, and the others (containing 179 inversions were detected in the “ATCC” LUHMES (Fig. S2_2A). We then identified all genes in the proximity of SV(Fig. S2_2B). This list of candidate factors for altered toxicant sensitivity were examined for reported functions, and none of them offered a simple explanation for the difference of the two LUHMES SP.. We therefore analyzed in a next step the copy number variations (CNV) as potential candidates. A sizeable number (n=298) of CNV was identified, some of them occurring only in the “UKN” SP and others only in the “ATCC” SP (Fig. 2_2A). After filtering for overlap with protein coding regions, 16 CNV were found only in “UKN” cells and 35 only in “ATCC” cells (Fig. S3_2). As expected, both SP shared some (n=19) CNV, as they originate from the same ancestor. Illustrative examples for the latter group are a 4 kbp deletion on chromosome 9, located within the Muscle Associated Receptor Tyrosine Kinase (MUSK) gene, or a 100 kbp deletion on chromosome 13 located within the G Protein-Coupled Receptor Kinase 1 (GRK1) gene (Fig. 2_2A; Fig. S 4_2A+B).

Moreover, both cell lines had the same two transgene insertion sites (Fig. 2_2A), which were mapped to the intronic regions of the cullin 1 (Cul1) gene on chromosome 7 (Fig. 2_2B) and an intergenic region of chromosome 15 (Fig. 2_2C).

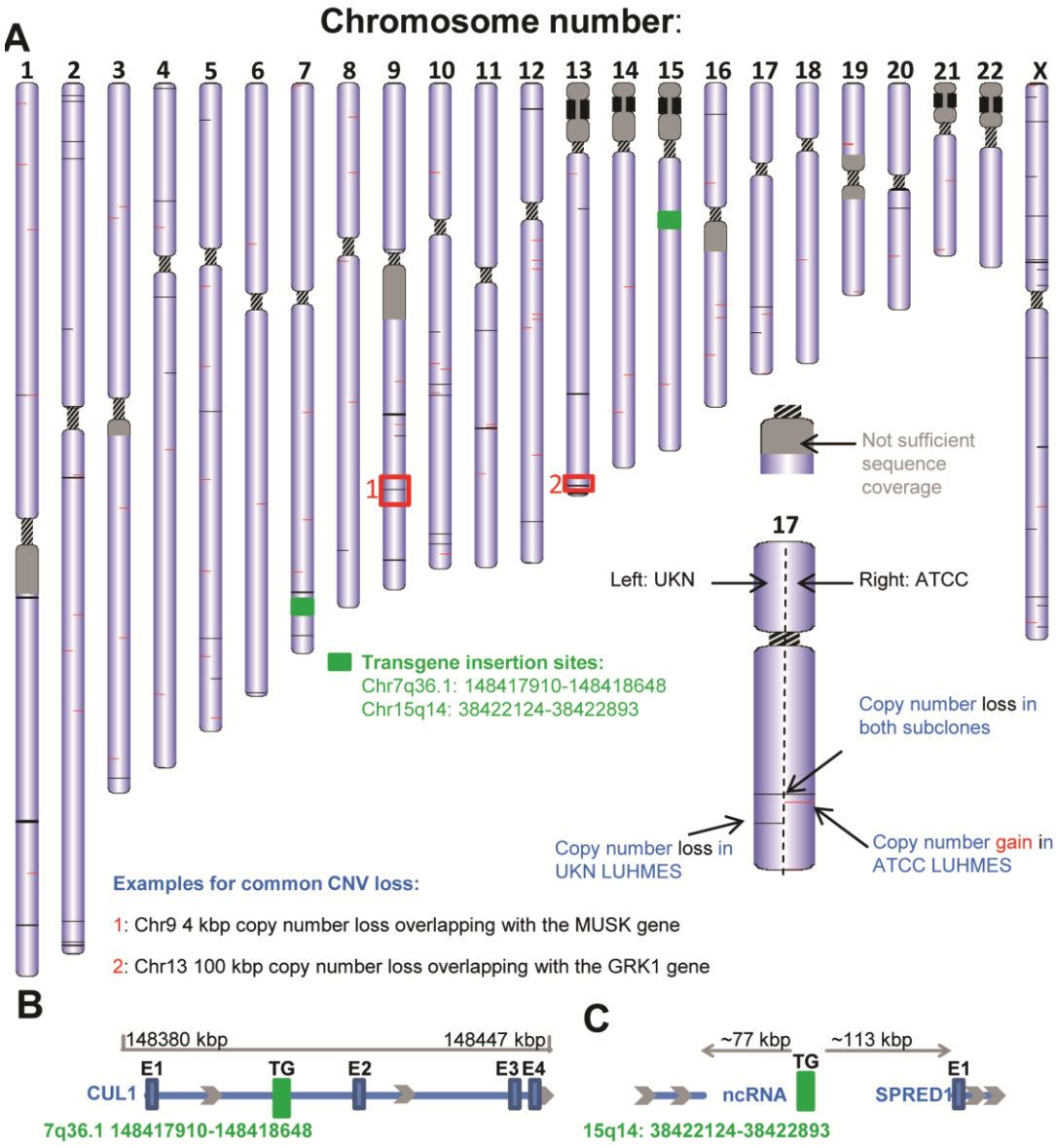

Figure 2_2: Genome wide ploidity status

LUHMES cells from two different sources (University of Konstanz (UKN); American Type Culture Collection (ATCC)) were sequenced by either complete genomics (UKN) or ilumina (ATCC) sequencing platforms. **A**: Copy number variations and transgene insertion sites were depicted on chromosome level. CNVs were visualized on the chromosomal level using the open source visualization tool (http://db.systemsbiology.net/cgi-pub/genomeMapBlocks.pl). Black lines indicate losses and red lines gain in CNV. Transgene insertion sites are marked in green. Examples chosen for detailed resolution are indicated with red boxes and labeled 1 and 2. Detailed resolutions are depeicted in Fig. S4_2 **B**: Graphical scheme of transgene insertion site on chromosome 7, which is located within an intron of the Cullin 1 gene. Coordinates are based on the NCBI Build 37.2 reference genome **C**: Graphical scheme of transgene insertion site on chromosome 15, which is located in the intergenic region.

Single nucleotide variants (SNV) affecting protein amino acid sequence

Altogether about 4.5 million SNV (= small mutations) were called, when the LUHMES genomes were compared to the reference genome (Fig. S5_2A). These were filtered for known and common variants (Fig. S5_2A-C), and corrected for sequencing technology differences. This left 23,400 specific SNV (not occurring in the general popu-

lation) in LUHMES genomes (Fig. S5_2B).Further selection for changes predicted to change an amino acid in proteins (Fig. S5_2C) resulted in a final set of 29 protein changes (Fig. 3_2A) that differed between “UKN” and “ATCC” LUHMES, and 33 rare variants found in both LUHMES SP (Fig. S5_2C).

From the group of differential mutations, we selected promising candidates (Fig. 3_2A marked in red), that might be responsible for toxicological differences observed between the SP. Western blotting was used to investigate altered expression levels of NRXN3 (neural cell adhesion molecule), HSF1 (master controller of the heat shock response), and SIRT6 (cell stress and progeria-associated protein deacetylase). For these three candidate genes, we observed indeed different protein levels in neuronally differentiated LUHMES (Fig. 3_2B-F). NRXN3 is known for extensive alternative splicing (285), and the ratio of its major bands differed strongly in “ATCC” vs. “UKN” neurons (Fig. 3_2B+C). SIRT6, although expressed normally in proliferating LUHMES (d0) was strongly down-regulated in d6 “ATCC”, compared to d6 “UKN” (Fig. 3_2B,D). Also HSF1 was found at lower levels in “ATCC” compared to “UKN” (Fig. 3E+F). To test for functional implication of this finding, cells were exposed to the HSP90 inhibitor geldanamycin. As expected, HSF-1 was down-regulated in both SP. At the same time, a counter-regulation of HSP70 was observed in both SP (Fig. 3_2F,G). This suggests that the mutation in HSF1 (“ATCC”) did not abolish the overall function of this transcription factor, but it affected its overall cellular expression levels (Fig. 3_2E+F). This was also confirmed when cells were exposed to heat stress. As described earlier (286) this leads to a rapid post-translational modification (higher apparent MW) of HSF-1, and this biochemical feature was observed in both SP (Fig. 3_2H). These findings provide proof of principle that genetic differences between the LUHMES SP, identified by sequencing lead to biochemically measurable alterations. Some of the identified genes are involved in controlling cellular resilience (e.g. HSF1) or aging/degeneration (SIRT6). To explore the functional implication of many potential candidates with respect to MPP^+ toxicity in LUHMES appeared to be impossible within a reasonable time span. We performed therefore additional toxicity experiments to narrow down the list of genes with matching biological properties. Rotenone has the same cellular target as MPP^+ (287), colchicine is general inducer of neuronal apoptosis (48), and antimycin A /DETA-NONOate trigger different types of oxidative stress and mitochondrial inhibition. They all showed the same toxicity to “ATCC” and “UKN” LUHMES (Fig. S6_2). These findings suggests that genes in-

volved in general cell death regulation do not account for the differences observed for MPP^+ (Fig. 1_2).

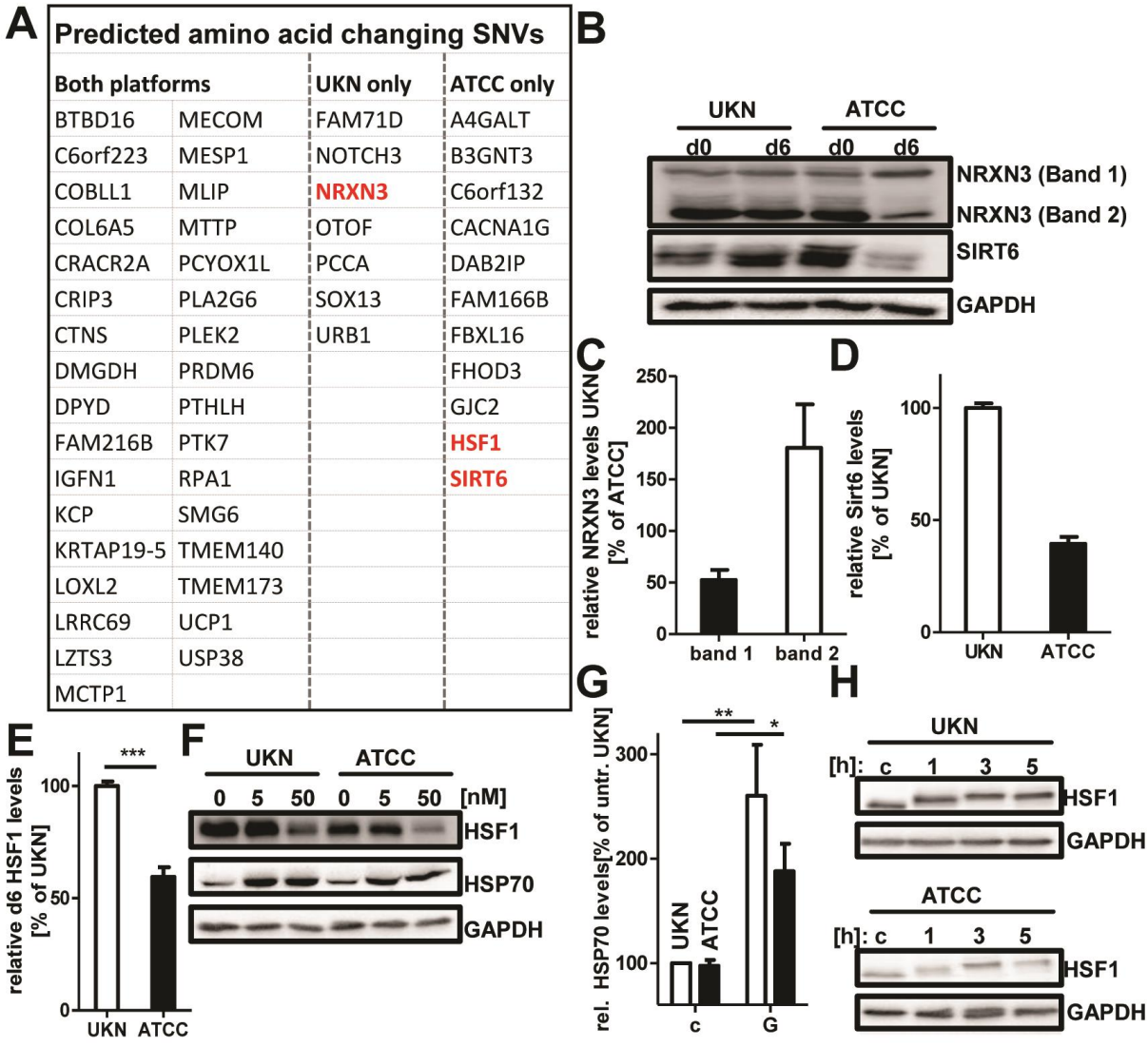

Figure 3_2: Amino acid changing SNVs

SNVs affecting proteins in LUHMES from two different sources (University of Konstanz (UKN); American Type Culture Collection (ATCC) were filtered from the total SNVs called as described in the material and methods section in detail.
A: Common and "UKN" or "ATCC" specific predicted proteins, that are affected by an amino acid changing SNV. The ones marked in red were further assessed on protein level for differences between the two SP. **B:** Undifferentiated (d0) and mature (d6) LUHMES cells were lysed and analysed by Western blot analysis using anti- NRXN3, anti-SIRT6 and anti-GAPDH antibodies. **C+D:** Densitometric quantification of band intensities of NRXN3 in d6 cells (C) and SIRT6 in d6 cells (D). **E:** Densitometric quantification of band intensities of HSF1 in d6 cells. Intensities are depicted relative to the intensity in the "UKN" SP. **F:** LUHMES (d6) cells of both SP were treated with indicated concentrations of Geldanamycin for 24h. After incubation cells were lysed and analysed by Western blot using anti-HSF1, anti-HSP70 and anti-GAPDH antibodies. **G:** Densitometric quantification of band intensities of HSP70 induction by Geldanamycin. Intensities are depicted relative to the intensity in the untreated "UKN" SP. Band intensities of 5 and 50 nM Geldanamycin were combined. **H:** LUHMES (d6) cells of both SP untreated (c) and with indicated time after start of heatshock (43° C/1 h). After incubation, cells were lysed and analysed by Western blot using anti-HSF1 and anti-GAPDH antibodies.

Detailed phenotypic characterization

The small genetic changes and the resultant biochemical modifications may subtly affect the neuronal differentiation of cells, and therewith their toxicological response to a specific neurotoxicant. Therefore, we undertook a detailed phenotypic characterization. The overall morphology of the two SP was assessed by immunocytochemistry (ICC), and expression of marker genes (evaluated for the initial characterization of "UKN" LUHMES (104)) was quantified by qPCR. Undifferentiated (d0) SP were similar with respect to the patterns of nestin and β-III-tubulin staining (Fig. 4_2A), and also differentiated cells (d6) appeared to be morphologically similar, as indicated by the distribution of microtubule associated protein-2 (MAP2), β-III-tubulin and post-synaptic density protein 95 (PSD95) (Fig. 4_2B; Fig. S7_2). We compared the changes in gene expression for marker genes, (Fig. 4_2C). No differences between the SP were observed for DRD2, GFRA1, TUBB3, SYP, SNAP25, GRIN1, HES5, VMAT-2 and ACHE, and the down-regulation of the v-myc transgene, upon tetracycline addition, was equally effective in both SP (Fig. 4_2C). Based on these data, the two SP would be rated as being similar.

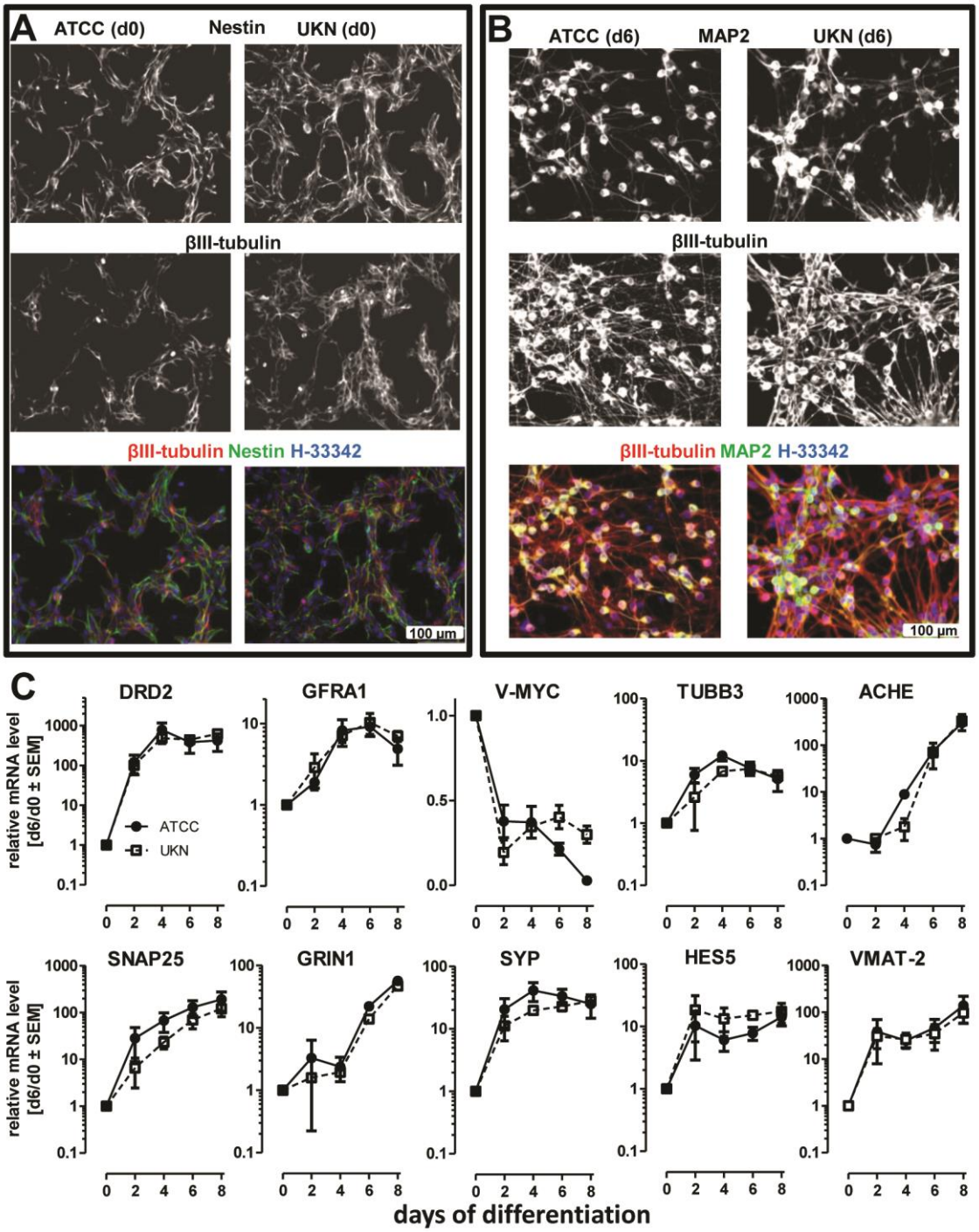

Figure 4_2: Similarities in neuronal differentiation

LUHMES cells from two different sources (University of Konstanz (UKN); American Type Culture Collection (ATCC)) were cultured and differentiated according to the published standard protocol. **A:** Morphology and structural properties of undifferentiated LUHMES (d0) cells (of both SP) were assessed by immunocytochemistry staining for β-III tubulin, Nestin and H-33342. **B:** Morphology and structural properties of differentiated LUHMES (d6) cells (of both SP) seeded at a density of $0.5*10^5$ cells/cm^2 were assessed by immunostaining for β-III tubulin (red), MAP2 (green) and H-33342 (blue). **C:**LUHMES cells were differentiated for the indicated time points (0; 2; 4; 6; 8 days) and mRNA samples were prepared Changes in gene expression of the neurodevelopmental marker genes DRD2, GFRA1, v-MYC, TUBB3; ACHE, SNAP25, GRIN1, SYP, HES5 and VMAT-2 of LUHMES cells from both SP were monitored by qPCR. Values are expressed relative to expression levels in undifferentiated LUHMES cells. Data are means ±SEM for three different experiments.

To unravel more subtle differences, we quantified neurite growth (Fig.5_2A) as functional endpoint (49, 57). Both SP formed an intricate neurite network, but "ATCC" LUHMES displayed a significantly higher neurite area per cell compared to "UKN" LUHMES at day 3 and 6 of differentiation (Fig. 5_2B+C). This hints to subtle differences in differentiation control between the two SP, possibly linked to signaling factors or transgene activity.

Differences in the reversal of differentiation

To scrutinize the efficiency of the tet-off system more thoroughly, an experimental setup was developed that triggered neuronal differentiation for 4 days, and then probed, to which extent it could be reversed by re-addition of FGF and withdrawal of GDNF/tetracycline (Fig. 5_2D). "Reversal" was measured as number of cells re-entering the cell cycle (EdU incorporation). A higher percentage of EdU positive (reversal) cells was observed in "UKN" compared to "ATCC" (Fig. 5_2E). This was confirmed by other cell cycle markers, such as Ki67 and CycA1, and it fully agreed with a stronger re-induction of cell cycle genes in "UKN" compared to "ATCC" LUHMES (Fig. 5_2E-F; Fig. S8_2A+B). These experiments hinted to a subtle difference in transgene shutoff and differentiation speed between the two SP. As "ATCC" attained the postmitotic neuronal phenotype faster than "UKN", the differentiation efficiency does not explain the reduced sensitivity to the neurotoxicant MPP^+. However, it may have impact on other types of experiments LUHMES may be used for.

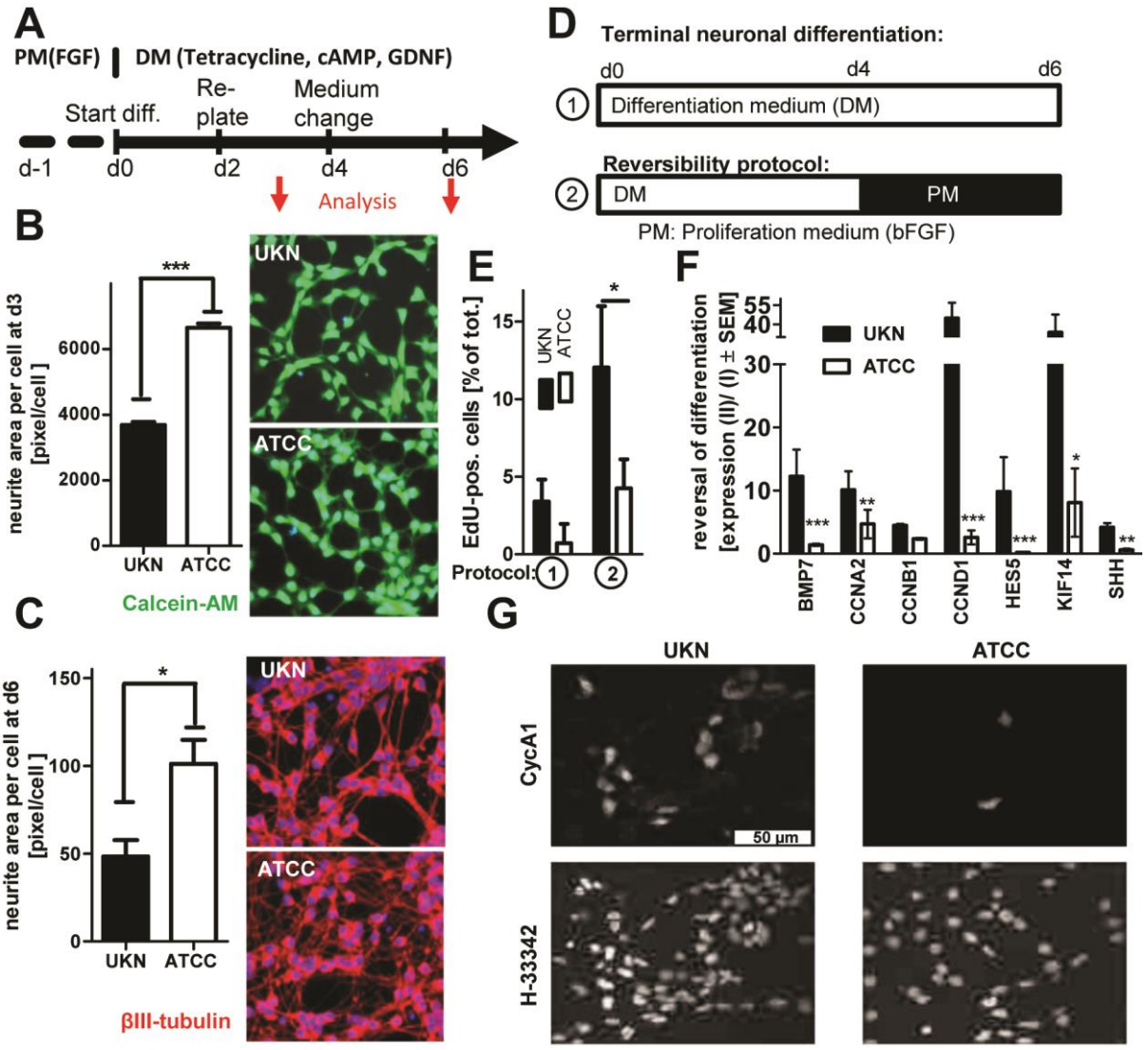

Figure 5_2: Comparison of neurite outgrowth and cell cycle exit

LUHMES cells from two different sources (University of Konstanz (UKN); American Type Culture Collection (ATCC)) were differentiated according to a published standard protocol. **A:** Cells were replated at d-1 and differentiation was started by removal of proliferation medium (PM) and the addition of differentiation medium (DM) containing tetracycline, cAMP and GDNF at d0. Cells were re-plated at a density of $1.5*10^5$ cells/cm^2 at d2. Medium was exchanged at d4 and "mature cells" were ready at d6, e.g. for measurement of the neurite network or toxicant exposure. **B**: Cells of both SP were stained on d3 with calcein-AM and H-33342. The neurite area per field was assessed in live cultures by automated microscopy in combination with an algorithm adapted for neurite area quantification (cellomics). In parallel, the number of cells per field was quantified (H-33342 positive nuclei), so that the average area/cell could be calculated. **C:** "UKN" and "ATCC" SP were differentiated until d6. These cells were fixed and neurites were assessed by immunocytochemistry staining for β-III tubulin and H-33342. The total neurite area per field (based on β-III-tubulin positive pixels) was measured by automated microscopy in combination with an algorithm adapted for neurite area quantification (cellomics). In parallel, the number of cells per field was quantified, so that the average area/cell could be calculated. **D**: LUHMES cells of both SP were cultured in two different cultivation procedures. Therefore medium was exchanged at d4 to either 1) differentiation medium (DM) or 2) proliferation medium (PM). **E:** Experiment was stopped at d6 and the EdU positive cells for both culture conditions were quantified using fluorescence microscopy and automated counting. **F**: Changes in gene expression in cell cycle related genes of cells treated with proliferation medium (2) relative to cells differentiated according to the standard protocol (1) were measured at d6 and expressed as ratio of condition(2)/ condition(1). **G**: Cell cycle activity of LUHMES cells of both SP cultured according to 2) was assessed by immunocytochemistry staining for cyclin A1 and H-33342 . Data are means ± SD for three independent cell differentiations of different passages. ***: $p \leq 0.001$ **: $p \leq 0.01$ *: $p \leq 0.5$

Differences in the dopaminergic phenotype

Another explanation of the sensitivity differences may be an effect on an upstream regulatory circuit related to the dopaminergic properties of LUHMES. To probe this hypothesis, we performed overrepresentation analysis of the identified mutations with respect to known signaling and regulation pathways (Ingenuity IPA package). Amongst the top 5 most over-represented pathways, we identified “cAMP signaling”, “dopamine receptor signaling” and “tetrahydrobiopterin biosynthesis” in “UKN” LUHMES and “protein kinase A signaling” in “ATCC” LUHMES as potential explanations. These pathways affect the dopaminergic differentiation and the key enzyme TH, and polygenic effects on these regulatory circuits could result in differences in the dopaminergic phenotype (Fig.S9_2-11_2).

Considering the results of the pathway enrichment analysis, we wondered whether differences in the dopaminergic phenotype might account for the observed differential toxicity, even though none of the central genes (DAT, TH, VDAC2, AADC, GFRA2, NURR1, LMX1, etc.) appeared to be directly mutated. LUHMES cells have been used as a model for dopaminergic neurons in several studies, and MPP+-toxicity depends on such properties (15, 34, 42, 275). We therefore compared the mRNA expression levels of dopaminergic markers during the differentiation. Interestingly, both SP strongly up-regulated the dopamine transporter (DAT) and GDNF receptor (GFRA2) at day 2 of differentiation, but the “ATCC” SP down-regulated these two genes at day 4-8 of differentiation, while they stayed up-regulated in the “UKN” LUHMES (Fig.6_2A). Furthermore, there were also significant differences in the regulation of tyrosine hydroxylase (TH), the rate determining enzyme of dopamine synthesis, and few other neuro-specific genes (DBH and SYN1) (Fig.6_2A). In line with the lower TH levels, there was a difference in the intracellular dopamine levels, which further confirmed a weaker dopaminergic phenotype of the “ATCC” subclone compared to “UKN” (Fig.6_2B). Relative expressions at day 8 differed between the two SP for DAT, GFRA2, DBH and TH (Fig.S12_2A). Accordingly, TH and DAT protein was abundant in “UKN” LUHMES on d8 but not in the “ATCC” SP (Fig. S12_2B+C). Moreover, the uptake of MPP^+ a substrate of the dopamine transporter was significantly higher in “UKN” compared to “ATCC” LUHMES (Fig. 6_2C). Use of the specific DAT-blocker GBR-129009 confirmed that all MPP^+ uptake was mediated by the DAT and that this functional difference would impact MPP^+ toxicity (Fig. 6_2D).

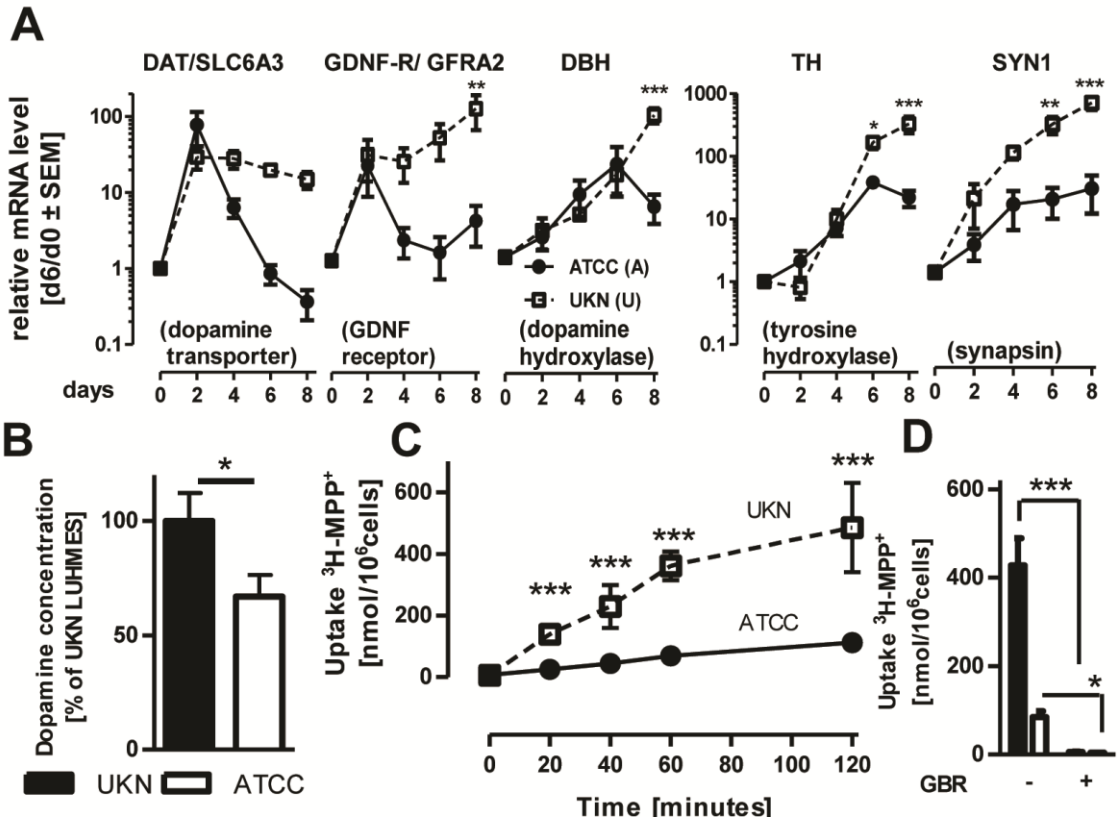

Figure 6_2: Significantly changed differentiation markers

LUHMES cells from two different sources (University of Konstanz (UKN); American Type Culture Collection (ATCC)) were cultured according to a standard protocol. **A:** LUHMES cells were differentiated for the indicated time points (0; 2; 4; 6; 8 days) and mRNA samples were prepared. Changes in gene expression of the neurodevelopmental marker genes DAT, GFRA2, DBH, TH and SYN1 were monitored for both SP. Values are expressed relative to expression levels in undifferentiated LUHMES cells and represent means ± SEM from three independent experiments. ***: $p<0.001$ **: $p<0.01$ *: $p<0.5$ **B:** Dopamine content of LUHMES (d6) cells of both SP was analyzed using a Dopamine ELISA Kit (Abnova). **C:** Uptake of ^{3}H-MPP^{+} in "UKN" and "ATCC" SP was assessed for incubation times as indicated. Therefore, 5µM MPP^{+} containing 0.3125 µCi ^{3}H-MPP^{+} were applied to the cultures and radioactivity in supernatant and cell lysates was measured using a scintillation counter. Data are means ±SD from three independent experiments ***: $p<0.001$ **D**: Uptake of ^{3}H-MPP^{+} in "UKN" and "ATCC" LUHMES was measured after 2 h incubation. Therefore, 5µM MPP^{+} containing 0.3125 µCi ^{3}H-MPP^{+} in presence or absence of GBR-12909 [1 µM] were applied to the cultures. Radioactivity in supernatant and cell lysates was measured using a scintillation counter. ***: $p<0.001$

3.2.5 Discussion

LUHMES are used as highly reproducible test system for neurotoxicity investigations or to model aspects of neurodegenerative disease (42, 49, 57, 58, 63, 70, 104, 275, 288-291). Since the MPP^{+} model for Parkinson's disease is frequently used by us and others (170, 287), the finding that the induction of cell death in LUHMES purchased from ATCC required 16 times higher concentration of the neurotoxicant MPP^{+} (275), than found for the original cells ("UKN") (35, 49, 63), raised concerns about the definitions of cell line identity. Even though we found here SP of LUHMES from different sources to be highly similar on the genomic level (same STR-profile; HAT

score ≈1), we identified clear phenotypic and toxicological differences using a targeted identity profiling. The attenuated dopaminergic phenotype identified in the “ATCC” SP, explained the selectively increased resistance to the parkinsonian toxicant MPP^+. The results of this study thus provide compelling evidence that standard measures of cell definition, ranging from phenotypic markers, over STR profiling and even WGS data are not sufficient to define cell identity. Rather targeted testing, related to the specific functional demands of cells in a given study, is required.

Here we successfully showed that the two LUHMES SP are indeed derived from the same cells. Although, this may appear trivial, it is an important confirmation, as a lot of commonly used cell lines are misidentified (e.g. wrong tissue origin or wrong species) or contaminated by other cells (e.g. HeLa)(148, 151, 274, 292-295). During the last decades, as cross-contaminations and cellular misidentifications became apparent, the importance of cell line identity gained increasing attention (150, 294, 296). The rapid development in the field of genome sequencing allowed us now to address questions on genetic drift and stability at higher levels of resolution.

Since we observed very high genetic concordance and two identical transgene insertion sites in each SP, our WGS data confirmed the common clonal origin of the two SP. Nevertheless, we also detected differences on the genome level, which initially appeared to be relatively high in number. This may be in part due to two different sequencing platforms used here to derive WGS data. However, after application of established software tools and quality assurance, to correct for the noise generated by the different sequencing platforms (282), the number reduced drastically and was in the range of other reports (264, 269). In such other studies, genome profiling has been used mainly to describe cellular differences, but even the most recent large-scale approaches (297, 298) fail to make predictions from genome changes to cell function (e.g. altered function or subtype of neoplastic disease). This is however, circumstantial evidence, that long-term culturing, genetic drift and altered functional properties of cells are causally related. It has been shown that over-subculturing with too many passages may affect cell line characteristics and thereby reproducibility. For example Caco2 cells display different transport and toxicological properties with increasing number of passages (148). Genetic heterogeneity of the parental line and sub-selection during culturing is suspected to be the underlying mechanism leading to genetic drift that might result in genetically different cell lines (149, 154, 266).

When cell lines are used for protein production, stringent single cell cloning has been suggested as favorable way to ensure cell identity and production quality. However, this was recently doubted as a study showed that also single-cell-clone-derived cell populations comprise variants of production efficiency and quality, up to the level of changes in copy number of transgene within the population (299).

Even though, we confirmed some of the amino acid changing events (e.g. HSF1), that distinguished the LUHMES SP, none of those explained the observed differences in the toxicological response. The similar sensitivity to largely diverse toxicants suggests that fundamental apoptosis and stress pathways did not differ between the SP.

Bioinformatic data-mining revealed that genetic alterations are particularly frequent within pathways related to the dopaminergic phenotype. Intracellular dopamine has been clearly identified as factor promoting neuronal cell death (300, 301). Therefore, the capacity of LUHMES to produce dopamine results in a selective pressure to accumulate mutations affecting their dopaminergic phenotype. Both SP seemed to have taken a different path to decrease potential dopamine toxicity. For “ATCC”, the down-regulation of tyrosine-hydroxylase (TH) is the most obviously reducing dopamine stress. Interestingly, this did not occur by inactivation of the TH gene, but rather by some upstream regulation. In the same vein, dopamine tansporter (DAT) was affected indirectly, and in a way that was not obviously predicted by genome data.

Direct phenotypic characterization helped to identify differences in the dopaminergic phenotype of the SP. Especially, the lower expression and activity levels of the DAT provides a conclusive and sufficient explanation for the observed differences in the toxicological response to MPP^+, as the toxicant requires this transporter (28, 170, 287) to enter the cells. The toxicity we observed at higher concentrations of MPP^+ (≥ 100 µM) in the “ATCC” SP might be mediated by low abundance of the DAT (down-regulated, but not totally deficient) or by other transporters, such as the organic cation transporter-3 (28, 170, 302). The fact that both SP reacted similarly to rotenone, a toxicant with the same target as MPP^+ (mitochondrial complex I), suggests that toxicokinetic (i.e. transport) factors were mainly responsible for the observed sensitivity difference with MPP^+.

In summary, the data presented here provide an important example for gaps in the commonly used cell identification approaches, and for the need to reconsider good practices in the field (274, 295, 303, 304). In order to ensure proper cell functionality, we suggest to include a “fit-for-purpose” phenotypic testing strategy in cell authentication procedures, and to define performance standards for desired cell functions. Adoption of such standards would improve reproducibility of *in vitro* data and comparability across studies. Therefore, an important issue concerning a perceived reproducibility crisis of science (146, 150, 296) would be addressed. Future refinements can be envisaged already now, e.g. addressing heterogeneity and genetic mosaicism within given SP, for example by single cell sequencing (272) or functional testing after subcloning.

3.2.6 Supplementary information

Source / STR marker	This study		ATCC website
	UKN LUHMES	ATCC LUHMES	ATCC LUHMES
Amelogenin	X	X	X
CSF1PO	13,14	13,14	13,14
D5S818	11,13	11,13	11,13
D13S317	9,11	9,11	9,11
D7S820	11,13	11,13	11,13
D16S539	11,12	11,12	11,12
vWA	14,17	14,17	14,17
THO1	7,9.3	7,9.3	7,9.3
TPOX	8	8	8
Penta D	12,13	12,13	
D8S1179	12,13	12,13	
FGA	19,21	19,21	
D3S1358	17,18	17,18	
D21S11	30,31	30,31	
D18S51	12	12	
Penta E	11,13	11,13	

Fig. S1_2: Short tandem repeat (STR) profiles of LUHMES SP

Identity of both SP "UKN" and "ATCC" was confirmed by STR (Short Tandem Repeat) analysis. DNA samples from the SPs were prepared using a commercial kit (Puregene Cell Kit, Qiagen). The kit GlobalFiler® PCR Amplification Kit (Thermofisher) was then used to determine the cell-specific profile for 16 different genomic loci (left column). Results from SP used in this study are listed in the two centre columns. STR-profile provided by the ATCC website (https://www.lgcstandards-atcc.org/Products/All/CRL-2927.aspx#specifications) is listed in the left column.

A:

Overview of structural variants detected			
	Deletions	**Duplications**	**Inversions**
Total	1726	273	435
Found in "DGV"	150	119	172
Overlap with "CG Baseline"	1706	252	128
Post-filtering for known SVs	**17**	**16**	**188**
Concordant	7	2	6
Only UKN	1	0	2
Only ATCC	9	14	179

B:

Genes overlapping with SVs			
Platform	**Deletions**	**Duplications**	**Inversions**
Both platforms		RMDN1	
UKN			ADCY8, TMEM167A
ATCC	CSMD1, C8orf44-SGK3, , EFHD1, FAM209A, FAM209B, GCNT7, MIR512-1, MIR512-2, SGK3	AHRR, CHST9, SLC12A7, SLC13A3, SMC1B, TCF25, VPS16, WDR27	ACTR3B, ADAMTS7, ANKRD36, ARHGEF7, ATP1B4, C14orf39, CCDC129, CD8B, CD97, CHRFAM7A, CHRNA7, CLYBL, CNTNAP5, CSF2RA, CYB5R4, DCK, DEFB107A, DEFB107B, DNM1P35, DNM1P46, DPP6, EMR2, ETFA, EVPL, EVPLL, EXOC6B, F11-AS1, F13A1, FAM184B, FAM65C, FAR2P1, FKBP14, GALNT13, GOLGA8A, GUSBP11, HERC2, HERC2P10, HERC2P9, KCNH5, KRTAP4-6, KRTAP4-7, LINC00607, LOC100288637, LOC101927437, LOC202181, LOC440910, LOC728554, MGLL, MIR4435-1HG, MOK, NOL10, NOMO1, NOMO2, NPSR1, NPSR1-AS1, NRXN1, OTUD7A, PDCD6IPP2, POTEF, RAD51B, RALYL, ROCK1, ROCK1P1, RPSAP58, SDHAP1, SDHAP2, SH3BP2, SIMC1, THOC3, TMEM207, TYRO3, TYW1, TYW1B, VCX, VCX2, ZGRF1, ZNF521, ZNF701, ZNF702P, ZNF91

Fig. S2_2: Filtering of SVs for location in protein-coding regions

A: Detected Structural variants were filtered using DGV and CG baseline database and number of SP specific deletions, duplications and Inversions was calculated. **B:** Detected SVs were tested for proximity to genes and possible affected genes were listed according to their occurrence (both SP or specific) and their property (Deletion, Duplication or Inversion)

Source of identified CNV in protein coding regions		
UKN	Both	ATCC
ACVR1C, ADARB1, ARHGAP21, ATP10B, CAMK4, CMYA5, CPAMD8, EFCAB1, GSG1L, ITGA9, NWD1, PRKAR1B, RNF17, SH3GL3, SPOCK1, SUPT3H	C1R, DLGAP4, DOCK1, DPP6, GAGE12J, GAGE13, GAGE2A, GAGE2C, GAGE2E, GAGE8, GRK1, HMCN2, INPP5D, MID1, MLXIP, MUSK, NRG3, SH3RF3, TWIST2	ADAMTS20, APP, C12orf42, C12orf66, CCDC138, CDH8, CENPP, IGSF11, LINC00922, LOC100507065, LOC728554, MARK1, MGMT, MME, MMP16, PRKCA, SCRN3, TNKS, TSHR, TUBA1A, ZNF814 ANTXR2, CSAG3, CXorf51A, CXorf51B, FAM72C, FAM72D, LINC00457, MAGEA2, MAGEA2B, MAGEA6, XAGE2, NXF2, NXF2B, TCP11X2

Fig. S3_2: List of copy number variations

The whole genome sequencing data from LUHMES "ATCC" and "UKN" SP were mined for copy number variations (CNV). They were filtered for those located in the region of a known gene. Those that were found to overlap with the same gene in both SP were identified (middle column). Gains in copy number are marked in blue and losses in copy number are marked in red. Notably, the latter group comprises partial and heterozygous (single-allelic) losses (i.e. not necessarily 'knock-outs')

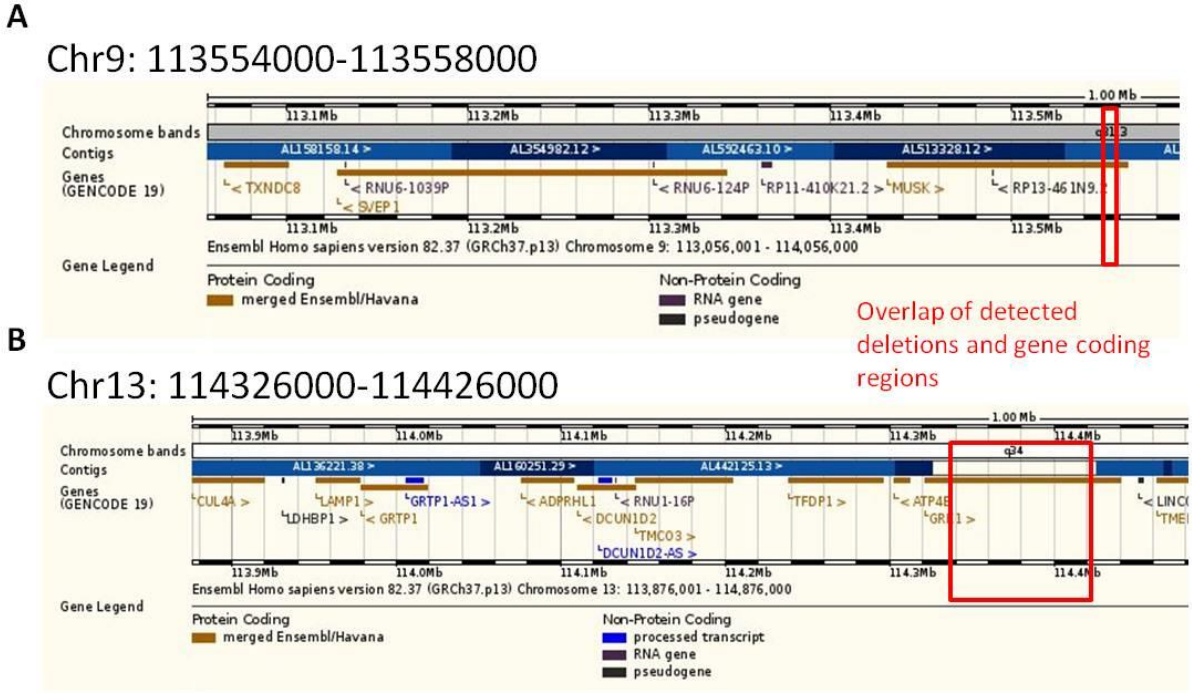

Fig. S4_2: Examples of CNVs

Examples for filtered copy number variations marked in Fig.2 and their location in the genome. Pictures were generated using the Ensembl genome browser 82.37 (*https://www.ensembl.org/)* with the human genome assembly GRCh37.p13. Coordinates of detected CNVs were entered into the genome browser and graphical depiction of the region of the corresponding chromosome was used to show where in the gene the CNV is located (red boxes). **A:** CNV of a size of 4 kbp in the Muscle Associated Receptor Tyrosine Kinase (MUSK) gene located on chromosome 9. **B:** CNV of a size of 100 kbp in the G Protein-Coupled Receptor Kinase 1 (GRK1) gene located on chromosome 13.

A:

Single nucleotide variants (SNVs)	
Database overlap	**Detected in one or both platforms**
Total variants	4 509 102
Exome Sequencing Project	43 160
1000 Genome Project	3 936 535
Complete Genomics 69 Genomes Baseline	3 749 949
dbSNP 138	4 182 029
avSNP	4 235 576
Found in one of the above databases	4 346 399
Somatic variants	**162 703**
Somatic variants after platform bias correction	**46800**

B

Somatic filtered variants			
Variant type	Concordant	discordant	partial
deletion	1105	2161	4
insertion	747	3828	7
SNV	12131	1916	10
substitution	421	1067	3
Sum	14404	8972	24

C

Somatic filtered amino acid changing variants			
Variant type	concordant	discordant	partial
deletion	1	1	0
insertion	0	21	0
SNV	29	6	0
substitution	3	1	0
sum	33	29	0

Fig. S5_2: Genomic differences- prediction of affected genes

A:Detected SNV found in both or only one of the SP were filtered against SNV found in the indicated databases in order to reduce the number and identify SP specific SNVs (somatic variants) **B:** List of filtered and platform bias corrected somatic variants. After filtering detected SNV against known databases (Fig .S6A) platform corrected SNVs were grouped into concordat (occurring in both SP), discordant (occurring only in one SP) and partial overlapping SNVs. **C:** Filtered SNVs obtained in B were tested for their potential to change the amino acid of a protein. The identified proteins are listed in Fig. 3A.

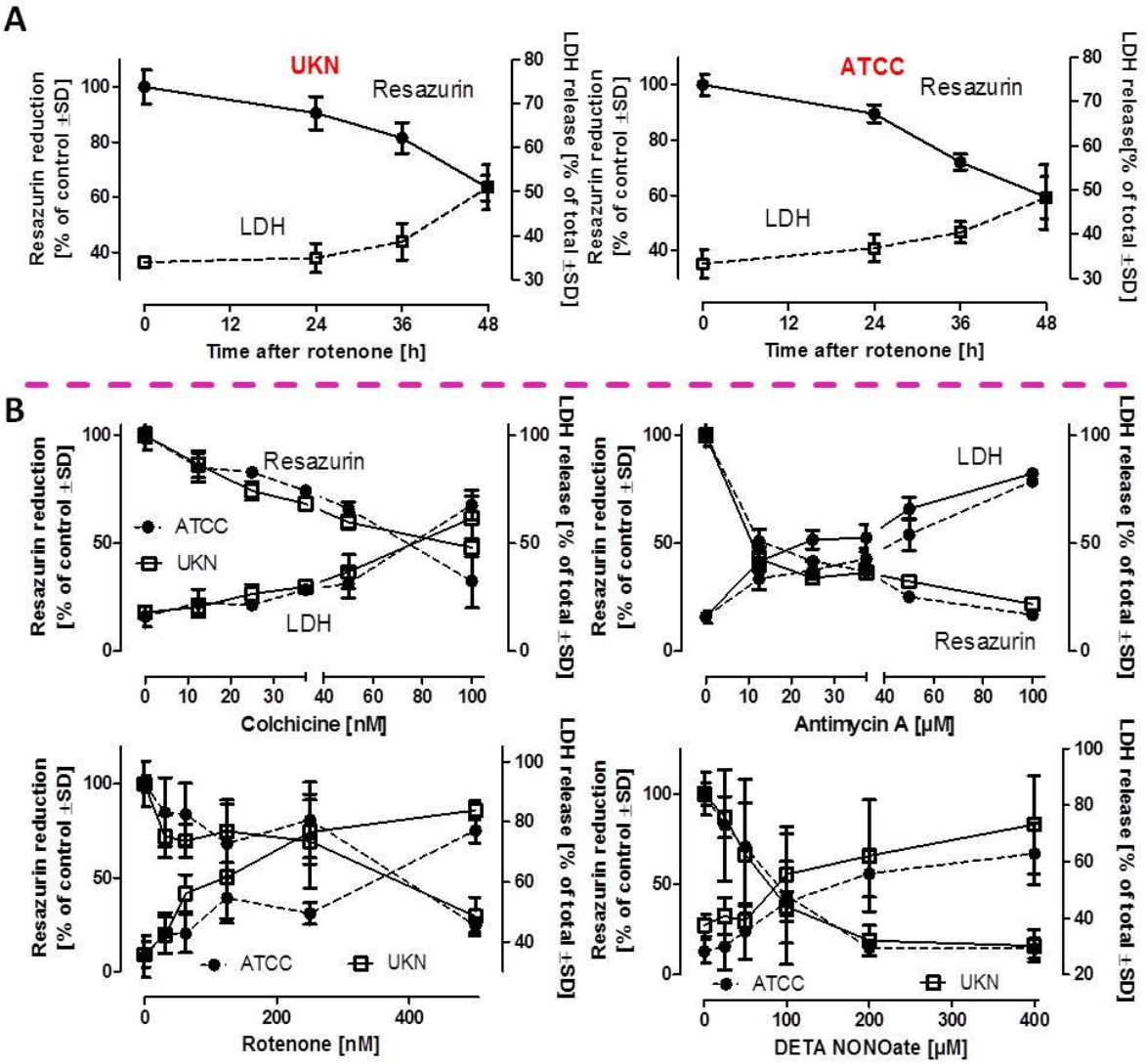

Fig. S6_2:Similar and different concentration response examples in UKN and ATCC LUHMES

LUHMES cell subpopulations (SP) from two different sources (University of Konstanz (UKN); American Type Culture Collection (ATCC)) were cultured according to a standard protocol. Cells were seeded at a density of $1.5x10^5$ cells/cm^2 at day (d2). Medium was exchanged at d4. Toxicant exposure started at d6. **A: "**UKN" and "ATCC" LUHMES were incubated with 750 nM rotenone for the indicated time periods. After incubation, viability was assessed measuring resazurin reduction and LDH release **B:** "UKN" and "ATCC" SP were incubated with different concentrations of colchicine, antimycin A, rotenone and DETA-NONOate for 48 h. After incubation, viability was assessed by measuring resazurin reduction and LDH release. Data are means ±SD of three independent experiments.

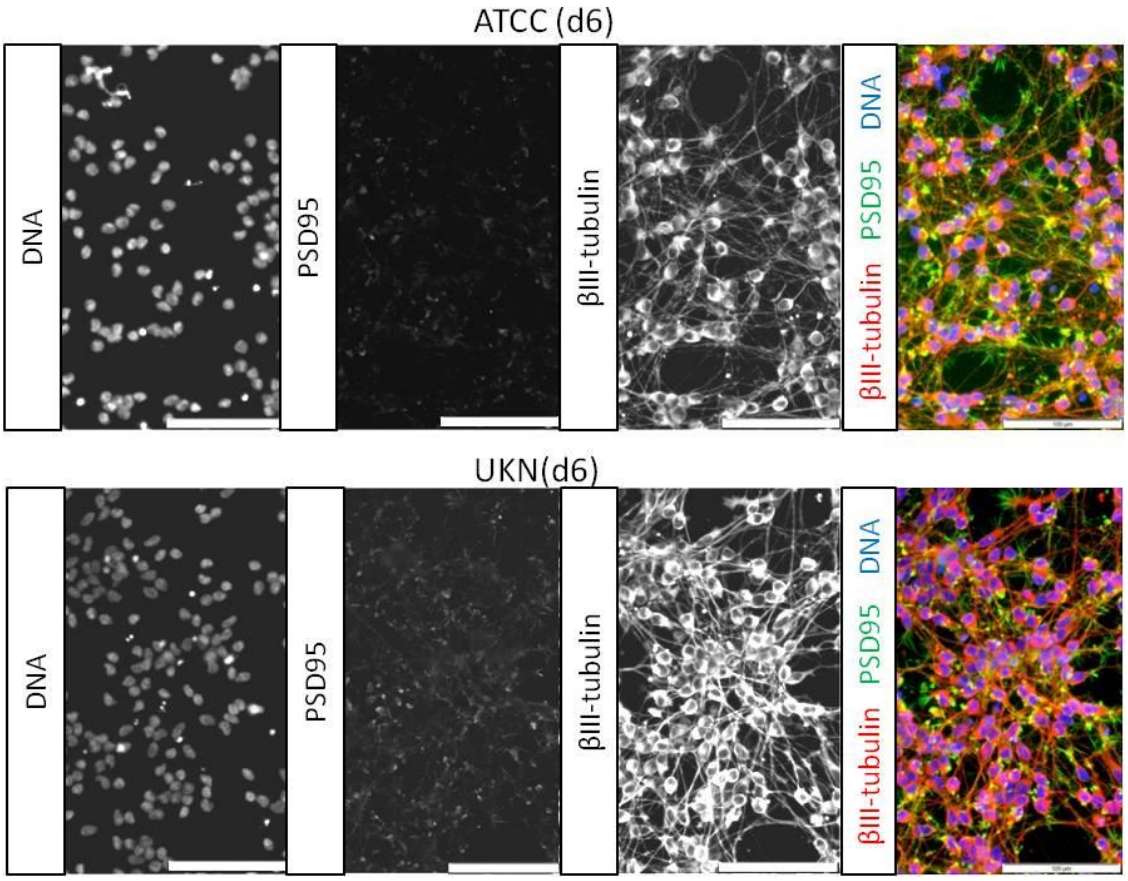

Fig. S7: Phenotypic similarities of LUHMES SP

LUHMES cells from two different sources (UKN and ATCC) were cultured and differentiated according to a published standard protocol. Differentiated (d6) LUHMES cells at a density of $1.5x10^5$ cells/cm^2 were stained for post synaptic density protein 95 (PSD95) and β-III-tubulin and morphological properties were examined by fluorescence microscopy

A **UKN**

Top Canonical Pathways		
Name	p-value	Overlap
Serotonin Receptor Signaling	1.22E-06	34.1 % 15/44
cAMP-mediated signaling	5.46E-04	15.1 % 33/219
Dopamine Receptor Signaling	5.47E-04	20.5 % 16/78
Tetrahydrobiopterin Biosynthesis I	5.62E-04	100.0 % 3/3
Tetrahydrobiopterin Biosynthesis II	5.62E-04	100.0 % 3/3

B **ATCC**

Top Canonical Pathways		
Name	p-value	Overlap
Breast Cancer Regulation by Stathmin1	6.31E-07	14.7 % 28/191
Role of NFAT in Cardiac Hypertrophy	6.00E-06	14.0 % 25/179
Protein Kinase A Signaling	5.44E-05	10.1 % 39/386
Cholecystokinin/Gastrin-mediated Signaling	2.12E-04	14.9 % 15/101
Calcium-induced T Lymphocyte Apoptosis	4.05E-04	17.2 % 11/64

Fig. S9_2: Top canonical pathways from ingenuity pathway analysis

For identification of SP specific pathways, possibly affected by genetic alterations, all CNV, SV and SNV specific for each SP were used to test for pathway overrepresentation. Therefore, identified and filtered variants were analyzed by Ingenuity pathway analysis software (*https://analysis.ingenuity.com/*) A: Top 5 canonical pathways for "UKN" LUHMES, pathways related to dopaminergic phenotype marked with red box. B: Top 5 canonical pathways for "ATCC" LUHMES, pathway related to dopaminergic phenotype marked with red box.

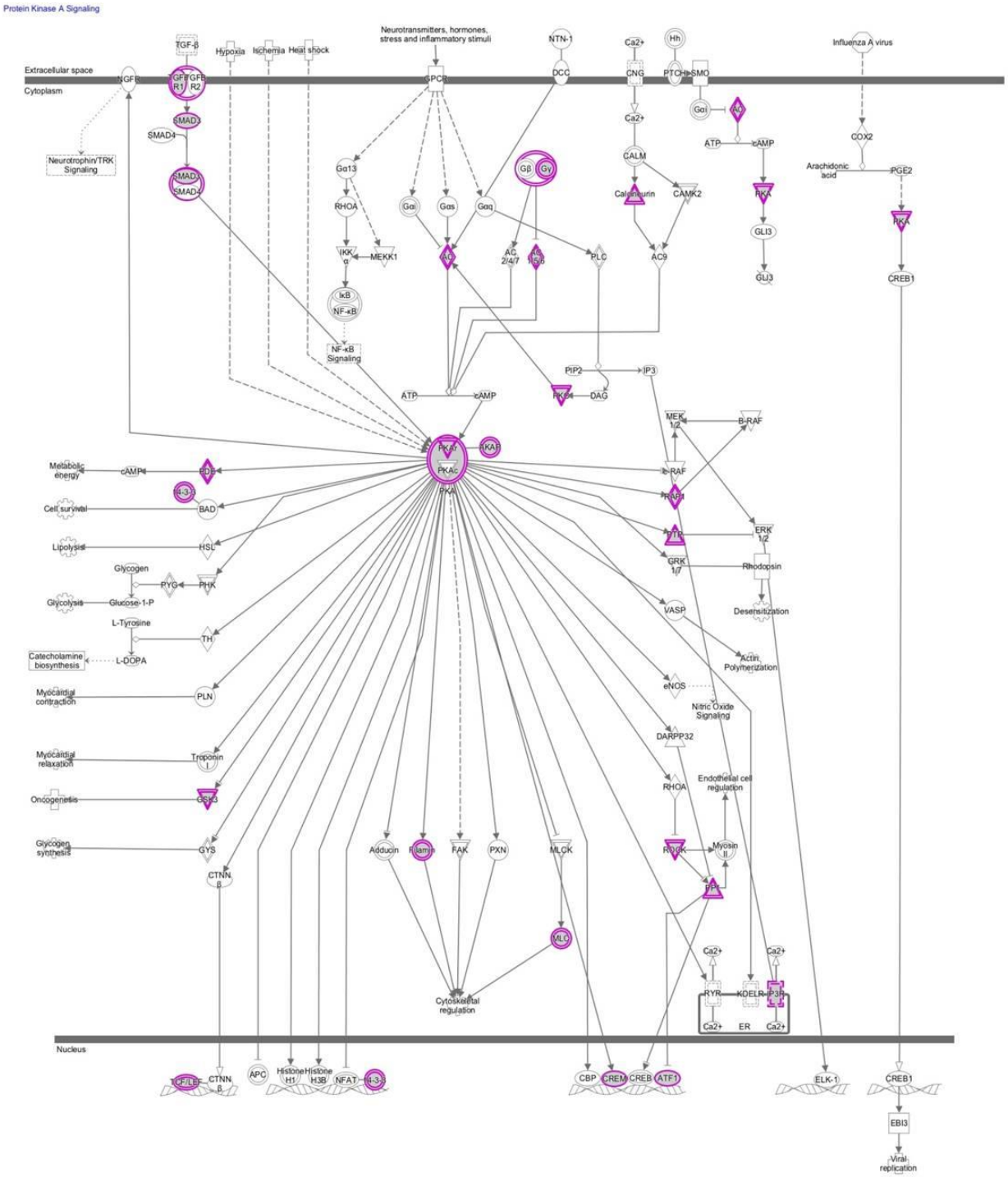

Fig. S10_2: Affected genes in the PKA signaling pathway of the "ATCC" SP

Pathway map of the PKA signaling retrieved from the Ingenuity platform. Proteins within this pathway possibly affected by a variant (CNV, SV and SNV) in the "ATCC" SP are circled in purple.

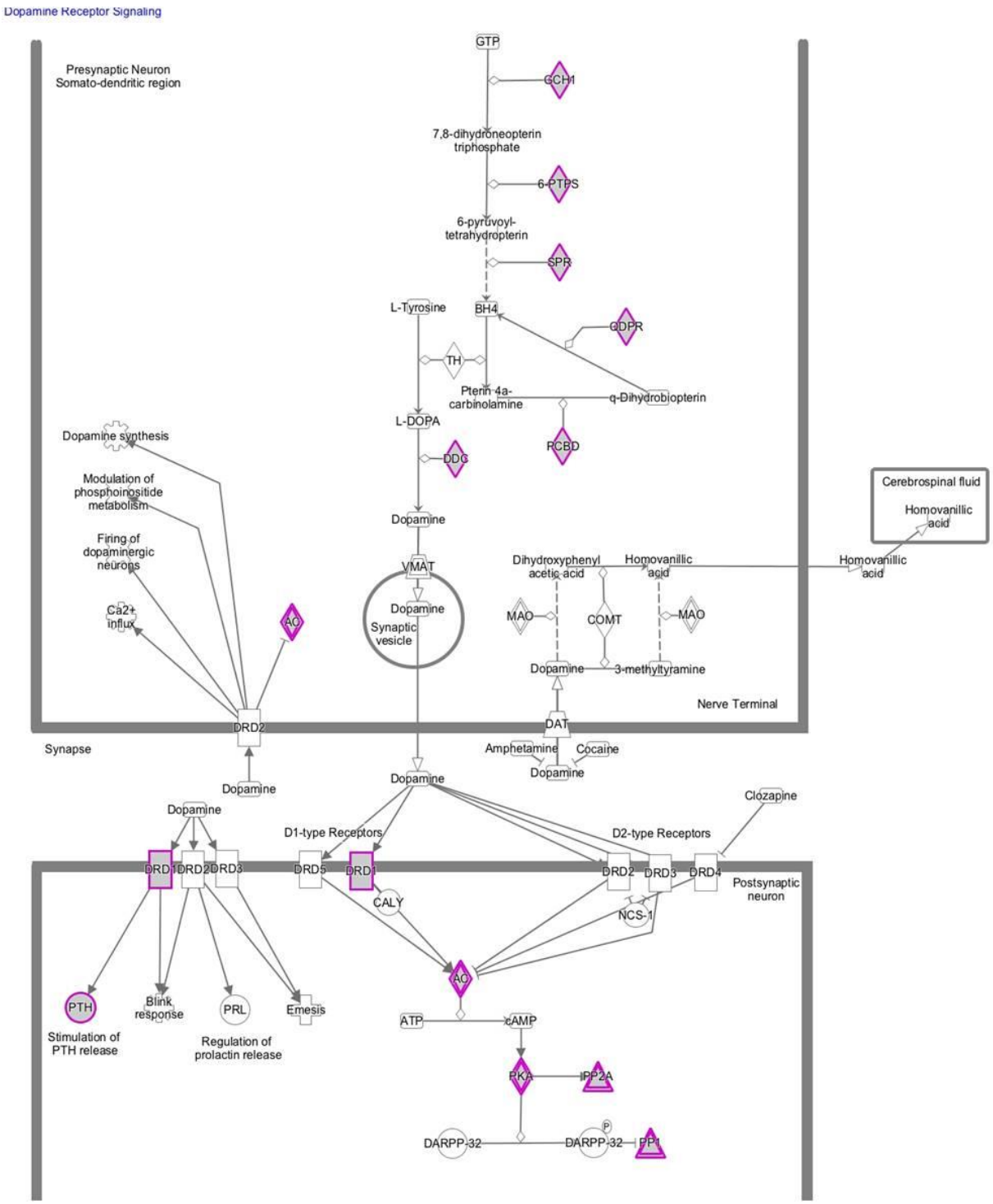

Fig. S11_2: Affected genes in the dopamine receptor signaling pathway of the "UKN" SP

Pathway map of the dopamine receptor signaling pathway retrieved from the Ingenuity platform. Proteins within this pathway possibly affected by a variant (CNV, SV and SNV) in the "UKN" SP are circled in purple.

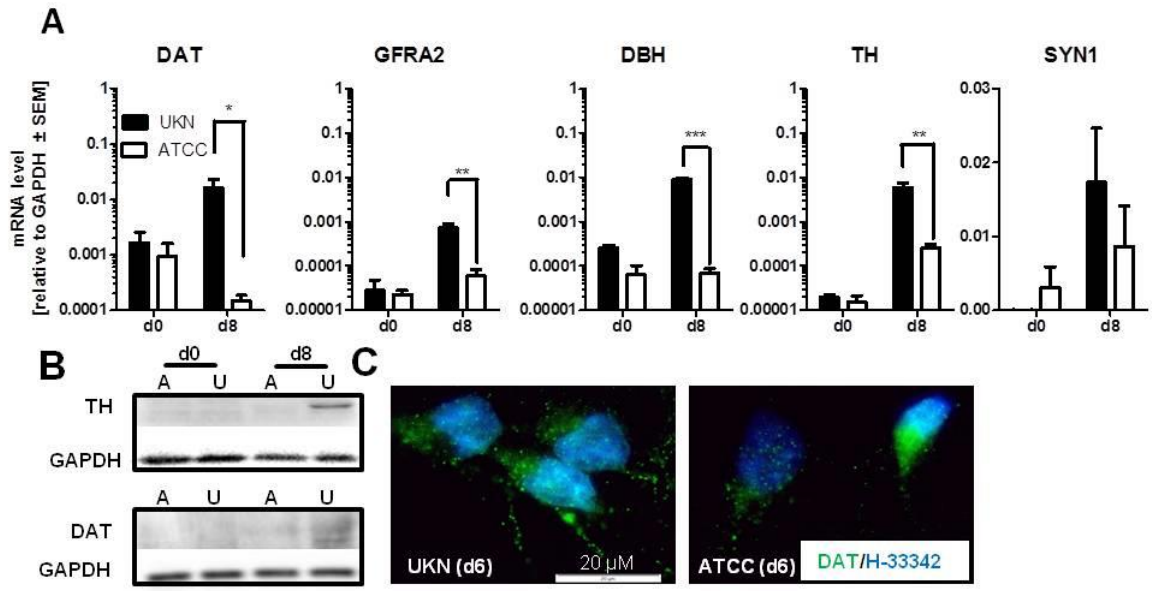

Fig. S12_2: Differentially expressed functional markers in the two LUHMES SP

Two different SP of LUHMES cells "UKN" and "ATCC" were cultured according to a standard protocol until d2 and than replated at a density of $1.5x10^5$ cells/cm^2. **A:** Changes in gene expression of the neurodevelopmental marker genes DAT, GFRA2, DBH, TH and SYN1 were compared at d0 and d8 of differentiation of LUHMES cells using qPCR. Values are expressed relative to expression levels in undifferentiated LUHMES cells and represent means ± SEM from three independent experiments. ***: $p<0.001$ **: $p<0.01$ *: $p<0.5$. **B:** Undifferentiated (d0) and mature (d8) LUHMES cells were lysed and analysed by Western blot using anti- TH (tyrosine hydroxylase), anti-DAT (dopamine transporter) and anti GAPDH antibodies. **C:** Distribution and abundance of dopamine transporter in both SP was assessed by immunocytochemistry staining for dopamine transporter (DAT) and H-33342.

Antibodies used in this study				
product	**host**	**dilution**	**supplier**	**Cat. No.**
Dopamine transporter antibody	rat	1:1000	Millipore	MAB369
GAPDH antibody	mouse	1:10000	Invitrogen	39-8600
Monoclonal MAP2 antibody, IgG1	mouse	1:500	Sigma	M9942
Monoclonal Nestin antibbody, IgG1	mouse	1:500	R & D systems	MAB1259
Monoclonal Synapsin 1	mouse	1:500	Synaptic Systems	106 011
Monoclonal Tyrosine hydroxylase antibody, IgG1	mouse	1:500	Sigma	T2928
Monoclonal β-Tubulin (TUJ1) antibody	mouse	1:500	Covance	MMS-435P-250
Polyclonal GAD1 antibody	rabbit	1:500	Synaptic Systems	198003
Polyclonal PSD-95 antibody	rabbit	1:500	Invitrogen	51-6900
HSP70 (6B3)	rat	1:1000	Cell Signaling	4873
HSF1	rabbit	1:1000	Cell Signaling	4356
SirT6 (D8D12)	rabbit	1:1000	Cell Signaling	12486
NRXN3	rabbit	1:1000	Sigma	SAB1305223
Ki67	mouse	1:200	BD Bioscience	5136525X
CCNA1	mouse	1:200	Santa Cruz	Sc-271682
H3S10P	rabbit	1:200	Cell Signaling	9701
Alexa Fluor 488, IgG1 (γ1), anti mouse	goat	1:1000	Invitrogen	A21121
Alexa Fluor 555, IgG2a (γ2a), anti mouse	goat	1:1000	Invitrogen	A21137
Alexa Fluor 488, IgG anti-rabbit	chicken	1:1000	Invitrogen	A21441
Peroxidase conjugated, anti Mouse, IgG	goat	1:5000	Jackson Immuno Research	115-035-174
ECL Anti Rabbit, IgG	donkey	1:5000	GE Healthcare	NA934V
ECL Anti Rat, IgG	goat	1:5000	GE Healthcare	NA935

Supplementary table 1_2: Antibodies

Primers used in this study		
qPCR (mRNA)	Forward	Reverse
ACHE	5'-CTT CCT CCC CAA ATT GCT C-3'	5'-TCC AGT GCA CCA TGT AGG AG-3
DBH	5'-GCC TTC ATC CTC ACT GGC TA-3'	5'-GAC CAC CTT TCT CCC AGT CA-3'
DAT	5'-TGA CTT CTA CCG GCT CTG CG-3'	5'-AGA AGA CGA CGA AGC CGG AG-3'
DRD2	5'-GCC GGG TTG GCA ATG ATG CA-3'	5'-ACG GCG AGC ATC CTG AAC TT-3'
GAPDH	5'-CAC CAT CTT CCA GGA GCG AGA TC-3'	5'-GCA GGA GGC ATT GCT GAT GAT C-3'
GFRA1	5'-TGG AGG ATT CCC CAT ATG AA-3'	5'-TTG TTC CCT TTG GGA ATG TG-3'
GFRA2	5'-GAG TCA CTG GTG CGC CAG GA-3'	5'-GAG TCA CTG GTG CGC CAG GA-3'
GRIN1	5'-GAG AAG GTG CTG CAG TTT GA-3'	5'-GGT ATA CAG TGG CAG CAT CG-3'
HES5	5'-TTG GAG TTG GGC TGG TG-3'	5'-CCC AAA GAG AAA AAC CGA-3'
SNAP25	5'-CTG TCT TTC CTT CCC TCC CT-3'	5'-GGG TCA GTG ACG GGT TTG-3'
SYN1	5'-TCA GAC CTT CTA CCC CAA TCA-3'	5'-GTC CTG GAA GTC ATG CTG GT-3'
SYP	5'-CGA GGT CGA GTT CGA GTA CC-3'	5'-AAT TCG GCT GAC GAG GAG TA-3'
TH	5'-GCG CAG GAA GCT GAT TGC TG-3'	5'-TGT CTT CCC GGT AGC CGC TG-3'
TUBB3	5'-CGC CCA GTA TGA GGG AGA T-3'	5'-AGT CGC CCA CGT AGT TGC-3'
v-myc	5'-TTT TGG TCT CCA GGC TCT TC-3'	5'-GGAGTCCTTTGTGGGTTCAG-3'
VMAT2	5'-TGG GGA GGT GGC TTT GTG CT-3'	5'-CCC ATA GAC GGA CAC GTG CC-3'
BMP7	5'-GCC CCT CAG TCC CTG TAT C-3'	5'-GTG GTG AGT GGG GAG AGG T-3'
CCNA2	5'-GTT GCC CAG CCT TTA GCT C-3'	5'-GTT GCC CAG CCT TTA GCT C-3'
CCNB1	5'-GTC GCT GAG CTT CAG TTC CT-3'	5'-CTA CGG TAG CAG CAA TAA TAT AGT TCA-3'
CCND1	5'-TCC CTC CTA GCT GTC CTC CT-3'	5'-CGG ACT GCT TCT CTC CAA AC-3'
KIF14	5'-TTT GCC CCC AAG TTA ATC AT-3	5'-TCT CAC AAG ATT TTC AGG ACT GTT-3'
SHH	5'-ATG CTG CTG CTG GCG AGA T-3'	5'-CTG CTT GTA GGC TAA AGG GGT CA-3'

Supplementary table 2_2: Primers

3.3 Manuscript #3:

Prevention of neuronal apoptosis by astrocytes through thiol-mediated stress response modulation and accelerated recovery from proteotoxic stress

Simon Gutbier[1,5], Anna-Sophie Spreng[1,6], Johannes Delp[1,5,7], Stefan Schildknecht[1], Christiaan Karreman[1], Thomas Brunner[2], Marcus Groettrup[3] and Marcel Leist[1,4]

[1]: In vitro Toxicology and Biomedicine, Dept inaugurated by the Doerenkamp-Zbinden foundation, University of Konstanz, 78457 Konstanz, Germany
[2]: Biochemical Pharmacology, Department of Biology, University of Konstanz, Konstanz, Germany.
[3]: Division of Immunology, Department of Biology, University of Konstanz, D-78457, Konstanz, Germany
[4]: CAAT-Europe, University of Konstanz, 78457 Konstanz, Germany.
[5]: Research Training Group RTG1331,University of Konstanz, Konstanz, Germany
[6]: Konstanz Research School Chemical Biology, University of Konstanz, Constance, Germany.
[7]: Cooperative Doctorate College InViTe, University of Konstanz, Konstanz, Germany

Running title: Astrocytic neuroprotection
Correspondence to be sent to:
Marcel Leist, PhD
In vitro Toxicology and Biomedicine, Dept inaugurated by the Doerenkamp-Zbinden foundation at the University of Konstanz, Konstanz, Germany
University of Konstanz
78457 Konstanz/Germany
Tel: +49 (0) 7531 88 5037 (Fax 5039)
Email: marcel.leist@uni-konstanz.de

Figures; X, supplementary tables; 0, tables; 0, pages; 26.Keywords:X.

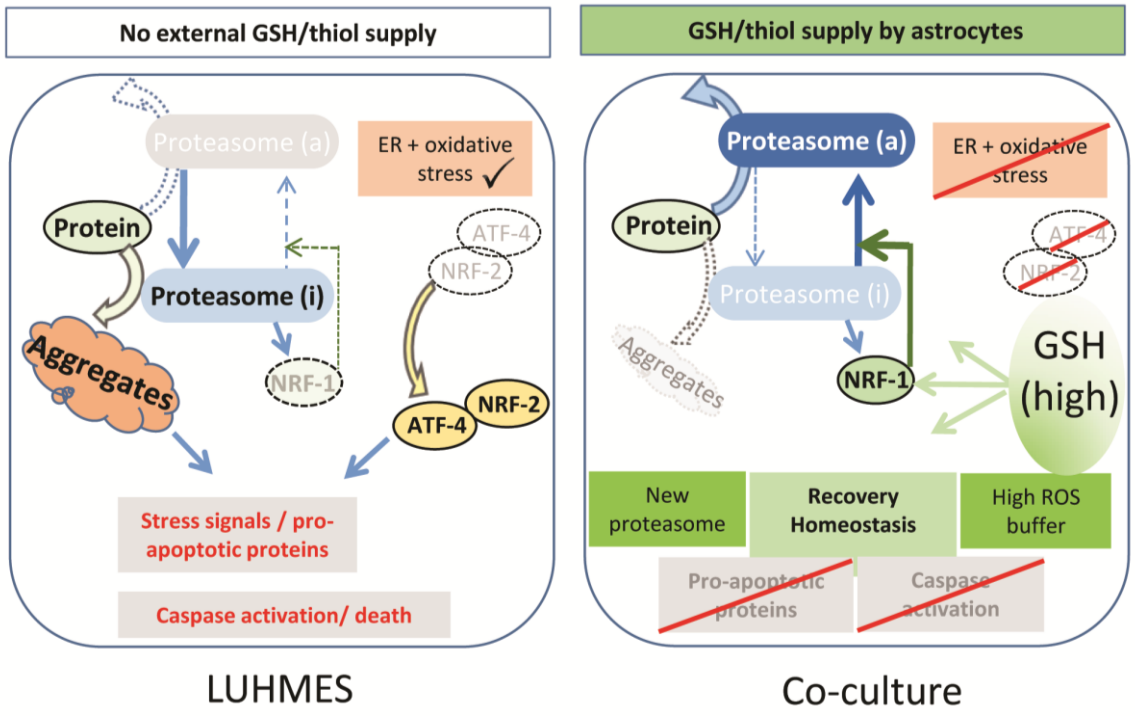

3.3.1 Abstract

The development of drugs directly interfering with neurodegeneration has proven to be astonishingly difficult. Alternative therapeutic approaches could result from a better understanding of the supportive function of glial cells for stressed neurons. Therefore, we investigated here mechanisms involved in the endogenous neuro-defensive activity of astrocytes. A well-established model of post-mitotic human dopaminergic neurons (LUHMES cells) was used in the absence ("LUHMES" mono-culture) or presence ("co-culture") of astrocytes. Inhibition of the LUHMES proteasome led to proteotoxic (protein aggregates; ATF-4 induction) and oxidative (GSH-depletion; NRF-2 induction) stress, followed by neuronal apoptosis. The presence of astrocytes attenuated the neuronal stress response, and drastically reduced neurodegeneration. A similar difference between LUHMES mono- and co-cultures was observed, when proteotoxic and oxidative stress was triggered indirectly by inhibitors of mitochondrial function (rotenone, MPP^+). Human and murine astrocytes continuously released glutathione (GSH) into the medium, and transfer of glia-conditioned medium was sufficient to rescue LUHMES, unless it was depleted for GSH. Also, direct addition of GSH to LUHMES rescued the neurons from inhibition of the proteasome. Astrocytes and GSH both blunted the neuronal ATF-4 response and similarly up-regulated NRF-1/NFE2L1, a transcription factor counter-regulating neuronal proteotoxic stress. Astrocyte co-culture also helped to recover the neurons' ability to degrade aggregated poly-ubiquitinated proteins. Over-expression of NRF-1 attenuated the toxicity of proteasome inhibition, while knockdown increased toxicity. Thus, astrocytic thiol supply increased neuronal resilience to various proteotoxic stressors by simultaneously attenuating cell death-related stress responses, and enhancing the recovery from proteotoxic stress through up-regulation of NRF-1.

3.3.2 Introduction

Neuronal stress response signals are a critical element in the pathogenesis of various neurodegenerative diseases. Endogenous mechanisms of neuronal resilience to stress are thus of high interest to develop new strategies for the modulation of neurodegenerative diseases, like Parkinson's disease (PD). The main hallmark of PD is the degeneration of dopaminergic neurons in the *substantia nigra*. The pathogenic mechanisms thought to take an important role in this process comprise mitochondrial dysfunction with ensuing oxidative stress, impairment of protein turnover, evidenced by dysfunction of the ubiquitin proteasome system (UPS), and aggregation of proteins like α-synuclein (287, 305, 306).

To study neurodegeneration and neuroprotection in PD, usually pathological features observed in affected human brains are modelled. For instance, impairment of mitochondrial function is triggered by their genetic inactivation (307, 308) or by the toxicants 1-methy-4-phenylpyridinium (MPP^+) and rotenone (170, 309). Proteotoxic stress can be induced by over-expression or injection of α-synuclein, or by direct inactivation of the UPS by proteasome inhibitors (310). The latter trigger several PD relevant processes, such as aggregation of α-synuclein and the death of dopaminergic neurons (311-313). One of the cellular stress responses induced by proteasome inhibition is the up-regulation of NRF-1 (= TCF-11/ NFE2L1; not to be confused with the mitochondrial biogenesis factor NRF1), a transcription factor involved in the regulation of proteasome synthesis (314).

The different pathological processes linked to PD are highly interconnected, and there are multiple examples for impairment of the UPS occurring because of mitochondrial impairment (287, 310) and vice versa (315). For instance, the proteasome biogenesis factor NRF-1 has been associated with increased cellular resistance to mitochondrial impairment (316).

Using a multi-omics approach, we recently identified the proteotoxic stress-related transcription factor (TF) ATF-4 as coordinator of the neuronal stress response following mitochondrial respiratory chain inhibition (49). Regulation of ATF-4 may indicate a cellular demand for thiol supply, as it up-regulates cystine import and cysteine generation via the transsulfuration pathway (49). Interestingly, shortage of cysteine has

also been identified as a critical factor determining cell death after proteasome inhibition (317).

We also observed that co-culturing neurons with astrocytes extends neuronal survival and provides trophic support under otherwise unfavorable conditions (183, 318). Astrocytes protected neurons also against nitric oxide (15). This is in line with many studies describing or implying astrocytic neuroprotection *in vitro* and *in vivo* (319-323). A better understanding of how astrocytes protect neurons, and how their presence affects neuronal stress responses might result in new strategies to treat neurodegenerative diseases.

Therefore, we here studied mechanisms of astrocytic neuroprotection. As model system, we used human neurons generated from the LUHMES cell-line. Such cells are known to differentiate to fully post-mitotic and electrically-active neurons with high expression of dopaminergic features, such as the dopamine transporter (104). These neurons were exposed to mitochondrial toxicants (MPP^+ and rotenone) or proteasome inhibitors. To provide a homogeneous (> 99% pure) and defined astrocytic population, we differentiated neural stem cells to glia. These ‘murine astrocytes generated from embryonic stem cells’ (mAGES) (182, 183, 189) displayed all typical metabolic features of tissue astrocytes. By comparing the responses of neurons cultured alone (“LUHMES”) or with astrocytes (“co-cultures”), pronounced neuroprotection by glia was observed. Astrocyte-derived GSH was identified as a key factor that not only attenuates neuronal stress (ATF-4) responses, but also increased neuronal resilience by supporting the up-regulation of NRF-1.

3.3.3 Results

Different sensitivities of neurons in mono- and co-culture

As mitochondrial impairment and proteasomal dysfunction are tightly inter-connected in the pathogenesis of PD, we investigated whether such an interdependence is also observed in the model system used for our study. We observed that both rotenone and MPP^+ decreased proteasome activity of LUHMES dopaminergic neurons (Fig. 1_3A). Moreover, the two compounds led to the accumulation of ubiquitinated proteins (Fig. S1_3A+B) and to the formation of intracellular protein aggregates (Fig. S2_3A+B). Having established these measures of proteotoxic stress, we asked how the presence of astrocytes (mAGES) would affect the neuronal response: we exposed LUHMES neurons to MPP^+ in the presence or absence of astrocytes, and noticed that the presence of even few astrocytes (10% of the neuronal cell number) was sufficient to promote a very robust neuroprotection (Fig. 1_3B). We also observed that the impairment of the UPS was less pronounced in co-cultures than in LUHMES mono-cultures (Fig. 1_3C). Notably, a large series of control experiments (data not shown) indicated that the astrocytes did not alter neuronal exposure to the toxicant (e.g. MPP^+ uptake).

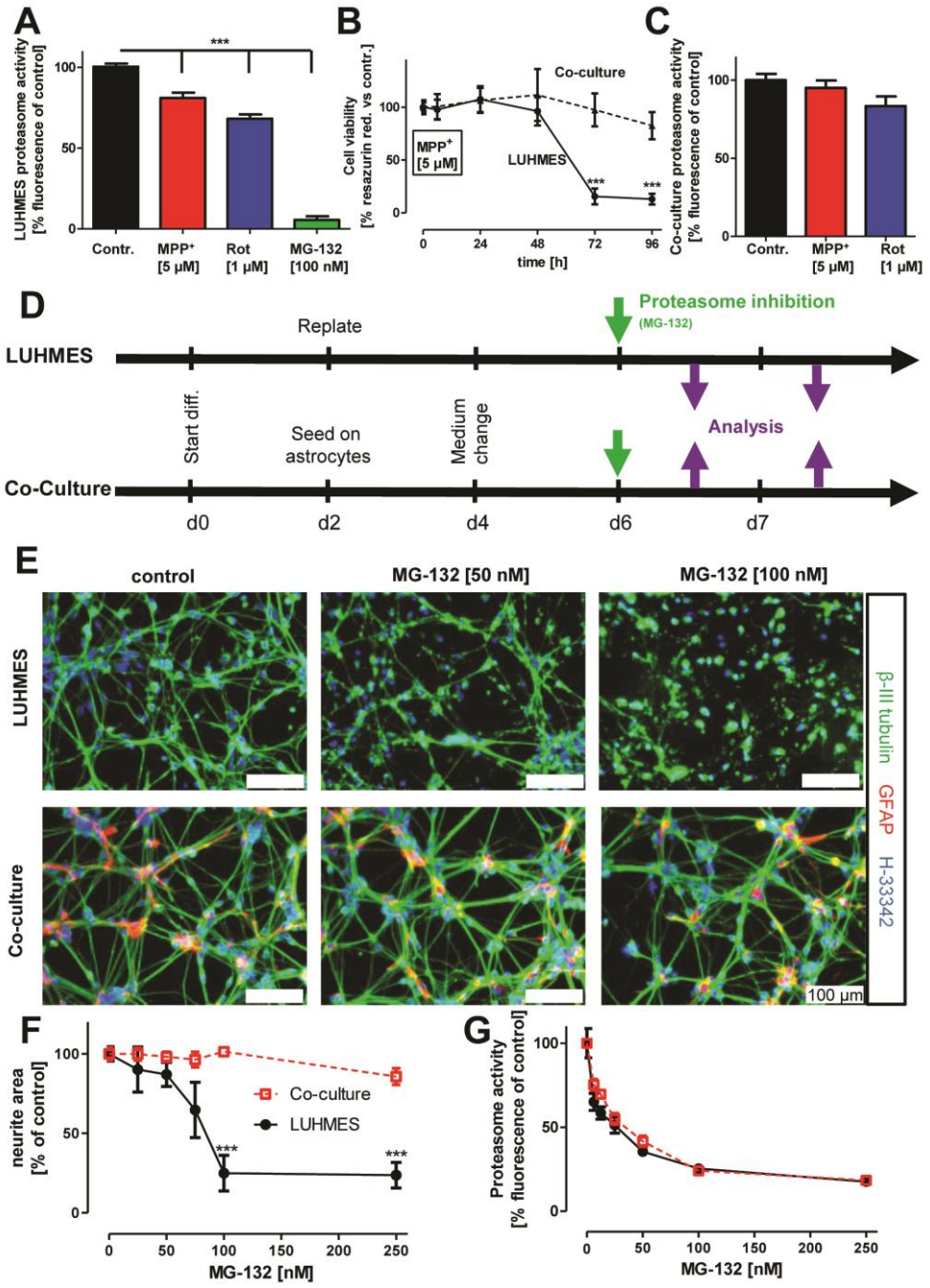

Figure 1_3: Increased tolerance to neuronal proteasome inhibition in the presence of astrocytes

A: LUHMES cells (d6) were treated with the indicated concentrations of MPP^+, rotenone and MG-132 for 24 h. Afterwards proteasome activity was assessed fluorometrically. Data are means + SD of three independent experiments ***: p<0.001. **B:** Differential toxicity of MPP^+ in co- and mono-culture was assessed by measuring cell viability after cultures were exposed to 5 µM MPP^+ for the indicated time periods. Data are means ± SD of three independent experiments ***: p<0.001. **C:** Co-cultures were treated with the indicated concentrations of MPP^+ and rotenone for 24 h. Afterwards proteasome activity was assessed fluorometrically. **D:** LUHMES cells and neuron-astrocyte co-cultures were differentiated according to the depicted differentiation scheme. LUHMES cells were replated at d-1 and differentiation was started by removal of proliferation medium (PM) and the addition of differentiation medium (DM) containing tetracycline, cAMP and GDNF at d0. LUHMES cells were replated at a density of $1.5*10^5$ cells/cm^2 at d2 either seeded in mono-culture or seeded on top on pre-differentiated astrocytes (mAGES). Medium was exchanged at d4 and "mature cells" were ready at d6, e.g. for toxicant exposure. **E:** Differential toxicity of MG-132 in co- and mono-culture was assessed by immunocytochemistry staining for β-III tubulin, GFAP, H-33342 after cultures were exposed for 24 h to MG-132 at the indicated concentrations. **F:** Toxicity of MG-132 on LUHMES and astrocyte LUHMES co-culture was assessed by measuring the neurite integrity after cells were exposed for 24 h to MG-132 at the indicated concentrations. Data are means + SD of three independent experiments ***: p<0.001. **G:** Proteasomal inhibition by MG-132 in LUHMES cells and in co-culture was assessed by measuring proteasome activity fluorometrically. Data are means ± SD of three independent experiments

As MPP^+ not only inhibits proteasome activity, but also affects neuronal energy generation and ROS formation, we inhibited the proteasome directly to better define the effect of astrocytes on neuronal proteotoxic stress. LUHMES mono-cultures were compared to astrocyte co-cultures (Fig. 1_3D). LUHMES neurons were found to be extremely sensitive to cell death triggered by MG-132 (50 nM) (Fig. 1_3E+F). This cell death was preceded by a strong accumulation of ubiqitinated proteins and protein aggregates within the neurons (Fig. S1_3C+D and Fig. S4_3A+B). In co-cultures, neurons were completely protected by astrocytes at drug concentrations of up to 250 nM (Fig. 1_3E+F), while the degree of proteasomal inhibition in LUHMES was not affected by the astrocytes (Fig. 1_3G). Notably, neuronal protection from MG-132 was also observed with human astrocytes (Fig. S3_3).

Stress response in neurons following proteasome inhibition

We further characterized the different responses of neurons in the presence or absence of astrocytes. Accumulation of poly-ubiquitinated proteins was detectable as soon as 2 h after MG-132 exposure (Fig. 2_3A). This was followed by an up-regulation of key TF associated with proteotoxic stress, ATF-4 and NRF-1 (314, 324, 325), after 6 h (Fig. 2_3B+ Fig. S4_3A). In order to investigate whether the relevant target of MG-132 in neurons was the proteasome, we tested the effect of three other proteasome inhibitors. LUHMES were found to be highly sensitive also to bortezomib, lactacystin and epoxomycin (Fig. 2_3C-E). As the proteasome is the common target of these highly diverse inhibitors (at low concentrations), we conclude that the neuronal cell death observed is triggered by reduced proteasome activity.

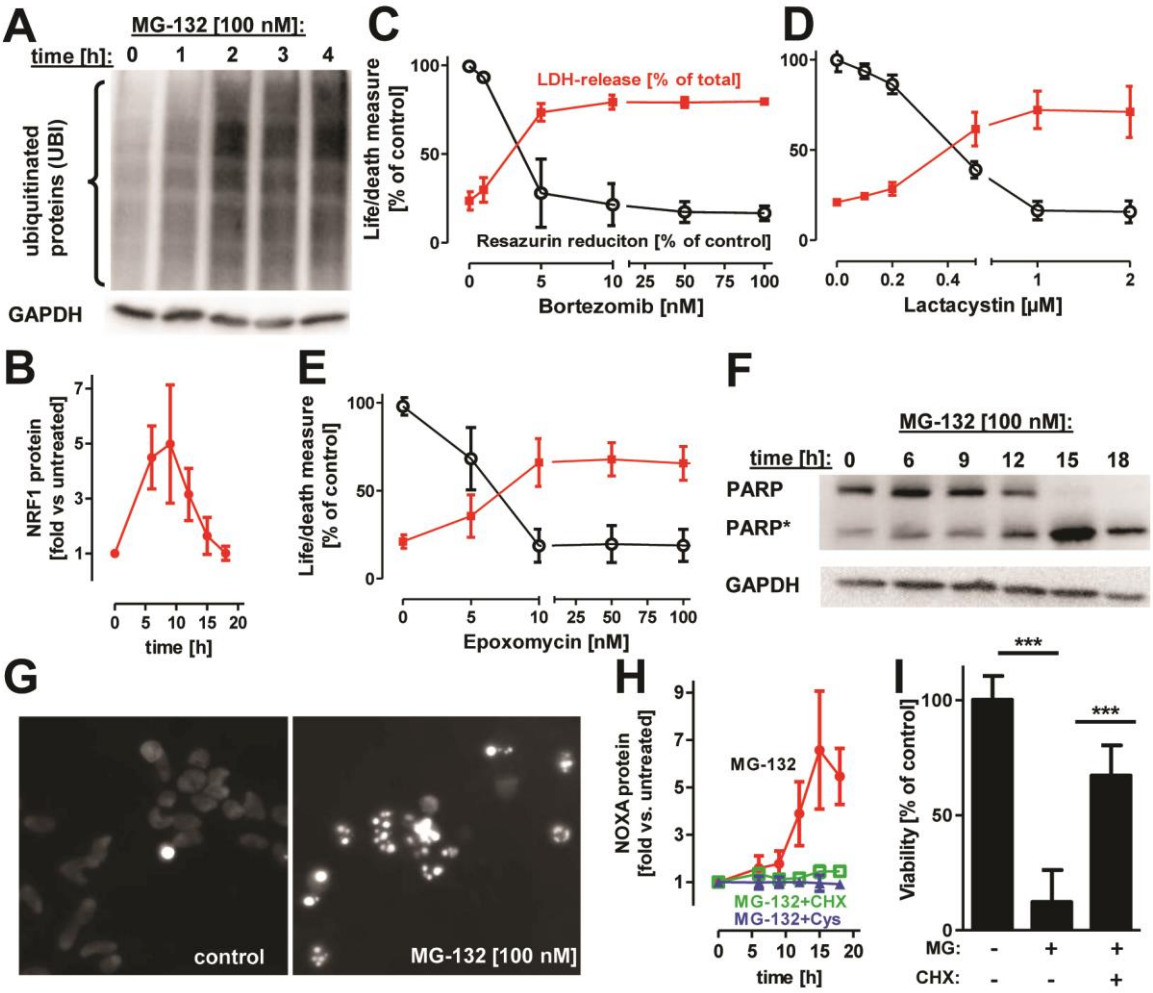

Figure 2_3: Formation of protein aggregates and triggering of neuronal apoptosis

A: LUHMES cells (d6) were treated with MG-132 [100 nM] for the indicated time periods. After incubation, cells were lysed and analysed by Western blot using anti-ubiquitin and anti-GAPDH antibodies. **B:** LUHMES cells (d6) were treated with MG-132 [100 nM] for the indicated time periods. After exposure, cells were lysed and analysed by Western blot with anti-NRF-1 and anti-GAPDH antibodies. Induction of NRF-1 was quantified densitometrically. **C:** Cell death of LUHMES cells following proteasome inhibition by bortezomib was monitored. Cells were exposed to indicated concentrations of bortezomib for 24 h. Viability was assessed measuring resazurin reduction and LDH release. **D:** Cell death of LUHMES cells following proteasome inhibition by clasto-Lactacystin β-lactone (lactacystin) was monitored. Cells were exposed to indicated concentrations of lactacystin for 24 h. Viability was assessed measuring resazurin reduction and LDH release. **E:** Cell death of LUHMES cells following proteasome inhibition by epoxomycin was monitored. Cells were exposed to indicated concentrations of epoxomycin for 24 h. Viability was assessed measuring resazurin reduction and LDH release. **F:** LUHMES cells (d6) were treated with MG-132 [100 nM] for the indicated time periods. After incubation cells were lysed and analysed by Western blot using anti-PARP and anti-GAPDH antibodies. **G:** LUHMES cells (d6) were treated with MG-132 [100 nM] and nuclei morphology of solvent treated cells and treated cells was compared by using DNA stain H-33342 **H:** LUHMES cells (d6) were treated with MG-132 [100 nM] in presence or absence of cycloheximide [10 µM] or Cysteine [1 mM] for the indicated time periods. After incubation cells were lysed and analysed by Western blot using anti-NOXA and anti-GAPDH antibodies. Induction of NOXA was quantified densitometrically. **I:** The effect of cycloheximide [10 µM] on neuronal survival following proteasome inhibition was investigated by measuring neurite integrity as surrogate for viability. Data are means + SD of three independent experiments ***: $p<0.001$

We observed typical apoptotic features after prolonged (>12 h) proteasome inhibition: PARP and fodrin cleavage (Fig. 2_3F, Fig. S5_3C), nuclear fragmentation (Fig. 2_3G) and caspase-3 activation. Cell death and caspase-3 processing were blocked

by caspase inhibitors (Fig. S5_3A+B), while the accumulation of ubiquitinated proteins persisted in caspase-inhibited cells (Fig. S5_3D).

As further sign of the induction of the mitochondrial apoptosis pathway, we observed an increased expression of the pro-apoptotic protein NOXA prior to caspase activation (starting 12 h after exposure to MG-132; Fig 2_3H+ Fig. S6_3A). Inhibition of protein synthesis by cycloheximide prevented NOXA induction and rescued neurons from cell death (Fig. 2_3I+ Fig. S6_3A). The findings that cycloheximide was still neuroprotective, when added up to 10 h after MG-132 (Fig. S6_3B), suggests that the biosynthesis of pro-apoptotic proteins (e.g. NOXA), is initiated at 10-12 h after proteasomal impairment and that the shifted balance of pro/anti-apototic proteins eventually leads to caspase activation and apoptosis induction.

Concerning cell death quantification, it is important that neurites and cell bodies (somata) may undergo different death programs. For neuroprotection experiments, it was therefore important to verify that not only neuronal somata survived, but also the neurite structure remained intact (326). We confirmed that this was the case for neuronal protection by astrocytes (Fig. 1_3E) or by the caspase inhibitor zVADfmk (Fig. S4_3B). For all further experiments, the intactness of the neurites was considered as most stringent measure of neuroprotection.

Rescue of neurons by cysteine

When evaluating the literature for mediators of astrocytic protection, we realized that neurons rely heavily on glia to maintain their cysteine pool, and this dependence may get more pronounced in the presence of MG-132 (known to deplete cellular cysteine levels) (317). We found cysteine supplementation to reduce neuronal sensitivity to MG-132 (Fig. 3_3A), lactacystin and bortezomib (Fig. S7_3). While proteasome inhibition was not altered by cysteine (Fig. 3_3B), the very low intracellular cysteine levels of neurons increased about 10-fold (Fig. 3_3C). Caspase activation and induction of apoptosis, as monitored by PARP cleavage (Fig. 3_3D) and NOXA levels (Fig. 2_3H), were completely prevented in the presence of cysteine. Moreover, the activation of ATF-4 and the induction of its target genes (CHOP and the cysteine transporter SLC7A11) was blocked (Fig. 3_3E+F and Fig. S8_3), indicating a pronounced attenuation of the neuronal stress response.

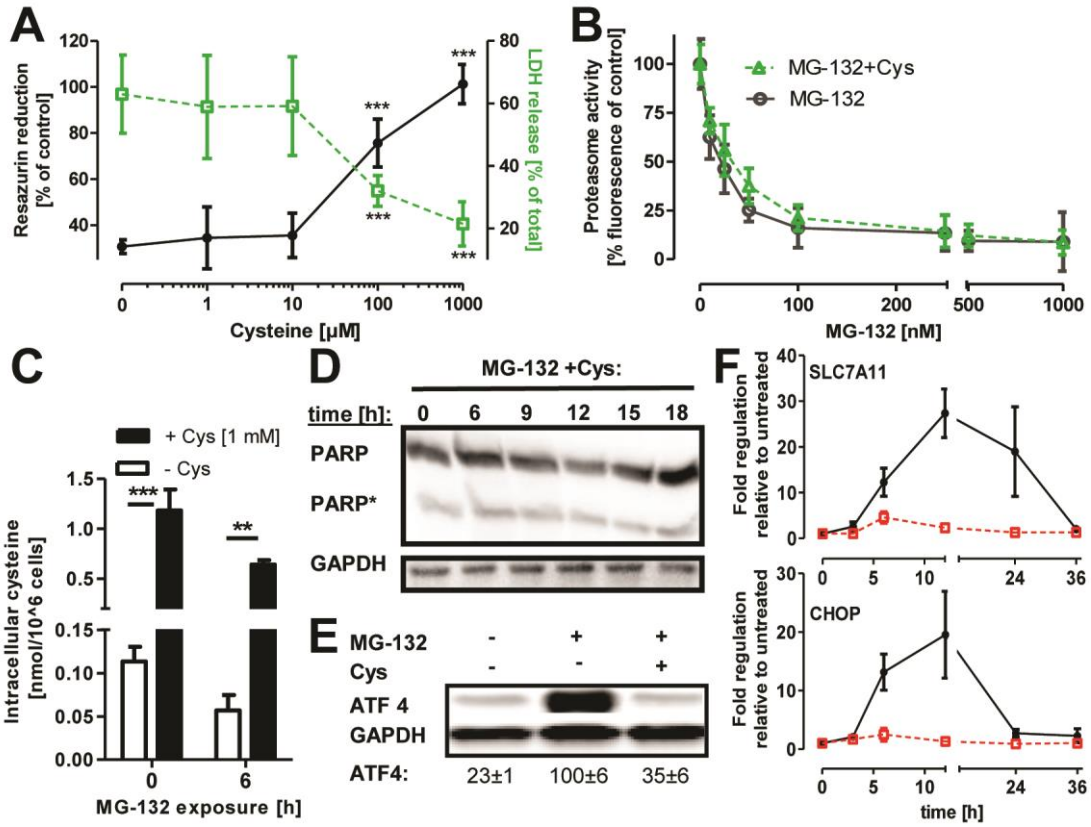

Figure 3_3: Protection by external cysteine from proteotoxic neuronal stress

A: LUHMES cells (d6) were incubated with MG-132 [100 nM] and the indicated concentrations of L-cysteine for 24 h. Viability was assessed measuring resazurin reduction and LDH release. **B:** Proteasomal inhibition by indicated concentrations of MG-132 in presence or absence of 1 mM L-cysteine was assessed in LUHMES cells by measuring proteasome activity fluorometrically. **C:** Intracellular cysteine levels of LUHMES cells that were exposed to MG-132 [100 nM] for 0 or 6 h in presence or absence of 1 mM extracellular L-cysteine were measured by amino acid analysis. **D:** LUHMES cells (d6) were treated with MG-132 [100 nM] and 1 mM L-cysteine for the indicated time periods. After incubation cells were lysed and analysed by Western blot using anti-PARP and anti-GAPDH antibodies. **E:** LUHMES cells (d6) were treated with MG-132 [100 nM] in presence or absence of 1 mM L-cysteine for 6 h. After incubation cells were lysed and analysed by Western blot using anti-ATF-4 and anti-GAPDH antibodies. ATF-4 induction was quantified densitometrically. **F:** Differentiated day 6 LUHMES cells were exposed to 100 nM MG-132 for the indicated time periods in presence or absence of 1 mM L-cysteine. Changes in mRNA levels were monitored by qPCR for target genes of ATF-4 Cystine/Glutamate transporter (SLC7A11) and DNA damage inducible transcript 3 (CHOP). Data are means ± SD of three independent experiments **: $p<0.01$ ***: $p<0.001$

Rescue of neurons by external GSH

Cysteine itself is unlikely to be released from astrocytes, as this amino acid has a high excitotoxic potential (327, 328). However, the cysteine-containing tripeptide GSH is a well-established candidate metabolite transferred from glia to neurons (329-332). We investigated therefore the effect of GSH on neuronal survival after MG-132 exposure. Addition of GSH to neuronal mono-cultures lead to an intracellular GSH increase (Fig. 4_3A), and blocked cysteine depletion after proteasome inhibition by MG-132 (Fig. 4_3B).

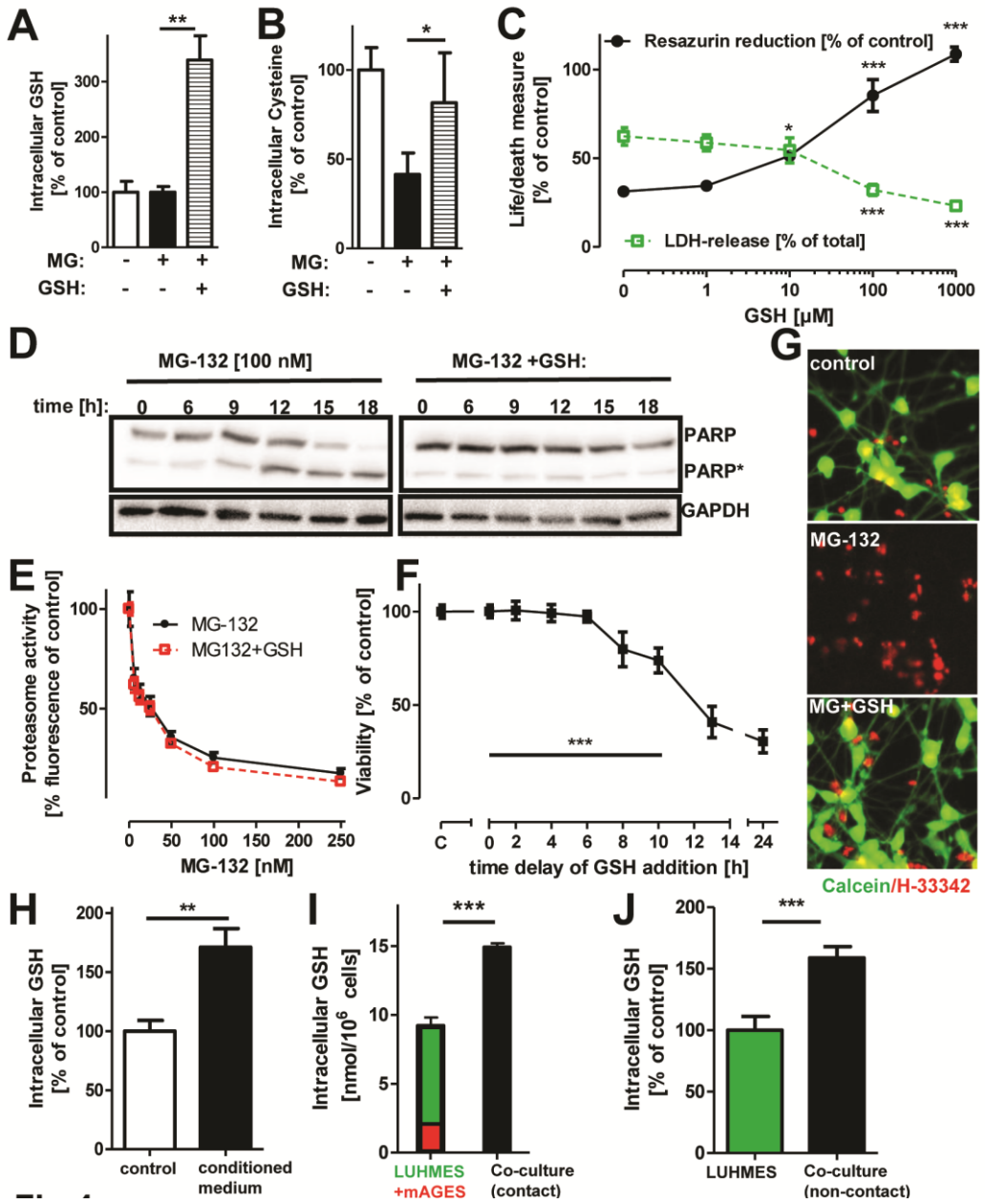

Figure 4_3: Rescue of neurons from proteasome inhibition by glutathione supply

A: Intracellular GSH levels of LUHMES cells that were exposed to MG-132 [100 nM] for 0 or 6 h in presence or absence of 1 mM extracellular GSH were measured by amino acid analysis. Data are means ± SD of three independent experiments **: $p<0.01$ **B:** Intracellular cysteine levels of LUHMES cells that were exposed to MG-132 [100 nM] for 0 or 6 h in presence or absence of 1 mM extracellular L-cysteine were measured by amino acid analysis. Data are means ± SD of three independent experiments *: $p<0.05$ **C:** LUHMES (d6) cells were incubated with MG-132 [100 nM] and the indicated concentrations of GSH for 24 h. Viability was assessed measuring resazurin reduction and LDH release. Data are means ± SD of three independent experiments *: $p<0.05$ ***: $p<0.001$ **D:** Cells were treated with MG-132 [100 nM] and 1 mM GSH for the indicated time periods. After incubation cells were lysed and analysed by Western blot using anti-PARP and anti-GAPDH antibodies. **E:** Proteasomal inhibition by indicated concentrations of MG-132 in presence or absence of 1 mM GSH was assessed in LUHMES cells by measuring proteasome activity fluorometrically. **F:** LUHMES cells (d6) were treated with MG-132 [100 nM], and GSH [1 mM] was added at various times after the exposure to MG-132. Viability was assessed 24 h after start of MG-132 exposure. For measurement of viability, cells were stained with the vital dye calcein-AM and H-33342. Double positive cells were counted by automated microscopy and normalized for all H-33342 positive cells. Data are means + SD of three independent experiments ***: $p<0.001$ (24 h delay vs. 0-10 h) **G:** Cells were treated as described in E. Representative pictures for solvent treated, MG-132 treated and cells treated with MG-132 and 8 h later with GSH are shown. **H:** Intracellular GSH levels of cells incubated for 6 h either with standard differentiation medium or astrocyte conditioned medium were determined by amino acid analysis. Data are means ± SD of three independent experiments **: $p<0.01$ **I:** GSH levels in co-culture and the GSH levels of both mono-cultures were determined by GSH assay. Values were normalized to cell number. Data are means + SD of three independent experiments ***: $p<0.001$ **J:** GSH levels of LUHMES cultured 1 mm above

mAGES (non-contact co-cultures) and LUHMES cultured alone were determined by GSH assay. Data are means ±SD of three independent experiments ***: $p<0.001$

Furthermore, GSH blocked MG-132-induced cell death (Fig. 4_3C) and prevented apoptotic PARP cleavage (Fig. 4_3D), while the inhibition of the proteasome by MG-132 was not altered by GSH (Fig. 4_3E). Importantly, GSH was still effective at preventing cell death when added 8-10 h after MG-132 (Fig. 4_3F+G). To get evidence on the role of astrocytes in providing GSH, we incubated neurons with astrocyte-conditioned medium, and observed an increase in neuronal GSH under this condition (Fig. 4_3H). The increase in neuronal GSH levels triggered by increasing fractions of glia-conditioned medium (from mAGES and human astrocytes) was paralleled by an increased survival after MG-132 exposure (Fig. S9_3A-C) and scavenging of thiols in conditioned medium from astrocytes blunted the protective properties (Fig. S9_3D+E). In a next step, we compared the GSH content of co-cultures (90 % neurons) with the content of neurons alone or with separate neurons and astrocytes. Co-cultures had significantly higher GSH levels than the two separate mono-cultures combined (Fig. 4_3I). Moreover, LUHMES cultured on coverslips 1mm above mAGES and then analysed separately had significant higher GSH levels compared to LUHMES cultured in the absence of mAGES (Fig. 4_3J). We conclude from this that the neuronal GSH was increased in the presence of astrocytes, similar as observed with conditioned medium.

Alterations in the neuronal stress response by GSH

To further characterize the effect of GSH supplementation on the neuronal stress response and cell death, we monitored the protein levels of the stress-associated TF ATF-4, NRF-2 and NRF-1 (Fig. 5_3A-C). In cells treated with MG-132 only, these TF were up-regulated from 6 h until 12 h after MG-132 exposure (Fig 5_3A+C). Cells co-treated with GSH displayed a weak ATF-4 and no detectable NRF-2 signal, while NRF-1 levels were elevated (Fig. 5_3B+C). Thus, GSH modulated different stress-response pathways in opposite ways. In line with this observation, the up-regulation of ATF-4 target genes was attenuated in the presence of GSH, while NRF-1 target genes showed an increased transcription (Fig. S10_3A+B). As NRF-2 is predominantly an indicator of oxidative stress, its down regulation by GSH confirms that pro-

teasome inhibition triggers neuronal stress, which is blunted by an improved GSH supply.

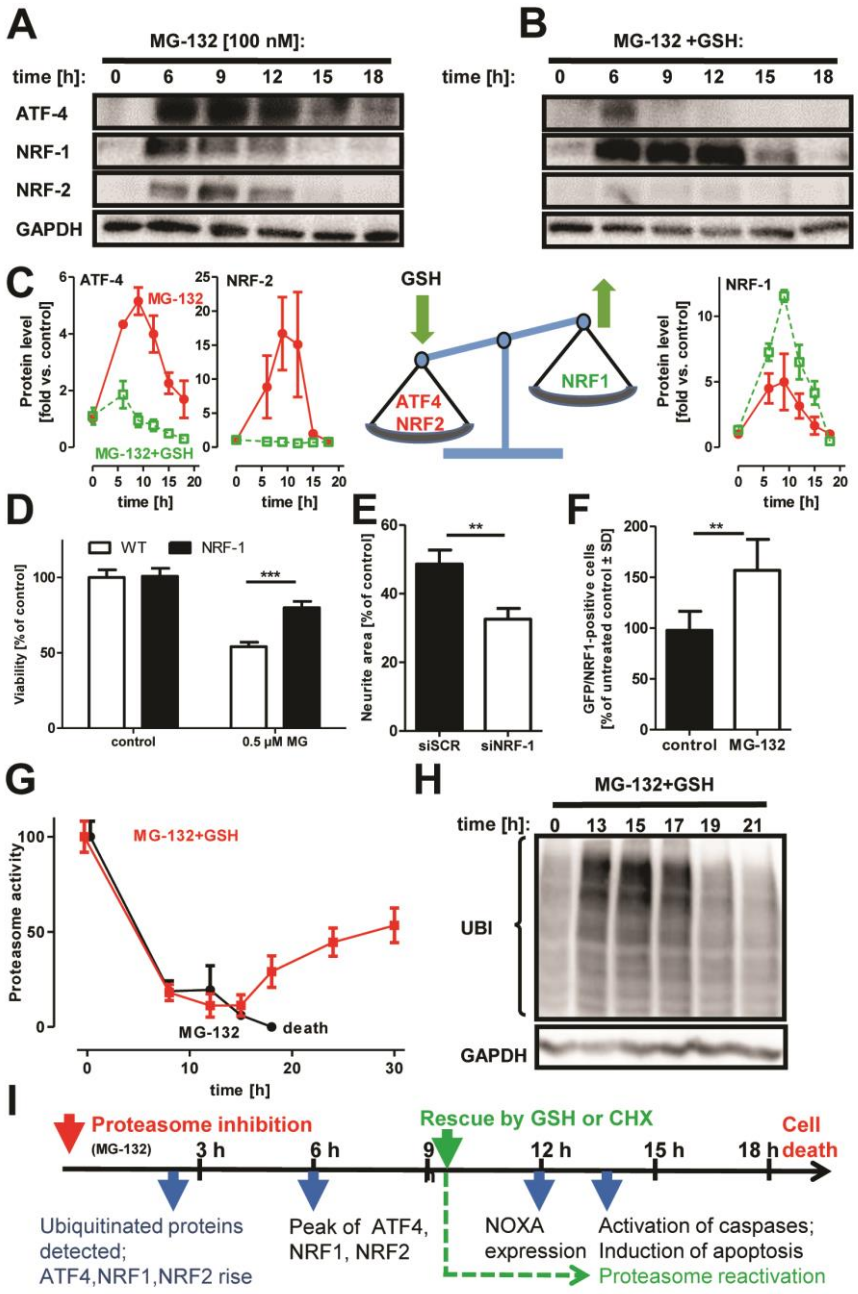

Figure 5_3: Influence of external thiols on the balance between ATF-4, NRF-1 and NRF-2

A+B: To address differences in the neuronal stress response following proteasome inhibition in the absence (A) or presence (B) of GSH [1 mM], cells were treated with MG-132 [100 nM] for the indicated time periods. After incubation cells were lysed and analysed by Western blot using anti-ATF-4, anti-NRF-1, anti-NRF-2 and anti-GAPDH antibodies. **C:** Densitometric quantification of A and B and a schematic depiction of the influence of GSH on the stress response following MG-132 exposure. **D:** HEK-293 cells over-expressing NRF-1 and wild type cells were incubated for 48 h with MG-132 [0.5 µM]. Viability was assessed by Resazurin. Data are means ± SD of three independent experiments ***: $p<0.001$ **E:** LUHMES were transfected with siRNA against NRF-1 or scrambled siRNA at d2 of differentiation. Cells were cultured till d6 of differentiation and then incubated with MG-132 [100 nM], GSH [1 mM] was added 7 h after MG-132 addition. 24 h after MG-132 addition viability was measured. For measurement of viability, cells were stained with the vital dye calcein-AM and the DNA stain H-33342. Neurite area of the cells was assessed by automated microscopy. Data are means ±SEM of three independent experiments **: $p<0.01$ **F:** LUHMES were transfected by electroporation with NRF-1 and GFP over-expression plasmids at d2 of differentiation. Cells were cultured till d6 of differentiation and then incubated with MG-132 [100 nM]. 18 h after MG-132 exposure cells were stained with DNA stain H-33342 and the vital dye calcein-AM. Double positive cells were counted

by automated microscopy. Data are means+ SEM of three independent experiments **: p<0.01 **G:** Proteasomal recovery after exposure to MG-132 [100 nM] in presence or absence of 1 mM GSH was assessed in LUHMES cells by measuring proteasome activity fluorometrically after indicated incubation times. 24 h after exposure to MG-132 there was no proteasomal activity detectable in cells treated only with MG-132, due to cell death. **H:** To confirm proteasomal recovery, cells were treated with MG-132 [100 nM] for the indicated time periods in presence of GSH [1 mM]. After incubation, cells were lysed and analysed by Western blot using anti-ubiquitin and anti-GAPDH antibodies. **I:** Time line of events in neurons following MG-132 exposure**.** The red arrow indicates the start of MG-132 exposure. The green arrow shows the latest time point for complete rescue by GSH and CHX. The blue arrows indicate events associated with the stress response and cell death.

The role of ATF-4 in neurodegeneration is ambiguous (49). This TF, when triggered by ER stress, can take a pro-apoptotic role, e.g. by induction of the apoptosis enhancer DDIT-4 (333, 334).We observed here that GSH blunted the DDIT-4 response (Fig. S11_3A). Moreover, partial knock-down of DDIT-4 in LUHMES attenuated cell death triggered by MG-132, while the counter-regulatory NRF-1 response was enhanced (Fig. S11_3B-D). Thus, attenuation of the ATF-4 arm of the stress response may contribute to neuroprotection or prolong the period of neuronal resilience. Notably, ATF-4 induced by amino acid starvation, regulates also pro-survival pathways (e.g. cystine import and transsulfuration) (49, 335). The observed down-regulation by GSH would also be in line with this role, as GSH counteracted the cysteine deficit (Fig. 4_3B), and abolished the need for increased GSH synthesis. Since all attempts to deplete LUHMES of ATF-4 failed, we produced ATF-4 deficient HEK-293 by Crisp/Cas technology. Such ATF-4 knockout cells failed to regulate typical ATF-4 target genes following exposure to MG-132 (Fig. S12_3A+B), and they had a slightly increased sensitivity to proteasome inhibition (Fig. S14_3C). This suggests that down-regulation of ATF-4 alone may not be sufficient to protect cells from apoptosis and to explain the neuroprotective effect of GSH. The parallel up-regulation of NRF-1 may offer such an explanation. NRF-1 may provide neuroprotection by up-regulating the proteasome (314, 324, 325) and thereby attenuating proteotoxic stress. As proof of principle, we overexpressed NRF-1 in HEK-293 cells and exposed them to MG-132. Under this condition, we observed a significant increase in survival (Fig. 5_3D-F). In LUHMES, attenuation of the NRF-1 response (by siRNA) reduced the protection provided by GSH (Fig. 5_3E; Fig. S14_3A), while over-expression of NRF-1 increased the neuronal survival following proteasome inhibition (Fig. 5_3F; Fig. S14_3B).

To obtain some evidence on mechanisms responsible for neuronal protection by NRF-1 super-induction, we studied proteasome activity and protein aggregation over time. Indeed, we observed that the addition of GSH allowed cells to recover pro-

teasome activity (Fig. 5_3G). The return of enzymatic activity was followed by a clearance of ubiquitinated proteins to baseline levels after 24 h (Fig. 5_3H). In line with this, GSH supplementation significantly reduced intracellular protein aggregation following MG-132 exposure (Fig. S13_3A+B).

These findings suggests following time course of events (Fig. 5_3I): stress response factors are induced in parallel with the accumulation of ubiquitinated proteins, starting few h after addition of MG-132. After about 10 h, neurons reach the point-of-no-return and start succumbing to proteotoxic stress. Death is executed by the activation of caspases at 12-15 h. GSH is likely to have a dual effect, first by attenuating oxidative stress (e.g. attenuated induction of DDIT-4) to such an extent that the point-of-no-return is delayed by some hours. We suggest that the second effect is enhanced recovery of proteasome activity and cell function related to up-regulated NRF-1.

Astrocytic modulation of neuronal stress responses and neuroprotection

Having established the dominant signaling events associated with GSH-mediated protection of neurons, we now asked whether astrocytes would lead to a similar modification of the stress response network. Indeed, the presence of astrocytes suppressed the activation of ATF-4 and increased the NRF-1 response in neurons (Fig. 6_3A, Fig. S15_3). When LUHMES were incubated with astrocyte-conditioned medium and treated with MG-132, the ATF-4 response was also weaker than in cells cultured in normal differentiation medium, while the NRF-1 response was increased (Fig. 6_3B+C). This indicates that astrocytic thiol supply is able to modulate the neuronal stress response following proteasome inhibition and thereby rescuing neurons.

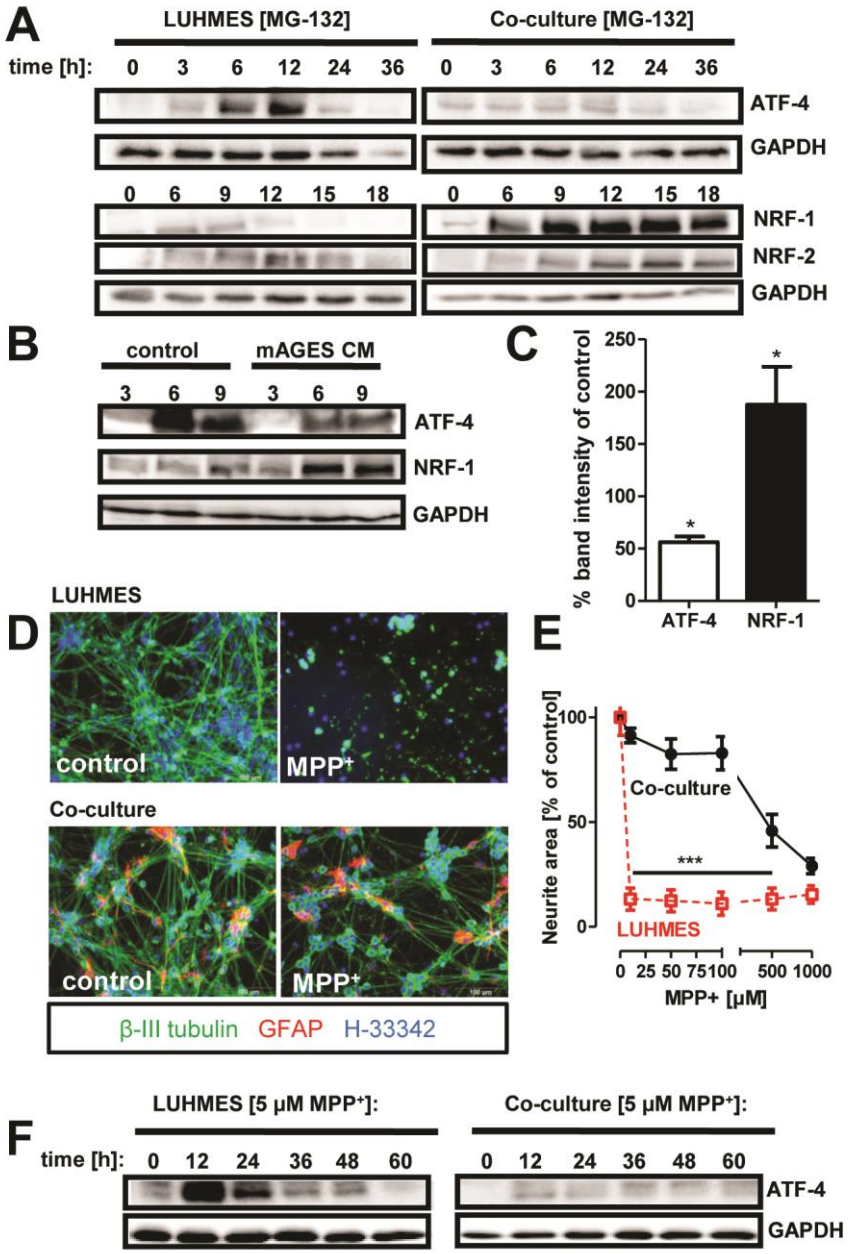

Figure 6_3: Alterations in neuronal stress response and rescue by astrocytes

A: LUHMES and co-cultures were treated with MG-132 [100 nM] for the indicated time periods. After incubation, cells were lysed and analysed by Western blot using anti-ATF-4, anti-NRF-1, anti-NRF-2 and anti-GAPDH antibodies. **B:** D6 LUHMES cells were incubated with either differentiation medium (control) or astrocyte-conditioned medium and incubated with MG-132 [100 nM] for the indicated time periods. After incubation, cells were lysed and analysed by Western blot using anti-ATF-4, anti-NRF-1 and anti-GAPDH antibodies. **C**: Densitometric quantification of 6 h and 9 h bands of NRF-1 and ATF-4 in B. Data are means ± SEM of two independent experiments *: $p<0.05$ (t-test) **D+E:** Neuronal survival of co- and mono-cultured LUHMES was assessed 72 h after incubation with the indicated concentrations of MPP^+. Representative pictures of cells treated with MPP^+ [5 µM] are shown in D. Quantification of the neurite area is shown in E. Data are means ± SD of three independent experiments ***: $p<0.001$. **F:** LUHMES and co-cultures were treated with MPP^+ [5 µM] for the indicated time periods. After incubation, cells were lysed and analysed by Western blot using anti-ATF-4 and anti-GAPDH antibodies.

Finally, we re-visited the protective role of astrocytes on neurodegeneration triggered by the parkinsonian toxicant MPP^+. The presence of astrocytes largely (100-fold) increased the non-toxic concentration range of MPP^+ (Fig. 6_3D+E), and also condi-

tioned medium supported neuroprotection (Fig. S16_3). Moreover, the MPP^+ induced ATF-4 stress response, a hallmark of mitochondrial stress in neurons (49), was largely attenuated by astrocyte co-culture (Fig. 6_3F, Fig. S17_3). As for MG-132, direct addition of GSH to the mono-cultures prevented intracellular aggregate formation triggered by MPP^+ or rotenone (Fig. S20_3A+B). These data indicate a broad role of astrocytic thiol supply in the modulation of neuronal stress responses.

3.3.4 Discussion

It has been known that any treatment that increases astrocytic NRF-2, leads to their release of thiols, which support neurons (320, 336-341). However, it remained unclear how this works on the level of neurons. The data presented here link the numerous observations on astrocytic neuroprotection (and the regulation within astrocytes) to the hitherto little explored alterations in neuronal stress response-signaling/cell death. Based on the established knowledge that neurons are in need of an extracellular thiol source (330, 332), and that astrocytes are the main suppliers of glutathione/glutathione precursors in the brain, we show here that this metabolic cooperation has a major impact on neurodegeneration. Using direct GSH supplementation, we found that changes in the regulation of key TF were linked to neuronal protection from insults as diverse as block of the mitochondrial respiration chain and proteasome inhibition. Thiol supply did not dampen all stress responses elicited by proteasome inhibitors, but it rather led to a re-adjustment of cellular homeostasis: while e.g. ATF-4 was strongly down-regulated, the NRF-1 response was found to be increased. The overall shift of the response pattern appeared to be responsible for the change in neuronal fate (Fig. 5_3I). The findings of this study implicate astrocytes, and in particular the regulation of their thiol supply to neurons, as potential therapeutic drug targets.

Neurodegeneration in PD is closely linked to mitochondrial dysfunction (287, 309), and accordingly, many PD models rely on experimental inhibition of mitochondria (170). A frequent observation in such models and human patients is that also protein degradation is impaired (287, 309). We found here, that this link also pertains to the frequently used LUHMES neuronal cultures (49, 288-291). Indeed, mitochondrial inhibition by two different compounds lead to an attenuation of proteasome activity, and to a subsequent accumulation of aggregated proteins. These mild, but significant

effects on the UPS are well in line with those observed in animal studies (342). Also in agreement with many *in vivo* observations (310, 311), we found that direct inhibitors of the proteasome had more pronounced proteotoxic effects. Astrocytes attenuated neuronal cell death triggered by all toxicants used here, and we found the survival of cells with a specifically inhibited UPS particularly intriguing, as such protection is not easily explained by the activation of known resilience pathways, such as a shifted energy supply (42) or the scavenging of ROS released from inhibited mitochondria (170). As the cellular damage in the proteasome inhibition model is more clearly defined than in the mitochondrial dysfunction models, we mainly focused on the resilience mechanisms relevant for this form of damage, even though the neuroprotective principles may be applicable also to other toxicants, such as mitochondrial inhibitors.

Others have observed that addition of cysteine or an increase of GSH can attenuate the ATF-4 stress response and increase survival following proteasomal inhibition (317, 343). From these studies it has been concluded that proteasome activity is important to maintain intracellular cysteine levels in order to support protein biosynthesis (317). Our data favor a different interpretation of the role of ATF-4 in human neurons: This TF appears to be a master controller of neuronal thiol supply by up-regulating the cystine transporter and by enabling the transsulfuration pathway. The latter provides neurons with an alternative route of cysteine generation from methionine, and thus augments their glutathione levels and ROS resilience (344-346). We have previously linked ATF-4 activation following mitochondrial respiratory chain inhibition to increased usage of the transsulfuration pathway in LUHMES, and we found that down-regulation of ATF-4 reduced the GSH levels of stressed neurons dramatically (49). This suggests that one consequence of ATF-4 up-regulation, i.e. an augmented cellular GSH content, may be beneficial rather than detrimental. In accordance with this we found ATF-4 -/- cells to be rather more sensitive to MG-132 than the corresponding wild type cells. We suggest that the drastic down-regulation of neuronal ATF-4 by cysteine, GSH or astrocytes reflects a decreased need of neurons to activate the transsulfuration pathway in order to secure their GSH levels. However, the ATF-4 pathway has several branches that need to be considered. Besides its role in resilience under nutrient stress, it can also activate a cell death program via induction of DDIT-4. We provided evidence that also this branch plays a role in our model system. In the presence of thiols, added to the medium, or provided by

astrocytes, this pro-death branch was blocked, while the protective branch was not necessary for the cells (transsulfuration is not required if cysteine supply is sufficient). We conclude that blunting of the ATF-4 response in the presence of additional GSH prevented an immediate execution of a death program, but did not explain the coping of the cell with the primary problem of accumulated proteins.

Thus, the observed NRF-1 up-regulation may be more critical. This TF has recently been identified as main regulator of proteasome abundance (314, 324, 325). In line with this, we observed recovery of proteasome activity and reduced aggregate formation in cells supplemented with GSH. Alterations in NRF-1 levels by over-expression or knockdown increased or decreased cellular resilience against proteasome inhibition, respectively. Thus, extra supply of thiols to the neurons seemed to have two major effects: first, cells were prevented from immediately undergoing programmed cell death (decreased ATF-4/DDIT4/caspase axis); second, this first effect 'bought sufficient time' for NRF-1 to become active, and allow recovery of proteasome activity and clearance of aggregated proteins.

By linking astrocytic thiol supply to an increased NRF-1 response and survival of neurons, we identified astrocytes as potential therapeutic target. One candidate pathway that may be targeted by drugs is the NRF-2 stress response. In brain tissue, astrocytes are the major cell type to activate this pathway (320, 347), and this response may be triggered by pharmacological or non-pharmacological pre-conditioning strategies (348, 349). Stimulation or over-expression of NRF-2 in astrocytes leads to an intracellular GSH increase, to GSH release into the medium and to augmented protection of co-cultured neurons (320, 336, 337, 350, 351). Moreover, some evidence suggest that activation of NRF-2 in astrocytes affects transcription in neurons (350). The co-culture system established here may be used in the future to further characterize such effects and to examine drugs harnessing the endogenous trans-cellular resilience pathways for neuroprotection.

3.3.5 Materials and Methods

3.3.5.1 Chemicals

Dibutyryl-cAMP (cAMP), fibronectin, hoechst bisbenzimide H-33342, resazurin sodium salt, tetracycline, L-cysteine and reduced glutathione (GSH) were purchased from

Sigma (Steinheim, Germany). Recombinant human FGF-2 and recombinant human GDNF were purchased from R&D Systems (Minneapolis, USA). Tween-20 and sodium dodecyl sulfate (SDS) were purchased from Roth (Karlsruhe, Germany). All cell culture reagents were purchased from Gibco/Fisher scientific (Hampton, New Hampshire,USA) unless otherwise specified. MG-132 was purchased from Selleckchem (Houston, USA)

3.3.5.2 Cell culture

Handling of LUHMES human neuronal precursor cells was performed as previously described in detail (104). Briefly, the conditionally-immortalized cells, maintained in proliferation medium, consisting of advanced DMEM/F12, 2 mM L-glutamine, 1 x N2 supplement (Invitrogen), and 40 ng/ml FGF-2 in a 5% CO_2/95% air atmosphere at 37° C, were passaged every other day. For differentiation, 8 million cells were seeded in a Nunclon T175 tissue culture flask pre-coated with 50 µg/ml poly-L-ornithine (PLO) and 1 µg/ml fibronectin in proliferation medium. After 24 h, medium was changed to differentiation medium (DM), consisting of advanced DMEM/F12 supplemented with 2 mM L-glutamine, 1 x N2, 2.25 µM tetracycline, 1 mM dibutyryl 3',5'-cyclic adenosine monophosphate (cAMP) and 2 ng/ml recombinant human glial cell derived neurotrophic factor (GDNF). After 48 h, cells were trypsinised, and seeded at a density of $1.5*10^5$ cells/cm² into dishes pre-coated with 50 µg/ml poly-L-ornithine (PLO) and 1 µg/ml fibronectin in DM. Medium of maintenance was regularly checked for mycoplasma contamination and working stock of LUHMES cells was validated by STR profiling to exclude cross-contamination.

Astrocytes generated from mouse embryonic stem cells (mAGES) were differentiated, as described previously (182, 183), Briefly, neural stem cells (NSC) were cultivated in N2B27 medium supplemented with 20 ng/ml FGF2 and 20 ng/ml EGF. For differentiation to mAGES, FGF2 and EGF were replaced by 20 ng/ml BMP4 (R&D Systems, Minneapolis, USA) for at least 3 days. The human iPSC derived astrocytes Astro.4U (Ncardia, Köln, Germany) were thawed according to manufacturer's instructions and cultivated in Astro.4U medium on matrigel-coated plates. For astrocyte-neuron co-cultures, pre-differentiated LUHMES (d2) were seeded either on top of mAGES (day 3) or onto Astro.4U (9 days after thawing).

Human embryonic kidney cells 293 (HEK-293) were cultured in DMEM (Gibco/Fisher scientific, Hampton, New Hampshire,USA) supplemented with 10% fetal calf serum and 1% pen/strep. Cells were passaged every other day. For viability experiments, cells were seeded 24 h prior to the start of the experiment at a density of $7*10^4$ cells/cm².

3.3.5.3 Astrocyte conditioned medium

Medium of differentiated astrocytes was aspirated and cells were washed with PBS, then LUHMES DM was added and astrocytes were cultivated in this medium for 72 h. After the incubation, medium was harvested, centrifuged 5 min at 350 x g, to remove cell debris, and added to differentiated LUHMES (d6) cells prior to start of the experiment.

3.3.5.4 General cell viability endpoints

Resazurin: Metabolic activity was detected by a resazurin assay. Briefly, resazurin solution was added to the cell culture medium to obtain a final concentration of 10 µg/ml. After incubation for 30 min at 37° C, the fluorescence signal was measured at an excitation wavelength of 530 nm, using a 590 nm long-pass filter to record the emission. Fluorescence values were normalized by setting fluorescence values of untreated wells as 100%.

LDH release: LDH activity was detected separately in the supernatant and in the corresponding cell homogenate. Medium was transferred into separate plate, then cells were lysed in PBS / 0.1% Triton X-100 for 2 h. Twenty µl of sample was added to 180 µl of reaction buffer containing NADH (100 µM) and sodium pyruvate (600 µM) in potassium-phosphate buffer (pH 7.4). Absorption at 340 nm was measured at 37°C in 1 min intervals over a period of 15 min. The slope of NADH consumption was calculated. The ratio of $LDH_{supernatant}/LDH_{total}$ was calculated using the slopes of supernatant and homogenate. LDH release was expressed in percent. Control data were subtracted from LDH values.

3.3.5.5 Specific neuronal viability assay (neurite area)

Calcein-AM: Labelling of live cells was performed with 1 µM Calcein-AM / 1 µg/ml H-33342 for 30 min at 37°C. Images were collected in two different fluorescent chan-

nels using an automated microscope (Array-Scan VTI HCS Reader (Thermo Fisher, PA, USA). Using an imaging software (vHCS SCAN, Thermo Fisher, PA, USA), nuclei were identified in channel 1 (365±50/461±15 nm) as objects according to their size, area, shape, and intensity. Calcein signal was detected in channel 2 (475±40/525±15 nm). An algorithm quantified all calcein positive cells as viable and only H-33342 positive nuclei as “not viable” cells. For evaluating the neurite areas, nuclei masks, determined in channel 1, were expanded and transferred to channel 2. All calcein positive pixels outside of these masks (somatic area) were counted as neurite area.

3.3.5.6 Determination of total glutathione

For glutathione determination, cells were washed with PBS and lysed in 400 µl of 1% sulfosalicylic acid (w/v). The lysates were collected, sonicated 5 times and centrifuged at 12,000 × g, 5 min, 4 °C to remove cell debris. Total glutathione content was determined by a DTNB (5,5‘-dithiobis(2-nitrobenzoic acid)) reduction assay. 20 µl sample was mixed with 180 µl assay mixture containing 300 µM DTNB, 1 U/ml glutathione-reductase, 400 µM NADPH, 1 mM EDTA in 100 mM sodium phosphate buffer, pH 7.5 (all Sigma, Steinheim, Germany). DTNB reduction was measured photometrically at 405 nm in 5 min intervals over 30 min. GSH standard curves were performed by serial dilutions ranging from 1000 nM to 7.8 nM, respectively.

3.3.5.7 Western blot analysis

Cells were lysed in 1x Laemmli buffer, boiled for 5 minutes at 95°C. For removal of long DNA strands, lysates were centrifuged 1 min, 10,000 × g using NucleoSpin Filters (Macherey-Nagel, Düren, Germany). Thirty-five µg of total protein were loaded onto 6-15% SDS gels according to the size of the protein of interest. Proteins were transferred onto nitrocellulose membranes (Amersham, Buckinghamshire, UK) using the Invitrogen iBlot 2 system. Membranes were blocked with 5% BSA (w/v) in TBS–Tween (0.1% (v/v)) for 1 h. Primary antibodies were incubated at 4° C over night. Following washing steps with TBS-Tween (0.1%), horseradish peroxidase-conjugated secondary antibodies were incubated for 1 h at RT. For visualization, ECL Western blotting substrate (Pierce/Thermo Fisher Scientific, Rockford, IL, USA) was used. Antibodies used for Western blot analysis can be found in Fig. S19_3. Relative band intensity was quantified using a self-developed image evaluation software. Intensities

were normalized to corresponding GAPDH loading control and expressed as fold induction relative to untreated. At least three blots from independent experiments were quantified.

3.3.5.8 Immunocytochemistry

Cells were grown on 13 mm glass cover slips (Menzel, Braunschweig, Germany) in 24-well plastic cell culture plates (NunclonTM) and fixed with 4% paraformaldehyde. After incubation with the primary antibody overnight and with the appropriate secondary antibody for 1 h, Hoechst-33342 (1 µg/ml) was added for 10 min prior to the final washing step. Cover slips were mounted on glass slides with Fluorsave reagent (Calbiochem/Millipore/Darmstadt/Germany). For visualization, an Olympus IX81 inverted epifluorescence microscope (Hamburg, Germany) was used. For image processing, Image J open source software was used.

3.3.5.9 Detection of apoptosis

Cells were stained with antibodies against cleaved caspase 3 and β-III-tubulin. Images were collected in three different fluorescent channels using an automated microscope (Array-Scan VTI HCS Reader (Thermo Fisher, PA; USA)). Using an imaging software (vHCS SCAN, Thermo Fisher, PA, USA), nuclei were identified in channel 1 (365±50/461±15 nm) as objects according to their size, area, shape, and intensity. Cleaved caspase 3 signal was detected in channel 2 (475±40/525±15 nm). An algorithm quantified all cleaved caspase 3-positive cells as apoptotic and only H-33342 positive nuclei as cells.

3.3.5.10 Detection of protein aggregates

For detection of protein aggregates, cells were treated with toxicants for the time period as indicated, fixed with 4% paraformaldehyde and stained with PROTEOSTAT Aggresome detection kit (ENZO, Lausen, Switzerland) following the manufacturer's instructions. Images were collected in two different fluorescent channels using an automated microscope (Array-Scan VTI HCS Reader (Thermo Fisher, PA, USA)). Using an imaging software (vHCS SCAN, Thermo Fisher, PA, USA) nuclei were identified in channel 1 as objects according to their size, area, shape, and intensity. PROTEOSTAT dye signal was detected in channel 2. For evaluating the intensity of PROTEOSTAT dye, the intensity in channel 2 was quantified.

3.3.5.11 Detection of proteasome activity

For detection of proteasome activity cleaveage of MeOSuc-Gly-Leu-Phe-AMC (Bachem , Bubendorf, Switzerland) was measured fluorometrically. Cells were treated with test compounds for time periods as indicated, as positive control MG-132 [10 µM] was added 4 hours prior to measurement of proteasome activity. Medium was replaced with HBSS containing MeOSuc-Gly-Leu-Phe-AMC [25 µM] and fluorescence was measured (ex: 360 nm ,em: 465 nm) directly and after 1 h incubation.

3.3.5.12 Quantitative PCR (qPCR)

For reverse transcription quantitative PCR (RT-qPCR) analysis, RNA was extracted with the PureLink RNA mini Kit (Invitrogen, Darmstadt, Germany) according to the manufacturer's instructions. For transcript analyses of LUHMES, primers (Eurofins MWG Operon, Ebersberg, Germany) were designed as described in (49) and can be found in Fig. S20_3. All RT-qPCRs were based on the SsoFast EvaGreen detection system and were run in a CFX96 Cycler (Biorad, München, Germany) and analysed with Biorad iCycler software. The threshold cycles (Ct) were determined for each gene and gene expression levels were calculated as relative expression compared to GAPDH ($2^{-(\Delta Ct)}$) or as fold change relative to control ($2^{-(\Delta\Delta Ct)}$). ΔCt and ΔΔCt were calculated according to the following formulas:

ΔCt = Ct(condition_gene Y) – Ct(condition_GAPDH).

ΔΔCt = ΔCt(condition_gene Y) – ΔCt(untreated control_gene Y).

gene Y= gene of interest; GAPDH was used as housekeeping gene for normalization

3.3.5.13 Amino acid analysis

12 million cells were washed once with PBS and quenched by 50% v/v methanol/H_2O. After shaking for 30 min at 1400 rpm at 4 °C in an Eppendorf Thermomix (Hamburg, Germany), the solution was centrifuged for 15 min at 21,000 x g at 4 °C to separate the supernatant from the protein precipitations. Samples were dried in a speedvac concentrator and reconstituted in 135 µl of sample dilution buffer (pH 2.2, 0.12 M) (Sykam, Fürstenfeldbruck, Germany). The amino acids were then quantified using a Sykam S433 Amino acid analyzer (Sykam, Fürstenfeldbruck, Germany).

Shortly, amino acids and ammonia were separated by HPLC and subsequent post-column derivatization with ninhydrin. Samples were injected in a volume of 100 µl. Chromatography was performed using a lithium based anion exchange column loaded with spherical polystyrene resin (7 µm diameter, 10% crosslinks, cat# 5125022). Elution was performed using buffers with increasing pH and ion strength (pH 2.9 --> pH 12; buffer concentration 0.12 M to 0.45 M), supported by a temperature gradient. Absorbance of the reaction products was quantified at 440 nm (intermediate product; quantifies cysteine and proline) or 570 nm (quantifies all other amino acids). Amino acid concentrations were determined relative to a reference standard using the area under the peak method in the ChromStar 7 software (SCPA, Weyhe-Leehste, Germany) (42)

3.3.5.14 Statistics and data mining

Cytotoxicity data (Neurite integrity, GSH, LDH, resazurin) and RT-qPCR are presented as means of at least three independent experiments. Unless differently noted, statistical differences were tested by ANOVA or students t-test with post-hoc tests as appropriate, using GraphPad Prism 5.0 (GraphPad Software, La Jolla, USA).

3.3.6 Acknowledgements:

We are indebted to many colleagues for valuable contributions and insightful discussions during the course of this work, especially Karsten Hiller and Xiangyi Dong for providing DDIT4-KD LUHMES. The work was facilitated by grants from the BMBF, the DFG and the EC (EU-ToxRisk)

3.3.7 Supplementary material:

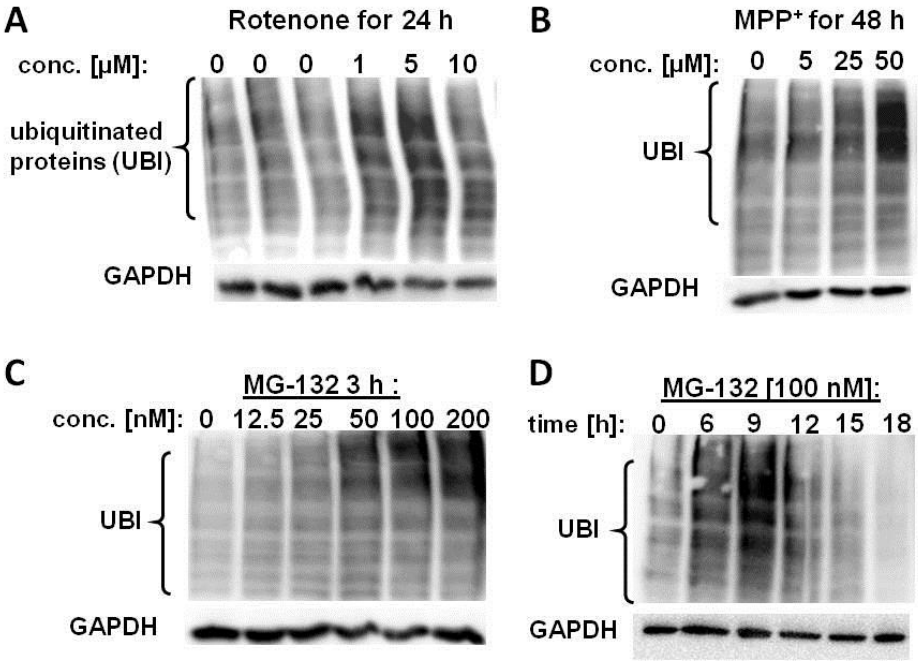

Fig. S1_3: Accumulation of ubiquitinated proteins (UBI) by different stressors

A/B/C: To test for proteasomal dysfunction, cells were treated with the indicated concentrations of rotenone for 24 h, or MPP^+ for 48 h or MG-132 for 3 h. The caspase inhibitor Q-VD-Oph [5 µM] was used as media supplement to prevent cells from dying. Then, cells were lysed and analysed by Western blot with anti-ubiquitin and anti-GAPDH (loading control) antibodies . **D**: To confirm proteasomal dysfunction, cells were treated with 100 nM MG-132 for the indicated time periods. After incubation cells were lysed and analysed by Western blot with anti-ubiquitin and anti-GAPDH antibodies.

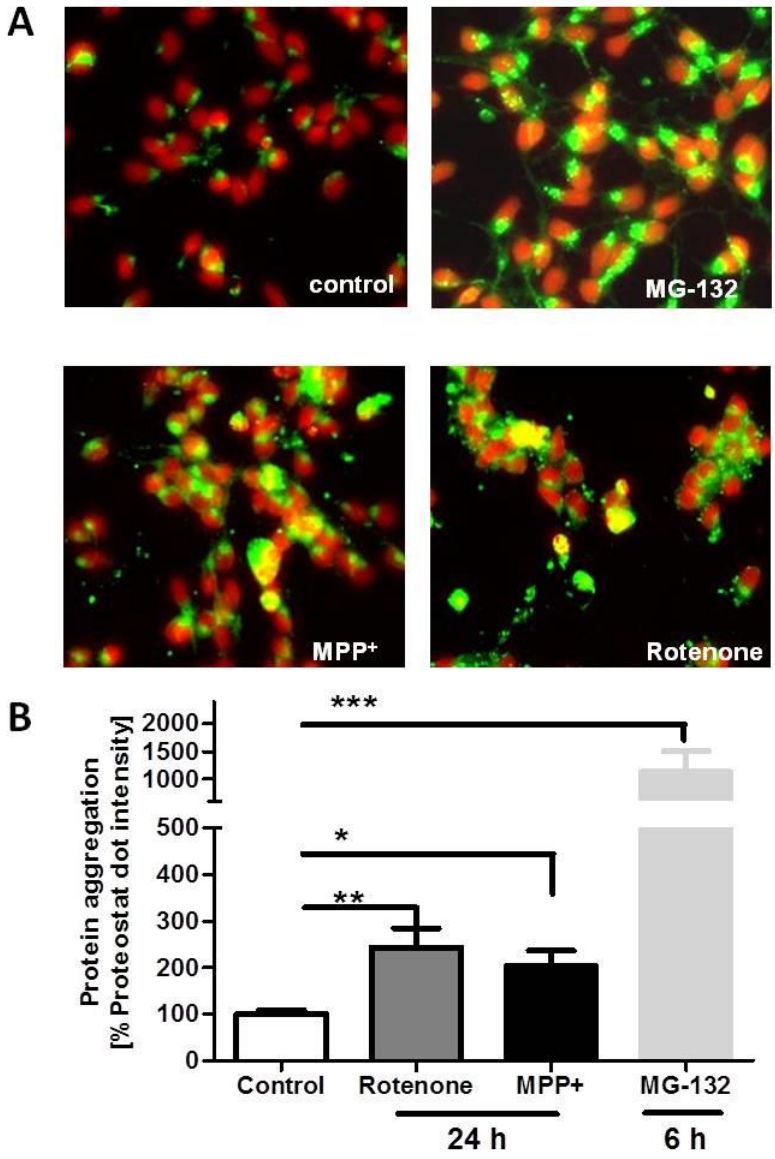

Fig. S2_3: Accumulation of protein aggregates in neurons

A: To test for proteasomal dysfunction, cells were treated with either rotenone [1 µM] or MPP^+ [5 µM] for 24 h or with MG-132 [100 nM] for 6 h. Then, cells were fixed with paraformaldehyde (PFA), stained with Proteostat detection reagent (Enzo, Lausen, Switzerland) based on a dye binding to β-sheet protein aggregates, and analysed by automated microscopy. Aggregates are displayed in green , DNA (nuclei) are shown in red.
B: Quantification of fluorescence intensity of the Proteostat reagent (measuring protein aggregates) in the samples described in A.

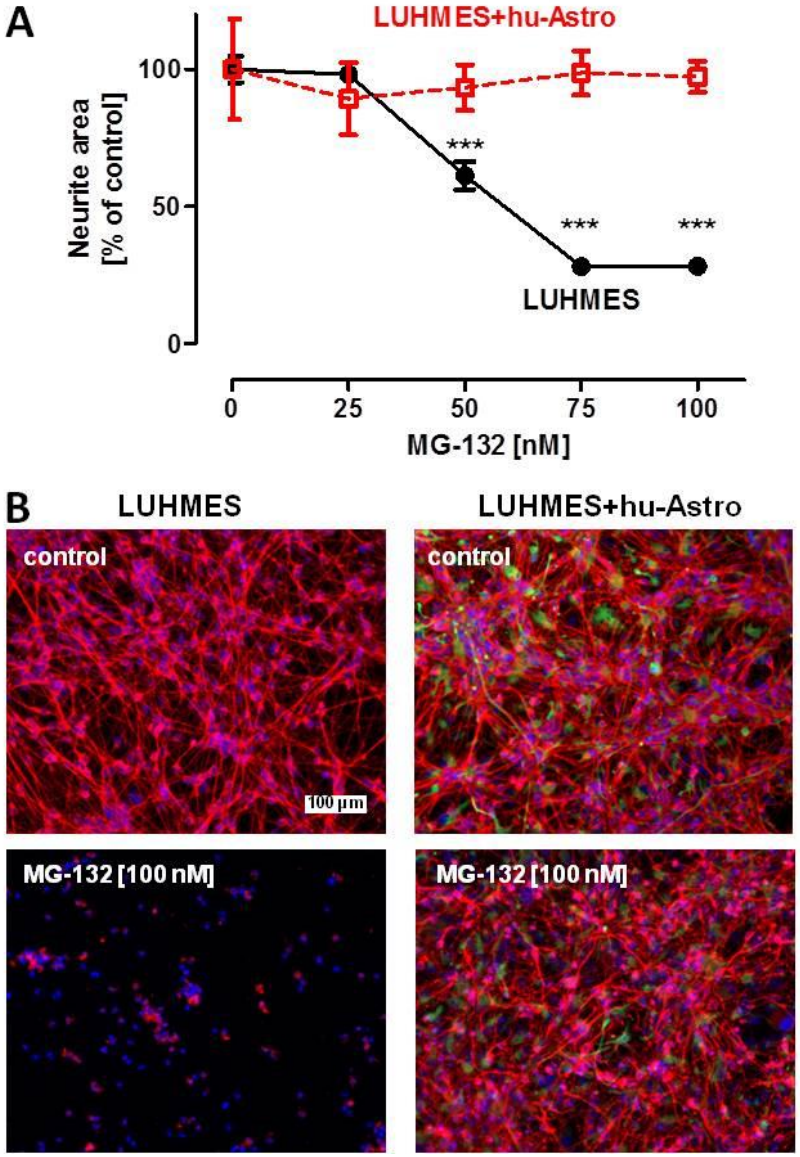

Fig. S3_3: Neuronal protection by human stem cell derived astrocytes (hu-Astro)

Human astrocytes (hu-Astro) were differentiated from induced pluripotent stem cells following established protocols (Chandrasekaran 2016). The cells were obtained as Astro.4U from Ncardia (Cologne, Germany) and plated according to manufacturer's instructions. More than 85% of the cells were GFAP positive (immunostaining). LUHMES were plated on top of the cells as described earlier (Efremova 2016).

A: Differential toxicity of MG-132 in co- and mono-culture was assessed by immunocytochemistry staining against β-III tubulin, GFAP and H-33342 after cultures were exposed for 24 h to MG-132 at the indicated concentrations. Toxicity of MG-132 on LUHMES and astrocyte-LUHMES co-culture was assessed by measuring the neurite integrity after cells were exposed for 24 h to MG-132 at the indicated concentrations. Data are means ± SD of three independent experiments, ***: $p<0.001$. **B**: Exemplary images of the different experimental conditions are displayed for the 24 h time point.

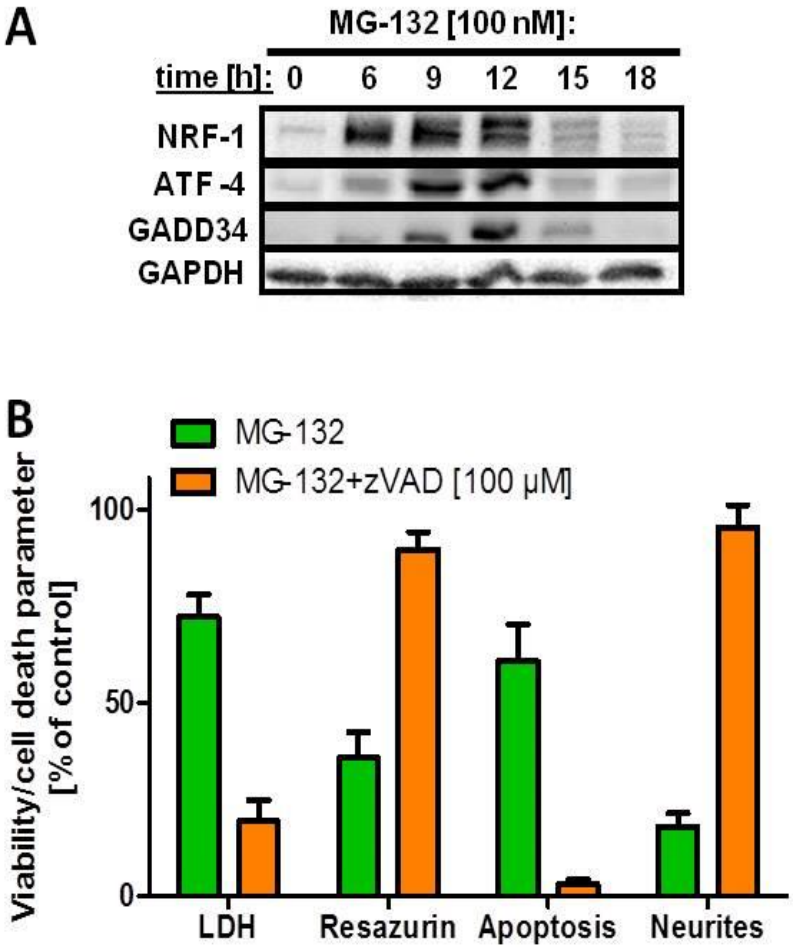

Fig. S4_3: Stress response and cell death signals triggered by MG-132 in neurons

A: To analyse the stress response following proteasome inhibition, cells were treated with 100 nM MG-132 for the indicated time periods. After incubation, cells were lysed and analysed by Western blot with anti-NRF-1, anti-ATF-4, anti-GADD34 and anti-GAPDH antibodies. The blots shown are representative for three experiments with similar results. **B:** LUHMES (d6) cells were exposed to MG-132 [100 nM] for 20 h in the presence or absence of z-Vad-fmk [100 µM]. The different cell death/viability endpoints were measured. LDH-release is indicated as the percentage of total enzymatic activity in the well that is found in the media supernatants. Resazurin data reflects viable cells (100% corresponds to all cells are viable). Apoptosis refers to counting of nuclei with apoptotic morphology relative to all nuclei. Neurites refers to the integrity of the neuronal network as determined by high content imaging. It is a viability measure (100% = healthy cells) like resazurin.

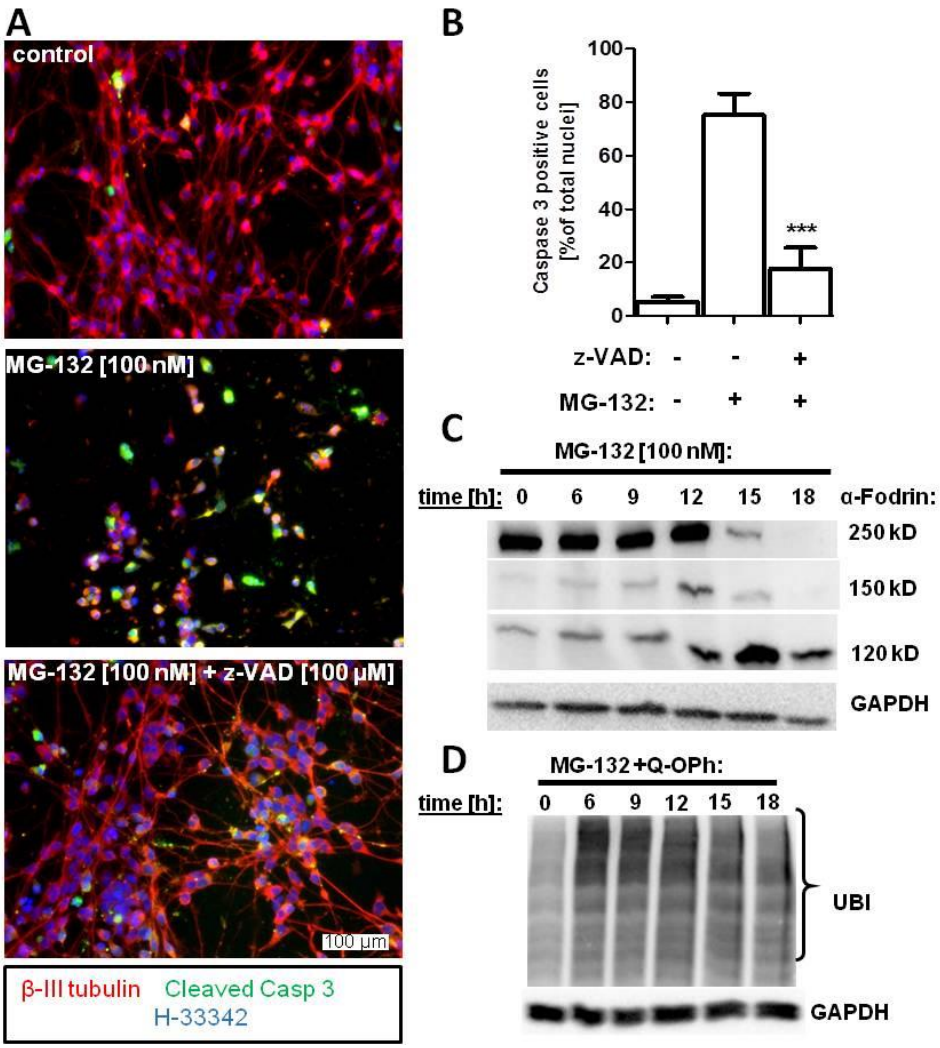

Fig. S5_3: Induction of caspases by treatment of neurons with MG-132

A: Differentiated LUHMES (d6) cells were exposed to either solvent, 100 nM MG-132 or 100 nM MG-132 plus 100 µM caspase inhibitor z-Vad for 18 h. After incubation, cells were fixed and immunostaining for β-III tubulin, cleaved caspase 3 (Casp3) and the DANN dye H-33342 was performed. Representative pictures for each condition are shown. **B**: Cells immunostained as in A were analysed for cleaved caspase 3 positive cells by automated microscopy using a scoring algorithm that counts Hoechst and cleaved caspase 3 double positive nuclei. Data are means ± SD from three independent experiments, ***: $p<0.001$. **C**: To confirm caspase activity, cells were treated with 100 nM MG-132 for the indicated time periods. After incubation, cells were lysed and analysed by Western blot with anti-Fodrin and anti-GAPDH antibodies**. D**: To test for proteasomal dysfunction and degradation of ubiquitinated proteins by caspases, cells were treated with MG-132 [100 nM] for the indicated time periods. The caspase inhibitor Q-VD-Oph [5 µM] was used as media supplement to prevent cells from dying and to test the effect of caspase inhibitor on ubiquitination. After incubation, cells were lysed and analysed by Western blot with anti-Ubiquitin and anti-GAPDH antibodies.

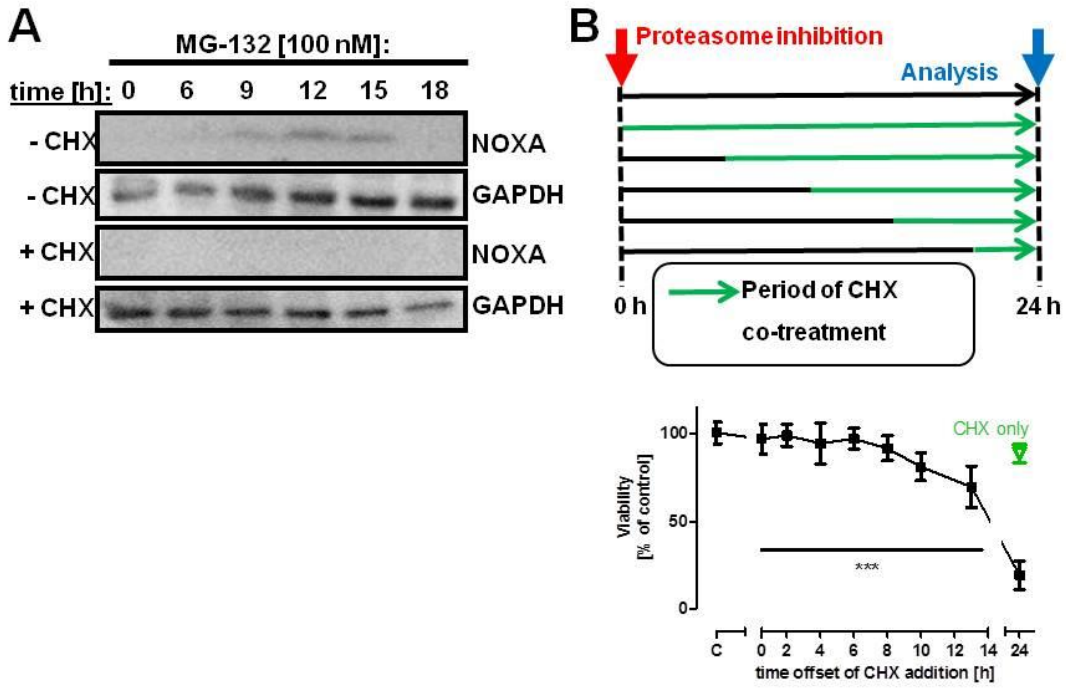

Fig. S6_3: Prevention of MG-132 induced neuronal apoptosis by the inhibition of protein synthesis

A: LUHMES cells (d6) were treated with MG-132 [100 nM] in presence or absence of cycloheximide (CHX) [10 µM] for the indicated time periods. After incubation, neurons were lysed and analysed by Western blot with anti-NOXA and anti-GAPDH antibodies. **B**: LUHMES cells (d6) were treated with MG-132 [100 nM], and cycloheximide [10 µM] was added at various time points after the exposure to MG-132 (green arrows). Viability was assessed 24 h after start of MG-132 exposure. For measurement of viability, cells were stained with the vital dye calcein-AM and H-33342. Double positive cells were counted by automated microscopy and normalized for all H-33342 positive cells. The green triangle indicates the viability of cells treated with only cycloheximide for 24 h. Data are means ± SD of three independent experiments, ***: $p<0.001$ (24 h delay vs. 0-14 h).

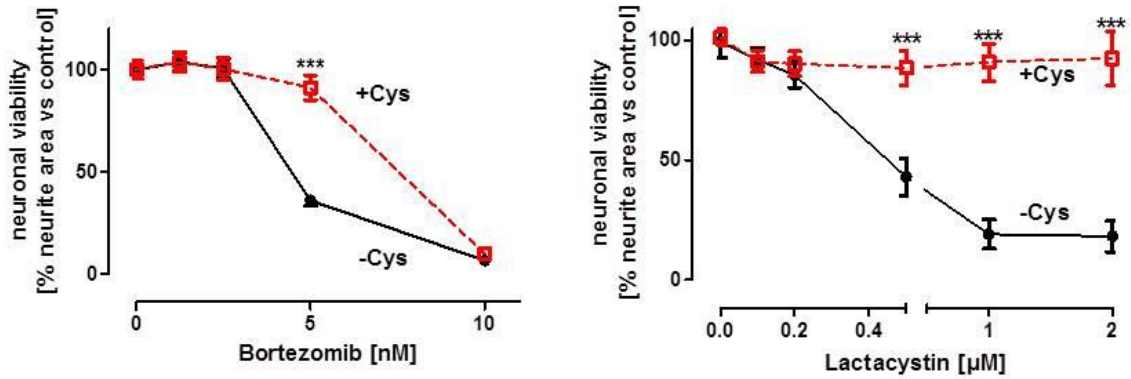

Fig. S7_3: Protective effect of cysteine against different proteasome inhibitors

Differentiated (d6)LUHMES cells were exposed to indicated concentrations of bortezomib (A) or lactacystin (B) in the presence or absence of L-cysteine [1 mM]. Neuronal viability was assessed after 24 h of exposure by measuring the calcein positive neurite area. Data are means ± SD of three independent experiments. ***: $p<0.001$.

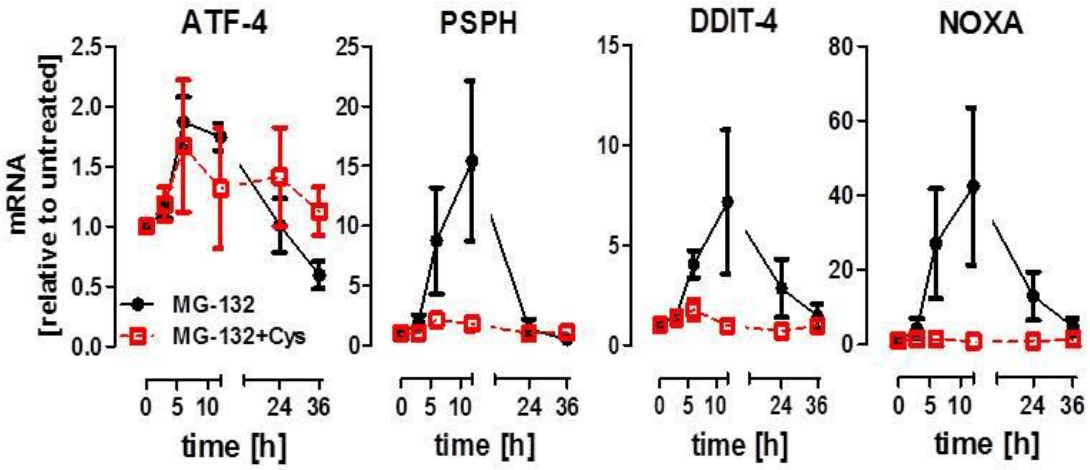

Fig. S8_3: Induction of ATF-4 target genes by MG-132

Differentiated (d6) LUHMES cells were exposed to MG-132 [100 nM] for the indicated time periods in the presence or absence of L-cysteine [1 mM]. Changes in mRNA levels were monitored by qPCR for activating transcription factor 4 (ATF-4) and its target genes phosphoserine phosphatase (PSPH), DNA damage inducible transcript 4 (DDIT-4) and phorbol-12-myristate-13-acetate-induced protein 1 (NOXA). Data are means ± SD of three independent experiments.

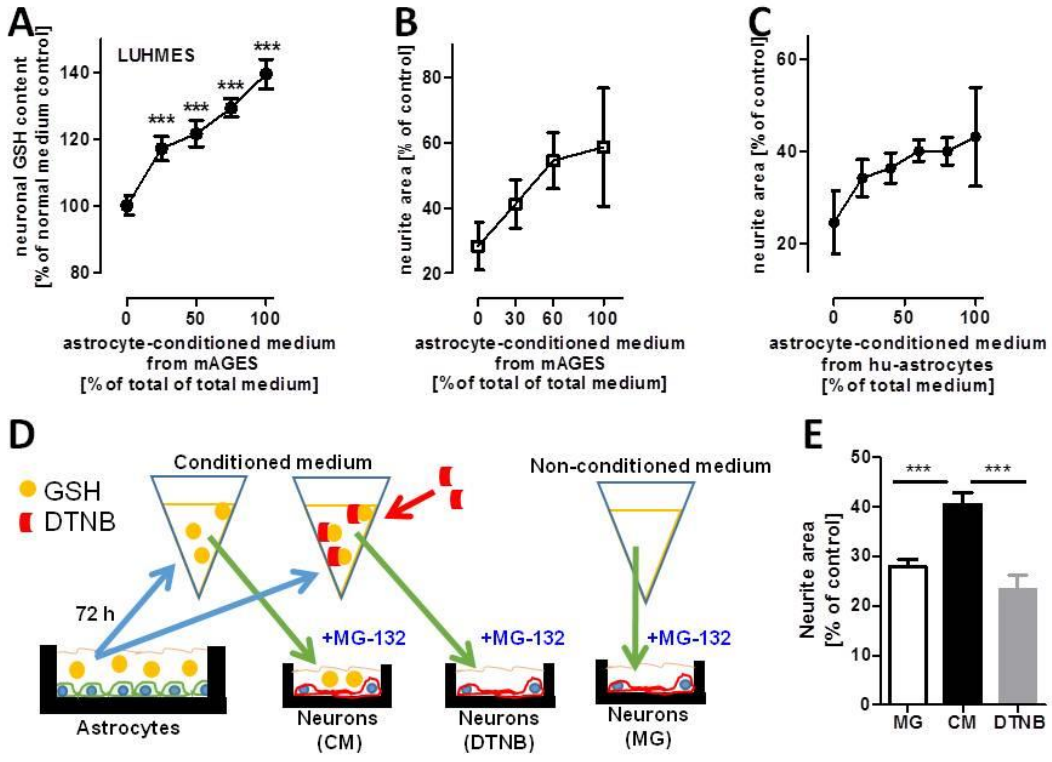

Fig. S9_3: Elevation of neuronal GSH and protection against MG-132 by astrocyte-conditioned medium

A: Differentiated (d6) LUHMES cells were exposed for 4 h to astrocyte-conditioned medium, diluted with fresh LUHMES culture medium. Neuronal intracellular total glutathione (GSH+GSSG) was measured after incubation. Data are means ± SD of three independent experiments, ***: p<0.001. **B**: Differentiated (d6) LUHMES cells were exposed to astrocyte-conditioned medium from mAGES, diluted with fresh LUHMES culture medium in the presence or absence of MG-132 [100 nM]. Viability was assessed 24 h after start of MG-132 exposure. For measurement of viability, cells were stained with the vital dye calcein-AM and the DNA stain H-33342. Neurite area of the cells was assessed by automated microscopy. Data are means ± SD of three independent experiments. **C**: Differentiated (d6) LUHMES cells were exposed to astrocyte-conditioned medium from hu-Astro (see Fig. S6) in the presence or absence of MG-132 [100 nM]. Viability was assessed as in B. Data

are means ± SD of three independent experiments. **D**: Experimental setup of thiol scavanging. Astrocyte conditioned medium from mAGES was harvested and treated either with 10 µM DTNB (5,5-dithio-bis-2-nitrobenzoic acid/ Ellman's reagent) or solvent control. Conditioned medium was transferred onto LUHMES cells. They were treated with MG-132 [100 nM] for 18 h. In parallel, LUHMES were incubated with un-conditioned medium and treated with MG-132 [100 nM] for 18 h. **E**: For the conditions described in D, viability of LUHMES was measured as in B. In parallel it was controlled that DTNB alone had no effect on neurite area (data not shown). Data are means ± SEM of three independent experiments, ***: p<0.001.

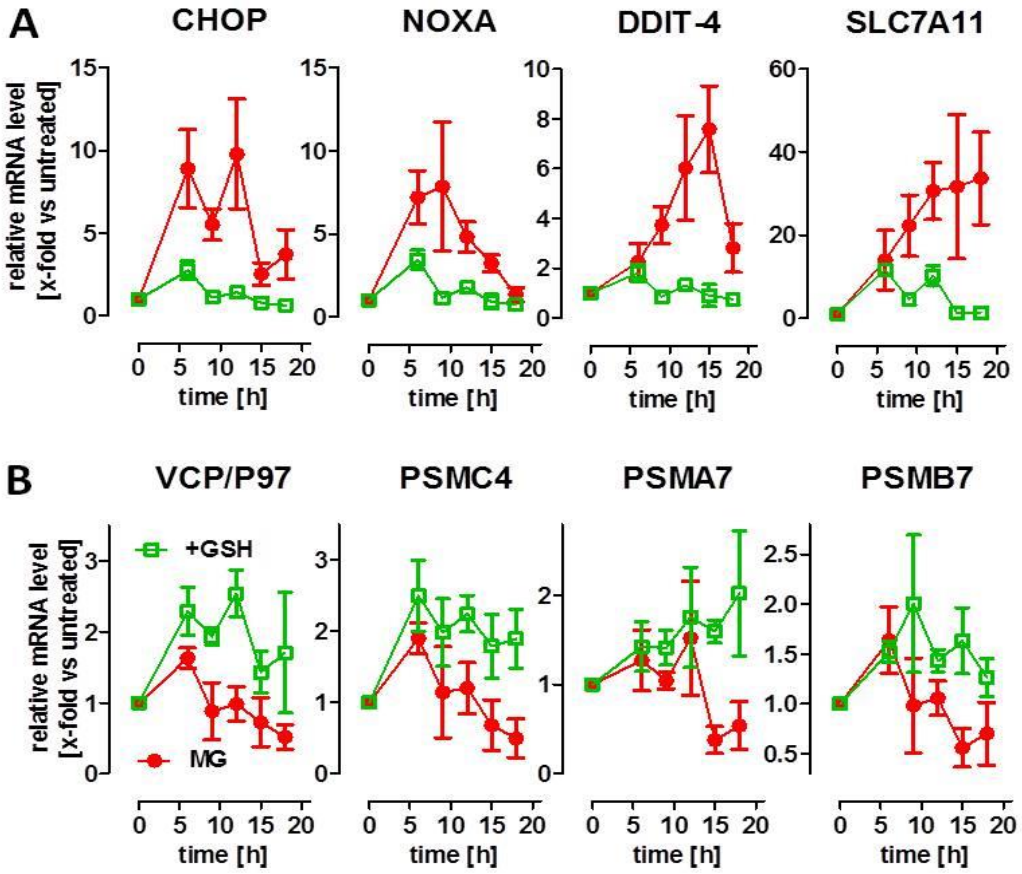

Fig. S10_3: Differences in the induction of ATF-4 and NRF-1 target genes by MG-132 in presence or absence of GSH

A: Differentiated d6 LUHMES cells were exposed to MG-132 [100 nM] for the indicated time periods in the presence or absence of GSH [1 mM]. Changes in mRNA levels were monitored by qPCR for the target genes of activating transcription factor 4 (ATF-4): cystine transporter (SLC7A11), DNA damage inducible transcript 4 (DDIT-4), Phorbol-12-Myristate-13-Acetate-Induced Protein 1 (NOXA) and DNA damage inducible transcript 3 (CHOP). **B**: Differentiated day 6 LUHMES cells were exposed to MG-132 [100 nM] for the indicated time periods in the presence or absence of GSH [1 mM]. Changes in mRNA levels were monitored by qPCR for the target genes of Nuclear Factor (Erythroid-Derived 2)-Like1(NRF1): valosin containing protein (VCP/p97), proteasome 26S subunit ATPase 4 (PSMC4), proteasome subunit alpha 7 (PSMA7) and proteasome subunit beta 7 (PSMB7). Data are means ± SEM of three independent experiments.

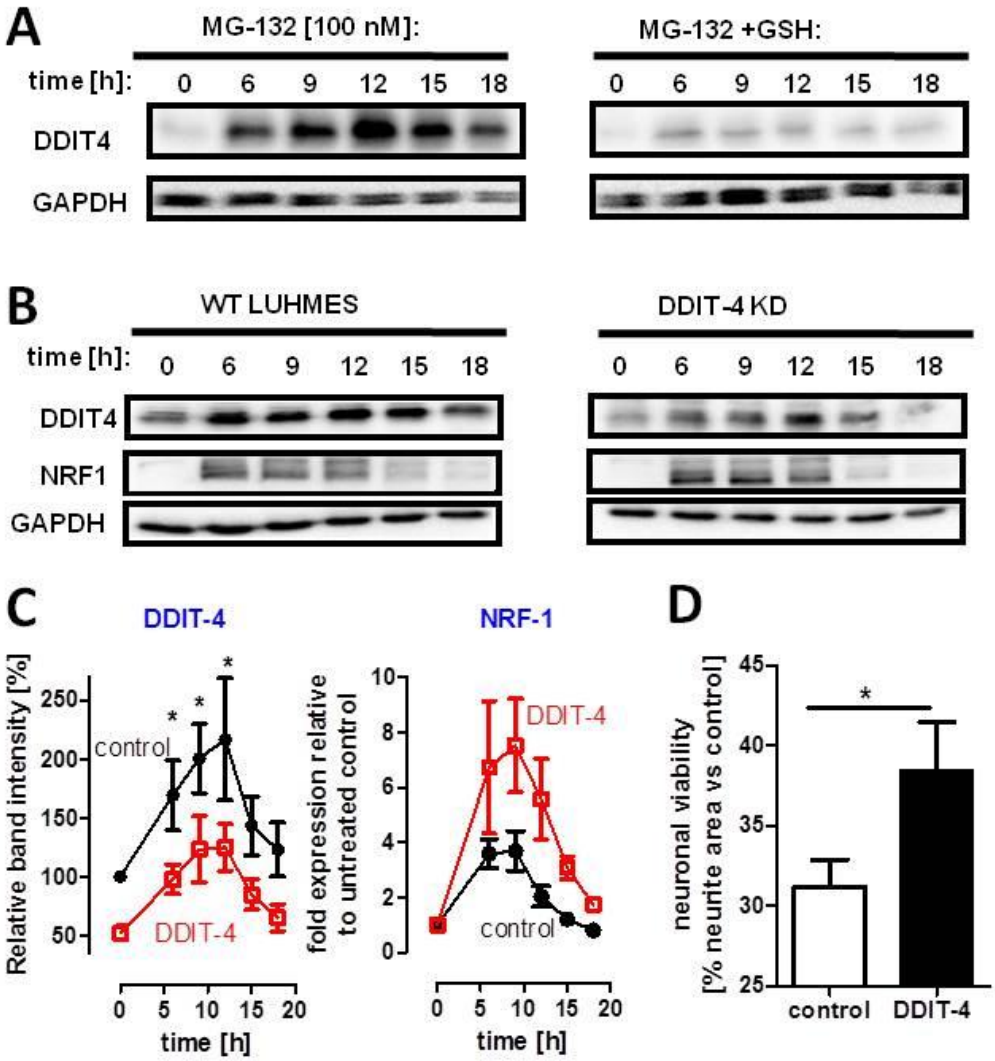

Fig. S11_3: Differences in the induction of ATF-4 target DDIT-4 by MG-132 in presence or absence of GSH

A:To address differences in the neuronal stress response following proteasome inhibition in the absence or presence of GSH [1 mM], cells were treated with MG-132 [100 nM] for the indicated time periods. After incubation, cells were lysed and analysed by Western blot using anti-DDIT4 and anti-GAPDH antibodies. **B**: LUHMES wilde type cells and DDIT4 knock down cells were incubated with MG-132 [100 nM] for indicated time periods. After incubation, cells were lysed and analszed by Western blot using anti-DDIT-4, anti-NRF-1 and anti-GAPDH antibodies. **C**: Densitometric quantification of the DDIT-4 and the NRF-1 stress response following MG-132 exposure. **D**: Differentiated (d6) LUHMES wild type and DDIT-4 knock down cells were exposed MG-132 [100 nM] for 18 h. Neurite viability was assessed by measuring the calcein positive neurite area. Data are means ± SD of three independent experiments, *: $p<0.05$

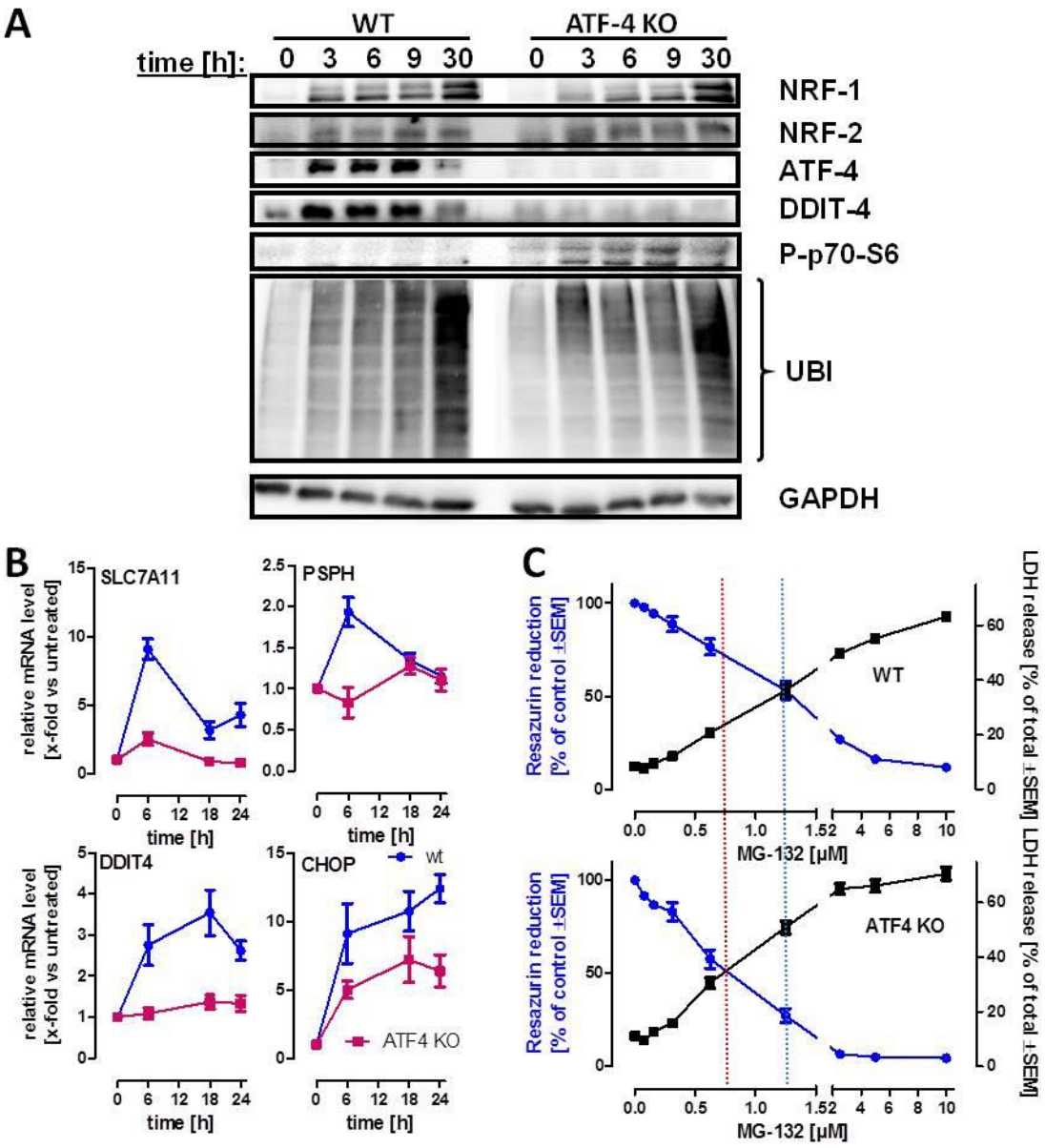

Fig.S12_3: The role of ATF-4 in the stress response to MG-132

To address the role of ATF-4 in the stress response following MG-132, we generated an ATF-4 knockout clone of HEK-293 cells using the CrispR/Cas9 system. For generation of the knockout, cells were transfected with the CREB-2 CRISPR/CAS9 KO Plasmid mix from Santa Cruz (sc-400155) and the CREB-2 HDR Plasmid (sc-400155-HDR). 24 h after transfection, cells were selected with puromycin [0.5 µg/ml] for 48 h. After selection, cells were plated by limiting dilution to obtain single cell clones. Several clones were assessed by Western blot for the absence of ATF-4 after MG-132 treatment. Three clones displaying no ATF-4 signal were further characterized. ATF-4 k.o. cells compared to wild type showed a decrease in growth rate, but looked morphologically normal. **A:** ATF-4 k.o. and wildtype cells were incubated with MG-132 [0.5 µM] for indicated time periods. After incubation, cells were lysed and analysed by Western blot using anti-ATF-4, anti-NRF-1, anti NRF-2, anti-DDIT-4, anti- phospho-p70S6, anti-ubiqitin and anti-GAPH antibodies **B:** ATF-4 k.o. and wildtype cells were incubated with MG-132 [0.5 µM] for indicated time periods. The mRNA levels for the ATF-4 target genes SLC7A11, PSPH, DDIT4 and CHOP were assessed using RT-qPCR. **C:** ATF-4 k.o. and wildtype cells were incubated for 48 h with MG-132 at the indicated concentrations. Viability was assessed by resazurin and LDH release measurement. Data are means ± SD of three independent experiments.

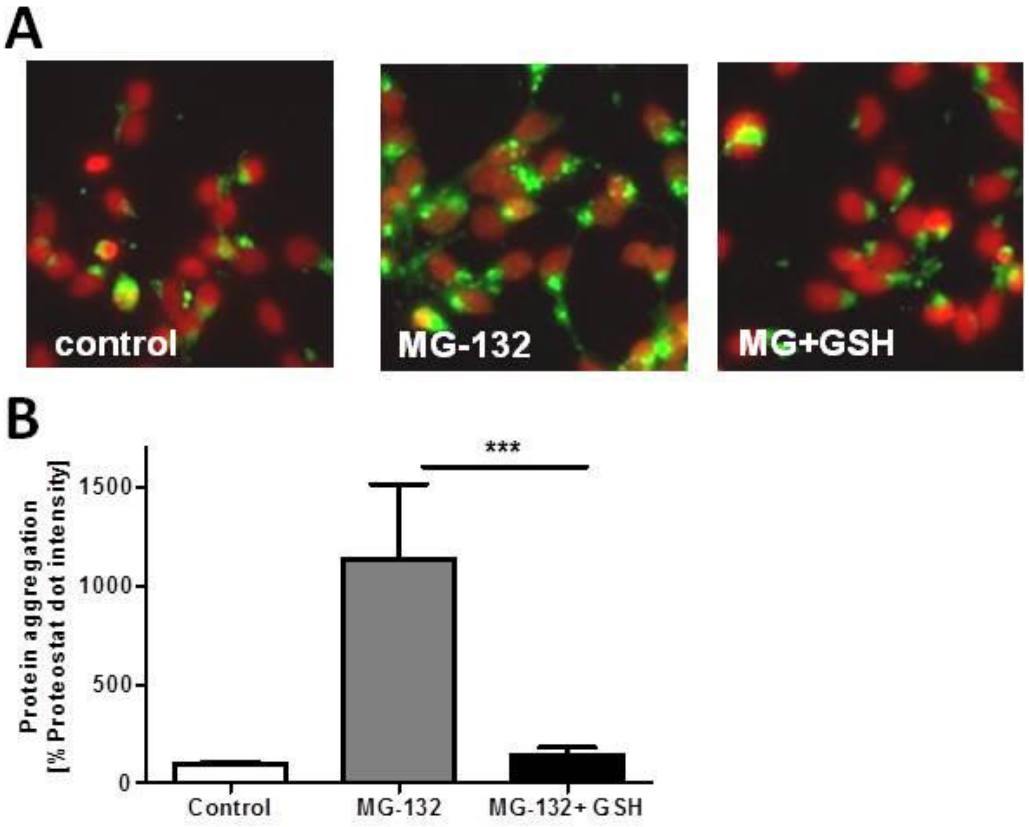

Fig. S13_3: Influence of GSH on the accumulation of protein aggregates in neurons

A: To test for proteasomal dysfunction, cells were treated with MG-132 [100 nM] for 6 h in the presence or absence of GSH [1 mM]. Then, cells were fixed with paraformaldehyde (PFA), stained with Proteostat detection reagent (Enzo, Lausen, Switzerland) based on a dye binding to β-sheet protein aggregates, and analysed by automated microscopy. Aggregates are displayed in green, DNA (nuclei) are shown in red.
B: Quantification of fluorescence intensity of the Proteostat reagent (measuring protein aggregates) in the samples described in A. Data are means + SD of three independent experiments, ***: $p<0.001$.

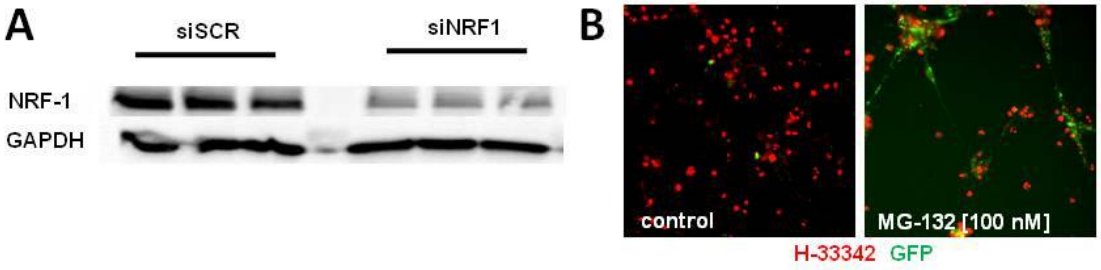

Fig. S14_3: Influence of NRF-1 abundance on survival after MG-132 exposure

A: LUHMES were transfected with siRNA against NRF-1 or scrambled siRNA at d2 of differentiation. Cells were cultured untill d6 of differentiation and then incubated with MG-132 [100 nM] for 7 h. After incubation, cells were lysed and analysed by Western blot using anti-NRF-1 and anti-GAPH antibodies **B**: LUHMES were transfected by electroporation with NRF-1 and GFP over-expression plasmids at d2 of differentiation. Cells were cultured untill d6 of differentiation and then incubated with MG-132 [100 nM]. 18 h after MG-132 exposure, cells were stained with DNA stain H-33342 and double positive cells were counted by automated microscopy.

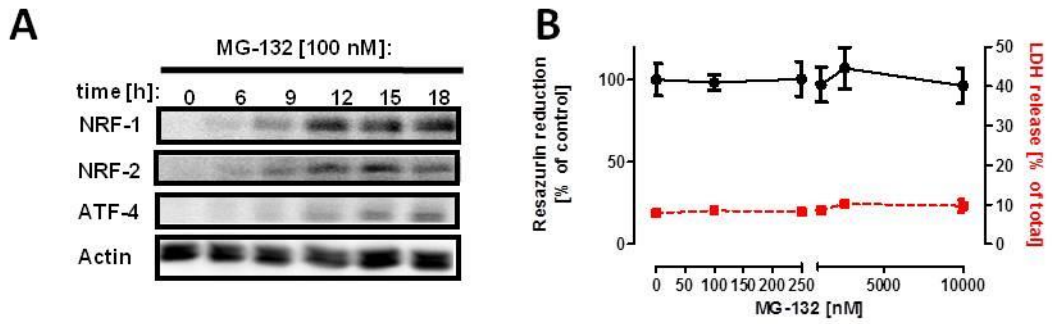

Fig. S15_3: Stress response in astrocytes triggered by MG-132

We observed in Figure 6A that the NRF-2 response was stronger in the co-culture compared to neuronal mono-cultures. This is consistent with published literature that astrocytes are the main cells in the brain showing an NRF-2 response (Vargas 2009), and in co-cultures we measured mainly astrocytic NRF-2. This was supported by the stress response observed in astrocytic mono-culture (Fig. S15A), and by resistance of astrocytes against MG-132 exposure (Fig. S15B).
A: To analyse the stress response following proteasome inhibition, cells were treated with 100 nM MG-132 for the indicated time periods. After incubation, cells were lysed and analysed by Western blot with anti-NRF1, anti-ATF4, anti-NRF-2 and anti-beta-actin antibodies. The blots shown are representative for three experiments with similar results. **B**: mAges were treated for 24 h. Viability was assessed by resazurin and LDH measurement. Data are means ± SD of three independent experiments.

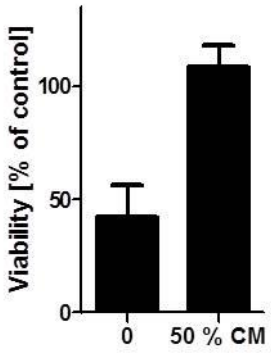

Fig. S16_3: Protection by astrocyte-conditioned medium against MPP^+

LUHMES cells (d6) were cultured in fresh LUHMES culture medium only, or in astrocyte-conditioned medium from mAG-ES, diluted with fresh LUHMES culture medium (1:1). They were exposed to MPP^+ [5 µM], and viability (resazurin reduction) was assessed 72 h after start of MPP^+ exposure. Data are means ± SD from three experiments. The difference in viability was tested by Student's t-test and it was significant at the $p < 0.01$ level.

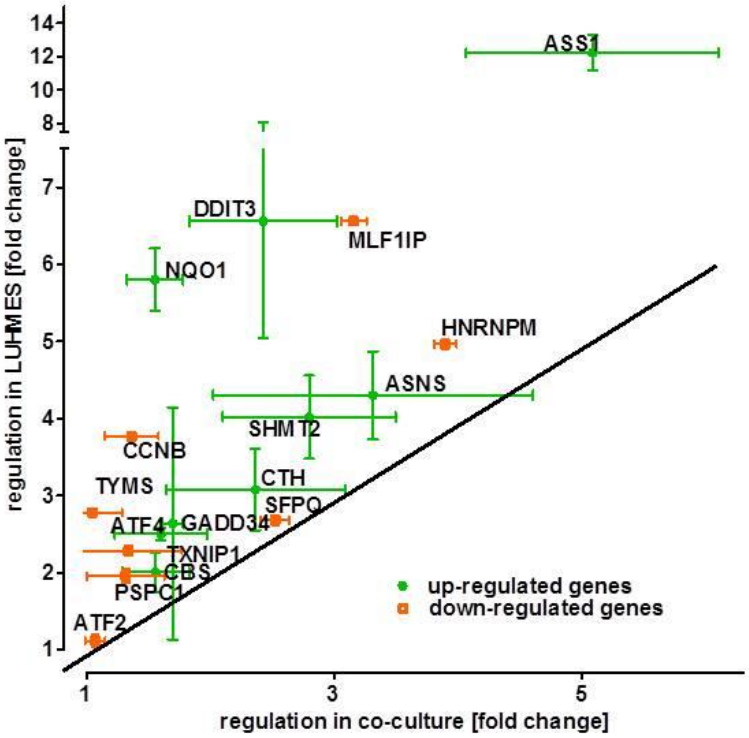

Fig. S17_3: Differential regulation of ATF-4 target genes in co- and mono-cultures following MPP$^+$ exposure

To address differences in the stress responses following MPP+ exposure of co- and mono-cultures, gene expression was monitored after 36 h exposure to MPP+ [5 µM]. Relative regulation in co-and mono-culture is displayed in a x-y-graph. Data are means ± SD of three independent experiments.

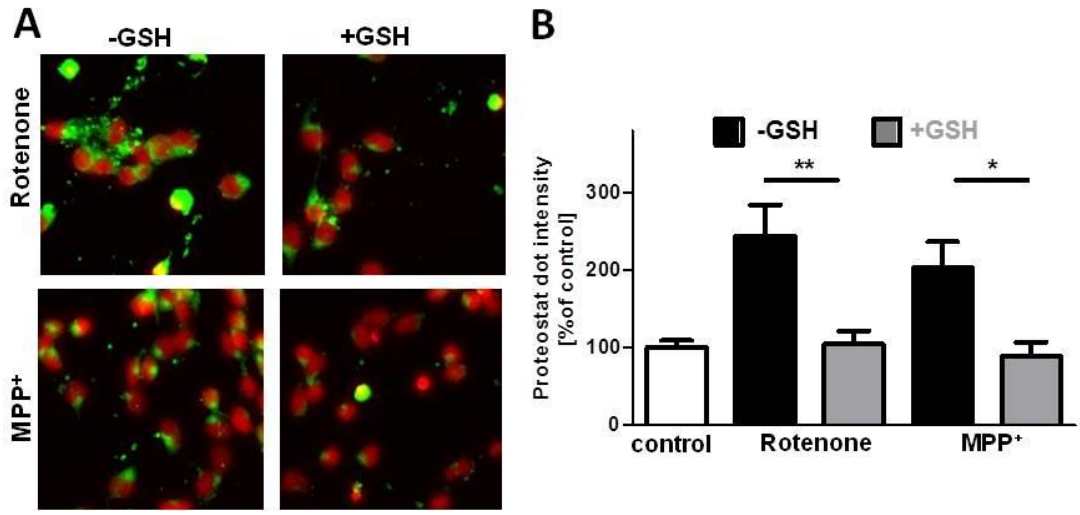

Fig. S18_3: Prevention of accumulation of protein aggregates in neurons

A: To test for proteasomal dysfunction, cells were treated with either rotenone [1 µM] or MPP$^+$ [5 µM] for 24 h in presence or absence of GSH [1 mM]. Then, cells were fixed with paraformaldehyde (PFA), stained with Proteostat detection reagent (Enzo, Lausen, Switzerland) based on a dye binding to β-sheet protein aggregates, and analysed by automated microscopy. Aggregates are displayed in green, DNA (nuclei) are shown in red. **B**: Quantification of fluorescence intensity of the Proteostat reagent (measuring protein aggregates) in the samples described in A. Data are means ± SD of three independent experiments, **: $p<0.01$; *: $p<0.05$.

Antigen	Antibody (clone; supplier; catalog number)	Dilution	Blocking (5%)	Species
ATF4 (CREB-2)	Anti-ATF4, Rabbit mAb, (D4B8), Cell Signaling, (11815)	1:1000	BSA	rabbit
β- III-Tubulin	Mono β-Tubulin (TUJ1) purified, Covance (MMS-435P-250)	1:500	FCS	mouse
Cleaved Caspase 3	Cleaved Caspase- 3, Rabbit mAb, (5A1E), Cell Signaling (9664)	1:500	BSA	rabbit
DDIT4	REDD1 Polyclonal Antibody, Proteintech, (10638-1-AP)	1:1000	BSA	rabbit
Fodrin	α-Fodrin, mAb (AA6), Enzo Life Sciences (BML-FG60909	1:1000	BSA	mouse
GADD34	Anti-GADD34 (proteintech)	1:1000	BSA	mouse
GFAP	Monoclonal Anti-glial fibrillary acidic protein, Clone G-A-5, Sigma (G3893)	1:800	FCS	mouse
GAPDH	Anti-GAPDH (Sigma; Clone GAPDH-71.1)	1:5000	BSA	mouse
NOXA	NOXA Antibody, Mouse mAb (114C307.1), Novus, (NB600-1159)	1:1000	BSA	mouse
NRF1	TCF11/NRF1, Rabbit mAb, (D5B10), Cell Signaling (8052)	1:1000	BSA	rabbit
NRF2	NRF2, Rabbit mAb, (D1Z9C), Cell Signaling (12721)	1:1000	BSA	rabbit
PARP	PARP antibody, Cell Signaling (9542)	1:1000	BSA	rabbit
P-p70S6	Phospho-p70 S6 Kinase (Thr389), Cell Signaling (9205)	1:1000	BSA	rabbit
P-p38	Phospho-p38 MAPK (Thr180/182) antibody, Cell Signaling, (9211)	1:1000	BSA	rabbit
Ubiquitin	Ubiquitin, Mouse mAb, (P4D1), Cell Signaling (3936)	1:1000	BSA	mouse
anti-mouse (WB)	anti-mouse HRP antibody (Jackson Immuno Research)	1:2500	BSA	goat
anti-rabbit (WB)	anti-rabbit HRP antibody (GE Healthcare)	1:5000	BSA	goat
anti-mouse (ICC)	Alexa 488, IgG1 (γ1), goat anti mouse, Invitrogen, A21121	1:1000	FCS	goat
anti-mouse (ICC)	Alexa 555, IgG2a (γ2a), goat anti mouse, Invitrogen, A21137	1:1000	FCS	goat

Fig. S19_3: Antibodies used for Western blot or imunocytochemistry

Name	Forward sequence	Reverse Sequence
ASNS	GGGGCTTGGACTCCAGCTTG	GAGCCTGAATGCCTTCCTCA
ASS1	TGCTCCCTGGAGGATGCCTG	GTGTAGAGACCTGGAGGCGC
ATF2	AGAGCGAAATAGAGCAGCAG	CATGGCGGTTACAGGGCAAT
ATF4	GGCTGGCTGTGGATGGGTTG	CTCCTGGACTAGGGGGGCAA
CBS	TCCTGGGAATGGTGACGCTT	GTGCTGTGGTACTGGATCTG
CCNB	TGGATGTGCCCCTGCAGAAG	CAGTGACTTCCCGACCCAGT
CTH	TGGATGATGTGTATGGAGGTACAAACAGG	GCCTTCAATGTCAATCACCTTCTGGG
DDIT3/CHOP	ATGGCAGCTGAGTCATTGCC	TCCTCAGTCAGCCAAGCCAG
DDIT4	AGTCCCTGGACAGCAGCAAC	AACTGGCTAGGCATCAGCAG
GADD34	GCATCACCCAGGCCCAGGAG	AGACGAGCGGGAAGGTGTGG
GAPDH	CACCATCTTCCAGGAGCGAGATC	GCAGGAGGCATTGCTGATGATC
HNRNPM	TGGTGTGGTGGTCCGAGCAG	GGACGCTCAGGAGGGAAGAA
MLF1IP	TTTGTAAGGCAGCCATCGCC	CTGTGGCTCTAACCGAAGCA
NOXA	CAGTGCCAACTCAGCACATTG	CGCCCAACAGGAACACATTGA
NQO1	TGGAGTCGGACCTCTATGCCA	CTTGTGATATTCCAGTTCCCCCTGC
PSMA7	GCC GTC AAG AAG GGC TCG AC	CCA CCC GGG CCC TGT TGA TG
PSMB7	TCT CCA CTG GCC GTC TTC CC	AGC CAT TGC TGC CAA GGA GC
PSMC4	CAT CCC GCT GGT CAT CGG AC	ATG ATG CTG CTG TCG GCT TC
PSPC1	CAGCAGCGTGAGCAGGTTGA	CGCCGATGCTCCTCTTCATG
PSPH	CCC CGG CAT AAG GGA GCT GG	GCT GTT GGC TGC GTC TCA TC
SFPQ	TCAGGCAAATCTTTTGCGCC	CTCTCTTTGGCGCCTCATTT
SHMT2	CAACCTGGCACTGACTGCTC	GATGTCCGCGTGCTTGAAAG
SLC7A11	GCA GCG TGG GCA TGT CTC TG	CAC AGC AGT AGC TGC AGG GC
TXNIP1	CATGGCGTGGCAAGAGCCTT	CTCAGAGCTGGTTCGGCTGG
TYMS	CAGCTTCAGCGAGAACCCAG	ACCTCGGCATCCAGCCCAAC
VCP/P97	ATC AGC ATC CAG CCA TGC CC	CAC AGC ACG CAT CCC ACC AC

Fig. S20_3: Primers used for RT-qPCR

4 Discussion:

The reasons driving the development of *in vitro* cell-based methods in neurotoxicology are manifold (22) and the number of cellular platforms and methods are rapidly increasing. In order to ensure the relevance of such new models the characterization of the cellular platforms used is essential. Until now, only few is known about the factors influencing the sensitivity of cell lines to certain toxicants.

Each of the three manuscripts included in this thesis addresses a different aspect that may influence toxicant sensitivity of neurons derived from the LUHMES cell line (summarized in scheme 3). By monitoring the metabolic changes occurring during differentiation and deducting special metabolic requirements of the different differentiation stages, the observed changes in toxicant sensitivity between proliferating neuronal precursors and mature neurons could be correlated with the alterations in the metabolism of the cell (manuscript #1).

The second manuscript focused on the impact on genetic alterations and the importance of cell line quality control. It was shown, that few passages of unintended selection in a different environment can have substantial impact on the cellular phenotype (e.g loss of the dopaminergic phenotype after differentiation), and that these changes in the phenotype hold responsible for a shift in the toxicant sensitivity of the cells. The differences in the regulation of the dopamine transporter between the two analysed subclones were correlated with the differential toxicity of the neurotoxicant MPP^+, which is a substrate of this transporter (170).

In the third manuscript, the increased resilience of neurons in the presence of astrocytes was in the focus. The presence of astrocytes provided protection against the PD model toxicant MPP^+ and the proteasome inhibitor MG-132. By linking the observation of increased neuronal GSH in the presence of astrocytes to changes in the stress response of neurons, the influence of astrocytes became apparent and modulation of the astrocytic support was identified as potential target for pharmacological intervention.

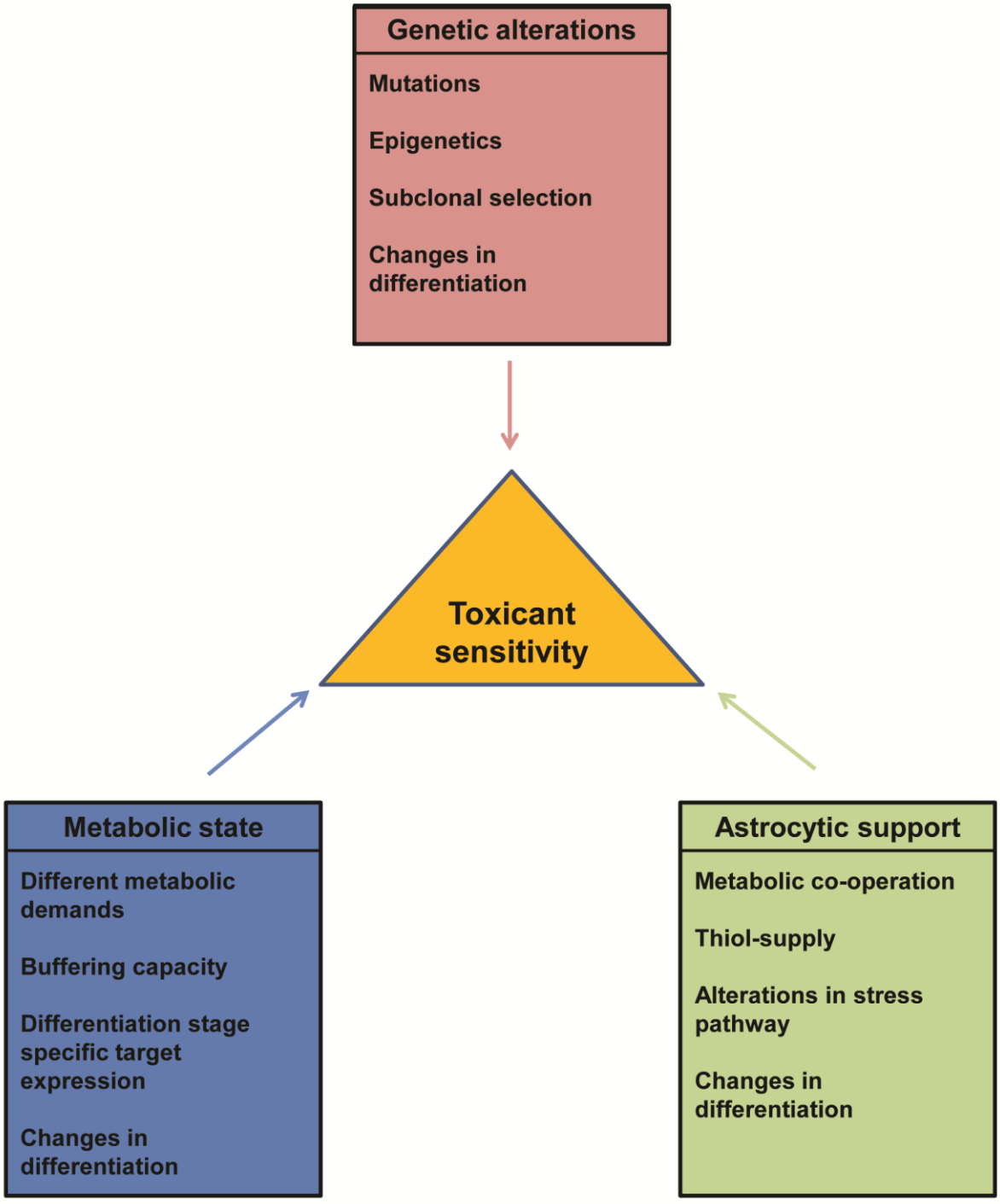

Scheme 3: Factors affecting toxicant sensitivity of LUHMES cells addressed in this study
Boxes represent the three different parts of the thesis (blue: part 1, red: part 2, green: part 3). In each box factors that were identified to contribute to an alterted toxicant sensitivity are summarized.

4.1 Influence of cellular metabolic state on toxicant sensitivity

LUHMES cells are used for screening assays to identify potential neurotoxicants and developmental neurotoxicants (49, 56, 58). This cell line is cultured in a proliferative state and upon addition of tetracycline the v-myc transgene is switched off and cells differentiate. Existing studies used diverse stages of this cells to identify developmental neurotoxicants, neurotoxicants or to monitor cellular stress responses induced by already known neurotoxicants (34, 35, 49, 56, 58, 63, 70). The first manuscript of this thesis focused on the metabolic characterization of the proliferating state and the "mature" state of this cells. Using pulsed stable isotope-resolved metabolomics (pSIRM) to determine intracellular metabolite pool sizes, and isotopically non-stationary ^{13}C-metabolic flux analysis (INST ^{13}C-MFA) to calculate metabolic fluxes, differences in the two stages of LUHMES were characterized. The factors influencing toxicant sensitivity are summarized in scheme 4.

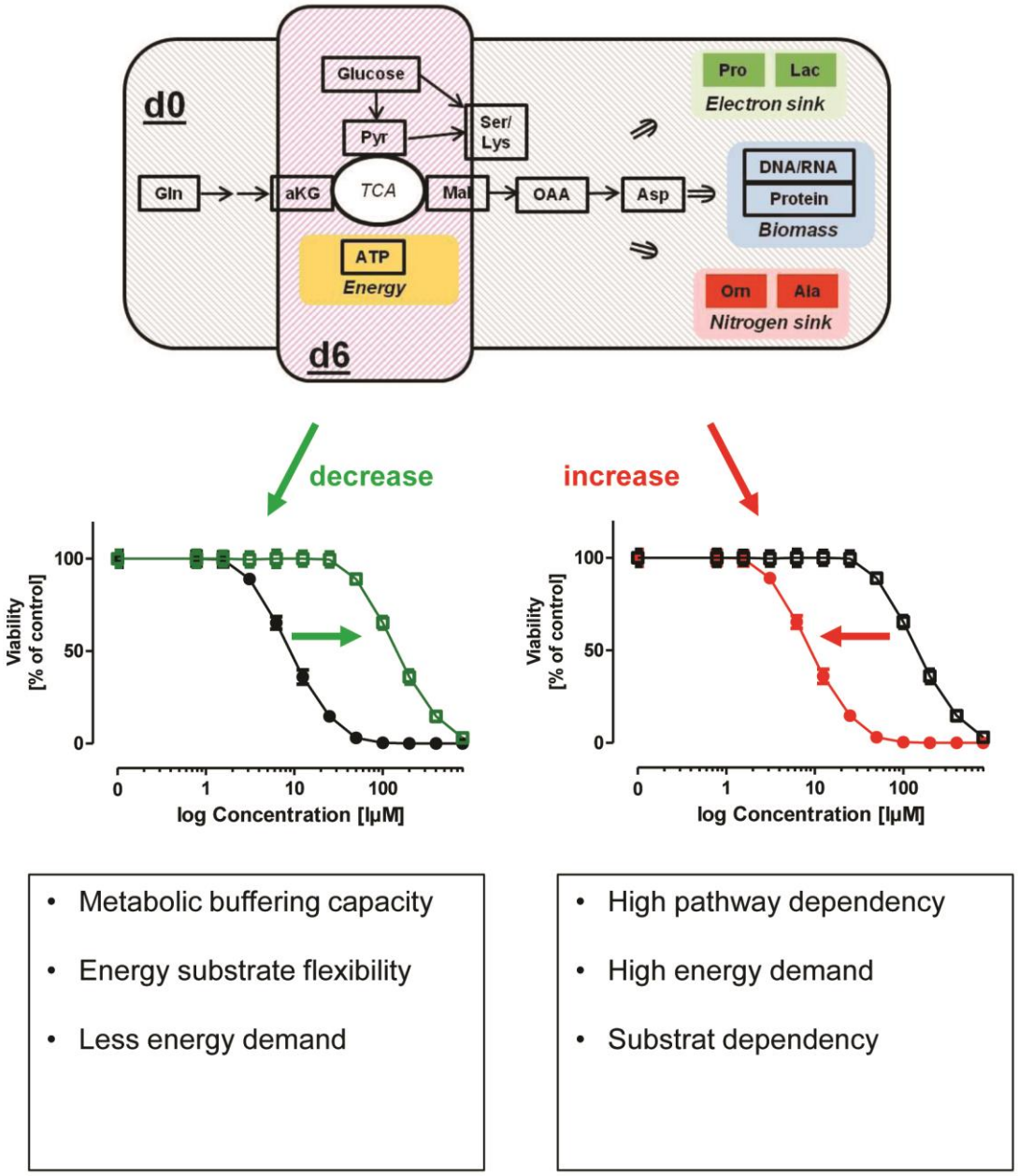

Scheme 4: Metabolic factors influencing toxicant sensitivity. Upper part of the scheme is part of the publication #1 and represents the changes in metabolic pathways used by the cells in the different differentiation stages.The scheme summarizes properties changing through metabolic alterations, which decrease (buffering, flexibility, less demand) or increase (dependency, higher demand) toxicant sensitivity of the LUHMES cells.

4.1.1 Different metabolic needs of proliferating cells and postmitotic neurons

Upon start of differentiation, neurons exit the cell cycle and thereby stop the proliferation. The differentiation process has been reported to go hand in hand with strong changes in the metabolic phenotype (67, 155). Dividing cells need more glucose and are characterized by an increased glycolytic rate, which is essential for the genera-

tion of ATP (156, 157). Furthermore, since they need to generate distinct metabolites for cellular growth, they exhibit a higher glutamine dependency (158, 159) and sustain oxidative phosphorylation for ATP production (157). “Adult” neurons in the brain have different metabolic needs: due to their signaling activity they have to continuously maintain and restore their membrane potential, which results in a higher basal energy demand. However, they do not have to produce building blocks needed for cell division. To cover their metabolic demands, neurons use oxidative phosphorylation to metabolize glucose to CO_2 via the tricarboxylic acid cycle (TCA) (194). Their capability to utilize alternative carbon sources such as glutamate and glutamine is limited to few special situations (195).

Interestingly, cancer cells and other proliferating cells are metabolically similar to the proliferating neuronal precursors used in this study, most likely due to their proliferating phenotype and the resulting requirements (198, 201, 202). This reports are in line with our observation that proliferative LUHMES are at their glycolytic and respiratory maximum and that they are highly glutamine dependent. One reason for d0 LUHMES to use glutamine in the TCA can be the demand of aspartate also described for cancer cells (156). Aspartate can be limiting for purine and pyrimidine synthesis (158, 243), and essential for maintenance of mitochondrial membrane potential and integrity (244).

A recent study suggests that changes in glycolysis and in the glutamine-glutamate use are essential for the process of neuronal differentiation (67). Differentiated d6 LUHMES cells maintain a high non-growth related metabolic activity, even though they do not have the same requirements as their proliferating precursors. The results from the fluxomics study suggest an increase in mitochondrial metabolism in d6 compared to d0 cells since an enhanced mitochondrial respiration was measured. Interestingly, d6 cells displayed respiratory as well as glycolitic spare capacity, which was not detected in the proliferating cells.

4.1.2 Changes in toxicant sensitivity

The understanding and characterization of the observed changes in metabolic phenotype is essential for the explanation of the changes in toxicant sensitivity. Since d0 LUHMES cells did not have metabolic reserves, such as mitochondrial and glycolytic spare capacity, they were found to have a higher sensitivity to UK5099, rotenone and

antimycin A compared to differentiated d6 neurons. D6 LUHMES were able to compensate toxicant induced mitochondrial deficits by an increase in glycolysis, which resulted in a decrease in sensitivity towards this toxicants. Interestingly, differentiated cells (d6) were found to be more sensitive for the glycolytic inhibitor 3-bromopyruvate, which suggests a higher sensitivity for differentiated d6 cells to a complete block of energy production. This indicates that the proliferating cells are not in general more sensitive compared to differentiated cells. For instance, a different study reported increased sensitivity of d6 LUHMES towards colchicine, vincristine and methylmercury (206). Moreover, our study did not include activity-dependent energy demand of mature neurons, which is increased, when neurons are integrated in an active neuronal network(170).

Stage specific toxicity has been described for some other examples, e.g. exposure to the cell cycle toxicant methylazoxymethylacetat (MAM) (39). However, given its importance in judgment of toxicological data and especially in regards to developmental neurotoxicity, further studies exploring stage specific toxicity and identifying underlying cellular differences are of great importance.

4.2 Genomic factors changing toxicant sensitivity

Genetic background of the human population is divers and there are well established examples of genetic differences (i.e. different CYP isoforms) that alter pharmacological or toxicological response of the whole organism (352, 353). On the cellular level it has also been shown in multiple cases that the expression level or the functionality of certain genes can affect cell survival (354). Therefore, considering population variation is one important part when developing a toxicological test system based on a cellular system. However, there are genetic alterations that are not founded necessarily in the donor and which might not be apparent directly, but become important during prolonged in vitro culturing (355). Graphical summary of the findings of this part of the study are depicted in scheme 5.

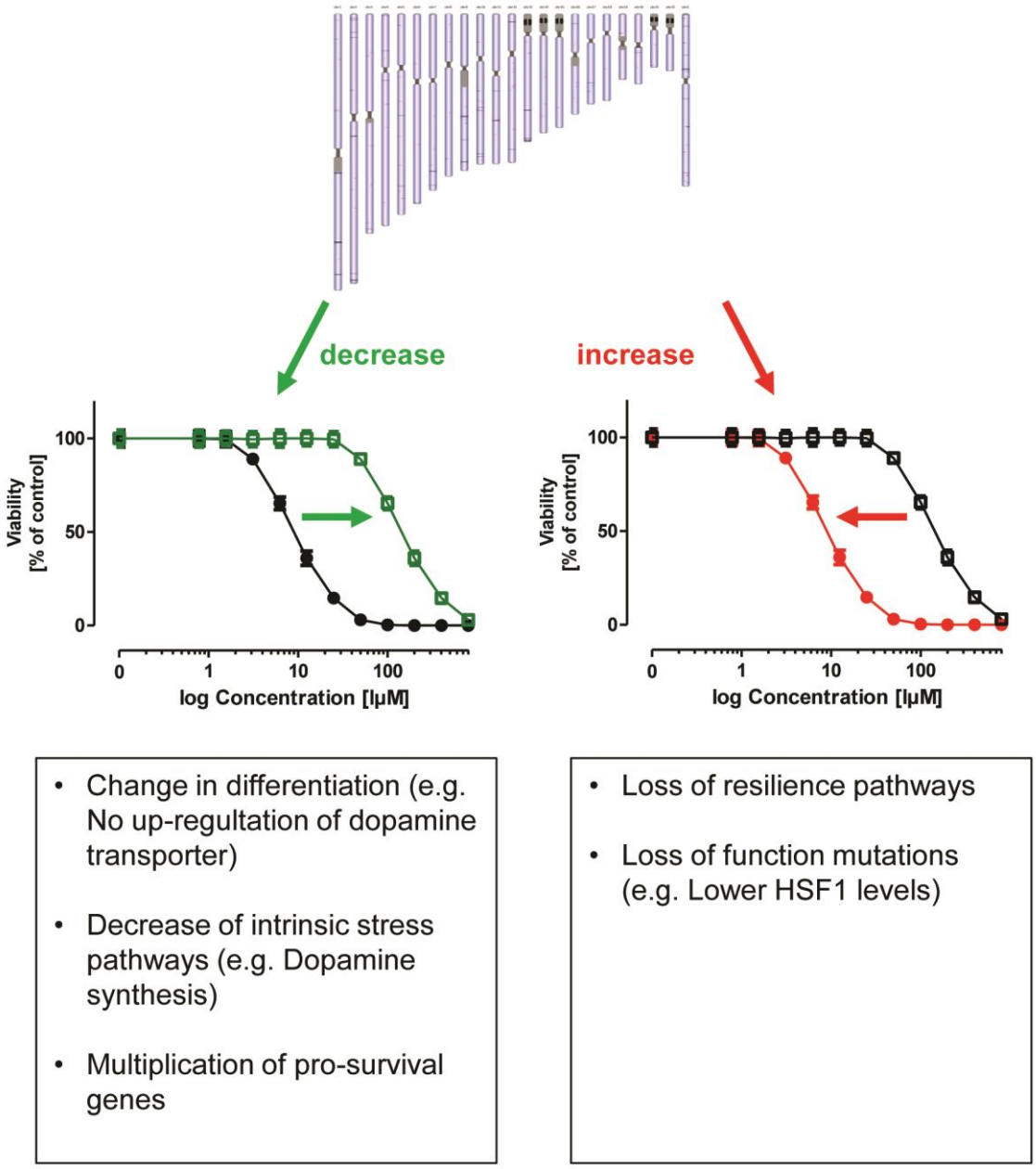

Scheme 5: Changes in toxicant sensitivity induced by genetic drift or changes in epigenetics Upper part of the scheme is part of the manuscript #2 and symbolizes genomic alterations in subclones. Scheme summarizes properties changing through genetiic alterations, which decrease (differentiation, pro-survival genes) or increase (loss of resilience pathways, loss of function) toxicant sensitivity of the LUHMES cells.

4.2.1 Genetic heterogeneity within a cell line

A lot of tumour cell-lines, such as HeLa cells, are, due to multiplication or loss of large parts or even complete chromosomes, aneuploid. This changes in genome integrity results often in alterations in cell cycle and DNA repair pathways (151). However, the karyotypes of various HeLa strains are similar, indicating that the hypertriploid state arose during tumorgenisis or early establishment of the cell line (356).

Similar observations have been reported for the neuroblastoma cell line SHSY-5Y, often used in neurodegenerative disease and neurotoxicological models. Within the genome of this cells, Mycn amplification, gain of 17q and deletion of 1p36 were detected (152, 153). The strong variation of this cell-lines in chromosomal copy number from the reference genome strongly affect their genetic stability and variation between laboratories. Furthermore, it limits the relevance and applicability of this cells as models for neurotoxicity and neurodegeneration. Cell material with less deviation from the reference genome (e.g. intact set of chromosomes) is therefore highly desirable. LUHMES cells have an intact set of chromosomes and the number of smaller genetic differences to the reference genome was in the range of what was detected for induced pluripotent stem cells (iPSCs) (269). However, there are several studies pointing to a number of pitfalls also applying for more stable cells such as LUHMES or stem cells. It was discovered that with increasing numbers of passages stem cells start accumulating SNVs in coding regions due to subclonal selection (154). Moreover, prolonged culturing of stem cells may also lead to aneuploidy in stemness or anti-apoptotic genes (e.g. trisomy 12 or X and amplification 17q). A further factor influencing the genetic background of the cells might be genetic mosaicism in the starting material followed by selection pressure in the cell-culture conditions (357).

To adequately control for cell line identity and stability SNP profiling has been suggested, since it provides more information about the cell identity than STR profiling (268). Another way to especially address genome imbalances is comparative genomic hybridization, which is recently also available in an array format (358). This technique allows to screen genome wide for variations in copy numbers, which would indicate losses or gains of parts of chromosomes (358). Whether this is sufficient to ensure identity, is doubtful and therefore was addressed in the scope of this study. Here evidence is provided that whole genome sequencing can be used to compare subclones. Some of the identified amino acid changing events had a direct influence on protein level, but did not correlate directly with changes in toxicant sensitivity observed between the two subclones. However, some of the phenotypic differences observed for the two subclones did not correlatesimply with changes in the genome. In general, there are multiple ways how the phenotype of a subclone might be altered: (i) direct mutation of a gene (e.g.multiplication, loss, amino acid changing event); (ii) mutations in a gene involved in a signaling cascade important for the regulation of a second gene; (iii) mutation in non-coding parts of a gene resulting in al-

tered expression (e.g. promoter regions; TF binding sites) or alternative splicing (e.g. loss of a splicing site). (i) and (ii) are in theory relatively easy to predict from whole genome data and to test by qPCR or on protein levels. However, the latter is more difficult to decipher and to validate by other methods. Beside genetic alterations, one should also be aware that epigenetic differences might also dramatically influence phenotypic appearance of the cells. Difference in the epigenetic profile of subclones might also result in changes in gene expression and alterations in the phenotype. Especially in a system like the LUHMES cells, this might be an important consideration, as those modifications could be phenotypically silent in the proliferating state but become apparent during the course of differentiation.

In the example chosen in this study, we observed significant differences between the two subclones in the regulation of the dopamine transporter, tyrosine hydroxylase and the GDNF receptor during differentiation. Strikingly, none of the respective genes was affected directly. The analysis of the genome did not provide a hypothesis for this change in regulation. Therefore, it can be speculated whether a not identified transcription factor is affected or epigenetic profile of this cells is altered. These findings underline the importance of basic phenotypic characterization of a cellular model system prior to using it as a testing platform. To reduce reproducibility issues, at least every newly generated working stock should be intensively compared to the prior one and in regards to cell line transfer to and from a cell bank this characterization is also inevitable. This comparison should comprise basic features described for the corresponding cell line and phenotypical properties of special importance for the used *in vitro* model (e.g. dopaminergic phenotype). However, the phenotypic characterization can only address certain aspects of a cell line, since this is cost and time intensive and limited to the comparison of already available data and standards.

4.2.2 Genomic alterations affecting toxicant sensitivity

Mutations affecting expression or functionality of genes associated with pro- or anti-apoptotic pathways are obvious candidates that can affect toxicant sensitivity of cells directly. Mutations in these genes leading to changes in gene expression or functionality can result in altered responses to a vareiety of toxicants and might not be specific for the reaction to a single toxicant. For example, expression of dominant negative TP53 has been reported to alter stress response of hematopoietic cells to inhibitors

of mTORC1, BCL2/BCLXL, MEK1 and the proteasome inhibitor MG-132 (359). Other factors affecting cellular resilience to toxicant exposure are involved in stress response pathways such as the heatshock response, the antioxidant response or the unfolded protein response (UPR) (82). Genetic changes leading to differences in such pathways might also result in a change in toxicant sensitivity (360).

Further factors concerning *in vitro* cellular models are changes in differentiation of the cells. Genetic differences affecting the differentiation process within a model system might lead to strong alterations in the sensitivity to specific toxicants. Here in this study, the changes in dopamine transporter abundance in one subclone resulted in a different sensitivity to the parkinsonian toxicant MPP^+. MPP^+ is a substrate of this transporter (170) and the diminished uptake in the subclone expressing low levels of dopamine transporter expression resulted in an increased survival of the cells.

Furthermore, the results of this study highlight a second important aspect. Both LUHMES subclones were observed to have low levels of dopamine, even though they display a dopaminergic phenotype. Analysis of the identified genetic differences to the reference genome revealed that one subclone accumulated mutations in non-coding regions of enzymes associated with the BH4-pathway (tetrahydrobipterin is an important co-factor in dopamine synthesis), while the other displayed a decrease in expression of genes relevant for the dopamine synthesis. This might be two mechanisms how these cells keep their dopamine production at a minimum to reduce basic cellular stress. Dopamine is also a good example for a factor that might alter toxicant sensitivity. Specific toxicants triggering the release or inhibiting the re-uptake of Dopamine are highly specific for dopaminergic neurons (34, 361, 362). The observation of such unintended modifications, that occurre after few passages of subculturing, indicates that the down-regulation or existing genetic alterations within the cell line are highly favored by selection.

4.3 From neurotoxicology to neurodegeneration

A lot of the identified neurotoxicants are, due to the special characteristics of the brain, cell-subtype specific toxicants. This means they are selectively destroying one neuronal subtype, without affecting the neighboring cells. Since for some of this toxicant the same subpopulation is affected as in a neurodegenerative disease, the loss

of this subtype of neurons leads to strikingly similar phenotypic properties as they are observed in the corresponding diseases. For instance, dopaminergic neurons are found to be selectively sensitive to inhibitors of complex I of the mitochondrial respiratory chain (287). The toxicants MPP^+ and rotenone, both inhibitors of complex I, induce selective loss of dopaminergic neurons *in vivo.* The loss of this neurons is also the main hallmark of PD and due to the loss of dopaminergic neurons following MPP^+ or rotenone exposure the toxicants reflecting well the disease phenotype. Therefore, they are widely used as model-toxicants to study underlying mechanisms and potential therapies *in vivo* as well as *in vitro*.

Moreover, the connection between complex I inhibiting substances and development of PD was also proposed by multiple epidemiological studies and a recent toxicological concept of AOPs (adverse outcome pathways) aimed to provide a framework for this connection (287). The concept of AOPs proposed that a molecular initiating event (in this case inhibitor binding to complex I), followed by a chain of key events (such as inhibition of complex I; mitochondrial dysfunction, impaired proteostasis and degeneration of dopaminergic neurons) leads to an adverse outcome (like Parkinsonian motor deficits) (287). Interestingly, this concept directly connects mitochondrial dysfunction with disturbances in proteostasis. In line with this, multiple studies reported reduced proteasome activity, protein accumulation and aggregate formation as hallmarks of PD (363-366).

4.4 Proteasome inhibitor as model toxicant of neurodegeneration in PD

4.4.1 Proteasome and proteasomal dysfunction- relevance to PD

The ubiquitin-proteasome-system (UPS) is the main cellular pathway of protein-degradation and recycling (367). In order to target proteins for the degradation by this pathway they have to be marked by a polyubiquitin chain. This process requires several enzymatic energy dependent steps (E1 enzyme activating ubiquitin, transfer to the ubiquitin conjugating E2 enzyme and ligation to the target protein by E3 ligase) (368). Ubiquitinated proteins are afterwards recognized and degraded by the 26S proteasome, which consists of a 20S core unit and a 19S regulatory particle, which unfolds the substrate and strips off the ubiquitin chain (310). Within the core particle

the proteins are then digested into small peptides by mainly three enzymatic reactions: chymotyrpsin-like, trypsin-like and caspase like protease activities (368). The 20S proteasome exists also as standalone system, where it mediates energy and ubiquitin independent degradation of partially missfolded proteins (310).

In PD the loss of neurons is paralleled with the formation of protein aggregates (Lewy bodies; LBs) within the residual neurons (369). These LBs contain proteins such as ubiquitin, proteasomal subunits and α-synuclein. Furthermore, alterations in the proteasome activity in the brain of PD patients have been detected (365, 370) and negative effects of dopamine, neuromelanin were shown to decrease proteasomal function (371, 372). Additionally, mutations in the E3 ligase Parkin are known to be the cause of familial forms of PD. These mutations have been linked to disturbances in cell signaling, mitochondrial function and protein degradation (373). All the observations mentioned above inspired the use of proteasome inhibitors to model this hallmark of PD.

4.4.2 Proteasome inhibitors and PD symptoms

Vice versa the observations obtained by administration of proteasome inhibitors reflected PD aspects to a far extent. In rodent models stereotaxic infusion of lactacystin or MG-132 into different regions of the brain, resulted in a loss of dopaminergic neurons and leads to the development of motor dysfunction with region specific differences (310, 374, 375). Another model that attracted a lot of interest, was the systemic administration of the proteasome inhibitor PSI. This model reproduces a slow degeneration phenotype, including major pathological hallmarks (310, 364, 365). However, due to reproducibility issues this model is currently still under debate (310).

In *in vitro* models using dopaminergic cell lines or primary cells, proteasome inhibitors such as MG-132 were found to induce selectively the loss of TH-positive cells (375), formation of intracellular LB-like aggregates (376) and mitochondrial dysfunction (377). All this highlights the value of proteasome inhibitors as toxicant models of PD and supports further effort in investigations in underlying mechanisms.

4.4.3 Stress responsens following proteasome inhibition in neurons

In this study we identified ATF-4 and NRF-1 as major stress responses following proteasomal inhibition in LUHMES cells. NRF-1 has been recently identified as regulator of proteasome *de-novo* synthesis following proteasome inhibition and as regulator of the homeostatic balance of the proteasome (314, 316, 325). In line with this, we observed strong up-regulation of NRF-1 after the proteasome was inhibited, and the modulation of the NRF-1 response in LUHMES had strong impact on cell survival. Moreover, increased NRF-1 levels over a prolonged time mediated the recovery of the proteasome activity in MG-132 treated cells. It has been suggested that NRF-1 is controlled via an mTORC1 (314) dependent mechanism, which regulates protein synthesis and protein degradation (via NRF-1 –proteasome- axis) in parallel. ATF-4 has been reported to trigger the expression of DDIT-4 (378), which has been suggested to inhibit mTORC dependent phosphorylation of S6K1(379). The mTORC-S6K1 signaling pathway might therefore be a potential connection point of the ATF-4 and the NRF-1 response. Interestingly, knockdown of the DDIT-4 in our study resulted in higher NRF-1 levels and increased survival following proteasome inhibition with MG-132. However, knock out of ATF-4 in HEK293 cells rather increased the sensitivity of the cells to the proteasome inhibitor.This indicates multiple functions of ATF-4 and points to a rather beneficial than deleterious role in the overall stress response. This is in line with our previous finding, suggesting ATF-4 as an early adaptive stress response that follows complex I inhibition in neurons (49). In this study the knockdown of ATF-4 in LUHMES induced a loss of GSH in neurons that were treated with the mitochondrial toxicant MPP^+(49). In line with this, the transcriptional targets of ATF-4 are genes involved in the transulfuration pathway and in cystine uptake (49). This indicates that the cells suffer from thiol limitation after treatment with different stressors. In context of proteasomal inhibition, others already connected cysteine limitation with the induction of ATF-4 (317) and pointed to thiol supplementation as a potential way of stress response modulation. Together with the observations of this study, one can suggest the following potential interplay of the TFs NRF-1 and ATF-4 in neurons: (i) proteasome inhibition leads to decrease in protein degradation and NRF-1 induction; (ii) Thiol shortage induces the expression of ATF-4 and increased thiol uptake; (iii) if enough thiols are present NRF-1 is further induced and proteasomal function it recovered, otherwise ATF-4 response proceeds and inhibits further NRF-1 induction.

Thiol availability might therefore be a critical factor of neuronal survival in different stress conditions (330).

4.5 Astrocytes affecting neuronal toxicant sensitivity

Astrocytes, the main glial cell type in the brain, have been shown to play important roles in homeostasis and functionality of the brain. They are coupled with neurons metabolically, by co-operating in the supply of energy metabolites and neurotransmitter recycling (319). Moreover, alterations in astrocytic functionality have been associated with the demise of neurons in neurodegenerative diseases (319). Therefore, co-cultures of astrocytes and neurons including some of this aspects, are an interesting tool to study the influence on toxicant sensitivity of neurons. Possible influences identified here are summarized in scheme 6.

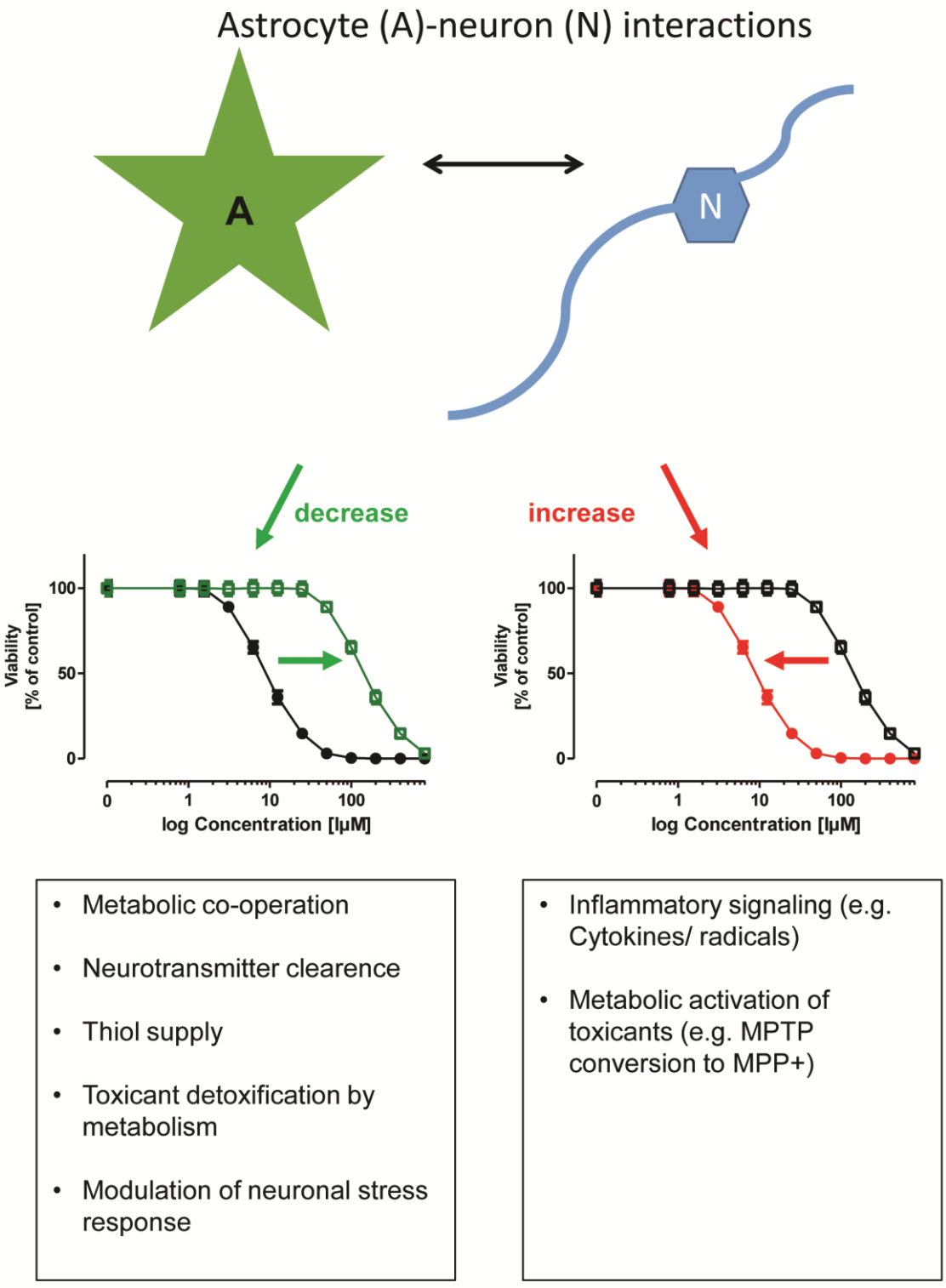

Scheme 6: Influence of astrocytes on neuronal toxicant sensitivity
Scheme summarizes properties changing through co-culture with astrocytes, which decrease (e.g. thiol supply) or increase (e.g. inflammatory signals) toxicant sensitivity of the LUHMES cells.

4.5.1 Existing co-culture systems

When establishing a co-culture system of astrocytes and neurons, the ideal preconditions are cellular model systems that allow the fast generation of highly homogenous, well characterized cells reflecting closely the *in vivo* situation. However, especially in case of astrocytes this is still challenging.

Early attempts tried to immortalize rodent and human premature astrocytes, which ensures availability, quality and defined characteristics (380-382). However, one restriction applying to this cell lines is the high proliferation rate which involved a reduction in glial markers (381). An alternative approach is the differentiation of astrocytes from murine or human stem cells. The protocols existing for astrocytes derived from human stem cells are still time consuming and often result in impure populations (383). One of the underlying reasons that might explain the difficulties in generation of human stem cell derived astrocytes, could be the existence of two stages (fetal and adult) of astrocytes also *in vivo,* which indicates a long maturation phase of this cell type (17). In contrast, in mice only neuronal precursor or mature astrocytes have been observed, pointing to a faster differentiation than in the human counterpart (17). In line with this, the differentiation of astrocytes from murine stem cells has been demonstrated to be fast, highly reproducible and with high purity, resulting in astrocytes expressing desired glial marker genes and fulfilling astrocyte specific functions (i.e. glutamate uptake, NFκB-translocation, cytokine release and neuronal support) (182, 183, 189). The limitations of cell lines and the restricted availability of differentiation protocols explains why primary astrocytes have been still the first choice in most of the existing models during the last decades (99). These primary astrocytes, are assumed to be “pure” as most of the cells stain positive for GFAP and S100β. However, contaminations with other cell types are possible and variations between preparations are routinely observed (384).

On side of the neurons the cellular availability is not a limiting factor, since a lot of neuronal differentiation protocols from stem cells, isolation protocols of primary neurons and neuronal cell lines are established. Interestingly, many studies combine primary astrocytes with primary murine neurons (385-387). In these models the area of the brain from which the cells are isolated can be selected according to experimental requirements (384). However, the application of primary neuronal cultures has the same restrictions as primary astrocytes. The isolation and culturing process is

time intensive and consumes animals, some of the established protocols need over three weeks to obtain a co-culture (388-390).

There are two forms of co-culture possible, seeding neurons on top of astrocytes or non-contact models where the cells are cultured separately but are present in the same medium (386, 387, 389-391). The latter gives the opportunity of separated toxicant exposure and analysis of each cell type (392). A third possibility to test for neuron astrocyte interactions is by culturing the two cell types separately and to transfer the culture medium conditioned by one cell type to the other. This technique is limited, since it focus only on one way and does not include reciprocal interactions of the different cell types that can alter the effects significantly (393).

The co-culture used in this study is a direct contact co-culture, with human dopaminergic neurons derived from the LUHMES cell line on top of astrocytes differentiated from mouse embryonic stem cells (182, 183). This gives several advantages over other culture systems: (i) nearly unlimited cell availability, which is one of the shortcomings of existing primary cultures; (ii) short culture time, this culture is ready for use within 6 days; (iii) high purity of the two cell types, which allows a homogenous culture and decreases batch to batch variations; (iiii) all three ways of co-culturing (contact, non-contact and conditioned medium) are feasible in this model. However, this model has also short comings: (i) LUHMES are a transformed cell line; (ii) the species difference between LUHMES (human) and astrocytes (mouse).Focussing on a defined and fast model, the arguments supporting this co-culture system outbalance the short comings mentioned above.

4.5.2 Astrocyte-neuron-support and metabolic interdependence:

Divers metabolic interactions, for example thiol transfer, lactate shuttling and glutamate-glutamine cycle, several protective effects (i.e. against hydrogen peroxide or glutamate toxicity), but also negative effects, such as increased oxidative stress in astrocyte-neuron co-culture have been reported (389, 394-397). In many of these cases the protective effect of astrocytes altering neuronal stress response is linked to one of these metabolic interactions.

Glutamate Glutamine cycle:

Glutamate is the most used excitatory neurotransmitter in the brain (344), and its excitotoxic potential towards neurons is well studied. Glutamate is cleared by astrocytes from the synaptic cleft and converted into glutamine, which is then transferred to neurons, where it is converted back to Glutamate (319). Transporters involved in this cycle link thiol metabolism and Glutamine-Glutamate shuttle (344). Astrocytes mainly use GLT1 and GLAST, which make use of the Na^+ gradient for glutamate uptake. The other transport by the cystine /glutamate antiporter, the Xc system, is energy independent but with lower affinities and requires high levels of cystine. This transporter is expressed predominantly in neurons (398) and its K_m for cystine is approx. 100 µM, which is in the range of circulating cystine concentrations (344). Aside the connection over this common transporter, glutamate has also directly been linked to glial GSH release (399, 400).

Neuron astrocyte interdependence in thiol metabolism

In contradiction to reports stating that neurons transport cystine via the Xc system (344, 398), other studies reported that adult neurons are not capable to efficiently transport cystine, the oxidized form of cysteine (386), and therefore rely on the astrocytic supply of cysteine or cysteine containing peptides for efficient GSH synthesis. In line with the latter, we observed low cystine uptake in our LUHMES cultures and increased GSH levels induced by astrocytic thiol supply. However, upon stress full conditions LUHMES up-regulated the expression of the cystine transporter and cystine uptake. The low expression of this transporter in *in vitro* neuronal mono-cultures could also be necessary to avoid glutamate toxicity (328, 344).

Others observed neuronal GSH elevation in the presence of astrocytes in non-contact co-culture systems and when neurons were cultured in conditioned medium (CM) from astrocytes (330, 386). They stated that GSH released from astrocytes is cleaved by the ecto-enzyme γ-glutamyl-transferase, producing a cysteine-glycin dipeptide (330), which then is cleaved by neuronal aminopeptidase N and cysteine is taken up into neurons (330) .

Interestingly, neurons are equipped with a functional transsulfuration pathway, which might be an alternative route of cysteine generation from methionine (344-346). However, we observed induction of this pathway only under neuronal stress condi-

tions and this response was blunted by the presence of astrocytes (49). The results of this study underline the importance of astrocytic thiol supply to neurons and suggest a stress response modulation. Interestingly, GSH has been shown to be lower in vulnerable regions of the brain, such as *substantia nigra* (401-404) and one study reports higher GSH levels and increased astrocyte number in unaffected brain regions of PD brains (405).

4.5.3 Examples of altered neuronal sensitivity in presence of glia:

Astrocytes are not only affecting neurons under basic conditions but also influence neuronal survival in multiple pathological conditions. They can be protective against oxidative stressors (406, 407), support neurons with mitochondrial dysfunctions (408) and influence clearance of misfolded protein. In general glial cells were found to be less sensitive to disturbances in the ubiquitin protease system (UPS) (409). However, there is evidence for disturbance of the UPS in glia in multiple neurodegenerative diseases, and astrocytes surviving a first proteotoxic stress were found to protect neurons against further disturbances in the UPS (410), indicating a high intrinsic resilience of this cell type against proteotoxic stress.

Beside their protective properties there are two more aspects that potentially influence toxicant sensitivity of neurons in *in vitro* models: (i) metabolic activation of toxicants by astrocyte metabolism giving rise to the actual neurotoxicant, the most prominent example is the conversion of MPTP into its active metabolite MPP+, which requires astrocytic MAO-B activity (28); (ii) inflammatory activation of astrocytes, which can, depending on the activation state, have protective or deleterious consequences for neurons (15, 173). Substances inducing glial activation might therefore be neurotoxic in co-culture but not in mono-culture.

4.5.4 Astrocytes potential therapeutic targets:

While the standard concept of neurodegenerative diseases is focused on the neurons and the neuron related deleterious processes, recently also glia received growing attention. Especially the astrocytic environment was recognized to play a central role in the disease outcome (320). Beside the protective aspects discussed in the previous paragraphs, astrocytes can also have negative effects and increase neu-

ronal injury (411, 412). For instance, if inflammatory activated, they were found to change their phenotype and lose their neuron-protective properties and induce neuronal death (412). In context of immunology, these astrocytes were grouped into A1 (reactive, neurotoxic astrocytes) and A2 astrocytes (in analogy to M1/M2 macrophages) (412). However, if this nomenclature is sufficient to categorize all subtypes present *in vivo* is still under debate (411).

Inflammatory stimulated A1 astrocytes are found in acute injury and in chronic neurodegenerative diseases, where they are suspected to drive neurodegeneration (411). One therapeutic approach therefore would be to modulate this phenotype or to prevent the transition of quiescent astrocytes into the reactive neuro-damaging state. Neutralizing pro-inflammatory cytokines such as IL-1α and TNFα can prevent transition to the A1 phenotype and drugs modulating this cytokines are already approved for other diseases (411). Furthermore, downstream of the cytokines NFκB and Stat3 are also interesting drug targets, which deserve further interest (411). In context of the study presented here, others observed that inflammatory stimulation of astrocytes can enhance intracellular GSH levels of and GSH release from astrocytes (413, 414). This observations would indicate positive properties of inflammatory activation. However, whether GSH increase following inflammatory activation is a primary effect or a compensatory response of astrocytes to inflammatory stimuli needs further investigation. Therefore, modulation or induction of inflammatory astrocytes as drug targets has to be handled with care and needs more effort to characterize the different inflammatory phenotypes (411).

A second approach to increase astrocytic thiol supply to neurons pharmacologically might be induction of the NRF-2 response in astrocytes. NRF2 activation in U373 astroglial cells was found to increase GSH release (415). In line with this, overexpression of NRF-2 in astrocytes was found to increase intracellular GSH, GSH release into the medium and increased protection of co-cultured neurons (336). In addition, the activation of NRF-2 response in astrocytes has been connected to transcriptional changes in neurons altering the astrocyte-neuron interactions (350). Interestingly, the NRF-2 inducible antioxidant defense in astrocyte can be up and down regulated by microglia (416) proposing potential involvement of inflammatory regulations also in this pathway.

Further suggestions to boost astrocytic GSH levels and release involved modulation of AMP-activated kinase AMPK (417) use of reservatrol (418) or zonisamide (419) and also indicated increase of protective properties.

Considering the finding of this study and the observation of others, astrocytes and especially thiol supply from astrocytes to neurons might be valuable drug targets or future therapeutic approaches.

4.6 Restrictions and limitations of this study

The results mentioned above point out important issues, which are of concern, when establishing or using *in vitro* test systems. Even though I think that each part makes a relevant and valid point, every study also has some shortcomings. Moreover, there are and topics that might require further attention. Some of those will be addressed and discussed in the following:

In the first manuscript, non-staionary ^{13}C metabolomics was used to address cellular fluxes through the main metabolic pathways of the cells. Therefore, samples were taken in very short intervals to provide a very high resolution of kinetics for many metabolites. However, the amount of data obtained exceeded the capacity for evaluation of the data and experiments became so large that they were hard to control. The study could not provide a fluxmap of the differentiated cells (d6), and due to high deviations within the biological replicates may have contributed to the flux balance inconsistencies. Reduction of sample number and the number of measured metabolites, would have allowed better data quality and enough time for data quality control and model calculations. For a future approach, it would be recommendable here to focus on the measurement of fewer metabolites, essential for the bioinformatic modeling process, and to increase the robustness of the measurements in order to allow data interpretation. Once this reduced model is established the extension to further metabolites or higher resolution might be attempted again. Furthermore, the flux balance calculations were difficult, as it was unclear how changing biomass (e.g. in growing cells) was to be measured and introduced into the model. For future approaches a measurement for membrane quantity, beside the counting of cells and the measurement of protein, could be helpful to estimate, if differentiating neurons still produce biomass.

In the second part of this thesis, the variability between two subpopulations (SP) of the LUHMES cells was assessed. As the SP originated from two sources, the original provider laboratory and the cell bank (ATCC), and the deposition took place ten years ago, the exact culture differences are not well documented. In order to address the effects of genetic drift in greater detail, one could, in a second attempt, test for differences occurring during culturing within one laboratory (e.g. different passage numbers, experimenters, plastic batches). This setup would then provide more evidence for the factors driving such drift and how they can be controlled. Moreover, the use of two different sequencing platforms for the whole genome sequencing (WGS) of the two subpopulations induced additional background noise, which had to be filtered by bioinformatic tools. Such noise increases the difficulty of WGS data interpretation and the filtering might cause errors that lead to the failure in detecting important differences. If repeated, the use of one provider for WGS is highly desirable. Furthermore, the RNA expression profile of both SP should be assessed on a global level (e.g. RNA-sequencing or microarray), which could help to identify affected transcription factors and regulatory pathways accounting for the difference in the dopaminergic phenotype.

In the third part of the thesis, the influence of thiol supply from astrocytes to neurons was identified as major mediator of trans-cellular resilience. However, even though we measured GSH increase in astrocyte conditioned medium, the increase of neuronal GSH mediated by astrocyte conditioned medium and confirmed that thiol depletion from the medium blunted the protection, the proof, that this is mediated by GSH, is still incomplete. Further investigations in this directions could involve astrocytes devoid of GSH production, measurements with higher specificity and resolution and target the exact mechanism of the transfer (e.g. transporter, gap junctions,etc.). Additionally, preliminary experiments point to possible interactions of thiols with MG-132. Therefore, the chemical stability of this compound in the presence of cysteine and GSH has to be addressed in greater detail in the near future. The use of murine derived astrocytes for this part of the study had its benefits, however, the development of a purely human system is of high interest and should be further extended in future. Moreover, for defining the exact contribution of factors like NRF-1; ATF-4 and DDIT-4, knockout cells with inducible expression would be ideal tools.

5 Conclusion and Outlook

The results presented in this study highlight the importance of three different aspects that might affect toxicant sensitivity of the LUHMES cell line and other test systems (scheme 1). With increasing use of *in vitro* models the identification of such factors and their potential influence on toxicological tests gains an important role in creating awareness of potential limitations and increasing toxicological safety.

In study #1 the importance of the metabolic state for toxicant sensitivity was highlighted. Addressing metabolic alterations within a cellular system and knowing the buffer capacities of the toxicological system used to study certain neurotoxicological aspects is essential for choosing the correct cellular model and for the correct data interpretation in the following process. Therefore, in the future such a basic study should be included in the characterization of test systems that address metabolic aspects.

In study #2 the impact of small phenotypic and genetic alterations occurring during few passages of subculturing was addressed. Even though, cell banking gets more and more standardized the bulk production of reference material might affect the genetic or phenotypic properties of a cell line deposited there. Characterization beyond STR profiling addressing phenotypic properties, which are important for a test system should be performed regularly, also after deposition at a cell bank in order to assure the comparability to original publications.

The third manuscript highlighted the complexity of cell-cell interactions between different cell types under toxicological conditions. The extension of a cellular model to a co-culture of multiple cell types can increase the information gain and alter the interpretation of stress responses. In context of the brain, addition of microglia and oligodentrocytes to this model might increase the relevance and give more information about cellular interactions. As they reflect more the *in vivo* situation, the trend in *in vitro* models favours the development of such complex models including several cell types and 3D structures. By comparing differential toxicological responses of such complex models with mono-cultures, will allow the identification of many cellular resilience pathways and potential therapeutic approaches in the future.

List of contributions:

Research articles (9):

Canagliflozin mediated dual inhibition of mitochondrial glutamate dehydrogenase and complex I: an off-target adverse effect. Secker PF, Beneke S, Schlichenmaier N, Delp J, **Gutbier** S, Leist M, Dietrich DR. Cell Death Dis. 2018 Feb 14;9(2):226. doi: 10.1038/s41419-018-0273-y

A high-throughput approach to identify specific neurotoxicants/ developmental toxicants in human neuronal cell function assays. Delp J, **Gutbier** S, Klima S, Hoelting L, Pinto-Gil K, Hsieh JH, Aichem M, Klein K, Schreiber F, Tice RR, Pastor M, Behl M, Leist M..ALTEX. 2018 Jan 21. doi: 10.14573/altex.1712182

Stage-specific metabolic features of differentiating neurons: Implications for toxicant sensitivity. **Gutbier** S*, Delp J*, Cerff M*, Zasada C*, Niedenführ S, Zhao L, Smirnova L, Hartung T, Borlinghaus H, Schreiber F, Bergemann J, Gätgens J, Beyss M, Azzouzi S, Waldmann T, Kempa S, Nöh K, Leist M.Toxicol Appl Pharmacol. 2017 Dec 24. pii: S0041-008X(17)30494-5. doi: 10.1016/j.taap.2017.12.013**(*shared first authorship)**

Conversion of Nonproliferating Astrocytes into Neurogenic Neural Stem Cells: Control by FGF2 and Interferon-γ. Kleiderman S, **Gutbier** S, Ugur Tufekci K, Ortega F, Sá JV, Teixeira AP, Brito C, Glaab E, Berninger B, Alves PM, Leist M. Stem Cells. 2016 Dec;34(12):2861-2874. doi: 10.1002/stem.2483.

Switching from astrocytic neuroprotection to neurodegeneration by cytokine stimulation. Efremova L, Chovancova P, Adam M, **Gutbier** S, Schildknecht S, Leist M.; Arch Toxicol. 2016 Apr 6.

Functional and phenotypic differences of pure populations of stem cell-derived astrocytes and neuronal precursor cells. Kleiderman S, Sá JV, Teixeira AP, Brito C, **Gutbier** S, Evje LG, Hadera MG, Glaab E, Henry M, Sachinidis A, Alves PM, Sonnewald U, Leist M. ; Glia. 2016 May;64(5):695-715. doi: 10.1002/glia.22954.

Prevention of the degeneration of human dopaminergic neurons in an astrocyte co-culture system allowing endogenous drug metabolism. Efremova L, Schildknecht S,

Adam M, Pape R, **Gutbier** S, Hanf B, Bürkle A, Leist M.; Br J Pharmacol. 2015 Aug;172(16):4119-32. doi: 10.1111/bph.13193.

Transcriptional and metabolic adaptation of human neurons to the mitochondrial toxicant MPP(+). Krug AK, **Gutbier** S, Zhao L, Pöltl D, Kullmann C, Ivanova V, Förster S, Jagtap S, Meiser J, Leparc G, Schildknecht S, Adam M, Hiller K, Farhan H, Brunner T, Hartung T, Sachinidis A, Leist M.*;* Cell Death Dis. 2014 May 8;5:e1222. doi: 10.1038/cddis.2014.166.

Generation of genetically-modified human differentiated cells for toxicological tests and the study of neurodegenerative diseases. Schildknecht S, Karreman C, Pöltl D, Efrémova L, Kullmann C, **Gutbier** S, Krug A, Scholz D, Gerding HR, Leist M.*;* ALTEX. 2013;30(4):427-44.

Reviews:

In vitro acute and developmental neurotoxicity screening: an overview of cellular platforms and high-throughput technical possibilities. **Gutbier** S*, Schmidt BZ*, Lehmann M*, Nembo E, Noel S, Smirnova L, Forsby A, Hescheler J, Avci HX, Hartung T, Leist M, Kobolák J, Dinnyés A.; Arch Toxicol. 2016 Aug 4. [Epub ahead of print] Review. **(*shared first authorship)**

Conference Presentations:

Neuronal stress response following proteasomal inhibition, and its prevention by astrocytic thiol supply

Gutbier S Leist M

Oral presentation at the German Pharm-Tox Summit 2016 (82. Jahrestagung der Deutschen Gesellschaft für experimentelle und klinische Pharmakologie und Toxikologie (DGPT) und 18. Jahrestagung der Klinischen Pharmakologie (VKliPha) in Zusammenarbeit mit der AGAH)

Conference Posters:

Prevention of neurodegeneration by astrocyte-mediated neuronal (re)-programming **Gutbier S**, Adam M, Schildknecht S, Leist M

Astrocytes in Health and Neurodegenerative Disease, A joint Biochmeical Society Meeting (April 2014; UCL, London, UK)

Record of contributions:

Manuscript 1: Stage-specific metabolic features of differentiating neurons: implications for toxicant sensitivity

I conceived and designed the experiments together with Johannes Delp, and Marcel Leist.

Amino acid analysis data, toxicological data and substrate dependency data was analyzed by Johannes Delp and me.

I designed the figures and wrote the manuscript together with Marcel Leist and Johannes Delp.

Manuscript 2: Major changes of cell function and toxicant sensitivity by mild, culture-dependent genetic drift

I conceived and designed the experiments for toxicant sensitivity and molecular characterization together with Marcel Leist, and prepared DNA samples for STR-profiling and whole genome sequencing.

I analyzed the toxicological data and the molecular phenotypic characterization data.

I designed the figures and wrote the manuscript together with Marcel Leist

Manuscript 3: Prevention of neuronal apoptosis by astrocytes through thiol-mediated stress response modulation and accelerated recovery from proteotoxic stress

I conceived and designed the experiments in collaboration with Marcel Leist.

I analyzed the data of the experiments.

I designed the figures and wrote the manuscript in collaboration with Marcel Leist.

Acknowledgements:

Zu Beginn möchte ich mich bei Marcel bedanken, dass ich an seinem Lehrstuhl meine Bachlor, Masterarbeit und Doktorarbeit anfertigen durfte. Über die vielen Jahre hinweg habe ich viel von dir gelernt und durchweg deine Unterstützung erfahren. Die Arbeitsatmosphäre und die Ausstattung der Labore erlaubten mir eine uneingeschränkte Verwirklichung meiner Ideen und effizientes und ertragreiches Arbeiten. Durch Besprechung mit dir und durch die Gruppenseminare bekam ich immer wieder sehr viele Denkanstöße und Inspirationen. Vielen Dank für die Unterstützung bei der Vollendung der Doktorarbeit und bei der Jobsuche.

Ich möchte Herrn Prof. Thomas Brunner für das Erstellen eines Zweitgutachtens meiner Arbeit und für den Input in Thesiskomiteemeetings und bei der Anfertigung des Manuskripts #3 bedanken.

Ich möchte Herrn Prof. Marcus Groettrup für die Übernahme des Prüfungsvorsitzes und für den Input in Thesiskomiteemeetings und bei der Anfertigung des Manuskripts #3 bedanken.

Des Weiteren möchte ich mich bei allen Kolaborationspartnern bedanken. Vor allem möchte ich Anne Krug, Liudmila Efremova, Susanne Kleidermann und Johannes Delp für die ertragreichen Kollaborationen danken. Insbesondere die Zusammenarbeit mit Johannes hat uns beiden sehr geholfen und ich hoffe, dass auch die übrigen Daten noch erfolgreich publiziert werden.

Ein herzliches Dankeschön möchte ich außerdem der gesamten Arbeitsgruppe aussprechen, die mir durch die angenehme Arbeitsatmosphäre und ihre große Hilfsbereitschaft eine schöne Zeit bereitet hat.

Vielen Dank Lisa, Johannes, Sophie, Xenia, Tanja, Stefan und Nadine für das Korrekturlesen meiner Arbeit.

Danke, an meine Freunde, die mich während des Studiums hier in Konstanz begleitet haben und es mit viel Freude und Abwechslung bereichert haben. Vielen Dank Axel für die vielen Laufrunden, gemeinsam haben wir doch einige Kilometer zurückgelegt, viele interessante Themen diskutiert und so immer einen guten Ausgleich zur Arbeit geschaffen.

Ich danke meinen Eltern, ohne eure Förderung und Unterstützung hätte ich nicht studiert. Ich möchte euch danken, dass ihr mich immer ermuntert habt weiter zu machen und es mir ermöglicht habt Biologie zu studieren.

In besonderer Weise möchte ich meiner Freundin Nadine für die letzten zehn Jahre danken in denen wir sehr viele schöne Erlebnisse teilen durften, und den Großteil des Studiums gemeinsam meisterten. Die Zeit mit dir und unserem Sohn erfüllt mein Leben und motiviert mich jeden Tag aufs Neue. Ich freue mich auf die Geburt unseres zweiten Kindes und hoffe, dass wir viele glückliche und ereignissreiche Jahre als Familie vor uns haben. Durch unsere Beziehung und unsere Kinder wurde die Studienzeit in Konstanz unvergesslich und vielleicht kehren wir irgendwann hierher zurück.

References:

1. Hartung T. Toxicology for the twenty-first century. *Nature*. 2009;**460**(7252):208-212.
2. Hartung T, Leist M. Food for thought ... on the evolution of toxicology and the phasing out of animal testing. *ALTEX*. 2008;**25**(2):91-102.
3. Bhattacharya S, Zhang Q, Carmichael PL, Boekelheide K, Andersen ME. Toxicity testing in the 21 century: defining new risk assessment approaches based on perturbation of intracellular toxicity pathways. *PLoS One*. 2011;**6**(6):e20887.
4. Hartung T, McBride M. Food for Thought ... on mapping the human toxome. *ALTEX*. 2011;**28**(2):83-93.
5. Leist M, Hartung T, Nicotera P. The dawning of a new age of toxicology. *ALTEX*. 2008;**25**(2):103-114.
6. Leist M, Hasiwa N, Rovida C, Daneshian M, Basketter D, Kimber I, et al. Consensus report on the future of animal-free systemic toxicity testing. *ALTEX*. 2014;**31**(3):341-356.
7. Olson H, Betton G, Robinson D, Thomas K, Monro A, Kolaja G, et al. Concordance of the toxicity of pharmaceuticals in humans and in animals. *Regul Toxicol Pharmacol*. 2000;**32**(1):56-67.
8. Azevedo FA, Carvalho LR, Grinberg LT, Farfel JM, Ferretti RE, Leite RE, et al. Equal numbers of neuronal and nonneuronal cells make the human brain an isometrically scaled-up primate brain. *J Comp Neurol*. 2009;**513**(5):532-541.
9. Herculano-Houzel S. Not all brains are made the same: new views on brain scaling in evolution. *Brain Behav Evol*. 2011;**78**(1):22-36.
10. DeFelipe J, Alonso-Nanclares L, Arellano JI. Microstructure of the neocortex: comparative aspects. *J Neurocytol*. 2002;**31**(3-5):299-316.
11. Florio M, Huttner WB. Neural progenitors, neurogenesis and the evolution of the neocortex. *Development*. 2014;**141**(11):2182-2194.
12. Fougerousse F, Bullen P, Herasse M, Lindsay S, Richard I, Wilson D, et al. Human-mouse differences in the embryonic expression patterns of developmental control genes and disease genes. *Hum Mol Genet*. 2000;**9**(2):165-173.
13. Allman JM, Tetreault NA, Hakeem AY, Manaye KF, Semendeferi K, Erwin JM, et al. The von Economo neurons in the frontoinsular and anterior cingulate cortex. *Ann N Y Acad Sci*. 2011;**1225**:59-71.
14. Seeley WW, Carlin DA, Allman JM, Macedo MN, Bush C, Miller BL, et al. Early frontotemporal dementia targets neurons unique to apes and humans. *Ann Neurol*. 2006;**60**(6):660-667.
15. Efremova L, Schildknecht S, Adam M, Pape R, Gutbier S, Hanf B, et al. Prevention of the degeneration of human dopaminergic neurons in an astrocyte co-culture system allowing endogenous drug metabolism. *Br J Pharmacol*. 2015;**172**(16):4119-4132.
16. Nedergaard M, Ransom B, Goldman SA. New roles for astrocytes: redefining the functional architecture of the brain. *Trends Neurosci*. 2003;**26**(10):523-530.
17. Zhang Y, Sloan SA, Clarke LE, Caneda C, Plaza CA, Blumenthal PD, et al. Purification and Characterization of Progenitor and Mature Human Astrocytes Reveals Transcriptional and Functional Differences with Mouse. *Neuron*. 2016;**89**(1):37-53.
18. Leist M, Hartung T. Inflammatory findings on species extrapolations: humans are definitely no 70-kg mice. *Arch Toxicol*. 2013;**87**(4):563-567.

19. Seok J, Warren HS, Cuenca AG, Mindrinos MN, Baker HV, Xu W, et al. Genomic responses in mouse models poorly mimic human inflammatory diseases. *Proc Natl Acad Sci U S A*. 2013;**110**(9):3507-3512.
20. Betarbet R, Sherer TB, MacKenzie G, Garcia-Osuna M, Panov AV, Greenamyre JT. Chronic systemic pesticide exposure reproduces features of Parkinson's disease. *Nat Neurosci*. 2000;**3**(12):1301-1306.
21. Dauer W, Przedborski S. Parkinson's disease: mechanisms and models. *Neuron*. 2003;**39**(6):889-909.
22. Schmidt BZ, Lehmann M, Gutbier S, Nembo E, Noel S, Smirnova L, et al. In vitro acute and developmental neurotoxicity screening: an overview of cellular platforms and high-throughput technical possibilities. *Arch Toxicol*. 2017;**91**(1):1-33.
23. Alepee N, Bahinski A, Daneshian M, De Wever B, Fritsche E, Goldberg A, et al. State-of-the-art of 3D cultures (organs-on-a-chip) in safety testing and pathophysiology. *ALTEX*. 2014;**31**(4):441-477.
24. Cecchelli R, Berezowski V, Lundquist S, Culot M, Renftel M, Dehouck MP, et al. Modelling of the blood-brain barrier in drug discovery and development. *Nat Rev Drug Discov*. 2007;**6**(8):650-661.
25. Abbott NJ, Patabendige AA, Dolman DE, Yusof SR, Begley DJ. Structure and function of the blood-brain barrier. *Neurobiol Dis*. 2010;**37**(1):13-25.
26. Hawkins BT, Davis TP. The blood-brain barrier/neurovascular unit in health and disease. *Pharmacol Rev*. 2005;**57**(2):173-185.
27. Zhao Z, Nelson AR, Betsholtz C, Zlokovic BV. Establishment and Dysfunction of the Blood-Brain Barrier. *Cell*. 2015;**163**(5):1064-1078.
28. Schildknecht S, Pape R, Meiser J, Karreman C, Strittmatter T, Odermatt M, et al. Preferential Extracellular Generation of the Active Parkinsonian Toxin MPP+ by Transporter-Independent Export of the Intermediate MPDP+. *Antioxid Redox Signal*. 2015;**23**(13):1001-1016.
29. Miyata S. New aspects in fenestrated capillary and tissue dynamics in the sensory circumventricular organs of adult brains. *Front Neurosci*. 2015;**9**:390.
30. Lohren H, Blagojevic L, Fitkau R, Ebert F, Schildknecht S, Leist M, et al. Toxicity of organic and inorganic mercury species in differentiated human neurons and human astrocytes. *J Trace Elem Med Biol*. 2015;**32**:200-208.
31. Gibbs KL, Greensmith L, Schiavo G. Regulation of Axonal Transport by Protein Kinases. *Trends Biochem Sci*. 2015;**40**(10):597-610.
32. Zsurka G, Kunz WS. Mitochondrial dysfunction and seizures: the neuronal energy crisis. *Lancet Neurol*. 2015;**14**(9):956-966.
33. Fernandez-Moya SM, Bauer KE, Kiebler MA. Meet the players: local translation at the synapse. *Front Mol Neurosci*. 2014;**7**:84.
34. Lotharius J, Falsig J, van Beek J, Payne S, Dringen R, Brundin P, et al. Progressive degeneration of human mesencephalic neuron-derived cells triggered by dopamine-dependent oxidative stress is dependent on the mixed-lineage kinase pathway. *J Neurosci*. 2005;**25**(27):6329-6342.
35. Schildknecht S, Poltl D, Nagel DM, Matt F, Scholz D, Lotharius J, et al. Requirement of a dopaminergic neuronal phenotype for toxicity of low concentrations of 1-methyl-4-phenylpyridinium to human cells. *Toxicol Appl Pharmacol*. 2009;**241**(1):23-35.
36. Leist M, Nicotera P. Calcium and neuronal death. *Rev Physiol Biochem Pharmacol*. 1998;**132**:79-125.
37. Zimmer B, Kuegler PB, Baudis B, Genewsky A, Tanavde V, Koh W, et al. Coordinated waves of gene expression during neuronal differentiation of embryonic

stem cells as basis for novel approaches to developmental neurotoxicity testing. *Cell Death Differ*. 2011;**18**(3):383-395.
38. van Thriel C, Westerink RH, Beste C, Bale AS, Lein PJ, Leist M. Translating neurobehavioural endpoints of developmental neurotoxicity tests into in vitro assays and readouts. *Neurotoxicology*. 2012;**33**(4):911-924.
39. Penschuck S, Flagstad P, Didriksen M, Leist M, Michael-Titus AT. Decrease in parvalbumin-expressing neurons in the hippocampus and increased phencyclidine-induced locomotor activity in the rat methylazoxymethanol (MAM) model of schizophrenia. *Eur J Neurosci*. 2006;**23**(1):279-284.
40. Kuegler PB, Zimmer B, Waldmann T, Baudis B, Ilmjarv S, Hescheler J, et al. Markers of murine embryonic and neural stem cells, neurons and astrocytes: reference points for developmental neurotoxicity testing. *ALTEX*. 2010;**27**(1):17-42.
41. Kadereit S, Zimmer B, van Thriel C, Hengstler JG, Leist M. Compound selection for in vitro modeling of developmental neurotoxicity. *Front Biosci (Landmark Ed)*. 2012;**17**:2442-2460.
42. Delp J, Gutbier S, Cerff M, Zasada C, Niedenfuhr S, Zhao L, et al. Stage-specific metabolic features of differentiating neurons: Implications for toxicant sensitivity. *Toxicol Appl Pharmacol*. 2017.
43. Bal-Price A, Crofton KM, Leist M, Allen S, Arand M, Buetler T, et al. International STakeholder NETwork (ISTNET): creating a developmental neurotoxicity (DNT) testing road map for regulatory purposes. *Arch Toxicol*. 2015;**89**(2):269-287.
44. Bal-Price A, Crofton KM, Sachana M, Shafer TJ, Behl M, Forsby A, et al. Putative adverse outcome pathways relevant to neurotoxicity. *Crit Rev Toxicol*. 2015;**45**(1):83-91.
45. Galofre M, Babot Z, Garcia DA, Iraola S, Rodriguez-Farre E, Forsby A, et al. GABAA receptor and cell membrane potential as functional endpoints in cultured neurons to evaluate chemicals for human acute toxicity. *Neurotoxicol Teratol*. 2010;**32**(1):52-61.
46. Gustafsson H, Runesson J, Lundqvist J, Lindegren H, Axelsson V, Forsby A. Neurofunctional endpoints assessed in human neuroblastoma SH-SY5Y cells for estimation of acute systemic toxicity. *Toxicol Appl Pharmacol*. 2010;**245**(2):191-202.
47. Latta M, Kunstle G, Leist M, Wendel A. Metabolic depletion of ATP by fructose inversely controls CD95- and tumor necrosis factor receptor 1-mediated hepatic apoptosis. *J Exp Med*. 2000;**191**(11):1975-1985.
48. Volbracht C, Leist M, Nicotera P. ATP controls neuronal apoptosis triggered by microtubule breakdown or potassium deprivation. *Mol Med*. 1999;**5**(7):477-489.
49. Krug AK, Gutbier S, Zhao L, Poltl D, Kullmann C, Ivanova V, et al. Transcriptional and metabolic adaptation of human neurons to the mitochondrial toxicant MPP(+). *Cell Death Dis*. 2014;**5**:e1222.
50. Pamies D, Sogorb MA, Fabbri M, Gribaldo L, Collotta A, Scelfo B, et al. Genomic and phenotypic alterations of the neuronal-like cells derived from human embryonal carcinoma stem cells (NT2) caused by exposure to organophosphorus compounds paraoxon and mipafox. *Int J Mol Sci*. 2014;**15**(1):905-926.
51. Leist M, Gantner F, Kunstle G, Bohlinger I, Tiegs G, Bluethmann H, et al. The 55-kD tumor necrosis factor receptor and CD95 independently signal murine hepatocyte apoptosis and subsequent liver failure. *Mol Med*. 1996;**2**(1):109-124.
52. Wong JK, Kennedy PR, Belcher SM. Simplified serum- and steroid-free culture conditions for high-throughput viability analysis of primary cultures of cerebellar granule neurons. *J Neurosci Methods*. 2001;**110**(1-2):45-55.

53. Hogberg HT, Kinsner-Ovaskainen A, Coecke S, Hartung T, Bal-Price AK. mRNA expression is a relevant tool to identify developmental neurotoxicants using an in vitro approach. *Toxicol Sci*. 2010;**113**(1):95-115.
54. Lein P, Locke P, Goldberg A. Meeting report: alternatives for developmental neurotoxicity testing. *Environ Health Perspect*. 2007;**115**(5):764-768.
55. Radio NM, Breier JM, Shafer TJ, Mundy WR. Assessment of chemical effects on neurite outgrowth in PC12 cells using high content screening. *Toxicol Sci*. 2008;**105**(1):106-118.
56. Krug AK, Balmer NV, Matt F, Schonenberger F, Merhof D, Leist M. Evaluation of a human neurite growth assay as specific screen for developmental neurotoxicants. *Arch Toxicol*. 2013;**87**(12):2215-2231.
57. Stiegler NV, Krug AK, Matt F, Leist M. Assessment of chemical-induced impairment of human neurite outgrowth by multiparametric live cell imaging in high-density cultures. *Toxicol Sci*. 2011;**121**(1):73-87.
58. Delp J, Gutbier S, Klima S, Hoelting L, Pinto-Gil K, Hsieh JH, et al. A high-throughput approach to identify specific neurotoxicants/ developmental toxicants in human neuronal cell function assays. *ALTEX*. 2018.
59. Bajinskis A, Lindegren H, Johansson L, Harms-Ringdahl M, Forsby A. Low-dose/dose-rate gamma radiation depresses neural differentiation and alters protein expression profiles in neuroblastoma SH-SY5Y cells and C17.2 neural stem cells. *Radiat Res*. 2011;**175**(2):185-192.
60. Frimat JP, Sisnaiske J, Subbiah S, Menne H, Godoy P, Lampen P, et al. The network formation assay: a spatially standardized neurite outgrowth analytical display for neurotoxicity screening. *Lab Chip*. 2010;**10**(6):701-709.
61. Pak YL, Swamy KM, Yoon J. Recent Progress in Fluorescent Imaging Probes. *Sensors (Basel)*. 2015;**15**(9):24374-24396.
62. Barayuga SM, Pang X, Andres MA, Panee J, Bellinger FP. Methamphetamine decreases levels of glutathione peroxidases 1 and 4 in SH-SY5Y neuronal cells: protective effects of selenium. *Neurotoxicology*. 2013;**37**:240-246.
63. Poltl D, Schildknecht S, Karreman C, Leist M. Uncoupling of ATP-depletion and cell death in human dopaminergic neurons. *Neurotoxicology*. 2012;**33**(4):769-779.
64. Schildknecht S, Pape R, Muller N, Robotta M, Marquardt A, Burkle A, et al. Neuroprotection by minocycline caused by direct and specific scavenging of peroxynitrite. *J Biol Chem*. 2011;**286**(7):4991-5002.
65. Prasad RY, McGee JK, Killius MG, Suarez DA, Blackman CF, DeMarini DM, et al. Investigating oxidative stress and inflammatory responses elicited by silver nanoparticles using high-throughput reporter genes in HepG2 cells: effect of size, surface coating, and intracellular uptake. *Toxicol In Vitro*. 2013;**27**(6):2013-2021.
66. Schultz L, Zurich MG, Culot M, da Costa A, Landry C, Bellwon P, et al. Evaluation of drug-induced neurotoxicity based on metabolomics, proteomics and electrical activity measurements in complementary CNS in vitro models. *Toxicol In Vitro*. 2015;**30**(1 Pt A):138-165.
67. Agostini M, Romeo F, Inoue S, Niklison-Chirou MV, Elia AJ, Dinsdale D, et al. Metabolic reprogramming during neuronal differentiation. *Cell Death Differ*. 2016;**23**(9):1502-1514.
68. Pham AH, Meng S, Chu QN, Chan DC. Loss of Mfn2 results in progressive, retrograde degeneration of dopaminergic neurons in the nigrostriatal circuit. *Hum Mol Genet*. 2012;**21**(22):4817-4826.

69. Simcox EM, Reeve A, Turnbull D. Monitoring mitochondrial dynamics and complex I dysfunction in neurons: implications for Parkinson's disease. *Biochem Soc Trans*. 2013;**41**(6):1618-1624.
70. Schildknecht S, Karreman C, Poltl D, Efremova L, Kullmann C, Gutbier S, et al. Generation of genetically-modified human differentiated cells for toxicological tests and the study of neurodegenerative diseases. *ALTEX*. 2013;**30**(4):427-444.
71. Koopman WJ, Visch HJ, Smeitink JA, Willems PH. Simultaneous quantitative measurement and automated analysis of mitochondrial morphology, mass, potential, and motility in living human skin fibroblasts. *Cytometry A*. 2006;**69**(1):1-12.
72. Leonard AP, Cameron RB, Speiser JL, Wolf BJ, Peterson YK, Schnellmann RG, et al. Quantitative analysis of mitochondrial morphology and membrane potential in living cells using high-content imaging, machine learning, and morphological binning. *Biochim Biophys Acta*. 2015;**1853**(2):348-360.
73. Mitra K, Lippincott-Schwartz J. Analysis of mitochondrial dynamics and functions using imaging approaches. *Curr Protoc Cell Biol*. 2010;**Chapter 4**:Unit 4 25 21-21.
74. van Vliet E, Daneshian M, Beilmann M, Davies A, Fava E, Fleck R, et al. Current approaches and future role of high content imaging in safety sciences and drug discovery. *ALTEX*. 2014;**31**(4):479-493.
75. Charoenkwan P, Hwang E, Cutler RW, Lee HC, Ko LW, Huang HL, et al. HCS-Neurons: identifying phenotypic changes in multi-neuron images upon drug treatments of high-content screening. *BMC Bioinformatics*. 2013;**14 Suppl 16**:S12.
76. Ho SY, Chao CY, Huang HL, Chiu TW, Charoenkwan P, Hwang E. NeurphologyJ: an automatic neuronal morphology quantification method and its application in pharmacological discovery. *BMC Bioinformatics*. 2011;**12**:230.
77. Billeci L, Magliaro C, Pioggia G, Ahluwalia A. NEuronMOrphological analysis tool: open-source software for quantitative morphometrics. *Front Neuroinform*. 2013;**7**:2.
78. Carpenter AE, Jones TR, Lamprecht MR, Clarke C, Kang IH, Friman O, et al. CellProfiler: image analysis software for identifying and quantifying cell phenotypes. *Genome Biol*. 2006;**7**(10):R100.
79. Dreser N, Zimmer B, Dietz C, Sugis E, Pallocca G, Nyffeler J, et al. Grouping of histone deacetylase inhibitors and other toxicants disturbing neural crest migration by transcriptional profiling. *Neurotoxicology*. 2015;**50**:56-70.
80. Robinson JF, Piersma AH. Toxicogenomic approaches in developmental toxicology testing. *Methods Mol Biol*. 2013;**947**:451-473.
81. Schwartz MP, Hou Z, Propson NE, Zhang J, Engstrom CJ, Santos Costa V, et al. Human pluripotent stem cell-derived neural constructs for predicting neural toxicity. *Proc Natl Acad Sci U S A*. 2015;**112**(40):12516-12521.
82. Smirnova L, Harris G, Leist M, Hartung T. Cellular resilience. *ALTEX*. 2015;**32**(4):247-260.
83. Krug AK, Kolde R, Gaspar JA, Rempel E, Balmer NV, Meganathan K, et al. Human embryonic stem cell-derived test systems for developmental neurotoxicity: a transcriptomics approach. *Arch Toxicol*. 2013;**87**(1):123-143.
84. Piersma AH, Hernandez LG, van Benthem J, Muller JJ, van Leeuwen FX, Vermeire TG, et al. Reproductive toxicants have a threshold of adversity. *Crit Rev Toxicol*. 2011;**41**(6):545-554.
85. Waldmann T, Rempel E, Balmer NV, Konig A, Kolde R, Gaspar JA, et al. Design principles of concentration-dependent transcriptome deviations in drug-exposed differentiating stem cells. *Chem Res Toxicol*. 2014;**27**(3):408-420.

86. Pallocca G, Grinberg M, Henry M, Frickey T, Hengstler JG, Waldmann T, et al. Identification of transcriptome signatures and biomarkers specific for potential developmental toxicants inhibiting human neural crest cell migration. *Arch Toxicol*. 2016;**90**(1):159-180.
87. Bouhifd M, Hartung T, Hogberg HT, Kleensang A, Zhao L. Review: toxicometabolomics. *J Appl Toxicol*. 2013;**33**(12):1365-1383.
88. Pietzke M, Zasada C, Mudrich S, Kempa S. Decoding the dynamics of cellular metabolism and the action of 3-bromopyruvate and 2-deoxyglucose using pulsed stable isotope-resolved metabolomics. *Cancer Metab*. 2014;**2**:9.
89. Bouhifd M, Beger R, Flynn T, Guo L, Harris G, Hogberg H, et al. Quality assurance of metabolomics. *ALTEX*. 2015;**32**(4):319-326.
90. Honegger P, Richelson E. Neurotransmitter synthesis, storage and release by aggregating cell cultures of rat brain. *Brain Res*. 1979;**162**(1):89-101.
91. Monnet-Tschudi F, Zurich MG, Honegger P. Neurotoxicant-induced inflammatory response in three-dimensional brain cell cultures. *Hum Exp Toxicol*. 2007;**26**(4):339-346.
92. Sunol C, Babot Z, Fonfria E, Galofre M, Garcia D, Herrera N, et al. Studies with neuronal cells: From basic studies of mechanisms of neurotoxicity to the prediction of chemical toxicity. *Toxicol In Vitro*. 2008;**22**(5):1350-1355.
93. Valdivia P, Martin M, LeFew WR, Ross J, Houck KA, Shafer TJ. Multi-well microelectrode array recordings detect neuroactivity of ToxCast compounds. *Neurotoxicology*. 2014;**44**:204-217.
94. Ni M, Li X, Rocha JB, Farina M, Aschner M. Glia and methylmercury neurotoxicity. *J Toxicol Environ Health A*. 2012;**75**(16-17):1091-1101.
95. Alwin Prem Anand A, Gowri Sankar S, Kokila Vani V. Immortalization of neuronal progenitors using SV40 large T antigen and differentiation towards dopaminergic neurons. *J Cell Mol Med*. 2012;**16**(11):2592-2610.
96. Davis JB, Maher P. Protein kinase C activation inhibits glutamate-induced cytotoxicity in a neuronal cell line. *Brain Res*. 1994;**652**(1):169-173.
97. Greene LA, Tischler AS. Establishment of a noradrenergic clonal line of rat adrenal pheochromocytoma cells which respond to nerve growth factor. *Proc Natl Acad Sci U S A*. 1976;**73**(7):2424-2428.
98. Behl C, Widmann M, Trapp T, Holsboer F. 17-beta estradiol protects neurons from oxidative stress-induced cell death in vitro. *Biochem Biophys Res Commun*. 1995;**216**(2):473-482.
99. Schildknecht S, Kirner S, Henn A, Gasparic K, Pape R, Efremova L, et al. Characterization of mouse cell line IMA 2.1 as a potential model system to study astrocyte functions. *ALTEX*. 2012;**29**(3):261-274.
100. Jana M, Jana A, Pal U, Pahan K. A simplified method for isolating highly purified neurons, oligodendrocytes, astrocytes, and microglia from the same human fetal brain tissue. *Neurochem Res*. 2007;**32**(12):2015-2022.
101. Hansson O, Castilho RF, Kaminski Schierle GS, Karlsson J, Nicotera P, Leist M, et al. Additive effects of caspase inhibitor and lazaroid on the survival of transplanted rat and human embryonic dopamine neurons. *Exp Neurol*. 2000;**164**(1):102-111.
102. Lotharius J, Barg S, Wiekop P, Lundberg C, Raymon HK, Brundin P. Effect of mutant alpha-synuclein on dopamine homeostasis in a new human mesencephalic cell line. *J Biol Chem*. 2002;**277**(41):38884-38894.
103. Paul G, Christophersen NS, Raymon H, Kiaer C, Smith R, Brundin P. Tyrosine hydroxylase expression is unstable in a human immortalized mesencephalic

cell line--studies in vitro and after intracerebral grafting in vivo. *Mol Cell Neurosci*. 2007;**34**(3):390-399.
104. Scholz D, Poltl D, Genewsky A, Weng M, Waldmann T, Schildknecht S, et al. Rapid, complete and large-scale generation of post-mitotic neurons from the human LUHMES cell line. *J Neurochem*. 2011;**119**(5):957-971.
105. Selenica ML, Jensen HS, Larsen AK, Pedersen ML, Helboe L, Leist M, et al. Efficacy of small-molecule glycogen synthase kinase-3 inhibitors in the postnatal rat model of tau hyperphosphorylation. *Br J Pharmacol*. 2007;**152**(6):959-979.
106. Villa A, Liste I, Courtois ET, Seiz EG, Ramos M, Meyer M, et al. Generation and properties of a new human ventral mesencephalic neural stem cell line. *Exp Cell Res*. 2009;**315**(11):1860-1874.
107. Donato R, Miljan EA, Hines SJ, Aouabdi S, Pollock K, Patel S, et al. Differential development of neuronal physiological responsiveness in two human neural stem cell lines. *BMC Neurosci*. 2007;**8**:36.
108. Bai Y, Hu Q, Li X, Wang Y, Lin C, Shen L, et al. Telomerase immortalization of human neural progenitor cells. *Neuroreport*. 2004;**15**(2):245-249.
109. Roy NS, Chandler-Militello D, Lu G, Wang S, Goldman SA. Retrovirally mediated telomerase immortalization of neural progenitor cells. *Nat Protoc*. 2007;**2**(11):2815-2825.
110. Smirnova L, Harris G, Delp J, Valadares M, Pamies D, Hogberg HT, et al. A LUHMES 3D dopaminergic neuronal model for neurotoxicity testing allowing long-term exposure and cellular resilience analysis. *Arch Toxicol*. 2016;**90**(11):2725-2743.
111. Pahlman S, Ruusala AI, Abrahamsson L, Mattsson ME, Esscher T. Retinoic acid-induced differentiation of cultured human neuroblastoma cells: a comparison with phorbolester-induced differentiation. *Cell Differ*. 1984;**14**(2):135-144.
112. Barenys M, Gassmann K, Baksmeier C, Heinz S, Reverte I, Schmuck M, et al. Epigallocatechin gallate (EGCG) inhibits adhesion and migration of neural progenitor cells in vitro. *Arch Toxicol*. 2017;**91**(2):827-837.
113. Gassmann K, Baumann J, Giersiefer S, Schuwald J, Schreiber T, Merk HF, et al. Automated neurosphere sorting and plating by the COPAS large particle sorter is a suitable method for high-throughput 3D in vitro applications. *Toxicol In Vitro*. 2012;**26**(6):993-1000.
114. Evans MJ, Kaufman MH. Establishment in culture of pluripotential cells from mouse embryos. *Nature*. 1981;**292**(5819):154-156.
115. Martin GR. Isolation of a pluripotent cell line from early mouse embryos cultured in medium conditioned by teratocarcinoma stem cells. *Proc Natl Acad Sci U S A*. 1981;**78**(12):7634-7638.
116. Leist M, Bremer S, Brundin P, Hescheler J, Kirkeby A, Krause KH, et al. The biological and ethical basis of the use of human embryonic stem cells for in vitro test systems or cell therapy. *ALTEX*. 2008;**25**(3):163-190.
117. Thomson JA, Itskovitz-Eldor J, Shapiro SS, Waknitz MA, Swiergiel JJ, Marshall VS, et al. Embryonic stem cell lines derived from human blastocysts. *Science*. 1998;**282**(5391):1145-1147.
118. Heuer J, Bremer S, Pohl I, Spielmann H. Development of an in vitro embryotoxicity test using murine embryonic stem cell cultures. *Toxicol In Vitro*. 1993;**7**(4):551-556.
119. Hayess K, Riebeling C, Pirow R, Steinfath M, Sittner D, Slawik B, et al. The DNT-EST: a predictive embryonic stem cell-based assay for developmental neurotoxicity testing in vitro. *Toxicology*. 2013;**314**(1):135-147.

120. Colaianna M, Ilmjarv S, Peterson H, Kern I, Julien S, Baquie M, et al. Fingerprinting of neurotoxic compounds using a mouse embryonic stem cell dual luminescence reporter assay. *Arch Toxicol*. 2017;**91**(1):365-391.
121. Adler S, Pellizzer C, Hareng L, Hartung T, Bremer S. First steps in establishing a developmental toxicity test method based on human embryonic stem cells. *Toxicol In Vitro*. 2008;**22**(1):200-211.
122. Nguyen HX, Nekanti U, Haus DL, Funes G, Moreno D, Kamei N, et al. Induction of early neural precursors and derivation of tripotent neural stem cells from human pluripotent stem cells under xeno-free conditions. *J Comp Neurol*. 2014;**522**(12):2767-2783.
123. Gorris R, Fischer J, Erwes KL, Kesavan J, Peterson DA, Alexander M, et al. Pluripotent stem cell-derived radial glia-like cells as stable intermediate for efficient generation of human oligodendrocytes. *Glia*. 2015;**63**(12):2152-2167.
124. Harrill JA, Freudenrich TM, Machacek DW, Stice SL, Mundy WR. Quantitative assessment of neurite outgrowth in human embryonic stem cell-derived hN2 cells using automated high-content image analysis. *Neurotoxicology*. 2010;**31**(3):277-290.
125. Hoelting L, Klima S, Karreman C, Grinberg M, Meisig J, Henry M, et al. Stem Cell-Derived Immature Human Dorsal Root Ganglia Neurons to Identify Peripheral Neurotoxicants. *Stem Cells Transl Med*. 2016;**5**(4):476-487.
126. Takahashi K, Yamanaka S. Induction of pluripotent stem cells from mouse embryonic and adult fibroblast cultures by defined factors. *Cell*. 2006;**126**(4):663-676.
127. Yu J, Vodyanik MA, Smuga-Otto K, Antosiewicz-Bourget J, Frane JL, Tian S, et al. Induced pluripotent stem cell lines derived from human somatic cells. *Science*. 2007;**318**(5858):1917-1920.
128. Malik N, Rao MS. A review of the methods for human iPSC derivation. *Methods Mol Biol*. 2013;**997**:23-33.
129. Raab S, Klingenstein M, Liebau S, Linta L. A Comparative View on Human Somatic Cell Sources for iPSC Generation. *Stem Cells Int*. 2014;**2014**:768391.
130. Hu BY, Weick JP, Yu J, Ma LX, Zhang XQ, Thomson JA, et al. Neural differentiation of human induced pluripotent stem cells follows developmental principles but with variable potency. *Proc Natl Acad Sci U S A*. 2010;**107**(9):4335-4340.
131. Nicholas CR, Chen J, Tang Y, Southwell DG, Chalmers N, Vogt D, et al. Functional maturation of hPSC-derived forebrain interneurons requires an extended timeline and mimics human neural development. *Cell Stem Cell*. 2013;**12**(5):573-586.
132. Kolaja K. Stem cells and stem cell-derived tissues and their use in safety assessment. *J Biol Chem*. 2014;**289**(8):4555-4561.
133. Phillips BW, Crook JM. Pluripotent human stem cells: A novel tool in drug discovery. *BioDrugs*. 2010;**24**(2):99-108.
134. Wobus AM, Loser P. Present state and future perspectives of using pluripotent stem cells in toxicology research. *Arch Toxicol*. 2011;**85**(2):79-117.
135. De Los Angeles A, Ferrari F, Xi R, Fujiwara Y, Benvenisty N, Deng H, et al. Hallmarks of pluripotency. *Nature*. 2015;**525**(7570):469-478.
136. Muller FJ, Schuldt BM, Williams R, Mason D, Altun G, Papapetrou EP, et al. A bioinformatic assay for pluripotency in human cells. *Nat Methods*. 2011;**8**(4):315-317.
137. Tsankov AM, Akopian V, Pop R, Chetty S, Gifford CA, Daheron L, et al. A qPCR ScoreCard quantifies the differentiation potential of human pluripotent stem cells. *Nat Biotechnol*. 2015;**33**(11):1182-1192.

138. Takahashi K, Tanabe K, Ohnuki M, Narita M, Ichisaka T, Tomoda K, et al. Induction of pluripotent stem cells from adult human fibroblasts by defined factors. *Cell*. 2007;**131**(5):861-872.
139. Chambers SM, Fasano CA, Papapetrou EP, Tomishima M, Sadelain M, Studer L. Highly efficient neural conversion of human ES and iPS cells by dual inhibition of SMAD signaling. *Nat Biotechnol*. 2009;**27**(3):275-280.
140. Karumbayaram S, Novitch BG, Patterson M, Umbach JA, Richter L, Lindgren A, et al. Directed differentiation of human-induced pluripotent stem cells generates active motor neurons. *Stem Cells*. 2009;**27**(4):806-811.
141. Vazin T, Ball KA, Lu H, Park H, Ataeijannati Y, Head-Gordon T, et al. Efficient derivation of cortical glutamatergic neurons from human pluripotent stem cells: a model system to study neurotoxicity in Alzheimer's disease. *Neurobiol Dis*. 2014;**62**:62-72.
142. Yan Y, Shin S, Jha BS, Liu Q, Sheng J, Li F, et al. Efficient and rapid derivation of primitive neural stem cells and generation of brain subtype neurons from human pluripotent stem cells. *Stem Cells Transl Med*. 2013;**2**(11):862-870.
143. Chanda S, Marro S, Wernig M, Sudhof TC. Neurons generated by direct conversion of fibroblasts reproduce synaptic phenotype caused by autism-associated neuroligin-3 mutation. *Proc Natl Acad Sci U S A*. 2013;**110**(41):16622-16627.
144. Pfisterer U, Kirkeby A, Torper O, Wood J, Nelander J, Dufour A, et al. Direct conversion of human fibroblasts to dopaminergic neurons. *Proc Natl Acad Sci U S A*. 2011;**108**(25):10343-10348.
145. Wapinski OL, Vierbuchen T, Qu K, Lee QY, Chanda S, Fuentes DR, et al. Hierarchical mechanisms for direct reprogramming of fibroblasts to neurons. *Cell*. 2013;**155**(3):621-635.
146. Freedman LP, Cockburn IM, Simcoe TS. The Economics of Reproducibility in Preclinical Research. *PLoS Biol*. 2015;**13**(6):e1002165.
147. Lorsch JR, Collins FS, Lippincott-Schwartz J. Cell Biology. Fixing problems with cell lines. *Science*. 2014;**346**(6216):1452-1453.
148. Hughes P, Marshall D, Reid Y, Parkes H, Gelber C. The costs of using unauthenticated, over-passaged cell lines: how much more data do we need? *Biotechniques*. 2007;**43**(5):575, 577-578, 581-572 passim.
149. Baker D, Hirst AJ, Gokhale PJ, Juarez MA, Williams S, Wheeler M, et al. Detecting Genetic Mosaicism in Cultures of Human Pluripotent Stem Cells. *Stem Cell Reports*. 2016;**7**(5):998-1012.
150. Freedman LP, Gibson MC, Ethier SP, Soule HR, Neve RM, Reid YA. Reproducibility: changing the policies and culture of cell line authentication. *Nat Methods*. 2015;**12**(6):493-497.
151. Landry JJ, Pyl PT, Rausch T, Zichner T, Tekkedil MM, Stutz AM, et al. The genomic and transcriptomic landscape of a HeLa cell line. *G3 (Bethesda)*. 2013;**3**(8):1213-1224.
152. Bate-Eya LT, Ebus ME, Koster J, den Hartog IJ, Zwijnenburg DA, Schild L, et al. Newly-derived neuroblastoma cell lines propagated in serum-free media recapitulate the genotype and phenotype of primary neuroblastoma tumours. *Eur J Cancer*. 2014;**50**(3):628-637.
153. Krishna A, Biryukov M, Trefois C, Antony PM, Hussong R, Lin J, et al. Systems genomics evaluation of the SH-SY5Y neuroblastoma cell line as a model for Parkinson's disease. *BMC Genomics*. 2014;**15**:1154.
154. Cai J, Miao X, Li Y, Smith C, Tsang K, Cheng L, et al. Whole-genome sequencing identifies genetic variances in culture-expanded human mesenchymal stem cells. *Stem Cell Reports*. 2014;**3**(2):227-233.

155. Shyh-Chang N, Daley GQ, Cantley LC. Stem cell metabolism in tissue development and aging. *Development*. 2013;**140**(12):2535-2547.
156. Vander Heiden MG, Cantley LC, Thompson CB. Understanding the Warburg effect: the metabolic requirements of cell proliferation. *Science*. 2009;**324**(5930):1029-1033.
157. Fan J, Kamphorst JJ, Mathew R, Chung MK, White E, Shlomi T, et al. Glutamine-driven oxidative phosphorylation is a major ATP source in transformed mammalian cells in both normoxia and hypoxia. *Mol Syst Biol*. 2013;**9**:712.
158. Birsoy K, Wang T, Chen WW, Freinkman E, Abu-Remaileh M, Sabatini DM. An Essential Role of the Mitochondrial Electron Transport Chain in Cell Proliferation Is to Enable Aspartate Synthesis. *Cell*. 2015;**162**(3):540-551.
159. Sullivan LB, Gui DY, Hosios AM, Bush LN, Freinkman E, Vander Heiden MG. Supporting Aspartate Biosynthesis Is an Essential Function of Respiration in Proliferating Cells. *Cell*. 2015;**162**(3):552-563.
160. Tanner CM, Langston JW. Do environmental toxins cause Parkinson's disease? A critical review. *Neurology*. 1990;**40**(10 Suppl 3):suppl 17-30; discussion 30-11.
161. Heikkila RE, Hess A, Duvoisin RC. Dopaminergic neurotoxicity of 1-methyl-4-phenyl-1,2,5,6-tetrahydropyridine (MPTP) in the mouse: relationships between monoamine oxidase, MPTP metabolism and neurotoxicity. *Life Sci*. 1985;**36**(3):231-236.
162. Heikkila RE, Hess A, Duvoisin RC. Dopaminergic neurotoxicity of 1-methyl-4-phenyl-1,2,5,6-tetrahydropyridine in mice. *Science*. 1984;**224**(4656):1451-1453.
163. Burns RS, Chiueh CC, Markey SP, Ebert MH, Jacobowitz DM, Kopin IJ. A primate model of parkinsonism: selective destruction of dopaminergic neurons in the pars compacta of the substantia nigra by N-methyl-4-phenyl-1,2,3,6-tetrahydropyridine. *Proc Natl Acad Sci U S A*. 1983;**80**(14):4546-4550.
164. Langston JW, Ballard P, Tetrud JW, Irwin I. Chronic Parkinsonism in humans due to a product of meperidine-analog synthesis. *Science*. 1983;**219**(4587):979-980.
165. Langston JW, Irwin I, Langston EB, Forno LS. 1-Methyl-4-phenylpyridinium ion (MPP+): identification of a metabolite of MPTP, a toxin selective to the substantia nigra. *Neurosci Lett*. 1984;**48**(1):87-92.
166. Trevor AJ, Castagnoli N, Jr., Caldera P, Ramsay RR, Singer TP. Bioactivation of MPTP: reactive metabolites and possible biochemical sequelae. *Life Sci*. 1987;**40**(8):713-719.
167. Singer TP, Castagnoli N, Jr., Ramsay RR, Trevor AJ. Biochemical events in the development of parkinsonism induced by 1-methyl-4-phenyl-1,2,3,6-tetrahydropyridine. *J Neurochem*. 1987;**49**(1):1-8.
168. Melamed E, Rosenthal J, Cohen O, Globus M, Uzzan A. Dopamine but not norepinephrine or serotonin uptake inhibitors protect mice against neurotoxicity of MPTP. *Eur J Pharmacol*. 1985;**116**(1-2):179-181.
169. Langston JW, Irwin I, Langston EB, Forno LS. Pargyline prevents MPTP-induced parkinsonism in primates. *Science*. 1984;**225**(4669):1480-1482.
170. Schildknecht S, Di Monte DA, Pape R, Tieu K, Leist M. Tipping Points and Endogenous Determinants of Nigrostriatal Degeneration by MPTP. *Trends Pharmacol Sci*. 2017;**38**(6):541-555.
171. Kettenmann H, Ransom BR. Neuroglia. 2nd ed. Oxford: Oxford University Press; 2005. xix, 601 p. p.
172. Falsig J, van Beek J, Hermann C, Leist M. Molecular basis for detection of invading pathogens in the brain. *J Neurosci Res*. 2008;**86**(7):1434-1447.

173. Efremova L, Chovancova P, Adam M, Gutbier S, Schildknecht S, Leist M. Switching from astrocytic neuroprotection to neurodegeneration by cytokine stimulation. *Arch Toxicol*. 2017;**91**(1):231-246.
174. Fritsche E, Crofton KM, Hernandez AF, Hougaard Bennekou S, Leist M, Bal-Price A, et al. OECD/EFSA workshop on developmental neurotoxicity (DNT): The use of non-animal test methods for regulatory purposes. *ALTEX*. 2017;**34**(2):311-315.
175. Aschner M, Ceccatelli S, Daneshian M, Fritsche E, Hasiwa N, Hartung T, et al. Reference compounds for alternative test methods to indicate developmental neurotoxicity (DNT) potential of chemicals: example lists and criteria for their selection and use. *ALTEX*. 2017;**34**(1):49-74.
176. Lau C, Mole ML, Copeland MF, Rogers JM, Kavlock RJ, Shuey DL, et al. Toward a biologically based dose-response model for developmental toxicity of 5-fluorouracil in the rat: acquisition of experimental data. *Toxicol Sci*. 2001;**59**(1):37-48.
177. Leist M, Lidbury BA, Yang C, Hayden PJ, Kelm JM, Ringeissen S, et al. Novel technologies and an overall strategy to allow hazard assessment and risk prediction of chemicals, cosmetics, and drugs with animal-free methods. *ALTEX*. 2012;**29**(4):373-388.
178. Hartung T, Hoffmann S, Stephens M. Mechanistic validation. *ALTEX*. 2013;**30**(2):119-130.
179. Balmer NV, Weng MK, Zimmer B, Ivanova VN, Chambers SM, Nikolaeva E, et al. Epigenetic changes and disturbed neural development in a human embryonic stem cell-based model relating to the fetal valproate syndrome. *Hum Mol Genet*. 2012;**21**(18):4104-4114.
180. Waldmann T, Grinberg M, Konig A, Rempel E, Schildknecht S, Henry M, et al. Stem Cell Transcriptome Responses and Corresponding Biomarkers That Indicate the Transition from Adaptive Responses to Cytotoxicity. *Chem Res Toxicol*. 2017;**30**(4):905-922.
181. Zimmer B, Lee G, Balmer NV, Meganathan K, Sachinidis A, Studer L, et al. Evaluation of developmental toxicants and signaling pathways in a functional test based on the migration of human neural crest cells. *Environ Health Perspect*. 2012;**120**(8):1116-1122.
182. Kleiderman S, Gutbier S, Ugur Tufekci K, Ortega F, Sa JV, Teixeira AP, et al. Conversion of Nonproliferating Astrocytes into Neurogenic Neural Stem Cells: Control by FGF2 and Interferon-gamma. *Stem Cells*. 2016;**34**(12):2861-2874.
183. Kleiderman S, Sa JV, Teixeira AP, Brito C, Gutbier S, Evje LG, et al. Functional and phenotypic differences of pure populations of stem cell-derived astrocytes and neuronal precursor cells. *Glia*. 2016;**64**(5):695-715.
184. Smirnova L, Hogberg HT, Leist M, Hartung T. Developmental neurotoxicity - challenges in the 21st century and in vitro opportunities. *ALTEX*. 2014;**31**(2):129-156.
185. Balmer NV, Klima S, Rempel E, Ivanova VN, Kolde R, Weng MK, et al. From transient transcriptome responses to disturbed neurodevelopment: role of histone acetylation and methylation as epigenetic switch between reversible and irreversible drug effects. *Arch Toxicol*. 2014;**88**(7):1451-1468.
186. Rempel E, Hoelting L, Waldmann T, Balmer NV, Schildknecht S, Grinberg M, et al. A transcriptome-based classifier to identify developmental toxicants by stem cell testing: design, validation and optimization for histone deacetylase inhibitors. *Arch Toxicol*. 2015;**89**(9):1599-1618.
187. Shinde V, Hoelting L, Srinivasan SP, Meisig J, Meganathan K, Jagtap S, et al. Definition of transcriptome-based indices for quantitative characterization of chemically disturbed stem cell development: introduction of the STOP-Toxukn and STOP-Toxukk tests. *Arch Toxicol*. 2017;**91**(2):839-864.

188. Shinde V, Perumal Srinivasan S, Henry M, Rotshteyn T, Hescheler J, Rahnenfuhrer J, et al. Comparison of a teratogenic transcriptome-based predictive test based on human embryonic versus inducible pluripotent stem cells. *Stem Cell Res Ther*. 2016;**7**(1):190.
189. Sa JV, Kleiderman S, Brito C, Sonnewald U, Leist M, Teixeira AP, et al. Quantification of Metabolic Rearrangements During Neural Stem Cells Differentiation into Astrocytes by Metabolic Flux Analysis. *Neurochem Res*. 2017;**42**(1):244-253.
190. Teslaa T, Teitell MA. Pluripotent stem cell energy metabolism: an update. *EMBO J*. 2015;**34**(2):138-153.
191. Cabre R, Jove M, Naudi A, Ayala V, Pinol-Ripoll G, Gil-Villar MP, et al. Specific Metabolomics Adaptations Define a Differential Regional Vulnerability in the Adult Human Cerebral Cortex. *Front Mol Neurosci*. 2016;**9**:138.
192. Esteban-Martinez L, Sierra-Filardi E, McGreal RS, Salazar-Roa M, Marino G, Seco E, et al. Programmed mitophagy is essential for the glycolytic switch during cell differentiation. *EMBO J*. 2017;**36**(12):1688-1706.
193. Jang S, Nelson JC, Bend EG, Rodriguez-Laureano L, Tueros FG, Cartagenova L, et al. Glycolytic Enzymes Localize to Synapses under Energy Stress to Support Synaptic Function. *Neuron*. 2016;**90**(2):278-291.
194. Magistretti PJ, Allaman I. A cellular perspective on brain energy metabolism and functional imaging. *Neuron*. 2015;**86**(4):883-901.
195. McKenna MC. The glutamate-glutamine cycle is not stoichiometric: fates of glutamate in brain. *J Neurosci Res*. 2007;**85**(15):3347-3358.
196. Folmes CD, Dzeja PP, Nelson TJ, Terzic A. Metabolic plasticity in stem cell homeostasis and differentiation. *Cell Stem Cell*. 2012;**11**(5):596-606.
197. Folmes CD, Nelson TJ, Martinez-Fernandez A, Arrell DK, Lindor JZ, Dzeja PP, et al. Somatic oxidative bioenergetics transitions into pluripotency-dependent glycolysis to facilitate nuclear reprogramming. *Cell Metab*. 2011;**14**(2):264-271.
198. Zhang J, Nuebel E, Daley GQ, Koehler CM, Teitell MA. Metabolic regulation in pluripotent stem cells during reprogramming and self-renewal. *Cell Stem Cell*. 2012;**11**(5):589-595.
199. Ahn WS, Antoniewicz MR. Metabolic flux analysis of CHO cells at growth and non-growth phases using isotopic tracers and mass spectrometry. *Metab Eng*. 2011;**13**(5):598-609.
200. Ahn WS, Antoniewicz MR. Parallel labeling experiments with [1,2-(13)C]glucose and [U-(13)C]glutamine provide new insights into CHO cell metabolism. *Metab Eng*. 2013;**15**:34-47.
201. Schuster S, Boley D, Moller P, Stark H, Kaleta C. Mathematical models for explaining the Warburg effect: a review focussed on ATP and biomass production. *Biochem Soc Trans*. 2015;**43**(6):1187-1194.
202. Vazquez A, Liu J, Zhou Y, Oltvai ZN. Catabolic efficiency of aerobic glycolysis: the Warburg effect revisited. *BMC Syst Biol*. 2010;**4**:58.
203. Gartlon J, Kinsner A, Bal-Price A, Coecke S, Clothier RH. Evaluation of a proposed in vitro test strategy using neuronal and non-neuronal cell systems for detecting neurotoxicity. *Toxicol In Vitro*. 2006;**20**(8):1569-1581.
204. Hu X, Xuan Y. Bypassing cancer drug resistance by activating multiple death pathways--a proposal from the study of circumventing cancer drug resistance by induction of necroptosis. *Cancer Lett*. 2008;**259**(2):127-137.
205. Ninomiya Y, Adams R, Morriss-Kay GM, Eto K. Apoptotic cell death in neuronal differentiation of P19 EC cells: cell death follows reentry into S phase. *J Cell Physiol*. 1997;**172**(1):25-35.

206. Tong ZB, Hogberg H, Kuo D, Sakamuru S, Xia M, Smirnova L, et al. Characterization of three human cell line models for high-throughput neuronal cytotoxicity screening. *J Appl Toxicol*. 2017;**37**(2):167-180.
207. Sengupta S, Johnson BP, Swanson SA, Stewart R, Bradfield CA, Thomson JA. Aggregate culture of human embryonic stem cell-derived hepatocytes in suspension are an improved in vitro model for drug metabolism and toxicity testing. *Toxicol Sci*. 2014;**140**(1):236-245.
208. Haghighat N, McCandless DW. Effect of 6-aminonicotinamide on metabolism of astrocytes and C6-glioma cells. *Metab Brain Dis*. 1997;**12**(1):29-45.
209. Swanson RA, Graham SH. Fluorocitrate and fluoroacetate effects on astrocyte metabolism in vitro. *Brain Res*. 1994;**664**(1-2):94-100.
210. Volbracht C, Leist M, Kolb SA, Nicotera P. Apoptosis in caspase-inhibited neurons. *Mol Med*. 2001;**7**(1):36-48.
211. Kempa S, Hummel J, Schwemmer T, Pietzke M, Strehmel N, Wienkoop S, et al. An automated GCxGC-TOF-MS protocol for batch-wise extraction and alignment of mass isotopomer matrixes from differential 13C-labelling experiments: a case study for photoautotrophic-mixotrophic grown Chlamydomonas reinhardtii cells. *Journal of Basic Microbiology*. 2009;**49**(1):82-91.
212. Kuich PH, Hoffmann N, Kempa S. Maui-VIA: A User-Friendly Software for Visual Identification, Alignment, Correction, and Quantification of Gas Chromatography-Mass Spectrometry Data. *Front Bioeng Biotechnol*. 2014;**2**:84.
213. Carinhas N, Pais DA, Koshkin A, Fernandes P, Coroadinha AS, Carrondo MJ, et al. Metabolic flux profiling of MDCK cells during growth and canine adenovirus vector production. *Sci Rep*. 2016;**6**:23529.
214. Duarte NC, Becker SA, Jamshidi N, Thiele I, Mo ML, Vo TD, et al. Global reconstruction of the human metabolic network based on genomic and bibliomic data. *Proc Natl Acad Sci U S A*. 2007;**104**(6):1777-1782.
215. Nicolae A, Wahrheit J, Bahnemann J, Zeng AP, Heinzle E. Non-stationary 13C metabolic flux analysis of Chinese hamster ovary cells in batch culture using extracellular labeling highlights metabolic reversibility and compartmentation. *BMC Syst Biol*. 2014;**8**:50.
216. Sheikh K, Forster J, Nielsen LK. Modeling hybridoma cell metabolism using a generic genome-scale metabolic model of Mus musculus. *Biotechnol Prog*. 2005;**21**(1):112-121.
217. Norton WT, Poduslo SE. Neuronal perikarya and astroglia of rat brain: chemical composition during myelination. *J Lipid Res*. 1971;**12**(1):84-90.
218. Weitzel M, Noh K, Dalman T, Niedenfuhr S, Stute B, Wiechert W. 13CFLUX2--high-performance software suite for (13)C-metabolic flux analysis. *Bioinformatics*. 2013;**29**(1):143-145.
219. Noh K, Wahl A, Wiechert W. Computational tools for isotopically instationary 13C labeling experiments under metabolic steady state conditions. *Metab Eng*. 2006;**8**(6):554-577.
220. Niedenfuhr S, ten Pierick A, van Dam PT, Suarez-Mendez CA, Noh K, Wahl SA. Natural isotope correction of MS/MS measurements for metabolomics and (13)C fluxomics. *Biotechnol Bioeng*. 2016;**113**(5):1137-1147.
221. Noh K, Droste P, Wiechert W. Visual workflows for 13C-metabolic flux analysis. *Bioinformatics*. 2015;**31**(3):346-354.
222. Shinde V, Klima S, Sureshkumar PS, Meganathan K, Jagtap S, Rempel E, et al. Human Pluripotent Stem Cell Based Developmental Toxicity Assays for Chemical Safety Screening and Systems Biology Data Generation. *J Vis Exp*. 2015(100):e52333.

223. Huang da W, Sherman BT, Lempicki RA. Systematic and integrative analysis of large gene lists using DAVID bioinformatics resources. *Nat Protoc*. 2009;**4**(1):44-57.
224. Huang da W, Sherman BT, Lempicki RA. Bioinformatics enrichment tools: paths toward the comprehensive functional analysis of large gene lists. *Nucleic Acids Res*. 2009;**37**(1):1-13.
225. Croft D, Mundo AF, Haw R, Milacic M, Weiser J, Wu G, et al. The Reactome pathway knowledgebase. *Nucleic Acids Res*. 2014;**42**(Database issue):D472-477.
226. Fabregat A, Jupe S, Matthews L, Sidiropoulos K, Gillespie M, Garapati P, et al. The Reactome Pathway Knowledgebase. *Nucleic Acids Res*. 2017.
227. Thomas PD, Campbell MJ, Kejariwal A, Mi H, Karlak B, Daverman R, et al. PANTHER: a library of protein families and subfamilies indexed by function. *Genome Res*. 2003;**13**(9):2129-2141.
228. Thomas PD, Kejariwal A, Guo N, Mi H, Campbell MJ, Muruganujan A, et al. Applications for protein sequence-function evolution data: mRNA/protein expression analysis and coding SNP scoring tools. *Nucleic Acids Res*. 2006;**34**(Web Server issue):W645-650.
229. Scholz D, Chernyshova Y, Leist M. Control of Abeta release from human neurons by differentiation status and RET signaling. *Neurobiol Aging*. 2013;**34**(1):184-199.
230. Smith TA. Mammalian hexokinases and their abnormal expression in cancer. *Br J Biomed Sci*. 2000;**57**(2):170-178.
231. Wilson JE. Isozymes of mammalian hexokinase: structure, subcellular localization and metabolic function. *J Exp Biol*. 2003;**206**(Pt 12):2049-2057.
232. Zheng X, Boyer L, Jin M, Mertens J, Kim Y, Ma L, et al. Metabolic reprogramming during neuronal differentiation from aerobic glycolysis to neuronal oxidative phosphorylation. *Elife*. 2016;**5**.
233. Kahn A, Meienhofer MC, Cottreau D, Lagrange JL, Dreyfus JC. Phosphofructokinase (PFK) isozymes in man. I. Studies of adult human tissues. *Hum Genet*. 1979;**48**(1):93-108.
234. Fernandez-de-Cossio-Diaz J, Vazquez A. Limits of aerobic metabolism in cancer cells. *Sci Rep*. 2017;**7**(1):13488.
235. Markert EK, Vazquez A. Mathematical models of cancer metabolism. *Cancer Metab*. 2015;**3**:14.
236. Wilmes A, Limonciel A, Aschauer L, Moenks K, Bielow C, Leonard MO, et al. Application of integrated transcriptomic, proteomic and metabolomic profiling for the delineation of mechanisms of drug induced cell stress. *J Proteomics*. 2013;**79**:180-194.
237. Carreras Puigvert J, von Stechow L, Siddappa R, Pines A, Bahjat M, Haazen LC, et al. Systems biology approach identifies the kinase Csnk1a1 as a regulator of the DNA damage response in embryonic stem cells. *Sci Signal*. 2013;**6**(259):ra5.
238. Wilmes A, Bielow C, Ranninger C, Bellwon P, Aschauer L, Limonciel A, et al. Mechanism of cisplatin proximal tubule toxicity revealed by integrating transcriptomics, proteomics, metabolomics and biokinetics. *Toxicol In Vitro*. 2015;**30**(1 Pt A):117-127.
239. Wiechert W, Noh K. Isotopically non-stationary metabolic flux analysis: complex yet highly informative. *Curr Opin Biotechnol*. 2013;**24**(6):979-986.
240. Hensley CT, Wasti AT, DeBerardinis RJ. Glutamine and cancer: cell biology, physiology, and clinical opportunities. *J Clin Invest*. 2013;**123**(9):3678-3684.

241. Cetinbas NM, Sudderth J, Harris RC, Cebeci A, Negri GL, Yilmaz OH, et al. Glucose-dependent anaplerosis in cancer cells is required for cellular redox balance in the absence of glutamine. *Sci Rep*. 2016;**6**:32606.
242. Ahn E, Kumar P, Mukha D, Tzur A, Shlomi T. Temporal fluxomics reveals oscillations in TCA cycle flux throughout the mammalian cell cycle. *Mol Syst Biol*. 2017;**13**(11):953.
243. Sauer JM, Hartung T, Leist M, Knudsen TB, Hoeng J, Hayes AW. Systems Toxicology: The Future of Risk Assessment. *Int J Toxicol*. 2015;**34**(4):346-348.
244. Wise DR, Thompson CB. Glutamine addiction: a new therapeutic target in cancer. *Trends Biochem Sci*. 2010;**35**(8):427-433.
245. Vasilakou E, Machado D, Theorell A, Rocha I, Noh K, Oldiges M, et al. Current state and challenges for dynamic metabolic modeling. *Curr Opin Microbiol*. 2016;**33**:97-104.
246. Ramirez T, Daneshian M, Kamp H, Bois FY, Clench MR, Coen M, et al. Metabolomics in toxicology and preclinical research. *ALTEX*. 2013;**30**(2):209-225.
247. Sturla SJ, Boobis AR, FitzGerald RE, Hoeng J, Kavlock RJ, Schirmer K, et al. Systems toxicology: from basic research to risk assessment. *Chem Res Toxicol*. 2014;**27**(3):314-329.
248. Bellmeyer A, Krase J, Lindgren J, LaBonne C. The protooncogene c-myc is an essential regulator of neural crest formation in xenopus. *Dev Cell*. 2003;**4**(6):827-839.
249. Garcia-Castro MI, Marcelle C, Bronner-Fraser M. Ectodermal Wnt function as a neural crest inducer. *Science*. 2002;**297**(5582):848-851.
250. Nagao M, Campbell K, Burns K, Kuan CY, Trumpp A, Nakafuku M. Coordinated control of self-renewal and differentiation of neural stem cells by Myc and the p19ARF-p53 pathway. *J Cell Biol*. 2008;**183**(7):1243-1257.
251. Varlakhanova NV, Cotterman RF, deVries WN, Morgan J, Donahue LR, Murray S, et al. myc maintains embryonic stem cell pluripotency and self-renewal. *Differentiation*. 2010;**80**(1):9-19.
252. Anso E, Mullen AR, Felsher DW, Mates JM, Deberardinis RJ, Chandel NS. Metabolic changes in cancer cells upon suppression of MYC. *Cancer Metab*. 2013;**1**(1):7.
253. Hirt UA, Gantner F, Leist M. Phagocytosis of nonapoptotic cells dying by caspase-independent mechanisms. *J Immunol*. 2000;**164**(12):6520-6529.
254. Nicotera P, Leist M, Manzo L. Neuronal cell death: a demise with different shapes. *Trends Pharmacol Sci*. 1999;**20**(2):46-51.
255. Buescher JM, Antoniewicz MR, Boros LG, Burgess SC, Brunengraber H, Clish CB, et al. A roadmap for interpreting (13)C metabolite labeling patterns from cells. *Curr Opin Biotechnol*. 2015;**34**:189-201.
256. Nyffeler J, Karreman C, Leisner H, Kim YJ, Lee G, Waldmann T, et al. Design of a high-throughput human neural crest cell migration assay to indicate potential developmental toxicants. *ALTEX*. 2017;**34**(1):75-94.
257. Brown JP, Lynch BS, Curry-Chisolm IM, Shafer TJ, Strickland JD. Assaying Spontaneous Network Activity and Cellular Viability Using Multi-well Microelectrode Arrays. *Methods Mol Biol*. 2017;**1601**:153-170.
258. Pamies D, Barreras P, Block K, Makri G, Kumar A, Wiersma D, et al. A human brain microphysiological system derived from induced pluripotent stem cells to study neurological diseases and toxicity. *ALTEX*. 2017;**34**(3):362-376.
259. Rohn H, Junker A, Hartmann A, Grafahrend-Belau E, Treutler H, Klapperstuck M, et al. VANTED v2: a framework for systems biology applications. *BMC Syst Biol*. 2012;**6**:139.

260. Nims RW, Reid Y. Best practices for authenticating cell lines. *In Vitro Cell Dev Biol Anim*. 2017;**53**(10):880-887.
261. Bian X, Yang Z, Feng H, Sun H, Liu Y. A Combination of Species Identification and STR Profiling Identifies Cross-contaminated Cells from 482 Human Tumor Cell Lines. *Sci Rep*. 2017;**7**(1):9774.
262. Youssoufian H, Pyeritz RE. Mechanisms and consequences of somatic mosaicism in humans. *Nat Rev Genet*. 2002;**3**(10):748-758.
263. Laurent LC, Ulitsky I, Slavin I, Tran H, Schork A, Morey R, et al. Dynamic changes in the copy number of pluripotency and cell proliferation genes in human ESCs and iPSCs during reprogramming and time in culture. *Cell Stem Cell*. 2011;**8**(1):106-118.
264. Gore A, Li Z, Fung HL, Young JE, Agarwal S, Antosiewicz-Bourget J, et al. Somatic coding mutations in human induced pluripotent stem cells. *Nature*. 2011;**471**(7336):63-67.
265. Kleensang A, Vantangoli MM, Odwin-DaCosta S, Andersen ME, Boekelheide K, Bouhifd M, et al. Genetic variability in a frozen batch of MCF-7 cells invisible in routine authentication affecting cell function. *Sci Rep*. 2016;**6**:28994.
266. Martins-Taylor K, Xu RH. Concise review: Genomic stability of human induced pluripotent stem cells. *Stem Cells*. 2012;**30**(1):22-27.
267. Frattini A, Fabbri M, Valli R, De Paoli E, Montalbano G, Gribaldo L, et al. High variability of genomic instability and gene expression profiling in different HeLa clones. *Sci Rep*. 2015;**5**:15377.
268. Miller JK, Buchner N, Timms L, Tam S, Luo X, Brown AM, et al. Use of Sequenom sample ID Plus(R) SNP genotyping in identification of FFPE tumor samples. *PLoS One*. 2014;**9**(2):e88163.
269. Cheng L, Hansen NF, Zhao L, Du Y, Zou C, Donovan FX, et al. Low incidence of DNA sequence variation in human induced pluripotent stem cells generated by nonintegrating plasmid expression. *Cell Stem Cell*. 2012;**10**(3):337-344.
270. Cai X, Evrony GD, Lehmann HS, Elhosary PC, Mehta BK, Poduri A, et al. Single-cell, genome-wide sequencing identifies clonal somatic copy-number variation in the human brain. *Cell Rep*. 2015;**10**(4):645.
271. Stefansson H, Meyer-Lindenberg A, Steinberg S, Magnusdottir B, Morgen K, Arnarsdottir S, et al. CNVs conferring risk of autism or schizophrenia affect cognition in controls. *Nature*. 2014;**505**(7483):361-366.
272. McConnell MJ, Lindberg MR, Brennand KJ, Piper JC, Voet T, Cowing-Zitron C, et al. Mosaic copy number variation in human neurons. *Science*. 2013;**342**(6158):632-637.
273. Coufal NG, Garcia-Perez JL, Peng GE, Yeo GW, Mu Y, Lovci MT, et al. L1 retrotransposition in human neural progenitor cells. *Nature*. 2009;**460**(7259):1127-1131.
274. Reid YA. Best practices for naming, receiving, and managing cells in culture. *In Vitro Cell Dev Biol Anim*. 2017;**53**(9):761-774.
275. Zhang XM, Yin M, Zhang MH. Cell-based assays for Parkinson's disease using differentiated human LUHMES cells. *Acta Pharmacol Sin*. 2014;**35**(7):945-956.
276. Karreman C. AiO, combining DNA/protein programs and oligo-management. *Bioinformatics*. 2002;**18**(6):884-885.
277. Drmanac R, Sparks AB, Callow MJ, Halpern AL, Burns NL, Kermani BG, et al. Human genome sequencing using unchained base reads on self-assembling DNA nanoarrays. *Science*. 2010;**327**(5961):78-81.

278. Raczy C, Petrovski R, Saunders CT, Chorny I, Kruglyak S, Margulies EH, et al. Isaac: ultra-fast whole-genome secondary analysis on Illumina sequencing platforms. *Bioinformatics*. 2013;**29**(16):2041-2043.
279. Purcell S, Neale B, Todd-Brown K, Thomas L, Ferreira MA, Bender D, et al. PLINK: a tool set for whole-genome association and population-based linkage analyses. *Am J Hum Genet*. 2007;**81**(3):559-575.
280. Glusman G, Severson A, Dhankani V, Robinson M, Farrah T, Mauldin DE, et al. Identification of copy number variants in whole-genome data using Reference Coverage Profiles. *Front Genet*. 2015;**6**:45.
281. MacDonald JR, Ziman R, Yuen RK, Feuk L, Scherer SW. The Database of Genomic Variants: a curated collection of structural variation in the human genome. *Nucleic Acids Res*. 2014;**42**(Database issue):D986-992.
282. Reumers J, De Rijk P, Zhao H, Liekens A, Smeets D, Cleary J, et al. Optimized filtering reduces the error rate in detecting genomic variants by short-read sequencing. *Nat Biotechnol*. 2012;**30**(1):61-68.
283. Pallocca G, Nyffeler J, Dolde X, Grinberg M, Gstraunthaler G, Waldmann T, et al. Impairment of human neural crest cell migration by prolonged exposure to interferon-beta. *Arch Toxicol*. 2017;**91**(10):3385-3402.
284. Yang X, Xu S, Consortium HP-AS, Indian Genome Variation C. Identification of close relatives in the HUGO Pan-Asian SNP database. *PLoS One*. 2011;**6**(12):e29502.
285. Rowen L, Young J, Birditt B, Kaur A, Madan A, Philipps DL, et al. Analysis of the human neurexin genes: alternative splicing and the generation of protein diversity. *Genomics*. 2002;**79**(4):587-597.
286. Budzynski MA, Puustinen MC, Joutsen J, Sistonen L. Uncoupling Stress-Inducible Phosphorylation of Heat Shock Factor 1 from Its Activation. *Mol Cell Biol*. 2015;**35**(14):2530-2540.
287. Terron A, Bal-Price A, Paini A, Monnet-Tschudi F, Bennekou SH, Members EWE, et al. An adverse outcome pathway for parkinsonian motor deficits associated with mitochondrial complex I inhibition. *Arch Toxicol*. 2018;**92**(1):41-82.
288. Harris G, Hogberg H, Hartung T, Smirnova L. 3D Differentiation of LUHMES Cell Line to Study Recovery and Delayed Neurotoxic Effects. *Curr Protoc Toxicol*. 2017;**73**:11 23 11-11 23 28.
289. Sarkar S, Malovic E, Harishchandra DS, Ghaisas S, Panicker N, Charli A, et al. Mitochondrial impairment in microglia amplifies NLRP3 inflammasome proinflammatory signaling in cell culture and animal models of Parkinson's disease. *NPJ Parkinsons Dis*. 2017;**3**:30.
290. Szego EM, Gerhardt E, Outeiro TF. Sirtuin 2 enhances dopaminergic differentiation via the AKT/GSK-3beta/beta-catenin pathway. *Neurobiol Aging*. 2017;**56**:7-16.
291. Xiang W, Schlachetzki JC, Helling S, Bussmann JC, Berlinghof M, Schaffer TE, et al. Oxidative stress-induced posttranslational modifications of alpha-synuclein: specific modification of alpha-synuclein by 4-hydroxy-2-nonenal increases dopaminergic toxicity. *Mol Cell Neurosci*. 2013;**54**:71-83.
292. Gartler SM. Apparent Hela cell contamination of human heteroploid cell lines. *Nature*. 1968;**217**(5130):750-751.
293. Dolgin E. Venerable brain-cancer cell line faces identity crisis. *Nature*. 2016;**537**(7619):149-150.
294. Dirks WG, Drexler HG. STR DNA typing of human cell lines: detection of intra- and interspecies cross-contamination. *Methods Mol Biol*. 2013;**946**:27-38.

295. Pamies D, Bal-Price A, Simeonov A, Tagle D, Allen D, Gerhold D, et al. Good Cell Culture Practice for stem cells and stem-cell-derived models. *ALTEX*. 2017;**34**(1):95-132.
296. Freedman LP. Know Thy Cells: Improving Biomedical Research Reproducibility. *Sci Transl Med*. 2015;**7**(294):294ed297.
297. Grobner SN, Worst BC, Weischenfeldt J, Buchhalter I, Kleinheinz K, Rudneva VA, et al. The landscape of genomic alterations across childhood cancers. *Nature*. 2018.
298. Ma X, Liu Y, Liu Y, Alexandrov LB, Edmonson MN, Gawad C, et al. Pan-cancer genome and transcriptome analyses of 1,699 paediatric leukaemias and solid tumours. *Nature*. 2018.
299. Ko P, Misaghi S, Hu Z, Zhan D, Tsukuda J, Yim M, et al. Probing the importance of clonality: Single cell subcloning of clonally derived CHO cell lines yields widely diverse clones differing in growth, productivity, and product quality. *Biotechnol Prog*. 2017.
300. Mor DE, Tsika E, Mazzulli JR, Gould NS, Kim H, Daniels MJ, et al. Dopamine induces soluble alpha-synuclein oligomers and nigrostriatal degeneration. *Nat Neurosci*. 2017;**20**(11):1560-1568.
301. Mosharov EV, Larsen KE, Kanter E, Phillips KA, Wilson K, Schmitz Y, et al. Interplay between cytosolic dopamine, calcium, and alpha-synuclein causes selective death of substantia nigra neurons. *Neuron*. 2009;**62**(2):218-229.
302. Cui M, Aras R, Christian WV, Rappold PM, Hatwar M, Panza J, et al. The organic cation transporter-3 is a pivotal modulator of neurodegeneration in the nigrostriatal dopaminergic pathway. *Proc Natl Acad Sci U S A*. 2009;**106**(19):8043-8048.
303. Stacey G. Sourcing and using stem cell lines for radiation research: Potential, challenges and good stem cell culture practice. *Int J Radiat Biol*. 2012;**88**(10):703-708.
304. Stacey G. Stem Cell Banking: A Global View. *Methods Mol Biol*. 2017;**1590**:3-10.
305. Dexter DT, Jenner P. Parkinson disease: from pathology to molecular disease mechanisms. *Free Radic Biol Med*. 2013;**62**:132-144.
306. Blesa J, Przedborski S. Parkinson's disease: animal models and dopaminergic cell vulnerability. *Front Neuroanat*. 2014;**8**:155.
307. Ekstrand MI, Galter D. The MitoPark Mouse - an animal model of Parkinson's disease with impaired respiratory chain function in dopamine neurons. *Parkinsonism Relat Disord*. 2009;**15 Suppl 3**:S185-188.
308. Langley M, Ghosh A, Charli A, Sarkar S, Ay M, Luo J, et al. Mito-Apocynin Prevents Mitochondrial Dysfunction, Microglial Activation, Oxidative Damage, and Progressive Neurodegeneration in MitoPark Transgenic Mice. *Antioxid Redox Signal*. 2017;**27**(14):1048-1066.
309. Schapira AH, Olanow CW, Greenamyre JT, Bezard E. Slowing of neurodegeneration in Parkinson's disease and Huntington's disease: future therapeutic perspectives. *Lancet*. 2014;**384**(9942):545-555.
310. Bentea E, Verbruggen L, Massie A. The Proteasome Inhibition Model of Parkinson's Disease. *J Parkinsons Dis*. 2017;**7**(1):31-63.
311. McNaught KS, Bjorklund LM, Belizaire R, Isacson O, Jenner P, Olanow CW. Proteasome inhibition causes nigral degeneration with inclusion bodies in rats. *Neuroreport*. 2002;**13**(11):1437-1441.
312. McNaught KS, Mytilineou C, Jnobaptiste R, Yabut J, Shashidharan P, Jennert P, et al. Impairment of the ubiquitin-proteasome system causes dopaminergic cell

death and inclusion body formation in ventral mesencephalic cultures. *J Neurochem*. 2002;**81**(2):301-306.
313. McNaught KS, Perl DP, Brownell AL, Olanow CW. Systemic exposure to proteasome inhibitors causes a progressive model of Parkinson's disease. *Ann Neurol*. 2004;**56**(1):149-162.
314. Zhang Y, Nicholatos J, Dreier JR, Ricoult SJ, Widenmaier SB, Hotamisligil GS, et al. Coordinated regulation of protein synthesis and degradation by mTORC1. *Nature*. 2014;**513**(7518):440-443.
315. Di Maio R, Barrett PJ, Hoffman EK, Barrett CW, Zharikov A, Borah A, et al. alpha-Synuclein binds to TOM20 and inhibits mitochondrial protein import in Parkinson's disease. *Sci Transl Med*. 2016;**8**(342):342ra378.
316. Sotzny F, Schormann E, Kuhlewindt I, Koch A, Brehm A, Goldbach-Mansky R, et al. TCF11/Nrf1-Mediated Induction of Proteasome Expression Prevents Cytotoxicity by Rotenone. *Antioxid Redox Signal*. 2016;**25**(16):870-885.
317. Suraweera A, Munch C, Hanssum A, Bertolotti A. Failure of amino acid homeostasis causes cell death following proteasome inhibition. *Mol Cell*. 2012;**48**(2):242-253.
318. Kuegler PB, Baumann BA, Zimmer B, Keller S, Marx A, Kadereit S, et al. GFAP-independent inflammatory competence and trophic functions of astrocytes generated from murine embryonic stem cells. *Glia*. 2012;**60**(2):218-228.
319. Allaman I, Belanger M, Magistretti PJ. Astrocyte-neuron metabolic relationships: for better and for worse. *Trends Neurosci*. 2011;**34**(2):76-87.
320. Gupta K, Chandran S, Hardingham GE. Human stem cell-derived astrocytes and their application to studying Nrf2-mediated neuroprotective pathways and therapeutics in neurodegeneration. *Br J Clin Pharmacol*. 2013;**75**(4):907-918.
321. Haskew-Layton RE, Payappilly JB, Smirnova NA, Ma TC, Chan KK, Murphy TH, et al. Controlled enzymatic production of astrocytic hydrogen peroxide protects neurons from oxidative stress via an Nrf2-independent pathway. *Proc Natl Acad Sci U S A*. 2010;**107**(40):17385-17390.
322. Gleixner AM, Hutchison DF, Sannino S, Bhatia TN, Leak LC, Flaherty PT, et al. N-Acetyl-l-Cysteine Protects Astrocytes against Proteotoxicity without Recourse to Glutathione. *Mol Pharmacol*. 2017;**92**(5):564-575.
323. Fernandez-Fernandez S, Almeida A, Bolanos JP. Antioxidant and bioenergetic coupling between neurons and astrocytes. *Biochem J*. 2012;**443**(1):3-11.
324. Radhakrishnan SK, Lee CS, Young P, Beskow A, Chan JY, Deshaies RJ. Transcription factor Nrf1 mediates the proteasome recovery pathway after proteasome inhibition in mammalian cells. *Mol Cell*. 2010;**38**(1):17-28.
325. Steffen J, Seeger M, Koch A, Kruger E. Proteasomal degradation is transcriptionally controlled by TCF11 via an ERAD-dependent feedback loop. *Mol Cell*. 2010;**40**(1):147-158.
326. Berliocchi L, Fava E, Leist M, Horvat V, Dinsdale D, Read D, et al. Botulinum neurotoxin C initiates two different programs for neurite degeneration and neuronal apoptosis. *J Cell Biol*. 2005;**168**(4):607-618.
327. Mathisen GA, Fonnum F, Paulsen RE. Contributing mechanisms for cysteine excitotoxicity in cultured cerebellar granule cells. *Neurochem Res*. 1996;**21**(3):293-298.
328. Hogins J, Crawford DC, Zorumski CF, Mennerick S. Excitotoxicity triggered by Neurobasal culture medium. *PLoS One*. 2011;**6**(9):e25633.

329. Do KQ, Trabesinger AH, Kirsten-Kruger M, Lauer CJ, Dydak U, Hell D, et al. Schizophrenia: glutathione deficit in cerebrospinal fluid and prefrontal cortex in vivo. *Eur J Neurosci*. 2000;**12**(10):3721-3728.
330. Dringen R, Hirrlinger J. Glutathione pathways in the brain. *Biol Chem*. 2003;**384**(4):505-516.
331. Grima G, Benz B, Parpura V, Cuenod M, Do KQ. Dopamine-induced oxidative stress in neurons with glutathione deficit: implication for schizophrenia. *Schizophr Res*. 2003;**62**(3):213-224.
332. Rana S, Dringen R. Gap junction hemichannel-mediated release of glutathione from cultured rat astrocytes. *Neurosci Lett*. 2007;**415**(1):45-48.
333. Li B, Chen R, Chen L, Qiu P, Ai X, Huang E, et al. Effects of DDIT4 in Methamphetamine-Induced Autophagy and Apoptosis in Dopaminergic Neurons. *Mol Neurobiol*. 2017;**54**(3):1642-1660.
334. Malagelada C, Ryu EJ, Biswas SC, Jackson-Lewis V, Greene LA. RTP801 is elevated in Parkinson brain substantia nigral neurons and mediates death in cellular models of Parkinson's disease by a mechanism involving mammalian target of rapamycin inactivation. *J Neurosci*. 2006;**26**(39):9996-10005.
335. Quiros PM, Prado MA, Zamboni N, D'Amico D, Williams RW, Finley D, et al. Multi-omics analysis identifies ATF4 as a key regulator of the mitochondrial stress response in mammals. *J Cell Biol*. 2017;**216**(7):2027-2045.
336. Shih AY, Johnson DA, Wong G, Kraft AD, Jiang L, Erb H, et al. Coordinate regulation of glutathione biosynthesis and release by Nrf2-expressing glia potently protects neurons from oxidative stress. *J Neurosci*. 2003;**23**(8):3394-3406.
337. Bell KF, Al-Mubarak B, Fowler JH, Baxter PS, Gupta K, Tsujita T, et al. Mild oxidative stress activates Nrf2 in astrocytes, which contributes to neuroprotective ischemic preconditioning. *Proc Natl Acad Sci U S A*. 2011;**108**(1):E1-2; author reply E3-4.
338. Gegg ME, Beltran B, Salas-Pino S, Bolanos JP, Clark JB, Moncada S, et al. Differential effect of nitric oxide on glutathione metabolism and mitochondrial function in astrocytes and neurones: implications for neuroprotection/neurodegeneration? *J Neurochem*. 2003;**86**(1):228-237.
339. Gupta K, Patani R, Baxter P, Serio A, Story D, Tsujita T, et al. Human embryonic stem cell derived astrocytes mediate non-cell-autonomous neuroprotection through endogenous and drug-induced mechanisms. *Cell Death Differ*. 2012;**19**(5):779-787.
340. Heales SJ, Lam AA, Duncan AJ, Land JM. Neurodegeneration or neuroprotection: the pivotal role of astrocytes. *Neurochem Res*. 2004;**29**(3):513-519.
341. Shih AY, Imbeault S, Barakauskas V, Erb H, Jiang L, Li P, et al. Induction of the Nrf2-driven antioxidant response confers neuroprotection during mitochondrial stress in vivo. *J Biol Chem*. 2005;**280**(24):22925-22936.
342. Betarbet R, Canet-Aviles RM, Sherer TB, Mastroberardino PG, McLendon C, Kim JH, et al. Intersecting pathways to neurodegeneration in Parkinson's disease: effects of the pesticide rotenone on DJ-1, alpha-synuclein, and the ubiquitin-proteasome system. *Neurobiol Dis*. 2006;**22**(2):404-420.
343. Starheim KK, Holien T, Misund K, Johansson I, Baranowska KA, Sponaas AM, et al. Intracellular glutathione determines bortezomib cytotoxicity in multiple myeloma cells. *Blood Cancer J*. 2016;**6**(7):e446.
344. Banerjee R, Vitvitsky V, Garg SK. The undertow of sulfur metabolism on glutamatergic neurotransmission. *Trends Biochem Sci*. 2008;**33**(9):413-419.

345. Diwakar L, Ravindranath V. Inhibition of cystathionine-gamma-lyase leads to loss of glutathione and aggravation of mitochondrial dysfunction mediated by excitatory amino acid in the CNS. *Neurochem Int*. 2007;**50**(2):418-426.
346. Vitvitsky V, Thomas M, Ghorpade A, Gendelman HE, Banerjee R. A functional transsulfuration pathway in the brain links to glutathione homeostasis. *J Biol Chem*. 2006;**281**(47):35785-35793.
347. Satoh T, Kosaka K, Itoh K, Kobayashi A, Yamamoto M, Shimojo Y, et al. Carnosic acid, a catechol-type electrophilic compound, protects neurons both in vitro and in vivo through activation of the Keap1/Nrf2 pathway via S-alkylation of targeted cysteines on Keap1. *J Neurochem*. 2008;**104**(4):1116-1131.
348. Sen E, Basu A, Willing LB, Uliasz TF, Myrkalo JL, Vannucci SJ, et al. Pre-conditioning induces the precocious differentiation of neonatal astrocytes to enhance their neuroprotective properties. *ASN Neuro*. 2011;**3**(3):e00062.
349. Silva-Palacios A, Colin-Gonzalez AL, Lopez-Cervantes SP, Zazueta C, Luna-Lopez A, Santamaria A, et al. Tert-buthylhydroquinone pre-conditioning exerts dual effects in old female rats exposed to 3-nitropropionic acid. *Redox Biol*. 2017;**12**:610-624.
350. Kraft AD, Johnson DA, Johnson JA. Nuclear factor E2-related factor 2-dependent antioxidant response element activation by tert-butylhydroquinone and sulforaphane occurring preferentially in astrocytes conditions neurons against oxidative insult. *J Neurosci*. 2004;**24**(5):1101-1112.
351. Bakshi R, Zhang H, Logan R, Joshi I, Xu Y, Chen X, et al. Neuroprotective effects of urate are mediated by augmenting astrocytic glutathione synthesis and release. *Neurobiol Dis*. 2015;**82**:574-579.
352. Ahmad T, Valentovic MA, Rankin GO. Effects of cytochrome P450 single nucleotide polymorphisms on methadone metabolism and pharmacodynamics. *Biochem Pharmacol*. 2018.
353. Lee J, Woo DH, Park HJ, Park K, Ko DS, Kim JH. Human induced pluripotent stem cell line with cytochrome P450 enzyme polymorphism (CYP2C19*2/CYP3A5*3C) generated from lymphoblastoid cells. *Stem Cell Res*. 2017;**27**:34-37.
354. Chung SY, Kishinevsky S, Mazzulli JR, Graziotto J, Mrejeru A, Mosharov EV, et al. Parkin and PINK1 Patient iPSC-Derived Midbrain Dopamine Neurons Exhibit Mitochondrial Dysfunction and alpha-Synuclein Accumulation. *Stem Cell Reports*. 2016;**7**(4):664-677.
355. O'Huallachain M, Karczewski KJ, Weissman SM, Urban AE, Snyder MP. Extensive genetic variation in somatic human tissues. *Proc Natl Acad Sci U S A*. 2012;**109**(44):18018-18023.
356. Adey A, Burton JN, Kitzman JO, Hiatt JB, Lewis AP, Martin BK, et al. The haplotype-resolved genome and epigenome of the aneuploid HeLa cancer cell line. *Nature*. 2013;**500**(7461):207-211.
357. Hussein SM, Batada NN, Vuoristo S, Ching RW, Autio R, Narva E, et al. Copy number variation and selection during reprogramming to pluripotency. *Nature*. 2011;**471**(7336):58-62.
358. Shaffer LG, Bejjani BA, Torchia B, Kirkpatrick S, Coppinger J, Ballif BC. The identification of microdeletion syndromes and other chromosome abnormalities: cytogenetic methods of the past, new technologies for the future. *Am J Med Genet C Semin Med Genet*. 2007;**145C**(4):335-345.
359. Abrams SL, Ruvolo PP, Ruvolo VR, Ligresti G, Martelli AM, Cocco L, et al. Targeting signaling and apoptotic pathways involved in chemotherapeutic drug-resistance of hematopoietic cells. *Oncotarget*. 2017;**8**(44):76525-76557.

360. Yang W, Shen Y, Wei J, Liu F. MicroRNA-153/Nrf-2/GPx1 pathway regulates radiosensitivity and stemness of glioma stem cells via reactive oxygen species. *Oncotarget*. 2015;**6**(26):22006-22027.
361. Xu X, Huang E, Tai Y, Zhao X, Chen X, Chen C, et al. Nupr1 Modulates Methamphetamine-Induced Dopaminergic Neuronal Apoptosis and Autophagy through CHOP-Trib3-Mediated Endoplasmic Reticulum Stress Signaling Pathway. *Front Mol Neurosci*. 2017;**10**:203.
362. Lepsch LB, Planeta CS, Scavone C. Cocaine Causes Apoptotic Death in Rat Mesencephalon and Striatum Primary Cultures. *Biomed Res Int*. 2015;**2015**:750752.
363. Kotzbauer PT, Cairns NJ, Campbell MC, Willis AW, Racette BA, Tabbal SD, et al. Pathologic accumulation of alpha-synuclein and Abeta in Parkinson disease patients with dementia. *Arch Neurol*. 2012;**69**(10):1326-1331.
364. McNaught KS. Proteolytic dysfunction in neurodegenerative disorders. *Int Rev Neurobiol*. 2004;**62**:95-119.
365. McNaught KS, Jackson T, JnoBaptiste R, Kapustin A, Olanow CW. Proteasomal dysfunction in sporadic Parkinson's disease. *Neurology*. 2006;**66**(10 Suppl 4):S37-49.
366. McNaught KS, Olanow CW. Proteolytic stress: a unifying concept for the etiopathogenesis of Parkinson's disease. *Ann Neurol*. 2003;**53 Suppl 3**:S73-84; discussion S84-76.
367. Aubertin E, Le Lourd R. [Professor Pierre Sourreil (1905-1972)]. *Bord Med*. 1972;**5**(15):1947.
368. Kisselev AF, van der Linden WA, Overkleeft HS. Proteasome inhibitors: an expanding army attacking a unique target. *Chem Biol*. 2012;**19**(1):99-115.
369. Pollanen MS, Dickson DW, Bergeron C. Pathology and biology of the Lewy body. *J Neuropathol Exp Neurol*. 1993;**52**(3):183-191.
370. McNaught KS, Jenner P. Proteasomal function is impaired in substantia nigra in Parkinson's disease. *Neurosci Lett*. 2001;**297**(3):191-194.
371. Shamoto-Nagai M, Maruyama W, Akao Y, Osawa T, Tribl F, Gerlach M, et al. Neuromelanin inhibits enzymatic activity of 26S proteasome in human dopaminergic SH-SY5Y cells. *J Neural Transm (Vienna)*. 2004;**111**(10-11):1253-1265.
372. Zafar KS, Inayat-Hussain SH, Ross D. A comparative study of proteasomal inhibition and apoptosis induced in N27 mesencephalic cells by dopamine and MG132. *J Neurochem*. 2007;**102**(3):913-921.
373. Do YJ, Yun SY, Park MY, Kim E. The M458L missense mutation disrupts the catalytic properties of Parkin. *FEBS Lett*. 2018;**592**(1):78-88.
374. Rath A, Klein A, Papazoglou A, Pruszak J, Garcia J, Krause M, et al. Survival and functional restoration of human fetal ventral mesencephalon following transplantation in a rat model of Parkinson's disease. *Cell Transplant*. 2013;**22**(7):1281-1293.
375. Sun F, Anantharam V, Zhang D, Latchoumycandane C, Kanthasamy A, Kanthasamy AG. Proteasome inhibitor MG-132 induces dopaminergic degeneration in cell culture and animal models. *Neurotoxicology*. 2006;**27**(5):807-815.
376. Fornai F, Lenzi P, Gesi M, Ferrucci M, Lazzeri G, Busceti CL, et al. Fine structure and biochemical mechanisms underlying nigrostriatal inclusions and cell death after proteasome inhibition. *J Neurosci*. 2003;**23**(26):8955-8966.
377. Lee CS, Han ES, Park ES, Bang H. Inhibition of MG132-induced mitochondrial dysfunction and cell death in PC12 cells by 3-morpholinosydnonimine. *Brain Res*. 2005;**1036**(1-2):18-26.
378. Kimball SR, Jefferson LS. Induction of REDD1 gene expression in the liver in response to endoplasmic reticulum stress is mediated through a PERK, eIF2alpha

phosphorylation, ATF4-dependent cascade. *Biochem Biophys Res Commun*. 2012;**427**(3):485-489.
379. Katiyar S, Liu E, Knutzen CA, Lang ES, Lombardo CR, Sankar S, et al. REDD1, an inhibitor of mTOR signalling, is regulated by the CUL4A-DDB1 ubiquitin ligase. *EMBO Rep*. 2009;**10**(8):866-872.
380. Ryder EF, Snyder EY, Cepko CL. Establishment and characterization of multipotent neural cell lines using retrovirus vector-mediated oncogene transfer. *J Neurobiol*. 1990;**21**(2):356-375.
381. Price TN, Burke JF, Mayne LV. A novel human astrocyte cell line (A735) with astrocyte-specific neurotransmitter function. *In Vitro Cell Dev Biol Anim*. 1999;**35**(5):279-288.
382. Frisa PS, Goodman MN, Smith GM, Silver J, Jacobberger JW. Immortalization of immature and mature mouse astrocytes with SV40 T antigen. *J Neurosci Res*. 1994;**39**(1):47-56.
383. Li L, Chao J, Shi Y. Modeling neurological diseases using iPSC-derived neural cells : iPSC modeling of neurological diseases. *Cell Tissue Res*. 2018;**371**(1):143-151.
384. Hansson E. Primary astroglial cultures. A biochemical and functional evaluation. *Neurochem Res*. 1986;**11**(6):759-767.
385. Rouach N, Glowinski J, Giaume C. Activity-dependent neuronal control of gap-junctional communication in astrocytes. *J Cell Biol*. 2000;**149**(7):1513-1526.
386. Dringen R, Pfeiffer B, Hamprecht B. Synthesis of the antioxidant glutathione in neurons: supply by astrocytes of CysGly as precursor for neuronal glutathione. *J Neurosci*. 1999;**19**(2):562-569.
387. Desagher S, Glowinski J, Premont J. Astrocytes protect neurons from hydrogen peroxide toxicity. *J Neurosci*. 1996;**16**(8):2553-2562.
388. Westergaard N, Sonnewald U, Petersen SB, Schousboe A. Characterization of microcarrier cultures of neurons and astrocytes from cerebral cortex and cerebellum. *Neurochem Res*. 1991;**16**(8):919-923.
389. Westergaard N, Fosmark H, Schousboe A. Metabolism and release of glutamate in cerebellar granule cells cocultured with astrocytes from cerebellum or cerebral cortex. *J Neurochem*. 1991;**56**(1):59-66.
390. Rudge JS, Pasnikowski EM, Holst P, Lindsay RM. Changes in neurotrophic factor expression and receptor activation following exposure of hippocampal neuron/astrocyte cocultures to kainic acid. *J Neurosci*. 1995;**15**(10):6856-6867.
391. Anderl JL, Redpath S, Ball AJ. A neuronal and astrocyte co-culture assay for high content analysis of neurotoxicity. *J Vis Exp*. 2009(27).
392. Roque PJ, Guizzetti M, Giordano G, Costa LG. Quantification of synaptic structure formation in cocultures of astrocytes and hippocampal neurons. *Methods Mol Biol*. 2011;**758**:361-390.
393. Gantner F, Leist M, Kusters S, Vogt K, Volk HD, Tiegs G. T cell stimulus-induced crosstalk between lymphocytes and liver macrophages results in augmented cytokine release. *Exp Cell Res*. 1996;**229**(1):137-146.
394. Westergaard N, Larsson OM, Jensen B, Schousboe A. Synthesis and release of GABA in cerebral cortical neurons co-cultured with astrocytes from cerebral cortex or cerebellum. *Neurochem Int*. 1992;**20**(4):567-575.
395. Walsh E, Ueda Y, Nakanishi H, Yoshida K. Neuronal survival and neurite extension supported by astrocytes co-cultured in transwells. *Neurosci Lett*. 1992;**138**(1):103-106.

396. Chen Y, Vartiainen NE, Ying W, Chan PH, Koistinaho J, Swanson RA. Astrocytes protect neurons from nitric oxide toxicity by a glutathione-dependent mechanism. *J Neurochem*. 2001;**77**(6):1601-1610.
397. Park LC, Zhang H, Gibson GE. Co-culture with astrocytes or microglia protects metabolically impaired neurons. *Mech Ageing Dev*. 2001;**123**(1):21-27.
398. Burdo J, Dargusch R, Schubert D. Distribution of the cystine/glutamate antiporter system xc- in the brain, kidney, and duodenum. *J Histochem Cytochem*. 2006;**54**(5):549-557.
399. Frade J, Pope S, Schmidt M, Dringen R, Barbosa R, Pocock J, et al. Glutamate induces release of glutathione from cultured rat astrocytes--a possible neuroprotective mechanism? *J Neurochem*. 2008;**105**(4):1144-1152.
400. Garg SK, Banerjee R, Kipnis J. Neuroprotective immunity: T cell-derived glutamate endows astrocytes with a neuroprotective phenotype. *J Immunol*. 2008;**180**(6):3866-3873.
401. Fitzmaurice PS, Ang L, Guttman M, Rajput AH, Furukawa Y, Kish SJ. Nigral glutathione deficiency is not specific for idiopathic Parkinson's disease. *Mov Disord*. 2003;**18**(9):969-976.
402. Pearce RK, Owen A, Daniel S, Jenner P, Marsden CD. Alterations in the distribution of glutathione in the substantia nigra in Parkinson's disease. *J Neural Transm (Vienna)*. 1997;**104**(6-7):661-677.
403. Sian J, Dexter DT, Lees AJ, Daniel S, Agid Y, Javoy-Agid F, et al. Alterations in glutathione levels in Parkinson's disease and other neurodegenerative disorders affecting basal ganglia. *Ann Neurol*. 1994;**36**(3):348-355.
404. Sofic E, Lange KW, Jellinger K, Riederer P. Reduced and oxidized glutathione in the substantia nigra of patients with Parkinson's disease. *Neurosci Lett*. 1992;**142**(2):128-130.
405. Mythri RB, Venkateshappa C, Harish G, Mahadevan A, Muthane UB, Yasha TC, et al. Evaluation of markers of oxidative stress, antioxidant function and astrocytic proliferation in the striatum and frontal cortex of Parkinson's disease brains. *Neurochem Res*. 2011;**36**(8):1452-1463.
406. Datta I, Ganapathy K, Razdan R, Bhonde R. Location and Number of Astrocytes Determine Dopaminergic Neuron Survival and Function Under 6-OHDA Stress Mediated Through Differential BDNF Release. *Mol Neurobiol*. 2017.
407. Liddell JR, Robinson SR, Dringen R, Bishop GM. Astrocytes retain their antioxidant capacity into advanced old age. *Glia*. 2010;**58**(12):1500-1509.
408. Mullett SJ, Di Maio R, Greenamyre JT, Hinkle DA. DJ-1 expression modulates astrocyte-mediated protection against neuronal oxidative stress. *J Mol Neurosci*. 2013;**49**(3):507-511.
409. Jansen AH, Reits EA, Hol EM. The ubiquitin proteasome system in glia and its role in neurodegenerative diseases. *Front Mol Neurosci*. 2014;**7**:73.
410. Gleixner AM, Posimo JM, Pant DB, Henderson MP, Leak RK. Astrocytes Surviving Severe Stress Can Still Protect Neighboring Neurons from Proteotoxic Injury. *Mol Neurobiol*. 2016;**53**(7):4939-4960.
411. Liddelow SA, Barres BA. Reactive Astrocytes: Production, Function, and Therapeutic Potential. *Immunity*. 2017;**46**(6):957-967.
412. Liddelow SA, Guttenplan KA, Clarke LE, Bennett FC, Bohlen CJ, Schirmer L, et al. Neurotoxic reactive astrocytes are induced by activated microglia. *Nature*. 2017;**541**(7638):481-487.
413. He Y, Jackman NA, Thorn TL, Vought VE, Hewett SJ. Interleukin-1beta protects astrocytes against oxidant-induced injury via an NF-kappaB-dependent upregulation of glutathione synthesis. *Glia*. 2015;**63**(9):1568-1580.

414. Steele ML, Fuller S, Maczurek AE, Kersaitis C, Ooi L, Munch G. Chronic inflammation alters production and release of glutathione and related thiols in human U373 astroglial cells. *Cell Mol Neurobiol*. 2013;**33**(1):19-30.
415. Steele ML, Fuller S, Patel M, Kersaitis C, Ooi L, Munch G. Effect of Nrf2 activators on release of glutathione, cysteinylglycine and homocysteine by human U373 astroglial cells. *Redox Biol*. 2013;**1**:441-445.
416. Correa F, Ljunggren E, Mallard C, Nilsson M, Weber SG, Sandberg M. The Nrf2-inducible antioxidant defense in astrocytes can be both up- and down-regulated by activated microglia:Involvement of p38 MAPK. *Glia*. 2011;**59**(5):785-799.
417. Guo X, Jiang Q, Tuccitto A, Chan D, Alqawlaq S, Won GJ, et al. The AMPK-PGC-1alpha signaling axis regulates the astrocyte glutathione system to protect against oxidative and metabolic injury. *Neurobiol Dis*. 2018;**113**:59-69.
418. Quincozes-Santos A, Nardin P, de Souza DF, Gelain DP, Moreira JC, Latini A, et al. The janus face of resveratrol in astroglial cells. *Neurotox Res*. 2009;**16**(1):30-41.
419. Asanuma M, Miyazaki I, Diaz-Corrales FJ, Kimoto N, Kikkawa Y, Takeshima M, et al. Neuroprotective effects of zonisamide target astrocyte. *Ann Neurol*. 2010;**67**(2):239-249.